

**A COMBINED ELECTROCHEMICAL AND
CATALYTIC STUDY OF THE
ENANTIOSELECTIVE HYDROGENATION OF
ETHYL PYRUVATE AT SUPPORTED PLATINUM**

**A thesis submitted to
Cardiff University
for the degree of
Philosophiae Doctor**

By

Abdullah Mohammad Alabdulrahman

**School of Chemistry
Cardiff University**

December 2007

UMI Number: U585025

All rights reserved

INFORMATION TO ALL USERS

The quality of this reproduction is dependent upon the quality of the copy submitted.

In the unlikely event that the author did not send a complete manuscript and there are missing pages, these will be noted. Also, if material had to be removed, a note will indicate the deletion.



UMI U585025

Published by ProQuest LLC 2013. Copyright in the Dissertation held by the Author.
Microform Edition © ProQuest LLC.

All rights reserved. This work is protected against
unauthorized copying under Title 17, United States Code.



ProQuest LLC
789 East Eisenhower Parkway
P.O. Box 1346
Ann Arbor, MI 48106-1346

ABSTRACT

The enantioselective hydrogenation of ethyl pyruvate to ethyl lactate (the Orito reaction) has been studied over cinchonidine-modified Pt/graphite moderated by the adsorption of S, Bi, Rh and Pd onto the Pt surface. The effect of the moderating elements on reaction rate (at 293 K, 30 bar, 100% conversion) has been examined in detail. The types of Pt site ($\{111\}$ -terraces, $\{100\}$ -terraces, steps) at which the moderating element is adsorbed has been determined by use of cyclic voltammetry.

The effect of heating Pt/graphite in H_2/Ar at temperatures between 450 and 900 K was investigated. Sintering occurred, as observed by high resolution transmission electron microscopy, causing a reduction in activity due to a decrease in surface area. A complex variation in the enantiomeric excess (ee) occurred: which reflected the relative abundance of step sites (giving high ee), $\{111\}$ -terraces (modest ee) and $\{100\}$ -terraces (low ee) on Pt particles of various size. S-adsorption favoured terrace occupation and the remaining step sites provided an increased ee. By contrast adsorption of Bi, Rh and Pd onto Pt/graphite resulted in preferential step site occupation at first and to a decrease in ee. In the case of Bi only, very low doses resulted in preferential $\{100\}$ -terrace occupation and to a transient increase in ee. Rh and Pd, unlike Bi, are potentially catalytically active metals. Rh, like Pt, favoured R-lactate formation (in the presence of cinchonidine) whereas Pd favoured S-lactate formation. The effect of Pd was therefore more extreme than that of Rh. The effect on the activity of Pt/graphite of the adsorption of S, Bi, Rh, and Pd is described in detail. For adsorption of the Bi, reaction rate passed through a maximum with increasing coverage as initial step site blocking led to a reduction in polymer formation and to a 'cleaner' surface; this was followed by deactivation as monolayer formation was approached and active surface area was reduced. In the case of Pd adsorption on Pt, the Pd catalysed the formation of a particular polymer that strongly poisoned reaction.

Novel experiments were performed in which ethyl pyruvate hydrogenation was catalysed by Pd/graphite moderated by the adsorption of Pt. [This appears to be the first study of the catalytic effects of the adsorption of Pt onto Pd]. Activity increased with increasing concentration of Pt, becoming similar to that of Pt/graphite as full surface coverage was achieved.

This investigation has mapped the relative importance of $\{111\}$ -terraces, $\{100\}$ -terraces and elementary steps in the determination of rate and enantiomeric excess in this classic enantioselective reaction, and has provided models that can be tested in future research.

PUBLICATIONS

1. D.J. Jenkins, A.M.S. Alabdulrahman, G.A. Attard, K.G. Griffin, P. Johnston, P.B. Wells, "*Enantioselectivity and catalyst morphology: step and terrace sites contributions to rate and enantiomeric excess in Pt-catalysed ethyl pyruvate hydrogenation*", *J. Catal.*, **234** (2005) 230.

ACKNOWLEDGMENT

I would like to extend my sincere thanks to my supervisor, Prof. Gary A. Attard, for his constant support, guidance, encouragement, and patience throughout the course of this study. I also thank Prof. Peter B. Wells for his advice and comments in writing of this thesis.

I also would like to thank my employer, King Abdulaziz City for Science and Technology, for funding my present study.

I also want to thank people in lab 0.117 and 0.119 for their help and support during this study.

I also wish to acknowledge all the chemistry academic staff, the technical staff in particular A. Davies, and the administrative staff in the School of Chemistry.

Finally, I would like to thank my family for their endless patience and understanding throughout the course of this study.

DEDICATION

To my family.

TABLE OF CONTENTS

CHAPTER ONE: INTRODUCTION	1
1.1 Introduction	2
1.2 Definitions	3
1.2.1 Catalysis	3
1.2.2 Adsorption	5
1.2.2.1 Physisorption	6
1.2.2.2 Chemisorption	7
1.2.3 Selectivity	8
1.2.4 Miller indices	9
1.3 Chirality	12
1.3.1 Surface molecular chirality	14
1.3.2 Intrinsic surface chirality	16
1.4 Bimetallic surface chemistry	21
1.5 Homogeneous enantioselective catalytic reactions	25
1.6 Enantioselective hydrogenation of α-ketoester in heterogeneous catalysis over cinchona-modified platinum	27
1.6.1 Orito reaction	27
1.6.1.1 Mechanistic models for α -ketoester enantioselective hydrogenation in the Orito reaction	28
1.6.1.2 Catalysts	37
1.6.1.3 Substrates	39
1.6.1.4 Modifiers and solvents	41
1.6.1 Side reaction accompanying enantioselective hydrogenation over supported Pt during the enantioselective hydrogenation of etpy	47

1.6.2.1 Transformation of CD	47
1.6.2.2 Aldol condensation of pyruvate esters catalysed by N-base of the modifier	48
1.6.2.3 Aldol polymerisation at Pt surfaces	50
1.7 Application of voltammetry for adsorption	53
1.7.1 Voltammetric techniques	53
1.7.1.1 Linear sweep voltammetry (LSV)	53
1.7.1.2 Cyclic voltammetry (CV)	54
1.7.2 Characteristics of a typical cyclic voltammogram of platinum	55
1.8 Objective of the present study	62
1.9 References	63
 CHAPTER TWO: EXPERIMENTAL	 74
 2.1 Introduction	 75
2.2 Materials	75
2.2.1 Catalysts	75
2.2.2 Reagents	76
2.2.3 Other materials	76
2.3 Apparatus and procedure	78
2.3.1 Reactors	78
2.3.1.1 Baskerville mechanically stirred reactor	78
2.3.1.2 Autoclave engineers magnadrive II mechanically stirred reactor	80
2.3.2 Experimental procedure	82
2.3.3 Product recovery	83
2.4 Procedure for catalyst modifications	83
2.4.1 Deposition of Bi on Pt/G and Pt/SiO ₂	83

2.4.2 Deposition of S, Pd, and Rh on Pt/G and Pt on Pd/G	84
2.5 Thermal annealing and sintering of catalyst	84
2.6 Product analysis	85
2.6.1 Determination of enantiomeric excess	87
2.6.2 Determination of conversion	87
2.7 Electrochemical study of catalysts	88
2.7.1 Equipment	88
2.7.2 The electrochemical cell	88
2.7.3 Water purification system	90
2.7.4 Procedure for cleaning and obtaining a typical cyclic voltammogram	91
2.7.6 Calculating of adsorbate coverage	92
2.7.6.1 Adsorbate coverage of Bi and S	92
2.7.6.1 Adsorbate coverage of Rh, Pd, and Pt	94
2.8 Transition electron microscopy	95
2.9 References	95
 CHAPTER THREE: RESULTS	 96
 3.1 Introduction	 97
3.2 Thermal annealing and its influence on enantioselective hydrogenation	98
3.2.1 CV and TEM characterisation	98
3.2.2 Catalyst sintering and reaction rate	106
3.2.3 Effect of thermal annealing on enantioselectivity	107
3.3 Bismuth adsorption on Supported platinum and its influence on enantioselective hydrogenation of ethyl pyruvate	108
3.3.1 Adsorption of Bi on Pt/G sintered at 450 K	108

3.3.1.1 CV characterisation	108
3.3.1.2 Reaction rates using bismuthated catalysts sintered at 450K	110
3.3.1.3 Enantioselectivity	112
3.3.2 Adsorption of Bi on Pt/G sintered between 600 K– 900 K	114
3.3.2.1 CV characterisation	114
3.3.2.2 Reaction rate	120
3.3.2.3 Enantioselectivity	127
3.3.3 Adsorption of Bi on Pt/SiO ₂	133
3.3.3.1 Reaction rate	133
3.3.3.2 Enantioselectivity	136
3.4 Sulphur adsorption on graphite supported platinum and its influence on enantioselective hydrogenation	139
3.4.1 CV characterisation	139
3.4.2 Reaction rate	144
3.4.3 Enantioselectivity	151
3.5 Palladium adsorption on Pt/G sintered at 700 K and its influence on enantioselective hydrogenation	156
3.5.1 CV characterisation	156
3.5.2 Reaction rate	158
3.5.3 Enantioselectivity	163
3.6 Platinum adsorption on Pd/G sintered at 700 K and its influence on enantioselective hydrogenation	166
3.6.1 CV characterisation	166
3.6.2 Reaction rate	168
3.6.3 Enantioselectivity	170
3.7 Rhodium adsorption on Pt/G sintered at 700 K and its influence on enantioselective hydrogenation	172

3.7.1 CV characterisation	172
3.7.2 Reaction rate	175
3.7.3 Enantioselectivity	177
3.8 References	179
 CHAPTER FOUR: DISCUSSION	 181
 4.1 Introduction	 182
4.2 Thermal annealing of Pt/G and its influence on enantioselective hydrogenation	182
4.3 Adatom adsorption on supported platinum and its influence on enantioselective hydrogenation	187
4.3.1 Differences in growth mode of the various adatoms on Pt	187
4.3.2 Reaction rate	192
4.3.2.1 Bismuth adsorption on supported platinum	192
4.3.2.2 Sulphur adsorption on Pt/G	197
4.3.2.3 Palladium adsorption on Pt/G	197
4.3.2.4 Platinum adsorption on Pd/G	202
4.3.2.5 Rhodium adsorption on Pt/G	202
4.3.3 Enantioselectivity	203
4.3.3.1 Bismuth adsorption	203
4.3.3.2 Sulphur adsorption	210
4.3.3.3 Palladium adsorption	211
4.3.3.4 Platinum adsorption	213
4.3.3.5 Rhodium adsorption	214
4.4 References	216

CHAPTER FIVE: SUMMARY AND FUTURE WORK	221
5.1 Summary and future work	222
5.2 References	226

CHAPTER ONE

INTRODUCTION

1.1 Introduction

In 2001, the Nobel Prize in Chemistry was awarded to Knowles, Noyori, and Sharpless for their contribution for the development of catalytic asymmetric synthesis and in 2007, the importance of surface science also was recognised by the award of the Nobel Prize to G. Ertl [1]. The present study straddles both of these important scientific fields.

The demand for chiral molecules, often as single enantiomers, has been significant in recent years. These molecules constitute an important class of pharmaceuticals, agrochemicals, flavours, and fragrances. Asymmetric catalysis is not only beneficial for the practical synthesis of high added-value compounds, but also stimulates the development of the life sciences and nanotechnology based on chiral molecules [2]. Homogeneous asymmetric catalysis is presently the most versatile and efficient [3]. However, recently, heterogeneous asymmetric catalysis has also become a rapidly growing and challenging field [4]. Chirality (handedness) is a phenomenon that is widely spread in the universe [5]. For example, all of the amino acids that form proteins in our body are nonsuperposable on their mirror image and are therefore chiral possessing a single handedness [5]. Generally only enantiomeric forms of such a compound are effective in a living system. One of the most important challenges facing heterogeneous catalysis is the control of enantioselectivity. This is because heterogeneous catalysis poses many advantages in relation to homogeneous catalysis, such as ease of separation and handling of catalyst together with potentially high throughputs of raw materials.

Catalyst modification by an adsorbed chiral organic molecule is a strategy which is applied extensively in enantioselective hydrogenation. In this study, a catalytic study of bi-metallic surfaces has been undertaken in relation to the enantioselective hydrogenation of ethyl pyruvate (etpy) over cinchona modified platinum catalysts in order to elucidate mechanistic steps in this prototypical enantioselective surface reaction.

1.2 Definitions

1.2.1 Catalysis

A catalyst is a substance which increases the rate at which a chemical system approaches equilibrium without itself being consumed in the process. Ostwald defined catalysts as “*agents which accelerate chemical reaction without affecting the chemical equilibrium*”. The term *catalysis* was first coined by Berzelius in 1835 [6]. In 1817, Doberenier reported that reaction of hydrogen and oxygen over a platinum surface at ambient temperature increased the reaction rate [7]. A catalyst accelerates the reaction rate by lowering the activation energy of the reaction as shown in Figure 1.1, and leads to the reaction proceeding via a different pathway. The relationship between rate constant (k) and activation energy (E_a) in a chemical reaction is described by the Arrhenius equation:

$$k = A \exp (-E_a/RT) \quad 1.1$$

(where A = collision frequency, R = gas constant, and T = temperature)

Catalysts cannot influence the equilibrium constant (and therefore ΔG°) but they can speed up reactions which are thermodynamically feasible. Catalysis does not change the equilibrium constant. Rather, it can enhance both the forward and the backward reaction rates equally.

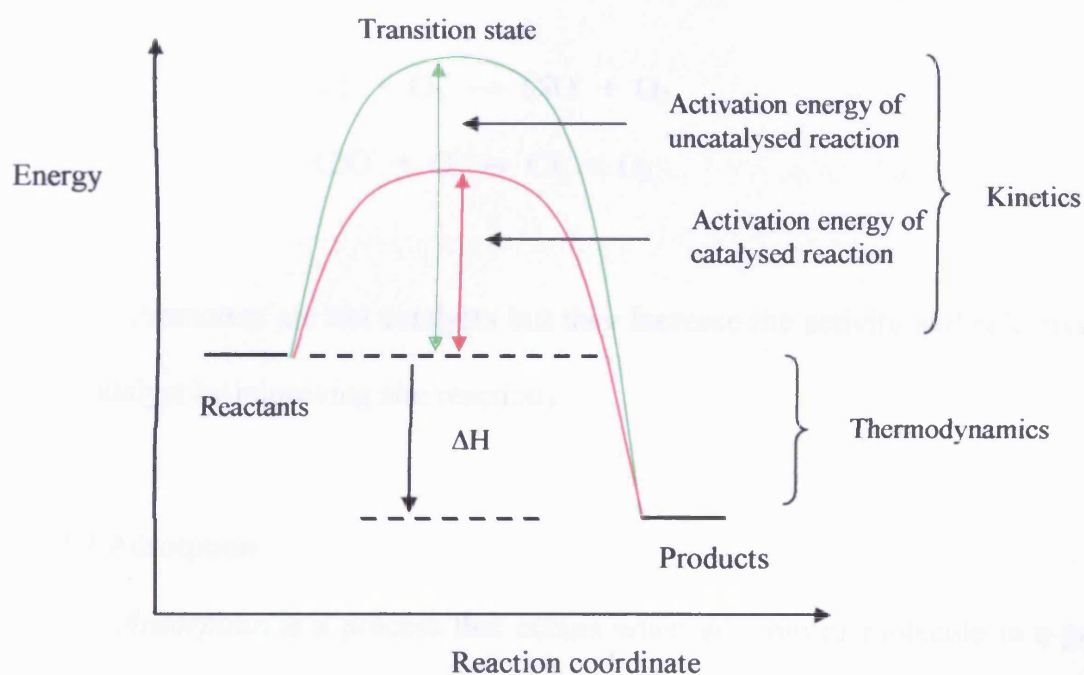


Fig. 1.1 The reaction profile for catalysed and uncatalysed exothermic reactions.

Catalysis can be classified according to the number of reaction phases as heterogeneous, homogenous, or enzymatic. In heterogeneous catalysis, the catalyst and the reactant are in different phases. An example of this type of catalysis is

ammonia synthesis from hydrogen and nitrogen catalysed by iron (Haber process)

[8]:



In homogeneous catalysis, the catalyst and the reactant are in the same phase. For example, ozone depletion in the upper atmosphere is catalysed by chlorine free radicals:



Promoters are not catalysts but they increase the activity and selectivity of the catalyst by improving site reactions.

1.2.2 Adsorption

Adsorption is a process that occurs when an atom or molecule in a gas or liquid phase (adsorbate) bonds to the surface of a solid or liquid (adsorbent). It differs from *absorption*, in which a molecule diffuses into the bulk of the substance. The fractional coverage of adsorbate, θ , is defined as:

$$\theta = \frac{\text{Number of adsorbed atoms or molecules}}{\text{Total number of substrate adsorption sites}} \quad 1.5$$

When $\theta = 1$, the adsorbate ensemble is called a monolayer [9].

The process whereby reactants or products leave the surface is called *desorption*. Adsorption/desorption processes are important to a large number of phenomena at the solid/gas or solid/liquid interface [10]. There are two types of adsorption depending on the nature of interaction between the adsorbate and adsorbent. These are physical adsorption (physisorption) and chemical adsorption (chemisorption).

1.2.2.1 Physisorption

Physisorption occurs when the adsorbate bonds to the surface through Van der Waals interactions which are long range and weak, when compared to covalent or ionic bonds [11]. Physisorption tends to be reversible. Hence, the adsorbate is normally in equilibrium with the gas phase. Van der Waals interactions are the only way that rare gases can interact, therefore they can bond to the surface via physisorption only [12]. Gases such as argon and krypton are used to determine the surface area of a solid via measurements of their Langmuir or BET isotherms [9]. When a molecule moves along a surface, it gradually loses its energy and finally adsorbs, which is called *accommodation* [13]. The process is exothermic and the enthalpy exhibits a range of small values (10-40 kJ mol⁻¹) [14]. This energy is of the same order of magnitude as the enthalpy of condensation. These small energies can be transferred to the lattice and dissipated as thermal motion. Physisorption bonding is characterised by a redistribution of charge density within the adsorbate and the surface atom or molecule separately.

1.2.2.2 Chemisorption

In chemisorption, a strong chemical (usually covalent) bond is formed between the surface (adsorbent) and the adsorbate (atoms or molecules). Adsorbates tend to adsorb at sites exhibiting low coordination number [15]. Chemisorption differs from physisorption in that the enthalpy of chemisorption is much larger than that of physisorption, ranging between 40 and 1000 kJ mol⁻¹ [14], and is characterised by electron transfer between the adsorbate and the surface. The bond distance between the adsorbate and the surface is shorter than that of physisorption. In order to satisfy the valences of surface atoms, a chemisorbed molecule may fragment and the formation of chemisorbed molecular fragments on the surface as a result of dissociation is one reason why solid surfaces catalyse reactions [15]. As a result, there are two types of chemisorption depending on the nature of the interaction with the surface. Associative or non-dissociative chemisorption occurs when the adsorbate molecule remains on the surface without dissociation. For instance, the adsorption of CO on a low index copper surface as shown below [14]:



where the “—” indicates a chemisorption bond.

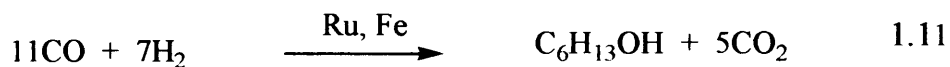
The other type of adsorption (dissociative chemisorption) occurs when the adsorbate molecule breaks up on the surface forming molecular fragments which

bond to the surface. An example of dissociative adsorption is adsorption of hydrogen on a copper surface, which forms a monolayer of hydrogen adsorption at a pressure of 100 mbar and at room temperature as follows [14]:



1.2.3 Selectivity

The term *selectivity* (S) is used to describe the extent to which a catalyst produces the desired product. This is important in industrial applications. The same reaction produces different products according to the type of catalyst that is used. For instance, the reaction of hydrogen with carbon monoxide can proceed along different pathways as follows [16]:



The above reactions are all thermodynamically possible and have negative values of ΔG . Different products are formed due to the use of a variety of catalysts, which make the reaction proceed via different energy pathways.

1.2.4 Miller indices

Most metals form in one of three crystal structures: face-centred cubic (fcc), body-centred cubic (bcc), and hexagonal-closed pack (hcp). The surface of a metal is usually heterogeneous. Hence structure sensitive reactions such as adsorption will occur to different extents with different Miller planes. Miller indices are used to define a particular crystal plane, the summation of surface reactivity on each crystal plane giving rise to total catalytic activity. To identify the Miller index of a particular set of planes in a three dimensional lattice the following steps are used [9, 14, 17]:

1. Find the intercepts of the required crystal with the three vectors \vec{a} , \vec{b} , and \vec{c} defining the unit cell (Figure 1.2(a)).
2. Let the distance from the origin to the points of intersection of the plane with the three vectors \vec{a} , \vec{b} , and \vec{c} be a , b , and c respectively.
3. Let $\frac{|\vec{a}|}{a} = h$, $\frac{|\vec{b}|}{b} = k$, $\frac{|\vec{c}|}{c} = l$
4. Form the triple (hkl)
5. If there are any fractions in the triple, reduce to the smallest integers having the same ratio: e.g. $(2/4 \ 1/4 \ 1/4) \rightarrow (2 \ 1 \ 1)$.
6. For intersection of the plane at negative values, a bar is placed above the appropriate h , k , or l .

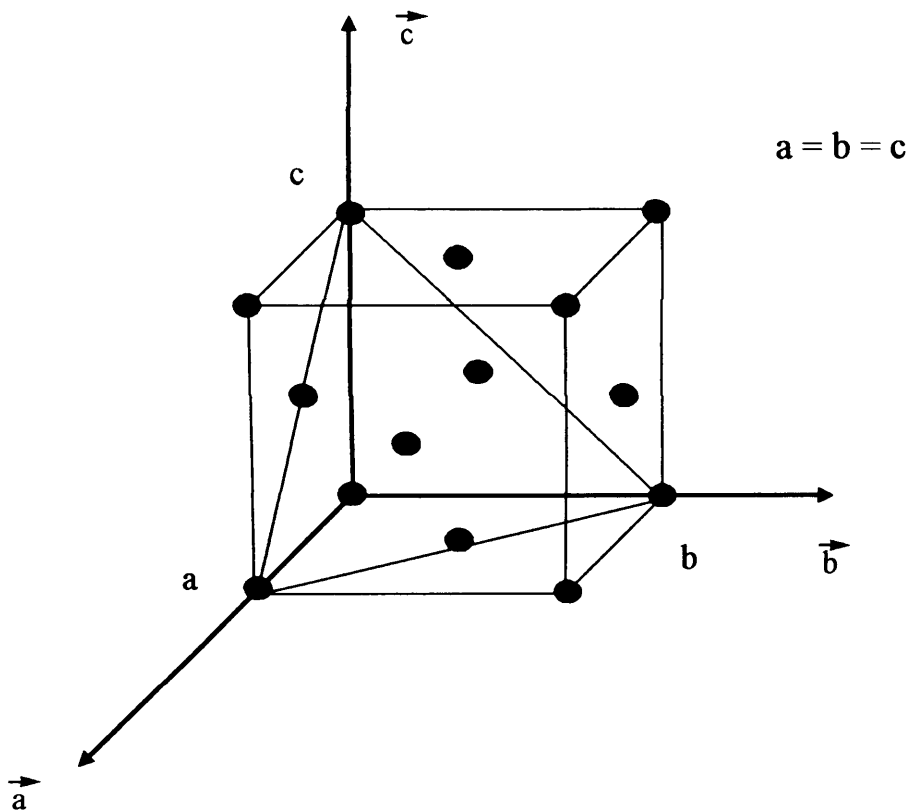


Fig. 1.2(a) The three vectors \vec{a} , \vec{b} , and \vec{c} defining the crystal unit cell and being intercepted by the $\{111\}$ Miller index.

Figure 1.2(b) shows the (100), (110), and (111) planes in a face centred cubic crystal and their corresponding face-centred cubic atomic structures. The triple of integers (hkl) is referred to as the Miller index of this plane and all planes parallel to this plane. Different planes have different geometric arrangement of the atoms, hence these planes contain different adsorption sites and chemical reactivity. Low Miller index surfaces are the most studied, due to their low surface free energy, high symmetries, and relative stabilities [13].

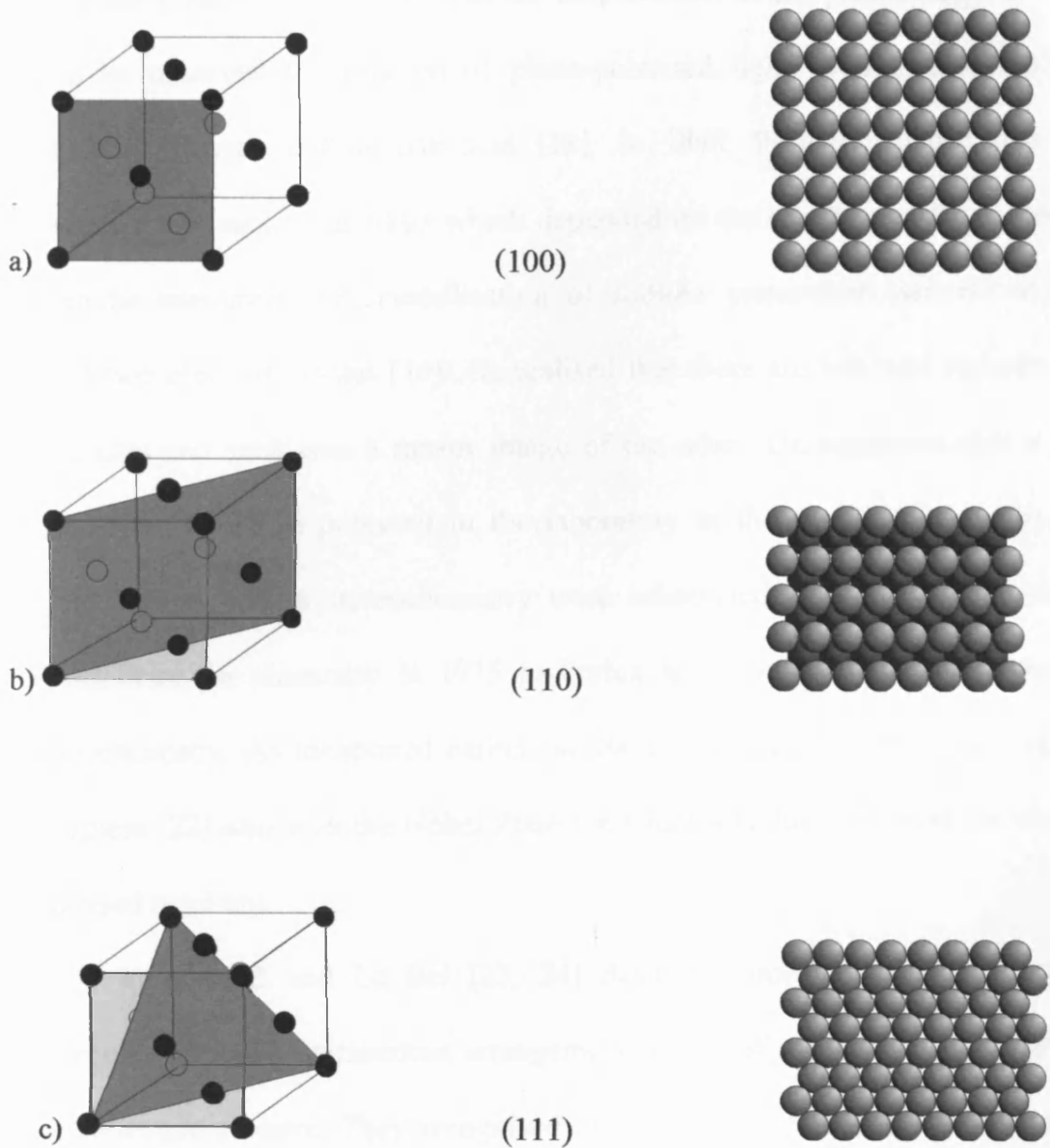


Fig. 1.2(b) Low Miller index planes of a) (100) , b) (110) , and c) (111) and their corresponding surface structure of a face-centred cubic lattice.

1.3 Chirality

Optically active molecules can be detected when chiral molecules interact with plane-polarised light. Biot was the first to observe this phenomenon in 1815 when he observed the rotation of plane-polarised light upon passing through solutions of sugar and tartaric acid [18]. In 1848, Pasteur deduced that this property had a molecular basis which depended on the structure of the molecule. When he examined the crystallisation of sodium ammonium para-tartrate, he found two types of crystal [19]. He realised that there are left- and right-handed molecules and each was a mirror image of the other. He suggested that a pure enantiomer could be prepared in the laboratory in the presence of a directing agent. Researchers in stereochemistry were acknowledged by the award of the Nobel Prize for chemistry in 1975 to Prelog and Cornforth for their work on stereochemistry. As mentioned earlier, in 2001, Knowles [20], Noyori [21], and Sharpless [22] also won the Nobel Prize for Chemistry for their work on chirally catalysed reactions.

Van't Hoff and Le Bel [23, 24] described optical activity in organic molecules using the tetrahedron arrangement model of substituent atoms around the stereogenic centre. They recognised that the four substituent atoms arranged tetrahedrally around the carbon atom must be different in order to generate two different *enantiomers*. In 1966, Cahn, Ingold, and Prelog addressed the nomenclature of chiral molecules [25]. A molecule can be chiral if it is not superimposable on its mirror image, as shown in Figure 1.3. Molecules which are

not superimposable on each other, but are mirror images of each other, are called enantiomers. Chiral molecules have the property to rotate plane-polarised light so they are optically active. When a molecule can be superimposed on its mirror image then it is called achiral. A racemic mixture is a mixture that contains two enantiomers in equal amounts. Enantiomers have the same chemical and physical properties. Cahn-Ingold-Prelog rules are used to assign the absolute configuration of a stereogenic centre [26] (Figure 1.3). The highest atomic number (Br) around the stereogenic centre will have the highest priority; it will be assigned Number 1. A lower atomic number substituent (Cl) will be given No.2, etc.. In the case where two atoms directly bonded to the stereogenic centre are the same, for instance, if -CH₃ and -CO are bonded to the stereogenic centre, -CO will have the highest priority because the carbon is bonded to O, which has a higher atomic number than H on the -CH₃ substituent. The molecule is then positioned such that the substituent of lowest priority is pointing down. If viewed from above with the sequence from the highest to the lowest priority substituent in a clockwise direction, the molecule will be designated an R-enantiomer whereas if the same sequence in an anti-clockwise direction, the molecule will be designated an S-enantiomer (Figure 1.3).

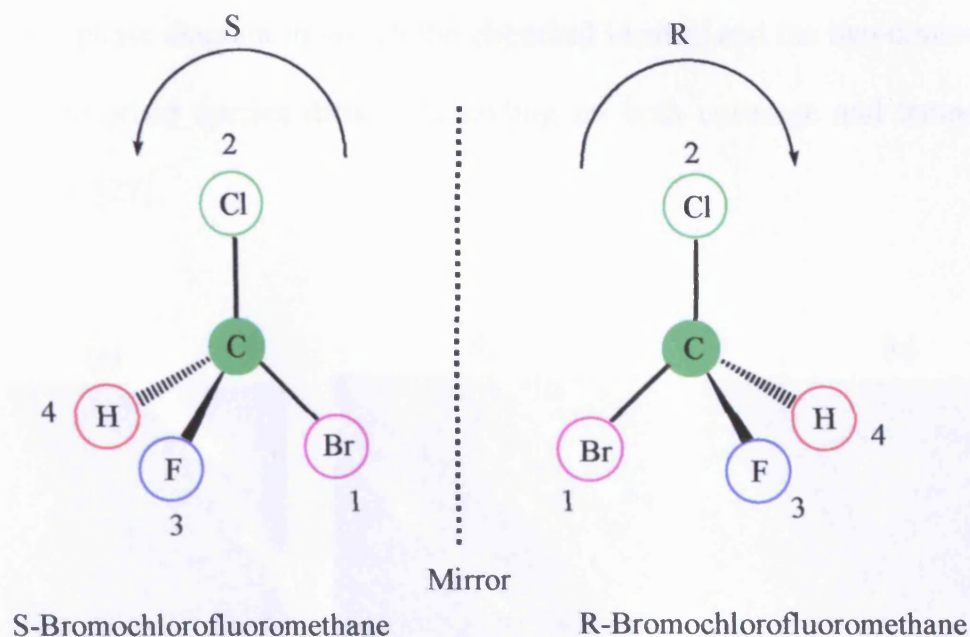


Fig. 1.3 Enantiomeric presentation of bromochlorofluoromethane.

A chiral metal surface can gain its chirality by adsorption of chiral molecules or by the metal surface itself being structurally chiral. These two types of chirality will be discussed below.

1.3.1 Surface molecular chirality

Adsorption of chiral molecules at an achiral metal surface can induce chirality to the metal surface as reported by Raval and co-workers [27]. R,R-Tartaric acid (which is known as an effective modifier in enantioselective hydrogenation of β -ketoesters over supported nickel catalysts) has been studied as a chiral modifier on an achiral Cu(110) surface. Raval and co-workers produce an

adsorption phase diagram in which the chemical identity and the two-dimensional order of adsorbed species differs depending on both coverage and temperature (Figure 1.4) [27].

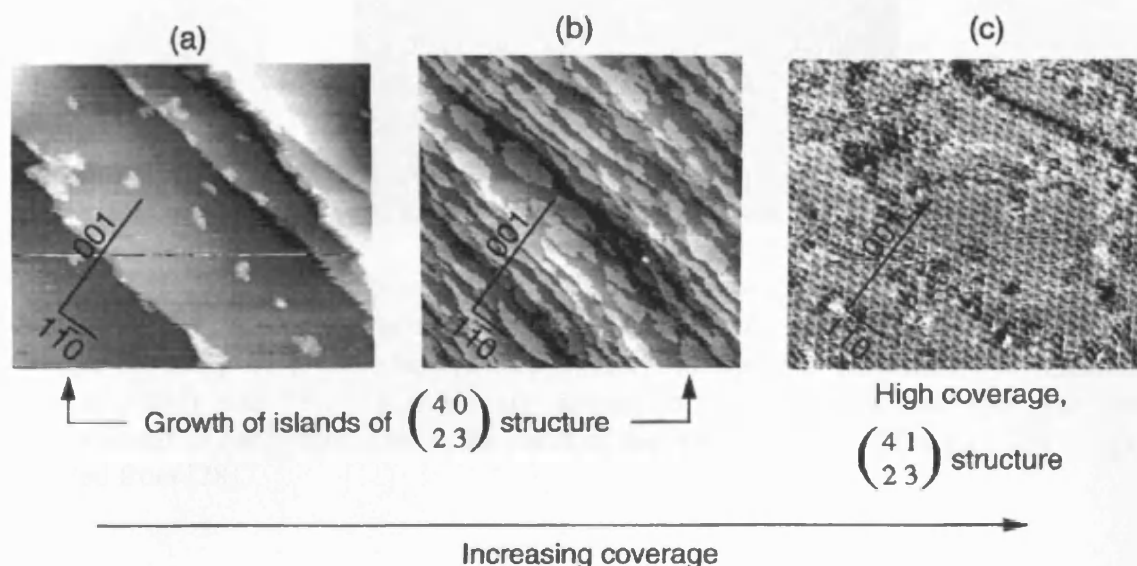


Fig 1.4 STM images of the adsorption of R,R-tartaric acid (different coverages) over Cu(110) at 300 K. STM images (a) (500 x 500 Å) and (b) (1000 x 1000 Å) show the formation of (4 0, 2 3) islands with increasing coverage. Image (c) (300 x 300 Å) shows the high coverage (4 1, 2 3) monolayer. Reproduced from [27].

Zhao later reported [28] adsorption of a chiral modifier (L-lysine) over a Cu(100) surface and the formation of chiral kink sites (see later) on the metal surface (Figure 1.5).

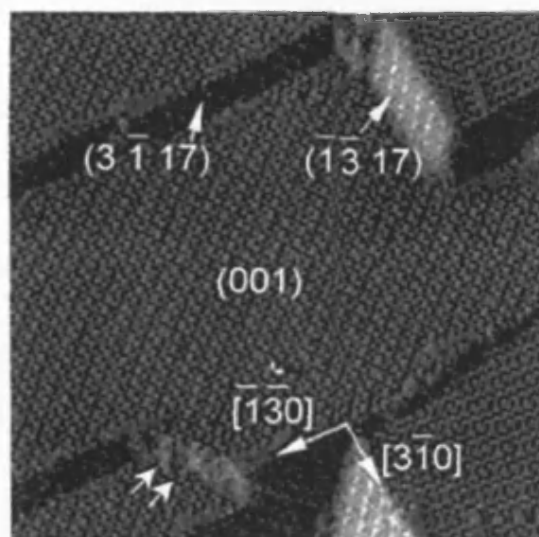


Fig 1.5 STM image ($550 \times 550 \text{ \AA}$) acquired from the L-lysine/Cu(001) surface annealed at 430 K for 20 mins, showing coexistence of (001) terraces and $\{3,1,17\}$ facets formed through bunching of $\langle 3\bar{1}0 \rangle$ faceted steps. Note that the two neighboring intersection lines of (001) and $\{3,1,17\}$ planes are always in $\langle 3\bar{1}0 \rangle$ directions and thus are perpendicular to each other. This is the result of the homochirality of the $\{3,1,17\}$ facets. Adapted from [28].

1.3.2 Intrinsic surface chirality

Gellman and co-workers [29] first introduced the notion of intrinsic chirality at solid surfaces when they proposed that kink sites on high Miller index metal surfaces of a single crystal may be chiral when the step lengths forming the kink sites were unequal (Figure 1.6). They investigated LEED patterns from both faces of a sides single crystal ($\text{Ag}(643)$ and $\text{Ag}(\bar{6}4\bar{3})$). These surfaces were named by those workers $\text{Ag}(643)^R$ and $\text{Ag}(643)^S$ according to a modified version of the Cahn-Ingold-Prelog rules. They tested the original hypothesis of surface chirality through adsorption and desorption of a chiral molecule, R- and S-2-

butanol on kink surfaces of $\text{Ag}(643)^{\text{R}}$ and $\text{Ag}(643)^{\text{S}}$ using thermal programmed desorption. They found that there was no chiral selectivity observed in the desorption of R- and S- 2-butanol [29]. Later, based on theoretical calculations, Sholl [30] predicted these to be an enantiospecific adsorption energy difference in chiral systems.

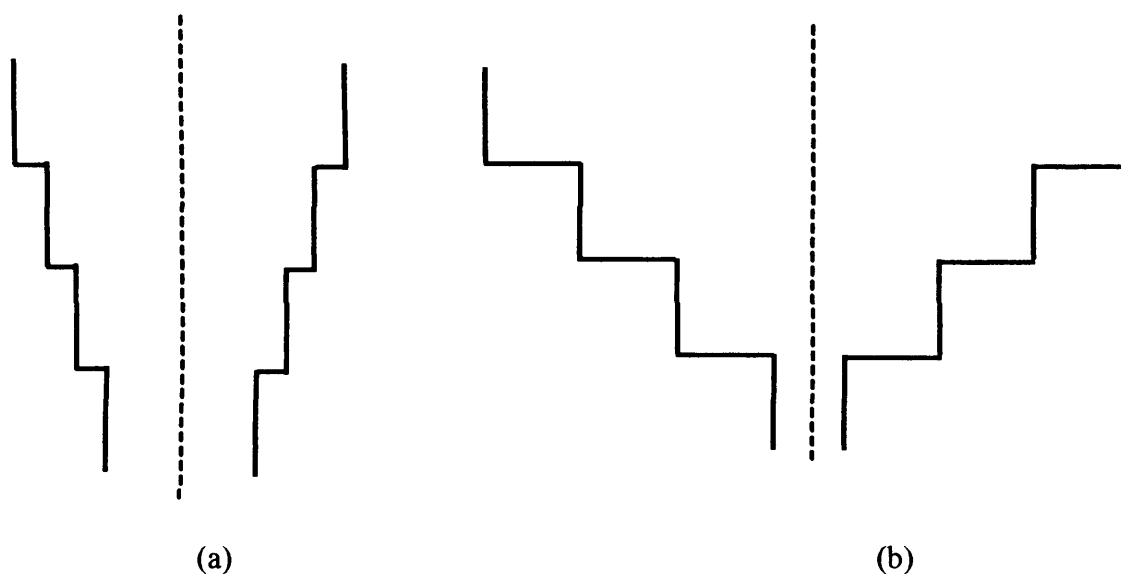


Fig. 1.6 Schematic diagram of metal kink sites: (a) a kink step edge of different lengths which is non superimposable on its mirror image upon rotation in the plane of the paper (the kink is chiral), and (b) a kink step edge of the same length that by rotation of 90° is superimposable on its mirror image (the kink is achiral). Reproduced from reference [31].

In 1999, Attard and Feliu [32, 33] broadened Gellman's model of surface chirality by introducing intrinsic chirality in the atomic microstructure of both the terrace and the two joining steps forming the kink site (Figure 1.7). Accordingly, all single crystal surfaces were chiral as long as their atomic microstructures were

different, irrespective of the step lengths which formed the kink sites as shown in Figure 1.6. This model did not differentiate between steps of different length as in Gellman's model. The kink site can be described as the junction of the three surface planes of the face-centred cubic (fcc) metal, namely (111), (100), and (110) planes. Attard assigned priority of these planes according to Cahn-Ingold-Prelog rules where the higher surface atom density will have the higher priority. For fcc metals, the surface atom density order for planes is $(111) > (100) > (110)$. When planes sequences are in the order of {111}-{100}-{110} in a clockwise direction, they will be considered R-kinks and where in an anti-clockwise direction they will be considered S-kinks as shown in Figure 1.7 [32].

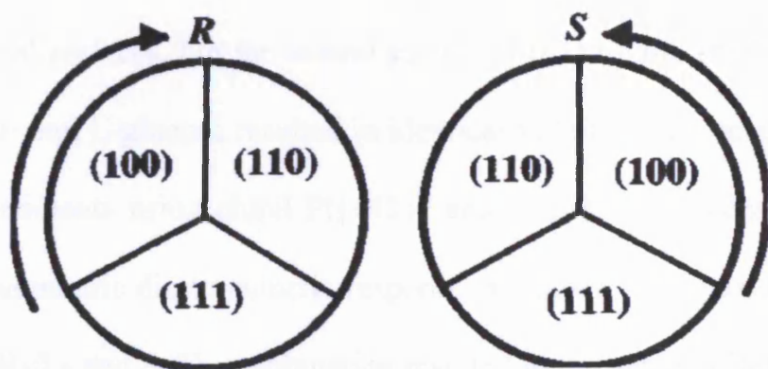
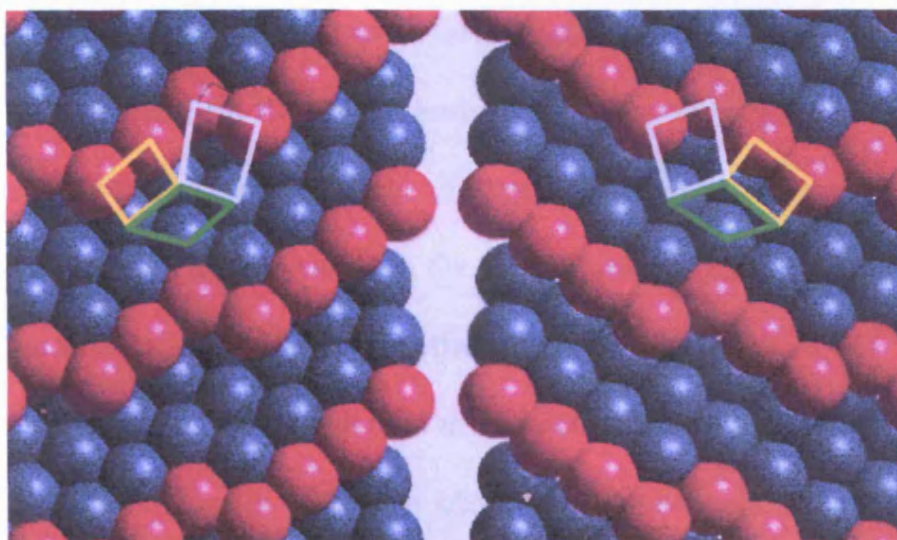


Fig 1.7 Diagram showing models of the $\text{Pt}(643)^R$ (left) and $\text{Pt}(643)^S$ (right) surfaces, where the $\{111\}$ terrace (green), $\{100\}$ (yellow), and $\{110\}$ (white) [top]. Kinked chiral surfaces may be represented as the junction between the three Miller index planes [bottom]. Reproduced from reference [32].

Kinked surfaces that contain $n(110) \times (100)$ or $(100) \times (110)$, where the step lengths are the same, are the exception to this rule, since the (110) step consists of the interception of two (111) planes. Such kinked surfaces are achiral due to the fact that there are two steps of equal length that also have the same atomic

microstructure. The nomenclature developed by Attard *et al.* [32] has recently been refined still further by Jenkins and co-workers [34] that can be applied for example to bcc metals which, although chiral, do not appear to exhibit “kink” sites as discussed above. Although the Jenkins nomenclature is applied to all materials, because for fcc systems the Attard nomenclature is somewhat more straightforward, it will be used to describe surface symmetry in this thesis.

Attard *et al.* [32] also observed the first experimental confirmation that kinked surfaces of metal single crystal have intrinsic chirality using the electrooxidation of D- and L-glucose on both achiral and chiral platinum single crystal surfaces. For the achiral surfaces Pt{111} and Pt{211}, the electrooxidation of D- and L-glucose resulted in identical voltammetric responses. Repeating these experiments using chiral Pt{643}^S and {643}^R electrodes resulted in a different voltammetric diastereomeric response, as shown in Figure 1.8. Electrooxidation of the R-/L- and S-/D- combination resulted in the same voltammetric profile. The R-/D- and S-/L- also produced identical voltammetric waves. However, each of these pairs of responses was different from each other. Further, the enantioselectivity towards glucose electrooxidation was found to increase with increasing surface density of kink sites [35], the Pt{531} surface (which contained most kinks) showed the greatest differences between the electrooxidation of D- and L-glucose for any chiral surface.

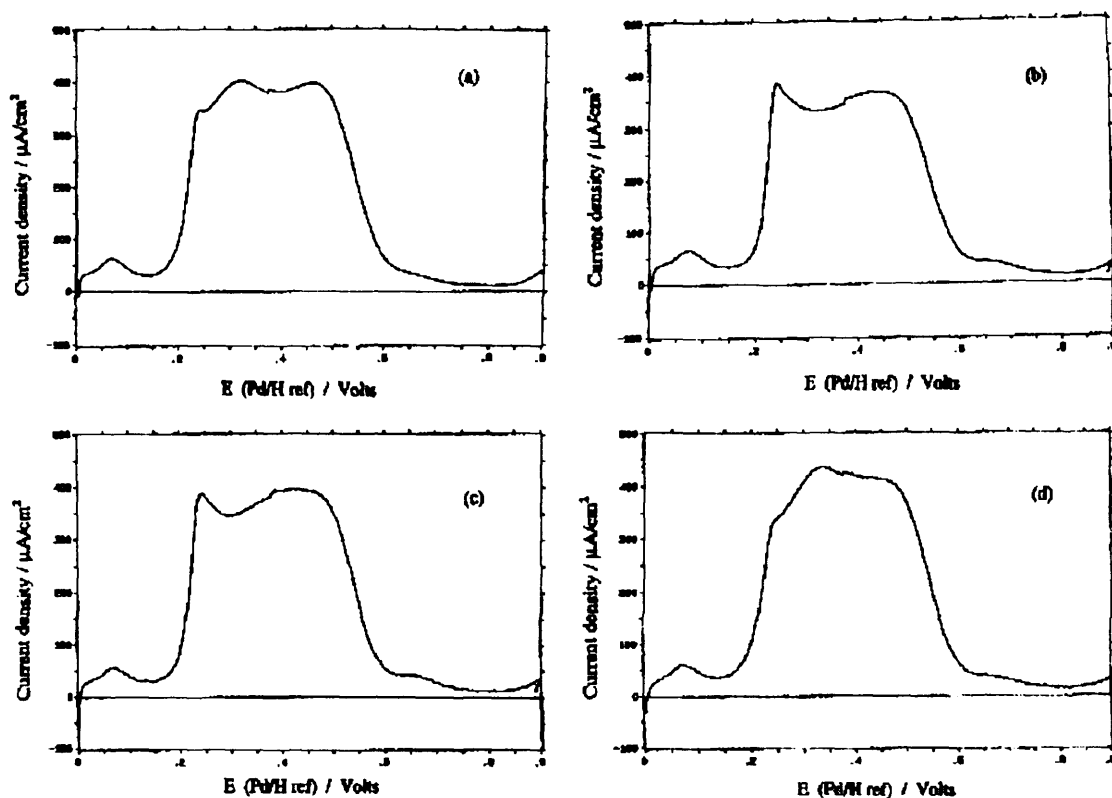


Fig. 1.8 Pt{643}^S voltammogram in (a) 0.05 M H₂SO₄ + 5 × 10⁻³ M D-glucose or (b) 0.05 M H₂SO₄ + 5 × 10⁻³ M L-glucose. Pt{643}^R voltammogram in (c) 0.05 M H₂SO₄ + 5 × 10⁻³ M D-glucose or (d) 0.05 M H₂SO₄ + 5 × 10⁻³ M L-glucose. Sweep rate = 50 mV/s. A clear enantiomeric difference in oxidation rate at 0.3 V is observed using the kinked electrode surface. Reprinted from [32].

1.4 Bimetallic surface chemistry

Bimetallic surfaces impart unique chemical and physical properties which differ from each of the individual metals comprising the bimetallic structure including electronic and catalytic properties [36]. They have an important application in catalysis, magneto-optical films, corrosion, and structural materials

[9]. In catalysis, the adsorption of a metal such as Bi on supported Pt increases catalyst activity and decreases the catalyst poisoning during the electrooxidation of HCOOH and glucose [37]. In 1958, Bauer [38] proposed a theoretical description of thin film growth based on a thermodynamic approach. This model was confirmed later after many experiments had been conducted [39]. The three basic growth modes of deposition on a metal surface are shown in Figure 1.9:

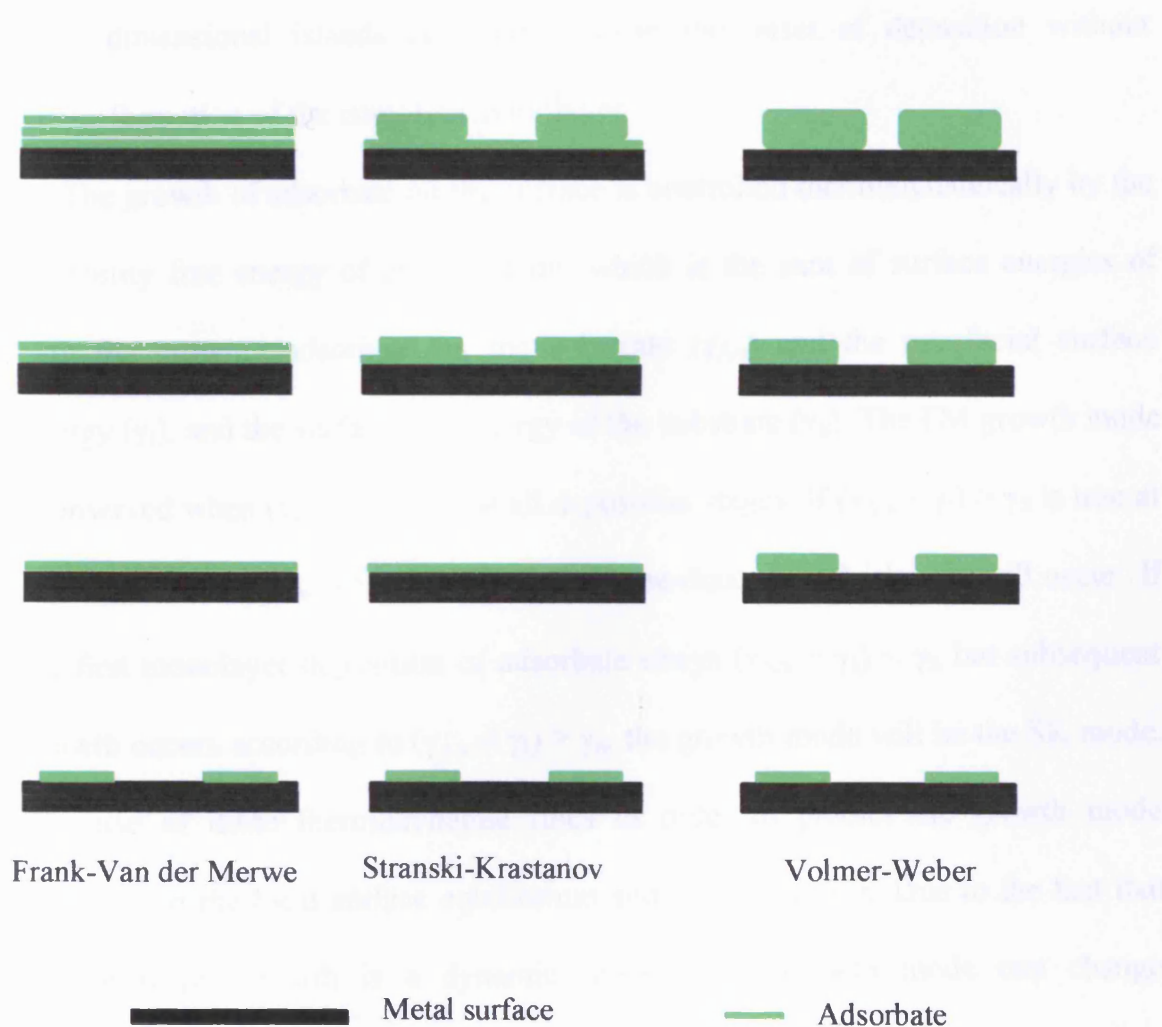


Fig 1.9 Schematic diagram of the basic three growth modes of thin film deposition on a metal surface.

1. Frank-van der Merwe (FM) [40, 41] or layer-by-layer growth in which the second layer commences to grow after the completion of the first, the subsequent layers growing in the same manner.
2. Stranski-Krastanov (SK) [42] growth where the complete first layer is formed as in FM growth followed by three-dimensional islands growth.
3. Volmer-Weber (VW) growth [43] in which the growth of the three-dimensional islands commences from the onset of deposition without formation of the complete monolayer.

The growth of adsorbate on the surface is controlled thermodynamically by the instability free energy of an adsorbate, which is the sum of surface energies of both the growing adsorbate on the substrate ($\gamma_{A/s}$) and the interfacial surface energy (γ_I), and the surface free energy of the substrate (γ_S). The FM growth mode is observed when $(\gamma_{A/s} + \gamma_I) < \gamma_S$ at all deposition stages. If $(\gamma_{A/s} + \gamma_I) > \gamma_S$ is true at all deposition stages, VW growth mode (three-dimensional islands) will occur. If the first monolayer deposition of adsorbate obeys $(\gamma_{A/s} + \gamma_I) < \gamma_S$ but subsequent growth occurs according to $(\gamma_{A/s} + \gamma_I) > \gamma_S$, the growth mode will be the SK mode. The use of these thermodynamic rules in order to predict the growth mode depends on the local surface equilibrium and kinetic factors. Due to the fact that the overlayer growth is a dynamic process, the growth mode can change depending on both temperature and crystallographic orientation of the substrate, indicating that kinetic factors can be more dominant than energetic considerations. Indeed, if equilibrium cannot be reached due to the kinetic limitations, the entire

energetic description is considered inappropriate [44, 45]. Limitations of the proposed thermodynamic model were observed with experiments involving scanning probe microscopies [46]. Determination of the theoretical growth mode requires accurate values of surface and interfacial energies which are generally unavailable. It is therefore, necessary to assume simplifications, where the surface energy of the adsorbate on the substrate $\gamma_{A/s}$ is assumed to be equal to the surface energy of the adsorbate (γ_A). This approximation is inadequate in the case of a few monolayers of adsorbate thickness and would be inaccurate if any lattice mismatch occurred between the two materials, because this lattice mis-match would induce stress energy into the adsorbate, which would gradually increase with adsorbate thickness, causing a change to the adsorbate surface energy. Hence, the adsorbate surface energy is necessary to determine the adsorbate energy as a function of adsorbate thickness. Further thermodynamic parameter simplifications were made [47] by assuming that the interfacial energy was very small in comparison with the surface energy of the adsorbate and the substrate. Therefore, FM growth mode occurred when $\gamma_A < \gamma_S$ while VW occurred when $\gamma_A > \gamma_S$. Although interfacial free energy is likely much smaller than other surface free energies, if the interfacial energy is significant, it will strongly influence the initial growth of adsorbate [48, 49]. The role of the dynamic processes which form the three basic growth modes has not been mentioned above. Particularly when the adsorbate is relatively refractory or low substrate temperatures are employed or when the vapour flux is high, an overlayer formed may display metastable

behaviour which is due to slow kinetic rather than equilibrium growth. This behaviour produces two additional growth modes: the simultaneous multilayers (SM) mode and the monolayer plus simultaneous multilayers (MSM) mode [50]. The SM growth mode was analysed by Kaschiev [51] who found it to be a metastable form of the FM growth mode, and is often referred to as pseudo-FM [52].

1.5 Homogeneous enantioselective catalytic reactions

In homogeneous catalysis, a chiral organometallic complex (which has a chiral ligand) catalyses the reaction of an achiral organic molecule and the reaction is carried out in the same phase. An active catalyst must have the ability for enantiodiscrimination and for lowering the energy of the transition state of the reaction. Hence, the formation of two diastereomeric complexes having substantially different energies will lead to high enantioselectivity. In homogeneous catalysis, the metal atom is directly influenced by the environment of the chiral ligand and at the same time provides the active site for the reaction [53]. Ligand substituents play an important role in the obtained enantiomeric excess (ee). The Binap-Ru catalysts are an example of excellent ligand-metal complexes that allow efficient enantioselective hydrogenation of functionalized olefin and ketones producing a high ee (up to 99%) [54]. For example, the enantioselective hydrogenation reaction of aromatic ketones (Figure 1.10) [55].

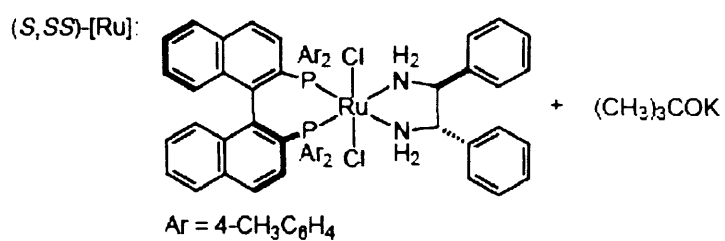
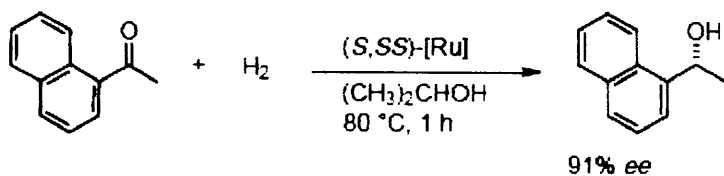


Fig. 1.10 Productive and fast homogeneous enantioselective hydrogenation. Reproduced from [55].

Homogeneous chiral catalysts exhibit high activity and selectivity and the reaction mechanism can be investigated via spectroscopic studies. However, difficulties of separation and handling are major disadvantages.

over cinchona-modified platinum

1.6.1 Orito reaction

In 1979, Orito *et al.* [56-58] reported the first enantioselective hydrogenation reaction over cinchona modified Pt/C (Figure 1.11). In this reaction, 5% Pt/C was pre-treated with a solution of CD and was used subsequently to catalyse the hydrogenation of methyl pyruvate and produce R-methyl lactate in high excess. In the absence of the modifier, hydrogenation was found to be slow and yielded a racemic mixture. Catalyst pre-heating was investigated by the same group who found that heating the catalyst in hydrogen to 573 K was optimal for high ee. The reaction is normally carried out in the liquid phase at room temperature and high pressure; different solvents can be used such as toluene, dichloromethane, ethanol, and acetic acid. The best results have been achieved upon using acetic acid [59].

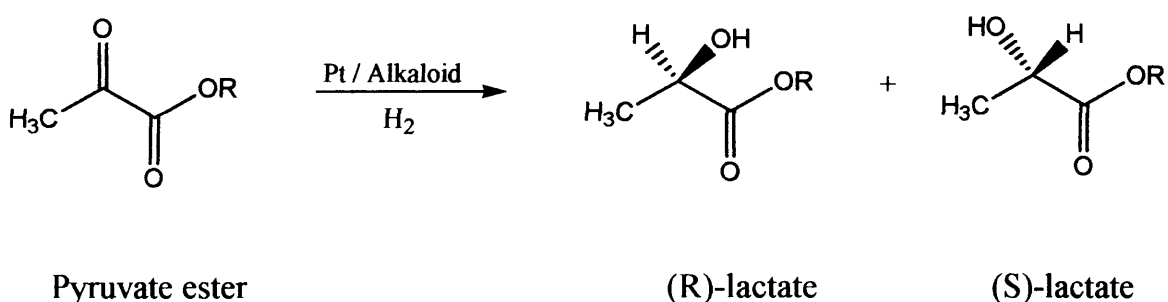


Fig. 1.11 The Orito reaction. (R = -CH₃, -C₂H₅).

1.6.1.1 Mechanistic models for α -ketoester enantioselective hydrogenation in the Orito reaction

Wells' model

In 1990, Wells *et al.* [60] proposed the first model (*Template Model*) interpreting the observed enantioselectivity on supported Pt. This model described ordered arrays of adsorbed CD on a Pt surface which created preferential adsorption sites. Reactant-modifier interaction was not involved in this model. Later, in 1994, Wells *et al.* [61] replaced the template model with the 1:1 interaction model between the reactant which was methyl pyruvate and the adsorbed alkaloid on a Pt surface. In this model, hydrogen bonding between CD in the open-3 conformer (most stable) with the quinuclidine-N and methyl pyruvate with the carbonyl group in ant-conformation (lower energy conformation)(N...H-O type) is proposed as in Figure 1.12. The formed half-hydrogenated state (lhs) stabilized by the H-bonding can be used to interpret the rate enhancement induced by the modifier and the observed enantioselectivity [62].

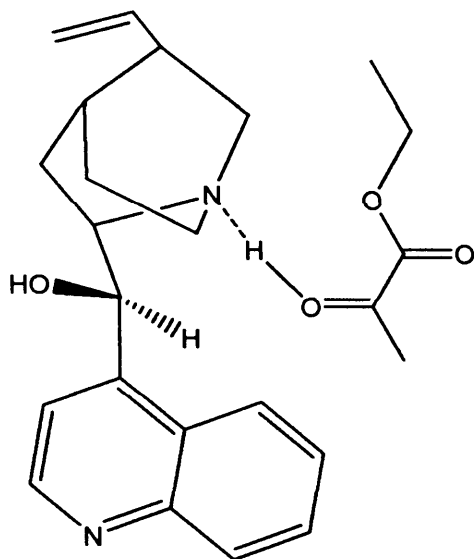


Fig. 1.12 Intermediate modifier-substrate interaction proposed by Wells *et al.*

Baiker's model

Baiker and co-workers suggested a model for enantioselection in acetic acid in which the formation of protonated quinuclidine-N of CD is proposed [63]. The protonated quinuclidine-N interacts with the oxygen atom of the keto-carbonyl of pyruvate ester with a 1:1 interaction via H-bonding (Figure 1.13). This model is supported by theoretical calculations [64, 65], and is similar to that proposed by Wells for aprotic solvent since both propose an N-H-O type interaction.

Later, Burgi [66] using theoretical calculations proposed the formation of a bifurcated H-bond interaction between the quinuclidine ring and the two adsorbed

diastereomeric pyruvate esters pro-(R) and pro-(S) (Figure 1.13). Figure 1.13 shows the proposed interaction of *cis* and *trans* ethyl pyruvate with the modifier (CD). The *trans* conformation is proposed to be more stable. A repulsive interaction occurs between the ethyl group of ethyl pyruvate in pro-(S) form and the quinoline ring of CD. This repulsion will produce different stabilization energies for pro-(S) and pro-(R) forms. It is postulated that this difference is responsible for both rate acceleration (hydrogen bonding to carbonyl) and enantioinduction in enantioselective hydrogenation.

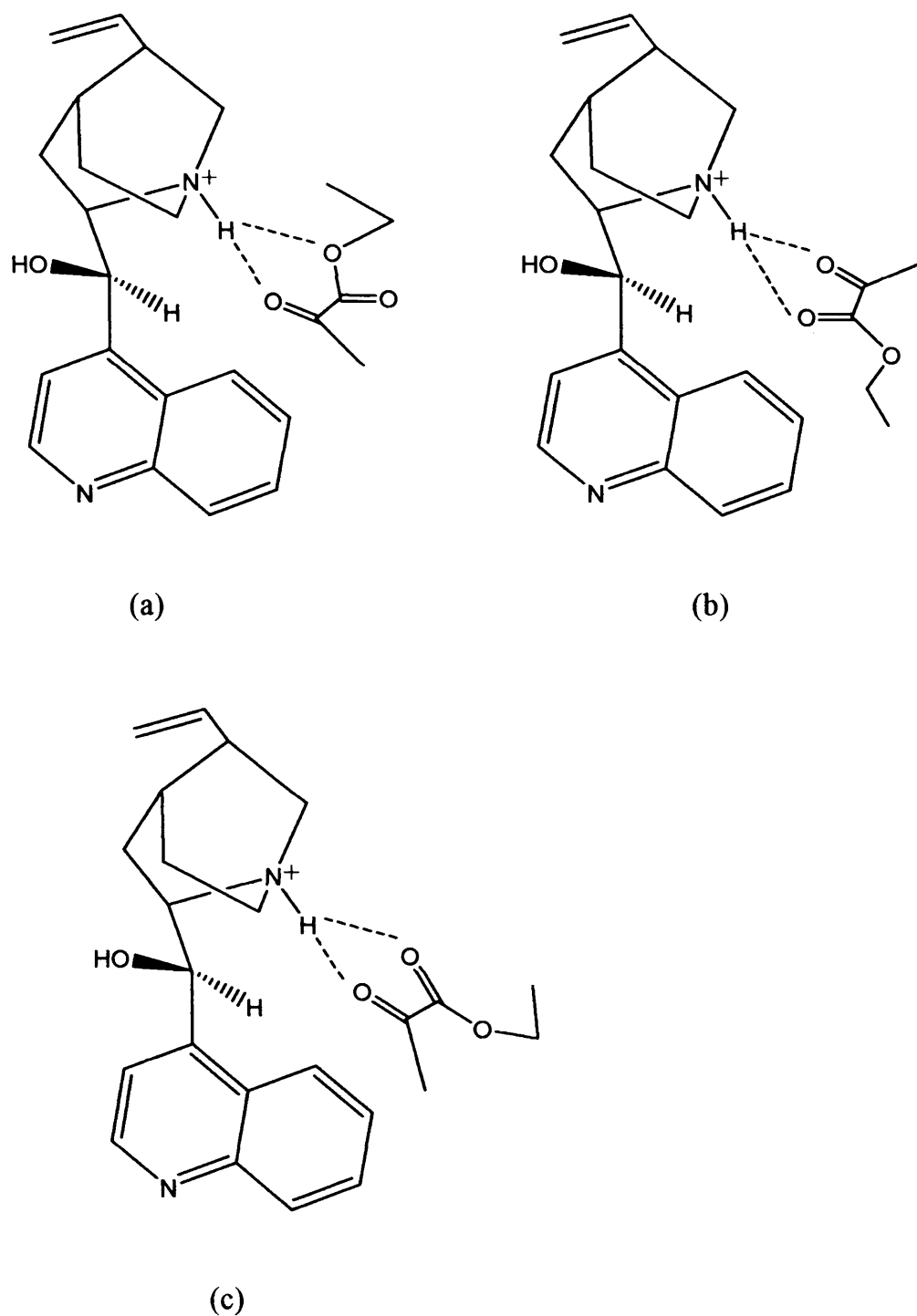


Fig. 1.13 Substrate-modifier interactions proposed by Baiker. (a) CD : *trans* pyruvate interaction (b) CD : *cis* pyruvate interaction (Pro-(S)) (c) CD : *cis* pyruvate interaction (Pro-(R)).

Augustine's model

In 1993, Augustine [67] proposed a model which differs from that of Wells and Baiker. This model postulated an edge-on adsorption of CD via the N of the quinoline ring in contrast to previous models which had suggested that adsorption of CD occurred via the quinoline ring parallel to Pt surface. Later studies performed by Augustine [68], suggested a change in the adsorption geometry of CD to be parallel to the Pt surface. It is proposed in both models that a "bidentate" complex was formed as a result of the modifier and pyruvate ester interacting via a six-membered ring (Figure 1.14). This bidentate interaction occurs via both the lone pairs of quinuclidine-N atom and the O atom at C₉ of the modifier with the carbon atom of the keto carbonyl and the pyruvate ester group. This proposed interaction is dependent on the ability of alcohols and amines to react with activated ketones via nucleophilic attack on the carbonyl group. However, this model cannot interpret the sense of the obtained ee when quinuclidine-N is protonated, the high ee when a protic solvent (AcOH) is used (the lone pairs of quinuclidine-N cannot interact with the reactant), and the obtained high ee when C₉-OH of CD methylated (as in O-methyl-CD) is used instead of CD [69].

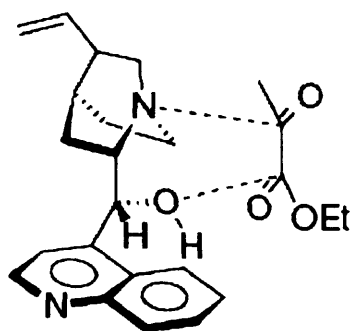


Fig. 1.14 Substrate- modifier interaction as proposed by Augustine. Reprinted from [70].

Margitfalvi's model

Margitfalvi *et al.* proposed what is known as “the shielding model”. This suggests a 1:1 interaction between the reactant and the modifier formed in solution through the electronic interaction of the quinoline ring of CD with π -orbitals of the keto pyruvate group [71-73]. The role of the quinoline ring is to shield one side of C=O of the prochiral pyruvate from hydrogenation and then the hydrogen can adsorb on the Pt surface on the unshielded side of C=O (Figure 1.15), favouring the predominant formation of one enantiomer. The role of the Pt surface is to provide activated hydrogen for C=O hydrogenation of the reactant. Hence, the enantioselectivity of this model is attributed to the modifier-substrate interaction in

solution. According to the cinchonidine-reactant interaction, CD must be in a closed conformation. This model, however, lacks the ability to interpret some experimental observations. First, this model cannot interpret the high ee observed when the quinuclidine-N of CD is protonated. Second, the observed rate acceleration at low modifier concentration could not be explained according to this model [74]. Third, it is reported by Bartok *et al.* [75, 76] that there is no decrease in enantioselection when the modifier is fixed in an open conformation. Furthermore, when α -isocinchonine (anti open conformation) is used a 76% ee was obtained [77]. These results contrast with the shielding model which suggests that only the closed form of alkaloid produced enantioinduction.

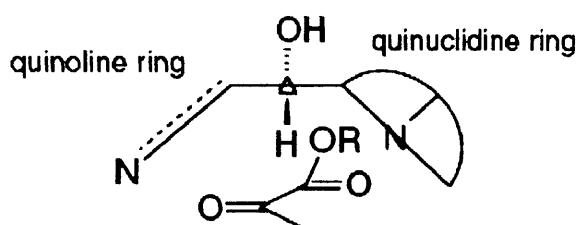


Fig. 1.15 Substrate- modifier interaction proposed by Margitfalvi. Reprinted from [70].

McBreen's model

Recently, McBreen *et al.* have proposed the two-point H-bonding model [78]. In this model two H-bonding interactions were proposed as in Figure 1.16. The first interaction is an aromatic-carbonyl H-bonding interaction between the aromatic ring hydrogen atoms and the carbonyl group. This proposed interaction depends on surface science studies supporting this type of interaction, especially the C—H \cdots O interactions between the adsorbed aromatics on Pt(111) and the carbonyl groups of coadsorbed molecules [79], i.e. the metal surface activates the quinoline C-H bonds to exhibit hydrogen bonding towards the carbonyl of the α -ketoester. The same interaction is reported between tetrafluorobenzene and oxygenated clusters [80-82]. The second H-bonding interaction is between the ester carbonyl O atom and the quinuclidine-N atom. This model, as in previous models, proposed a 1:1 substrate-modifier interaction adsorbed on the Pt surface.

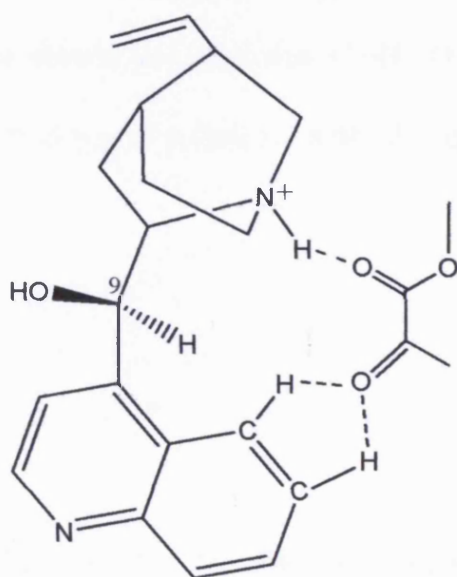
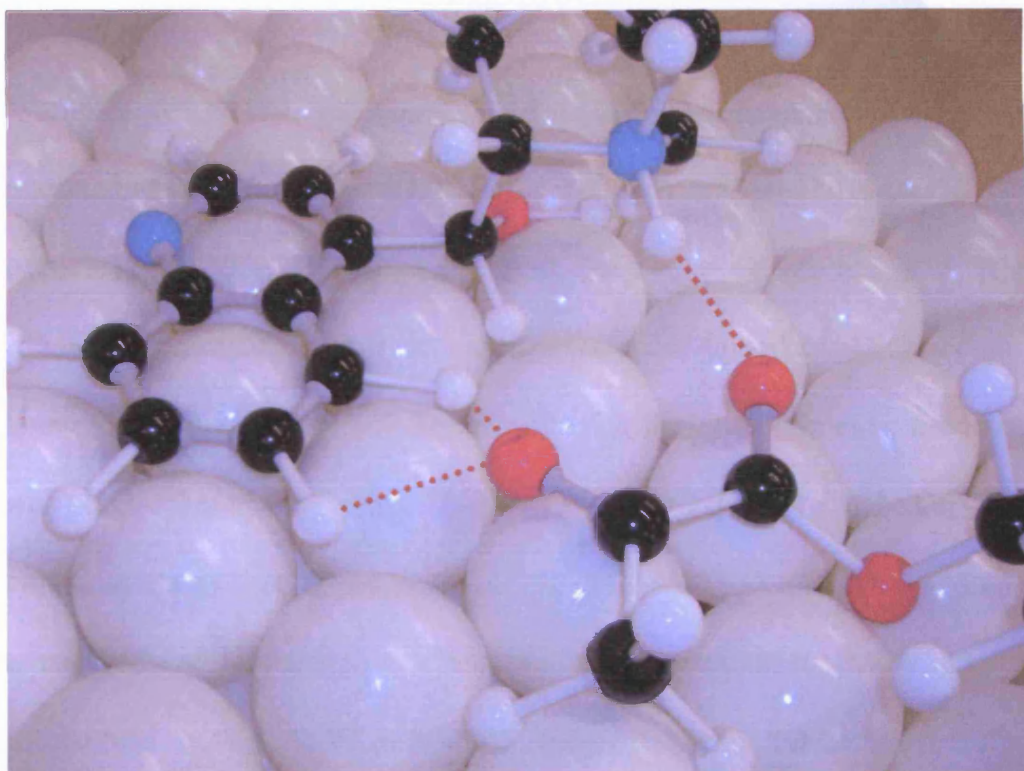


Fig 1.16 Upper: schematic representing Mc Breen model: red = O, black = C, blue = N, small white = H, and large white = Pt surface, dotted line = H-bonding interaction. Lower: the two-point H-Bonding model as proposed by McBreen *et al.* [78].

The two-point model predicts the correct enantioselectivity for reaction. For example, when CD was used as modifier, the formation of pro-(S) in the intermediate complex is expected to be sterically hindered by the substituents at C₉ (which is the OH group). The role of the C—H \cdots O interaction is important in enantioselectivity as shown by experiments conducted by Diezi *et al.* [83, 84] using CD with different substituent at C₉. In these experiments, the R-enantiomer was obtained in excess (when C₉ substituent = OH, OCH₃, and OC₂H₅) while S-enantiomer was formed when the substituent was O-phenyl. This was attributed to a competitive interaction for the phenyl substituent to the aromatic-carbonyl interaction. In this model, it is assumed that the prochiral carbonyl is not strongly chemisorbed to the Pt, since strong adsorption would weaken the carbonyl-aromatic interaction. It should be noted that C—H \cdots O binds to the surface while the ester carbonyl H-bonding interaction with the quinuclidine-N takes place above the surface.

1.6.1.2 Catalysts

Platinum is observed to be the best catalyst for enantioselective hydrogenation of functionalised ketones. The choice of support is crucial in order to obtain an active catalyst. A variety of supports have been used. Al₂O₃, SiO₂, TiO₂, and zeolites have been found to be the best for enantioselective

hydrogenation reactions. Alumina supported Pt has produced the best ee and rate [85, 86]. Bartok attributed this to the presence of oxonium cations formed continuously on alumina (the electrostatic acceleration) which can promote the directed adsorption of the surface complex in the course of competitive adsorption [85, 86]. Catalyst particle size is also important. Catalyst reduction pretreatment in hydrogen at a variety of temperatures has been found to increase Pt particle size and to remove impurities on the Pt surface which leads in the end to improved enantioselectivity and increased activity [57, 69, 87-89]. Catalysts that have a particle size of less than 2 nm exhibit lower activity and selectivity [90, 91]. In the present study, the Pt/G catalyst is used to broaden and extend the range of support studies.

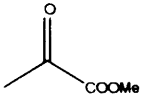
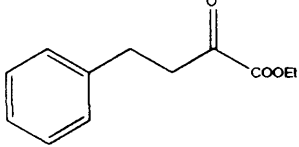
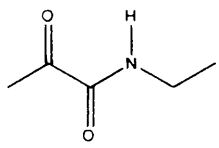
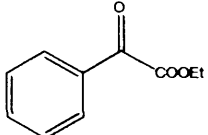
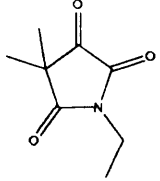
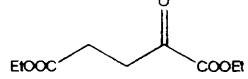
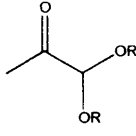
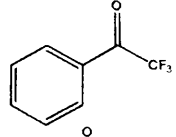
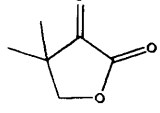
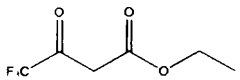
Attard *et al.* studied the effect of catalyst morphology on enantioselectivity [37, 88, 89]. This was achieved by using the conducting support graphite, and measuring the CV for the Pt surface. From the CV, step and terrace sites on Pt were separately identified and the effect of these sites on enantioselectivity during Orito reactions could be attempted.

Bartok and co-workers [92, 93] used ultrasound treatment in order to improve Pt catalysts performance. This was used in the hydrogenation of ethyl pyruvate modified using HCD-modified Pt/alumina; an ee of 97% and possibility of catalyst re-use was reported. The catalyst improvement was ascribed to the ultrasonic effect on Pt producing an optimal particle size [93].

1.6.1.3 Substrates

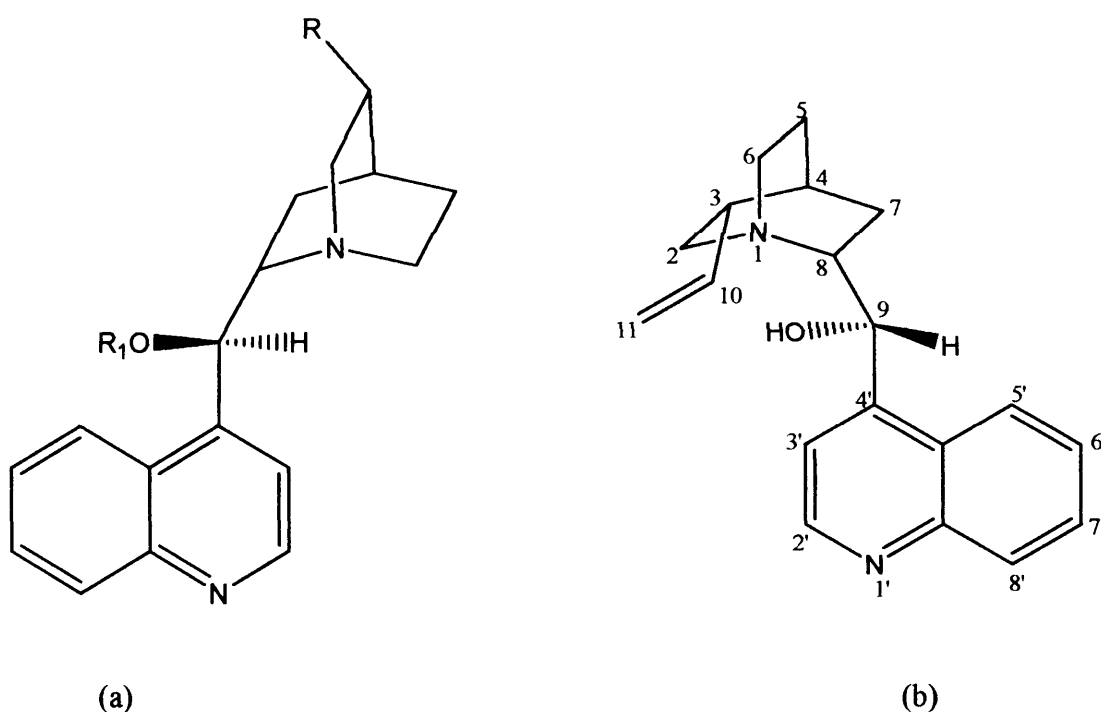
In enantioselective hydrogenation reactions using cinchona-modified Pt, the substrates that produce highest ee are limited to α -ketoesters, α -ketoacetals, α -ketoethers, and some trifluoromethyl [94]. α -ketoesters, such as ethyl and methyl pyruvate, are some of the best and most used in the enantioselective reaction [94]. In all enantioselective hydrogenation reactions, an activated electron-withdrawing group such as carbonyl, ester, carboxyl or acetal in the α -position, is required for rapid reaction. The presence of these activating groups is crucial for effective enantioselective hydrogenation. The best results have been obtained when Pt/alumina has been used as a catalyst in the presence of CD, methoxydihydrocinchonidine (MeOHCD) or HCD as modifiers in acetic acid or toluene as solvents (Table 1.1).

Table 1.1 Enantioselective hydrogenation using different substrates over Pt/alumina catalysts at room temperature.

Substrate	Modifier	Solvent	ee/ %(R)	Ref.
	CD	AcOH	98	[95]
	MeOHCD	AcOH	96	[96]
	HCD	AcOH	94	[97]
	CD	AcOH	58	[98]
	HCD	AcOH/Toluene	98	[99]
	CD	Toluene	91	[100]
	MeOHCD	AcOH	96	[101]
	MeOHCD	AcOH	97	[102]
	CD	Toluene/TFA	96	[103]
	CD	Toluene	92	[100]
	MeOHCD	THF/TFA	96	[104]

1.6.1.4 Modifiers and solvents

The presence of a modifier in enantioselective hydrogenation is crucial for the achievement of rate enhancement and enantioinduction [105-107]. The most efficient chiral modifiers to have been used in enantioselective hydrogenation over Pt are CD and its derivatives (Figure 1.17a) and its near enantiomer cinchonine, CN (Figure 1.17b) [59, 70, 108-110].



R1	R	Modifier
H	-CH=CH ₂	CD
H	-CH ₂ -CH ₃	HCD
Ph	-CH=CH ₂	PHOCD
OMe	-CH ₂ -CH ₃	O-MeHCD

Fig. 1.17 (a) Cinchonidinc, CD, and its simple derivatives (HCD = 10,11-Dihydrocinchonidine, PHOCD = O-Phenylcinchonidine, O-MeHCD = 10,11-Dihydro-O-methylcinchonidine); (b) CN.

There are three important parts of the modifier structure: an aromatic ring (quinoline in CD), the basic nitrogen atom at the quinuclidine ring, and the C₈ and C₉ part [70]. The stereogenic centres in the cinchona alkaloid are located at C₃, C₄, C₈, and C₉. It has been observed that C₈ and C₉ play an important role in controlling the sense of enantioselectivity. For example, CD (where C₈ and C₉ are configured as S and R, respectively) produced an R- excess, while CN (possessing the opposite configuration at C₈ and C₉) produces the S-enantiomer in excess. The configuration at C₈ was found to be responsible for the sense of enantioselectivity, and the substituent at C₉ to be important for high ee (OH and OMe substituent groups are the best whereas large bulky groups will reduce or even invert enantioselectivity) [59, 108]. Partial hydrogenation of the aromatic ring weakens the bond to the metal which leads to lowering of the ee; and the alkylation of quinuclidine-N leads to a complete loss of ee [108, 111]. Enantioselectivity can occur at low concentration of the modifier. Recently, Hutchings *et al.* [112, 113] reported an inversion in enantioselectivity sense depending solely on the modifier concentration. In this study, hydroquinidine 4-chlorobenzoate was used as a modifier of Pt at different concentrations. At low modifier concentration, S-enantiomer was produced in excess, and at higher concentration of modifier, R-enantiomer was favoured; the opposite trend was observed with hydroquinine 4-chlorobenzoate.

The conformation is also thought to be an important factor in controlling ee. Taking CD as an example, the two most important torsional angles are τ_1 : C₃-C₄-C₉-C₈ and τ_2 : C₄-C₉-C₈-N₁ [114]. Other rotations around C₃-C₁₀ and C₉-O single bonds were reported to be less important [114]. Six low energy conformations of CD were obtained according to these rotations. Optimisation of those conformers revealed the four most stable conformations of CD. The aforementioned findings have been confirmed recently by a theoretical study [115] of these conformations on Pt(111) as shown in Figure 1.18, which revealed closed-1, closed-2, open-3, and open-4. In the open conformation, the lone quinuclidine-N atom points away from the quinoline ring, whereas in the closed conformer the lone pair of the quinuclidine-N atom points towards the quinoline ring [114]. Both calculations and NMR [99,100] measurements for these conformers show that the open-3 conformer is the most stable conformer of CD in aprotic solvents [116].

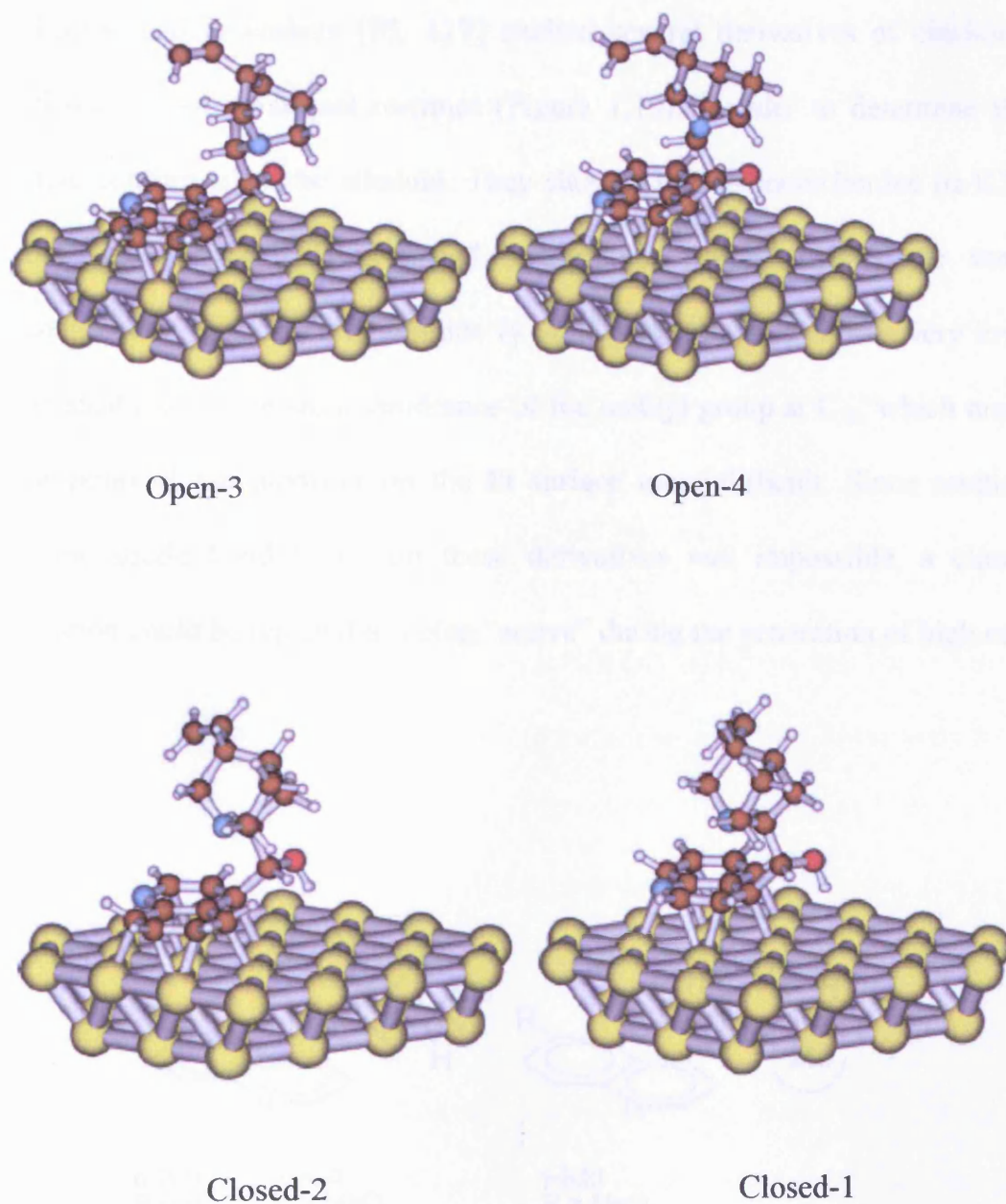


Fig. 1.18 Four most stable conformations of CD on a Pt(111) surface. Reprinted from reference [115].

Bartok and coworkers [75, 117] studied several derivatives of cinchona alkaloid using conformational restraint (Figure 1.19) in order to determine the productive conformer of the alkaloid. They showed that α -isocinchonine (α -ICn) and α -isoquinidine (α -IQd) produced a high ee, which exhibits the same conformation as CD. For γ -isoquinidine (γ -IQd), the obtained ee was very low; this was attributed to the steric hindrance of the methyl group at C₁₀, which made the adsorption of the modifier on the Pt surface more difficult. Since rotation around the single bond C₉-C₈ on these derivatives was impossible, a closed conformation could be rejected as being “active” during the generation of high ee.

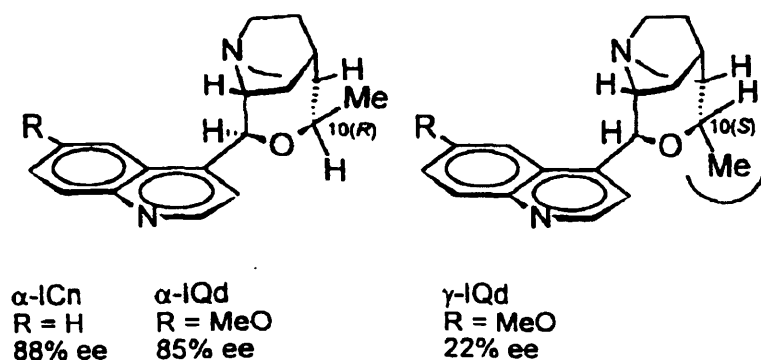


Fig. 1.19 Cinchona derivatives with conformational constraints. Reprinted from reference [94].

Adsorption of the alkaloid on the metal surface is crucial in the achievement of enantioselectivity. Blaser *et al.* [118] proposed that the modifier

adsorbs to the metal surface via the aromatic ring parallel to the metal surface. Deuterium exchange experiments by Wells *et al.* [119] confirmed this proposal. In these experiments, deuterium exchange between dihydrocinchonidine and D₂ on the Pt surface showed that all the H atoms of the quinoline ring and the H of O at C₉ exchanged for D. However, no exchange took place on the quinuclidine ring. These findings were confirmed by NEXAFS studies which found that 10,11-dihydrocinchonidine adsorbed parallel to the Pt(111) surface [120].

In general, solvents have been found to influence enantioselectivity via a weak dependence on their dielectric constants (ϵ). The best solvent exhibits a dielectric constant in the range 2-10 [59]. Acetic acid has been reported to generate high ee's when used as a solvent during the Orito reaction [59]. A NMR study of CD [116] showed that the effect of the solvent is related to the proportion of the modifier in an open-3 conformation (which is the best for modifier-substrate interaction) [116]. It has also been reported that the lower the ϵ (all ϵ measurements at room temperature), the higher the abundance of open-3 conformation during reaction, which leads to high ee. For example, the dielectric constants of toluene, tetrahydrofuran (THF), and acetone are 2.3, 7.6, and 20.7 respectively, and the open-3 conformations ratio was reported to be 70%, 62%, and 40% respectively [116] in these solvents. Calculations by Baiker [116] have shown that the open-4 conformation has high energy and by increasing the value of ϵ , the energy of closed -1 and closed-2 reaches the energy of the open-3

conformation. However, in acetic acid and ethanol ($\epsilon = 7.1$, and 24.3 respectively), the proportion of open-3 for acetic acid has been reported to be 100% and 77% for ethanol. This contrasts with findings reported above [59]. The difference in behaviour has been ascribed to the acetic acid protonating the quinuclidine-N and in ethanol to H-bonding formed between the solvent and alkaloid [121].

1.6.2 Side reactions accompanying enantioselective hydrogenation over supported Pt during the enantioselective hydrogenation of etpy

1.6.2.1 Transformation of CD

Cinchonidine is hydrogenated first at the quinuclidine part via hydrogenation of $C_{10}=C_{11}$ bond, which produces Dihydrocinchonidine (DHCD) which is also an efficient modifier (increased reaction rate observed while ee not effected) [122]. As long as hydrogenation was underway, the hydrogenation of the quinoline ring of the modifier was observed [122]. Reaction with complete conversion of etpy was found to contain CD hydrogenated derivatives [122]. At this stage, the efficiency of the modifier was reduced because hydrogenation of the aromatic ring was shown to weaken the interaction with the Pt surface, which leads to a decrease in the amount of adsorbed modifier on the metal surface [96, 122-124].

1.6.2.2 Aldol condensation of pyruvate esters catalysed by N-base of the modifier

The carbonyl group of α -pyruvate ester is reactive due to its electrophilicity. In addition, the α -hydrogen on the methyl group adjacent to the carbonyl group promotes the pyruvate esters reactivity. Enolisation of pyruvate ester during enantioselective hydrogenation over CD modified-Pt was reported first by Baiker [125] (Figure 1.20). Cinchonidine catalysed deprotonation of ethyl pyruvate by abstracting H at the α -position by quinuclidine-N of CD followed by an inter-molecular aldol reaction. A subsequent ethanol elimination and cyclisation (lactone formation) produced complex 1a which exist in two tautomeric forms. The enol form 1b protonates the quinuclidine-N of CD and enhances the ee by 4% [125].

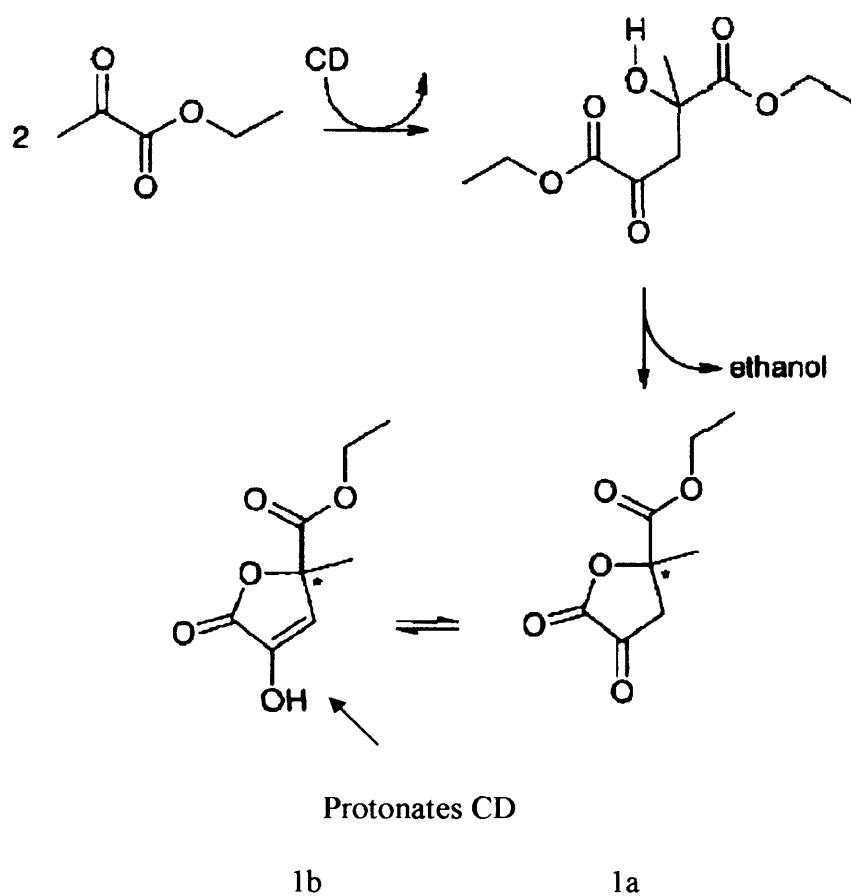


Fig. 1.20 Aldol condensation reaction catalysed by CD [125].

Aldol formation usually occurs before the hydrogenation reaction commences and prior to the addition of catalyst. IR and NMR analysis of mixtures of etpy and CD in dichloromethane showed protonation of CD by the complex 1b [125].

1.6.2.3 Aldol polymerisation at Pt surfaces

Aldol polymerisation also occurs by the pyruvate ester interaction with the Pt surface [126, 127]. Methyl pyruvate polymerises in the absence of CD and H_2 on the Pt surface. Using a continuous fixed-bed reactor, a hydrogenation of methyl pyruvate (mepy) over Pt/alumina was conducted by Baiker *et al.* [126]. In this experiment hydrogen and methyl pyruvate were reacted in the absence of modifier. Later, the hydrogen feed was stopped for 30 min (H_2 starvation) then H_2 addition restored to the reactor. It was found that conversion decreased from 80% before H_2 starvation to 40% after H_2 was restored (Figure 1.21). This behaviour was ascribed to the partial blockage of Pt active sites by the surface polymer during the hydrogen starvation stage.

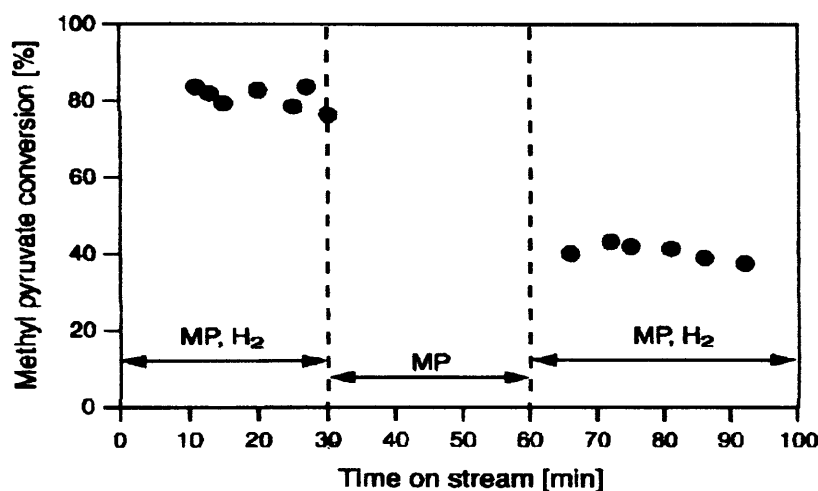


Fig. 1.21 Influence of hydrogen starvation during mepy hydrogenation in the absence of CD. Reproduced from [126].

The influence of mepy on Pt{111} in the presence and absence of hydrogen pressure was studied using STM and NEXAFS [126]. Figure 1.22(a) shows the STM image of adsorbed mepy in the presence of H₂. It is clear that mepy molecules exist on the Pt surface as monomers while in the absence of H₂, the STM image of mepy on the Pt surface reveals the formation of polymers (Figure 1.22(b)).

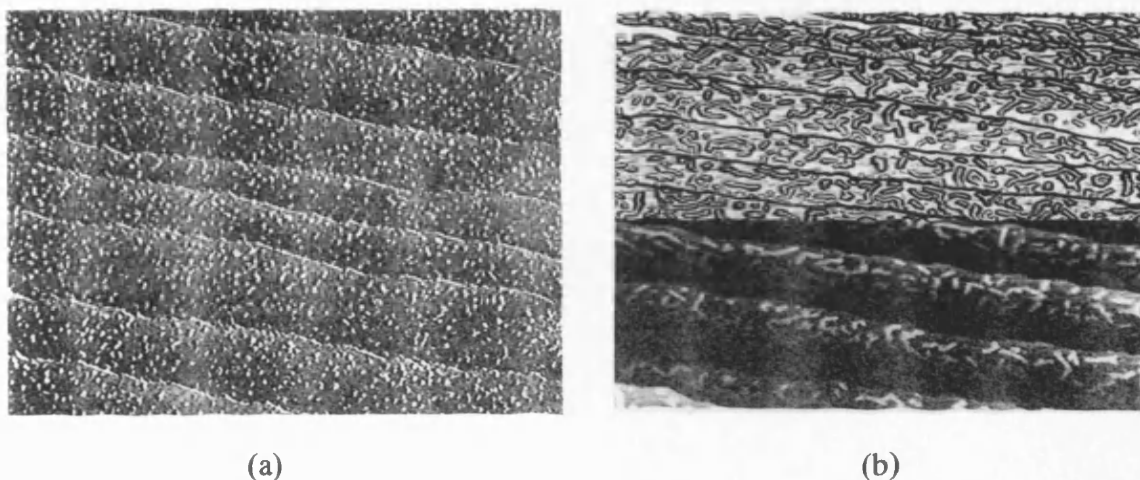


Fig. 1.22 (a) STM image of methyl pyruvate on Pt{111} at 298 K in the presence of a background pressure of H₂. (b) Composite STM image (raw data (above) and enhanced edge contrast (below)) of methyl pyruvate on Pt{111} at 298 K in the absence of H₂ showing the formation of polymeric chains. Reproduced from reference [126].

The proposed mechanism for this polymerisation is shown in Figure 1.23 [126]. It could be concluded that the presence of H₂ suppressed the formation of the polymerisation.

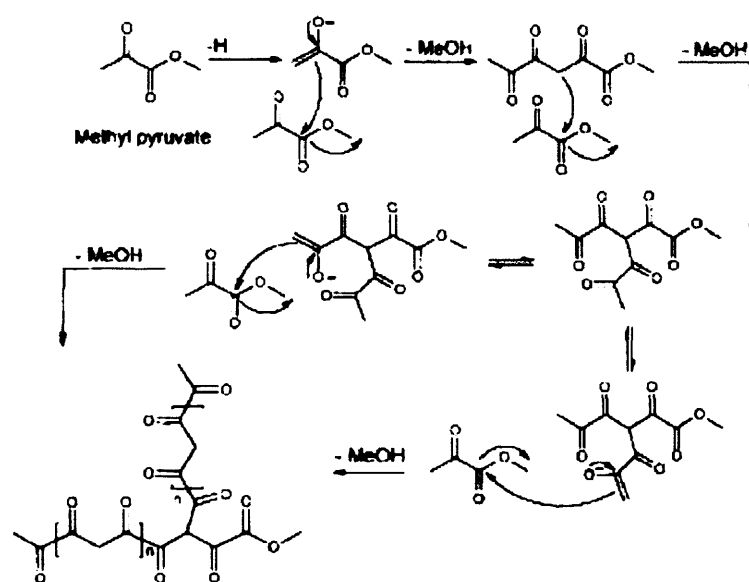


Fig. 1.23 Plausible mechanism of mepy polymerisation over Pt{111}. Reproduced from [126].

1.7 Application of voltammetry for adsorption

1.7.1 Voltammetric techniques

Voltammetry is an important electrochemical tool for investigating the electrochemical behaviour of a system. Linear sweep voltammetry and cyclic voltammetry are examples of these voltammetric techniques. In the voltammetric process, the electrode potential is swept between two limits at a particular sweep rate, while the electrode current is measured. The resulting curve is known as a voltammogram and shows peaks and troughs which may be ascribed to adsorption at various adsorption sites.

1.7.1.1 Linear sweep voltammetry (LSV)

Linear sweep voltammetry involves applying a linear potential sweep to the working electrode whilst monitoring simultaneously the current flowing in the circuit (Figure 1.24). A signal generator produces a voltage sweep from E_i to E_f and a potentiostat applies this potential wave to the electrode under study. Scanning can be in the positive or negative direction and, in principle, the sweep rate v can be defined as:

$$v = dE/dt \qquad 1.12$$

where dE is the difference in potential between E_i and E_f , and dt is the time taken to complete the modulation. This method of analysis is commonly employed in polarography whereby, under well-defined conditions, the limiting current derived from a redox process in solution during LSV may be used to quantitatively determine the concentration of electroactive species in solution.

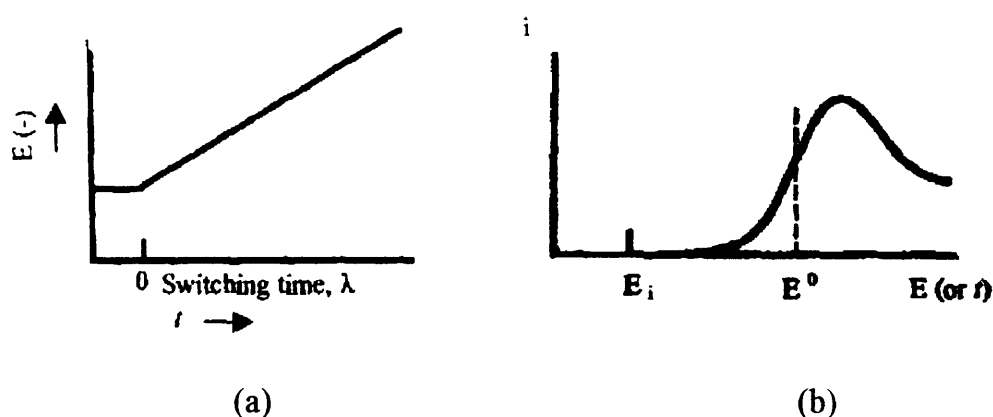


Fig 1.24(a) Linear potential sweep; (b) resulting voltammogram. Reprinted from [128].

1.7.1.2 Cyclic voltammetry (CV)

In cyclic voltammetry, the current passing between the electrode of interest and a counter electrode is measured under the control of the potentiostat. The working electrode is subjected to a triangular potential wave or the so-called saw tooth wave whereby the potential changes from an initial to a final value then reverses to the initial potential value. The resulting voltammogram is shown in Figure 1.25. Any voltammogram peak can be used to determine the potentials at

which electrochemical processes take place. The peak size depends on the sweep rate, electrolyte concentration, and electrode composition [128, 129].

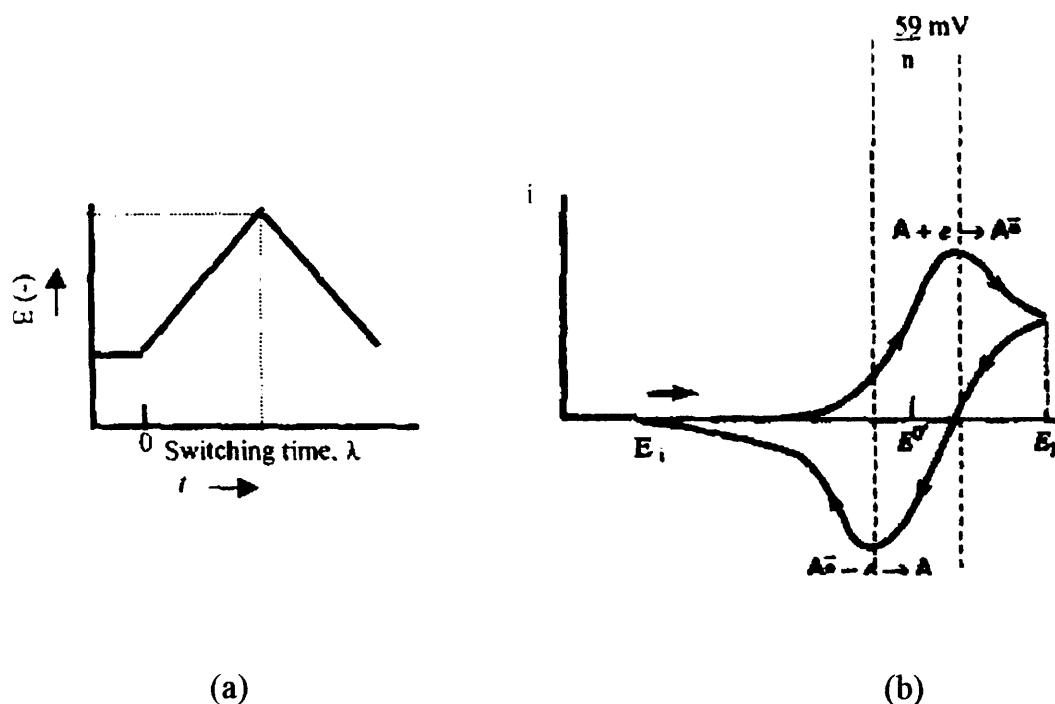
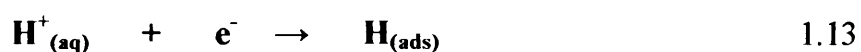


Fig 1.25 (a) A triangular potential wave (saw tooth wave). (b) Resulting cyclic voltammogram. Reprinted from [128].

1.7.2 Characteristics of a typical cyclic voltammogram of platinum

The first study of adsorption of hydrogen ions on platinum was carried out by Frumkin and Slygin [130, 131] in 1934. In this study, a monolayer of hydrogen atoms was adsorbed on platinum in the region 0.0 – 0.3 V positive of the hydrogen equilibrium potential (0.0 V):



In 1960, Will and Knorr [132] investigated the adsorption of hydrogen and oxygen on activated polycrystalline Pt using cyclic voltammetry by repeated cycling between the hydrogen and oxide regions. Two reversible hydrogen peaks were reported; the so-called “weakly” and “strongly” bonded states. Will [133] conducted experiments using activated Pt single crystals and found the more strongly bonded peak lay at the more positive potential, corresponding to adsorption of hydrogen on {100} sites, while the weakly bonded peak lay at the more negative potential, corresponding to adsorption of hydrogen on {110} or {111} surface sites. These findings using Pt single crystals were analogues to those using activated polycrystalline Pt.

The cyclic voltammogram for polycrystalline platinum in sulphuric acid is shown in Figure 1.26 [132]. Two characteristic regions are observed:

- (1) hydrogen desorption/adsorption regions (A and D)
- (2) oxide adsorption/desorption regions (B and C)

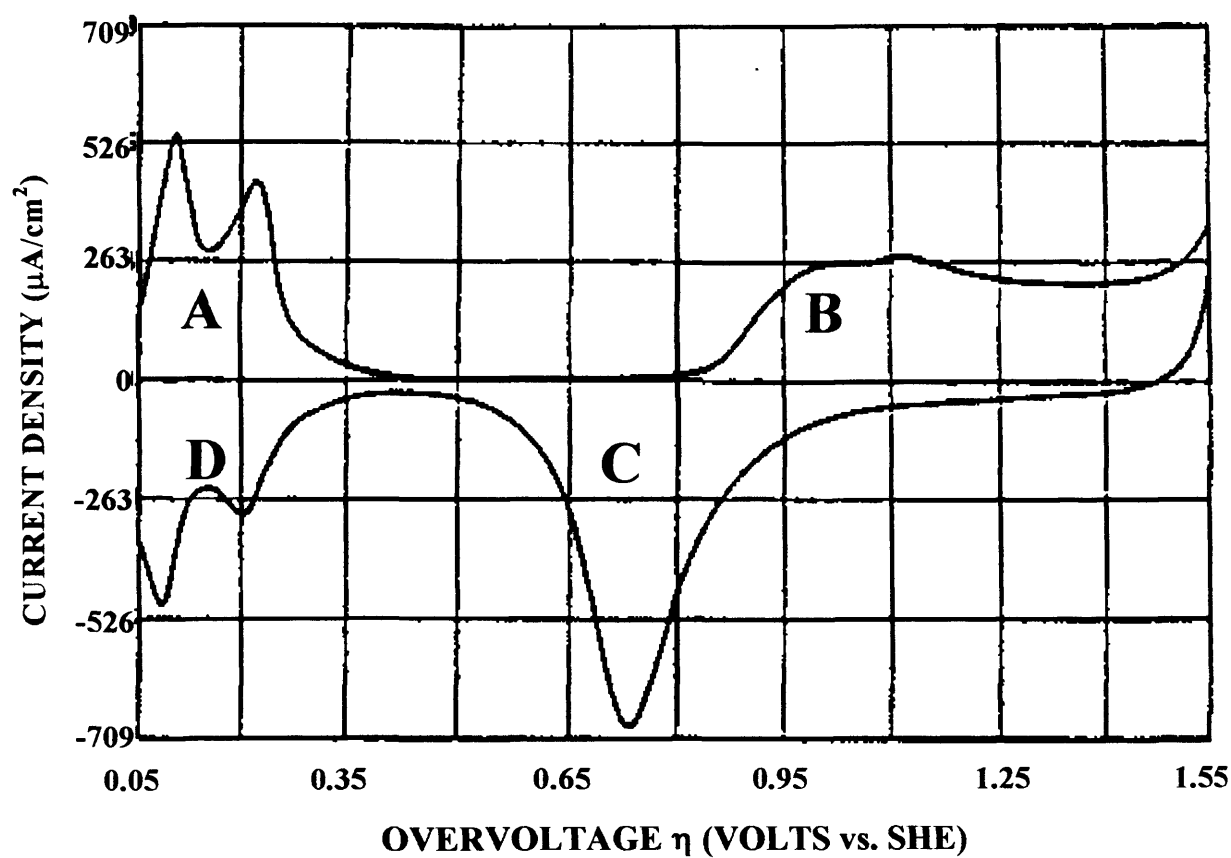
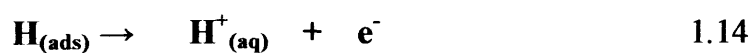


Fig. 1.26 Cyclic voltammogram for polycrystalline platinum electrode in sulphuric acid. Sweep rate 100 mV s^{-1} . Reprinted from [132].

Region A of the voltammogram represents hydrogen desorption:

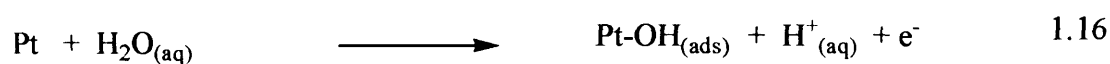


Electrons flow from the Pt –H covalent bond to the metal as a result of proton desorption, which generates a current each time this occurs. This generated current is proportional to the surface area of the Pt electrode.

Region D represents hydrogen adsorption which is the reverse of hydrogen desorption. It should be noted that regions A and D are symmetrical about the potential axis and these processes are therefore reversible.



Region B is associated with adsorption of an oxide species to form an oxide surface. This occurs via place exchange (Figure 1.27) between platinum atoms and adsorbed oxygen. These chemisorbed oxygen atoms may diffuse into the bulk of the electrode and formed a non-stoichiometric oxide [134].



The potential sweep is reversed upon reaching 1.55 V. Beyond this point, potential excursions result in a breakdown in solution and formation of oxygen gas. Similarly, potential excursions below 0.0 V result in hydrogen production.

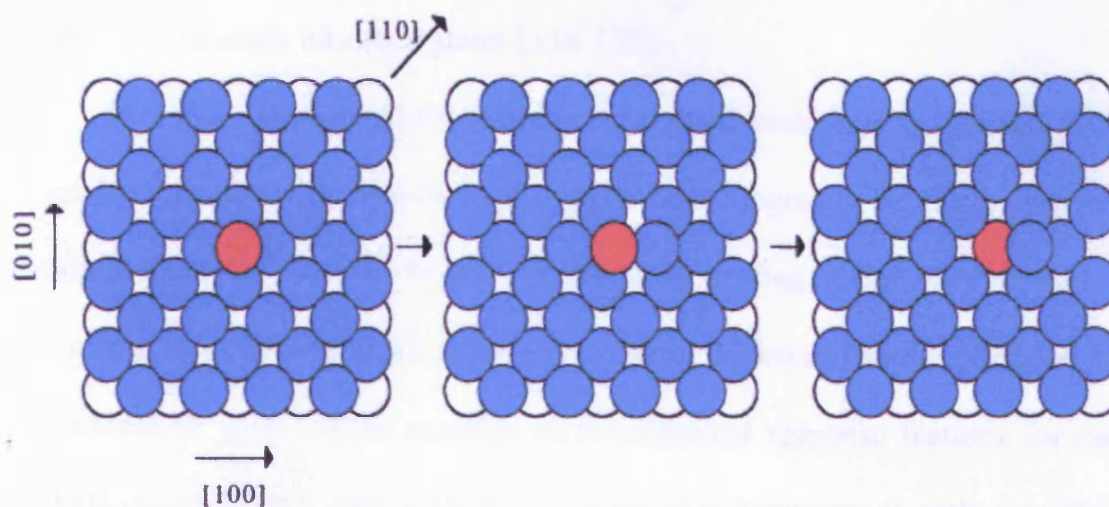


Fig. 1.27 Schematic representation of the place exchange mechanism for adatom diffusion on an fcc(100) surface. The diffusing adatom (red) takes the place of an atom from the top layer of the surface (blue); the latter emerges in a next nearest neighboring site and continues the diffusion process [135].

Region C is associated with oxide layer reduction. It is important to note that regions B and C are not symmetrical about the potential axis and exhibit significant hysteresis, which indicates that the oxidation processes are not reversible.



A study comparing these hydrogen adsorption states with adsorption on specific crystallographic planes was carried out by combining cyclic voltammetry

with ultra-high vacuum (UHV). This study confirmed Will's assertions regarding weakly and strongly adsorbed states [136-138].

In 1980, Clavilier [139] introduced a novel technique to prepare single crystal electrodes with well-defined surface crystallography by flame annealing (heating them to 1000 °C in air). Subsequent cooling under H₂ followed by quenching in ultra-pure water in order to protect the crystal surface from surface contamination gave rise to singular electrochemical response features for each Pt{hkl} electrode. In Figure 1.28, the potential of voltammetry to probe specific Pt catalysts adsorption sites, based on Clavilier's results [139-141], is proposed. It is seen that the individual adsorption site of the idealised cubo-octahedron nanoparticle may be detected and their surface density evaluated assuming that the electrical double layer population of the nanoparticle mimics the bulk single crystal results. It may therefore be expected that a superposition of all possible Miller planes may be obtained using “real” supported catalysts.

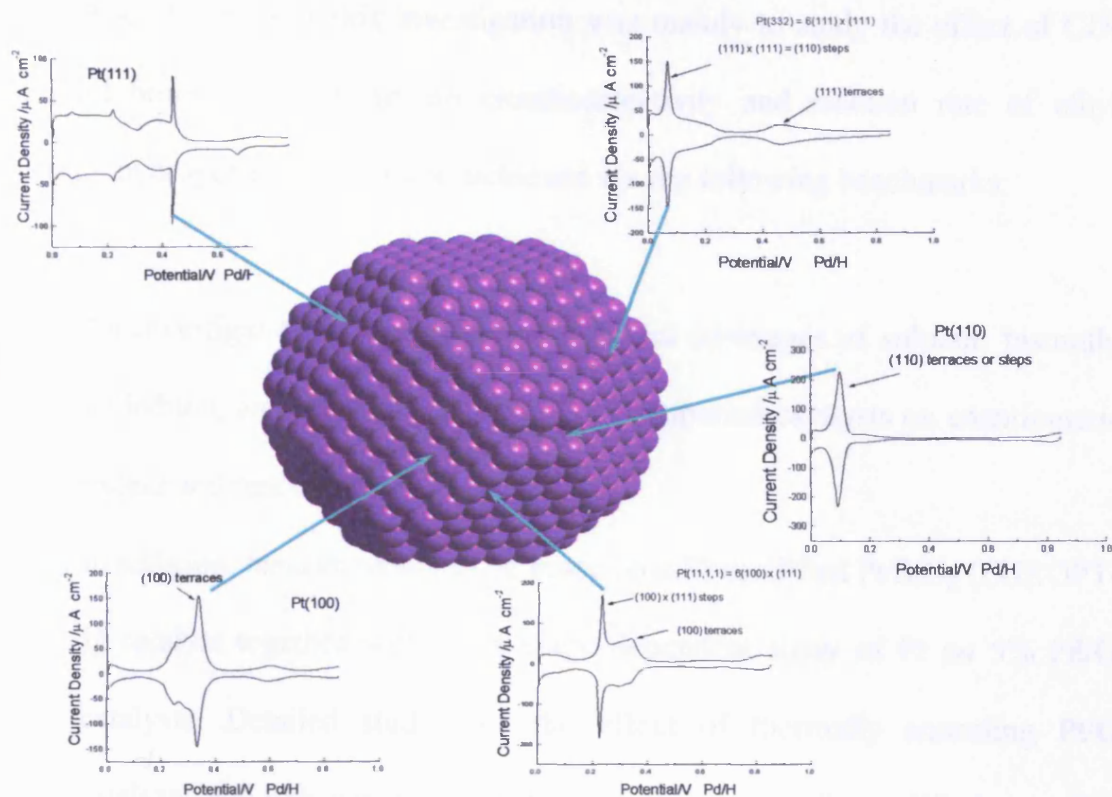


Fig. 1.28 CVs for a variety of single crystal Pt electrodes. The various voltammetric peaks observed are associated with particular fundamental adsorption sites in relation to a model cubo-octahedral Pt nanocluster (centre). Sweep rate = 50 mVs^{-1} , electrolyte = 0.1 M sulphuric acid [142].

1.8 Objective of the present study

The objective of this investigation was mainly to study the effect of CD-modified bimetallic catalysts on enantioselectivity and reaction rate of ethyl pyruvate hydrogenation. This was achieved via the following benchmarks:

1. An investigation of the effect of different coverages of sulphur, bismuth, palladium, and rhodium on a 5% Pt/G supported catalysts on enantiomeric excess and reaction rate.
2. In addition, measurements to be made on a Bi-modified Pt/SiO₂ (EUROPT-1) catalyst together with a coverage dependent study of Pt on 5% Pd/G catalysts. Detailed studies of the effect of thermally annealing Pt/G catalysts and subsequent deposition of Bi to form Bi-modified annealed catalyst in relation to the enantioselective hydrogenation of ethyl pyruvate was also to be carried out.
3. To study the effect of nanoparticle size on the enantiomeric excess and reaction rate of the Orito reaction.
4. To use cyclic voltammetry as a probe to study the catalyst surface morphology.
5. To investigate the effect of adsorption at step/kink and terrace sites on the catalyst performance in enantioselective reactions.

1.9 References

1. <http://almaz.com/nobel/chemistry/chemistry.html>.
2. R. Noyori, *Adv. Synth. Catal.*, **345** (2003) 1.
3. R. Noyori, *Asymmetric Catalysis in Organic Synthesis* John Wiley & Sons, Inc, New York, 1995.
4. Y. Huang, Y. Li, J. Hu, P. Cheng, H. Chen, R. Li, X. Li, C.W. Yip, A.S.C. Chan, *J. Mol. Catal. A:Chemical*, **189** (2002) 219.
5. T.W.G. Solomons, C.B. Fryhle, *Organic Chemistry*. John Wiley & Sons, Inc, New York, 1998.
6. J.J. Berzelius, *Edinburgh New Philosophical Journal.*, **XXI** (1836) 223.
7. I.M. Campbell, *Catalysis at Surfaces*. Chapman and Hall, London, 1988.
8. M. Bowker, *The Basic and Applications of Heterogeneous Catalysis* Oxford University Press, Oxford, 1998.
9. G. Attard, C. Barnes, *Surfaces*. Oxford University Press, Oxford, New York, 1998.
10. G.P. Brivio, T.B. Grimley, *Surf. Sci. Reports*, **17** (1993) 1.
11. P.W. Atkins, *Physical Chemistry*. Oxford University Press, Oxford, 1994.
12. K.W. Kolasinski, *Surface Science : Foundations of Catalysis and Nanoscience*. John Wiley & Sons, Ltd, Chichester, 2002.
13. G.A. Somorjai, *Introduction to Surface Chemistry and Catalysis*. John Wiley & Sons, INC, New York, 1994.

14. E.M. McCash, *Surface Chemistry*. Oxford University Press, Oxford, 2001.
15. P.W. Atkins, J. Paula, *Elements of Physical Chemistry*. Oxford University Press, Oxford, 1992.
16. X. Li. Ph.D. Thesis, Cardiff University, 2001.
17. A.R. West, *Basic Solid State Chemistry*. John Wiley & Sons, LTD, England, 1999.
18. J.B. Biot, *Bull. Soc. Philomath* (1815) 190.
19. L. Pasteur, *Acad. Sci.*, **26** (1848) 535.
20. W.S. Knowles, *Adv. Synth. Catal.*, **345** (2003) 1.
21. R. Noyori, *Adv. Synth. Catal.*, **345** (2003) 15.
22. [http:// en.wikipedia.org/wiki/Nobel_Prize_in_Chemistry](http://en.wikipedia.org/wiki/Nobel_Prize_in_Chemistry).
23. J.H. van't Hoff, *Arch. Neerl. Sci. Exacts. Nat.*, **9** (1874) 445.
24. J.A. Le Bel, *Bull. Soc. Com. Fr.*, **22** (1874) 337.
25. R.S. Cahn, C.K. Ingold, V. Prelog, *Angew. Chem. Int. Ed. Engl.*, **5** (1966) 385.
26. J. Clayden, N. Greeves, S. Warren, P. Wothers, *Organic Chemistry*. Oxford University Press, Oxford, 2001.
27. M.O. Lorenzo, S. Haq, T. Bertrams, P. Murray, R. Raval, C.J. Baddeley, *J. Phys. Chem. B*, **103** (1999) 10661.
28. X. Zhao, *J. Am. Chem. Soc.*, **122** (2000) 12584.

-
29. C.F. McFadden, P.S. Cremer, A.J. Gellman, *Langmuir*, **12** (1996) 2483.
 30. D.S. Sholl, *Langmuir*, **14** (1990) 862.
 31. D.J. Watson. Ph.D. Thesis, Cardiff University, 2003.
 32. A. Ahmadi, G. Attard, J. Feliu, A. Rodes, *Langmuir*, **15** (1999) 2420.
 33. G.A. Attard, A. Ahmadi, J. Feliu, A. Rodes, E. Herrero, S. Blais, G. Jerkiewicz, *J. Phys. Chem. B*, **103** (1999) 1381.
 34. S.J. Pratt, S.J. Jenkins, D.A. King, *Sur. Sci.*, **585** (2005) L159.
 35. G.A. Attard, *J. Phys. Chem. B*, **105** (2001) 3158.
 36. J. Clavilier, A. Fernandez-Vega, J.M. Feliu, A. Aldaz, *J. Electroanal. Chem.*, **258** (1989) 89.
 37. D.J. Jenkins, A.M.S. Alabulrahman, G.A. Attard, K.G. Griffin, P. Johnston, P.B. Wells, *J. Catal.*, **234** (2005) 230.
 38. E. Bauer, *Z. Kristallogr.*, **110** (1958) 372.
 39. E. Bauer, H. Poppa, *Thin Solid Films*, **12** (1972) 167.
 40. F.C. Frank, J.H. van der Merwe, *Proc. Roy. Soc., A* **198** (1949) 205.
 41. F.C. Frank, J.H. van der Merwe, *Proc. Roy. Soc., A* **200** (1949) 125.
 42. J.N. Stranski, L. Krastanov, *Ber. Akad. Wiss. Wien.*, **46** (1938) 797.
 43. M. Volmer, A. Weber, *Z. Phys. Chem.*, **119** (1926) 277.

-
44. R. Kinkel, B. Poelsema, L.K. Verheji, G. Comsa, *Phys. Rev. Lett.*, **65** (1990) 733.
 45. R. Stumpf, M. Scheffler, *Phys. Rev. Lett.*, **72** (1994) 254.
 46. W.J. Lorenz, G. Staikov, *Surf. Sci.*, **335** (1995) 32.
 47. E. Bauer, J.H. van der Merwe, *Phys. Rev. B*, **33** (1986) 3657.
 48. C.H.F. Peden, K.B. Kidd, N.D. Shinn, *J. Vac. Sci. Technolo. A*, **9** (1991) 1518.
 49. U. Diebold, J.-M. Ban, T.E. Madey, *Surf. Sci.*, **287/288** (1993) 896.
 50. G.E. Rhead, M.G. Barthes, C. Argile, *Thin Solid Films*, **82** (1981) 201.
 51. D. Kashchiev, *J. Crystal Growth*, **40** (1977) 29.
 52. E. Bauer, *Appl. Surf. Sci.*, **11/12** (1982) 479.
 53. P.B. Wells, A. Wilkinson, *Top. Catal.*, **5** (1998) 39.
 54. R. Noyori, M. Koizumi, D. Ishii, T. Ohkuma, *Pure Appl. Chem.*, **73** (2001) 227.
 55. R. Noyori, T. Ohkuma, *Angew. Chem. Int. Ed. Engl.*, **40** (2001) 40.
 56. Y. Orito, S. Imai, S. Niwa, *J. Chem. Soc. Jpn.*, **8** (1979) 1118.
 57. Y. Orito, S. Imai, S. Niwa, *J. Chem. Soc. Jpn.*, (1980) 670.
 58. Y. Orito, S. Imai, S. Niwa, *J. Chem. Soc. Jpn.*, (1982) 137.
 59. H.-U. Blaser, H.P. Jalett, J.T. Wehrl, *J. Mol. Catal.*, **68** (1991) 215.

-
60. I.M. Sutherland, A. Ibbotson, R.B. Moyes, P.B. Wells, *J. Catal.*, **125** (1990) 77.
 61. K.E. Simons, P.A. Meheux, S.P. Griffiths, I.M. Sutherland, P. Johnston, P.B. Wells, A.F. Carley, M.K. Rajumon, M.W. Roberts, A. Ibbotson, *Recl. Trav. Chim. Pays-Bas*, **113** (1994) 465.
 62. G. Bond, P.A. Meheux, A. Ibbotson, P.B. Wells, *Catal. Today*, **10** (1991) 371.
 63. B. Minder, T. Mallat, P. Skrabal, A. Baiker, *Catal. Lett.*, **29** (1994) 115.
 64. O. Schwalm, J. Weber, J. Margitfalvi, A. Baiker, *J. Mol. Struct.*, **297** (1993) 285.
 65. O. Schwalm, B. Minder, J. Weber, A. Baiker, *Catal. Lett.*, **23** (1994) 271.
 66. T. Burgi, A. Baiker, *J. Catal.*, **194** (2000) 445.
 67. R.L. Augustine, S.K. Tanielyan, L.K. Doyle, *Tetrahedron: Asym.*, **4** (1993) 1803.
 68. R.L. Augustine, S.K. Tanielyan, *J. Mol. Catal. A*, **112** (1996) 93.
 69. H.-U. Blaser, H.D. Jalett, M. Muller, S. Studer, *Catal. Today*, **37** (1997) 441.
 70. M. von Arx, T. Mallat, A. Baiker, *Top. Catal.*, **19** (2002) 75.
 71. J.L. Margitfalvi, M. Hegedus, E. Tfirst, *Stud. Surf. Sci. Catal.*, **101A** (1996) 241.

-
72. J.L. Margitfalvi, E. Talas, E. Tfirst, C.V. Kumar, A. Gergely, *Appl. Catal.*, **191** (2000) 177.
73. J.L. Margitfalvi, E. Tfirst, *J.Mol. Catal. A.* **139** (1999) 81.
74. A. Baiker, *J. Mol. Catal. A.* **163** (2000) 205.
75. M. Bartok, K. Felfoldi, G. Szollosi, T. Bartok, *Catal. Lett.*, **61** (1999) 1.
76. M. Bartok, K. Felfoldi, B. Torok, M. Bartok, *Chem. Commun.*, (1998) 2605.
77. M. Bartok, B. Torok, K. Balazsik, T. Bartok, *Catal. Lett.*, **73** (2001) 127.
78. S. Lavoie, M.-A. Laliberte, I. Temprano, P.H. McBreen, *J. Am. Chem. Soc.*, **128** (2006) 7588.
79. S. Lavoie, P.H. McBreen, *J. Phys. B.* **109** (2005) 11986.
80. V. Venkatesan, A. Fujii, T. Ebata, N. Mikami, *Chem. Phys. Lett.*, **394** (2004) 45.
81. V. Venkatesan, A. Fujii, T. Ebata, N. Mikami, *Chem. Phys. Lett.*, **409** (2005) 57.
82. V. Venkatesan, A. Fujii, T. Ebata, N. Mikami, *J. Phys. Chem. A.* **109** (2005) 915.
83. S. Diezi, T. Mallat, A. Szabo, A. Baiker, *J.Catal.*, **228** (2004) 162.
84. N. Bonalumi, A. Vargas, D. Feri, T. Burgi, T. Mallat, A. Baiker, *J. Am. Chem. Soc.*, **127** (2005) 8467.

-
85. M. Bartok, K. Balazsik, G. Szollosi, T. Bartok, *Catal. Commun.*, **2** (2001) 269.
86. M. Bartok, K. Balazsik, G. Szollosi, T. Bartok, *J. Catal.*, **205** (2002) 168.
87. T. Mallat, S. Frauchiger, P.J. Kooyman, M. Schürch, A. Baiker, *Catal. Lett.*, **63** (1999) 121.
88. G.A. Attard, K.G. Griffin, D.J. Jenkins, P. Johnston, P.B. Wells, *Catal. Today*, **114** (2006) 346.
89. G.A. Attard, J.E. Gillies, C.A. Harris, D.J. Jenkins, P. Johnston, M.A. Price, D.J. Watson, P.B. Wells, *Appl. Catal. A: General*, **222** (2001) 393.
90. A. Baiker, *J. Mol. Catal.*, **115** (1997) 473.
91. G. Webb, P.B. Wells, *Catal. Today*, **12** (1992) 319.
92. B. Torok, K. Felfoldi, G. Szakonyi, M. Bartok, *Ultrasonic Sonochemistry*, **4** (1997) 301.
93. B. Torok, K. Felfoldi, G. Szakonyi, K. Balazsik, M. Bartok, *Ultrasonic Sonochemistry*, **52** (1998) 81.
94. M. Studer, H.-U. Blaser, C. Exner, *Adv. Synth. Catal.*, **345** (2003) 45.
95. X. Zuo, H. Liu, D. Guo, X. Yang, *Tetrahedron*, **55** (1999) 7787.
96. C. LeBlond, J. Wang, J. Liu, A.T. Andrews, Y.-K. Sun, *J. Am. Chem. Soc.*, **121** (1999) 4920.
97. B. Torok, K. Balazsik, M. Torok, G. Szollosi, M. Bartok, *Ultrasonics Sonochemistry*, **7** (2000) 151.

-
98. G.Z. Wang, T. Mallat, A. Baiker, *Tetrahedron : Asym.*, **8** (1997) 2133.
99. M. Sutyinszki, K. Szori, K. Felfoldi, M. Bartok, *Catal. Commun.*, **3** (2002) 125.
100. N. Kunzle, A. Szabo, M. Schurch, G.Z. Wang, T. Mallat, A. Baiker, *Chem. Commun.*, (1998) 1377.
101. K. Balazsik, K. Szori, K. Felfoldi, B. Torok, M. Bartok, *Chem. Commun.*, (2000) 555.
102. B. Torok, K. Felfoldi, K. Balazsik, M. Bartok, *Chem. Commun.*, (1999) 1725.
103. T. Mallat, M. Bonder, A. Baiker, *Catal. Lett.*, **44** (1997) 95.
104. M. von Arx, T. Mallat, A. Baiker, *Catal. Lett.*, **78** (2002) 267.
105. P.A. Meheux, A. Ibbotson, P.B. Wells, *J. Catal.*, **128** (1991) 387.
106. G. Bond, K.E. Simons, A. Ibbotson, P.B. Wells, D.A. Whan, *Catal. Today*, **12** (1992) 421.
107. M. Garland, H.-U. Blaser, *J. Am. Chem. Soc.*, **112** (1990) 7048.
108. H.-U. Blaser, H.P. Jalett, D.M. Monti, A. Baiker, J.T. Wehrl, *Stud. Surf. Sci. Catal.*, **67** (1991) 147.
109. H.-U. Blaser, *Chem. Commun.*, (2003) 293.
110. B. Minder, T. Mallat, A. Baiker, G. Wang, T. Heinz, A. Pfaltz, *J. Catal.*, **154** (1995) 371.
111. M. Bartok, T. Bartok, G. Szollosi, K. Felfoldi, *Catal. Lett.*, **61** (1999) 57.

-
112. N.F. Dummer, R. Jenkins, X. Li, S.M. Bawaked, P. McMorn, A. Burrows, C.J. Kiely, R.P.K. Wells, D.J. Willock, G. Hutchings, *J. Catal.*, **243** (2006) 165.
113. R.L. Jenkins, N.F. Dummer, X. Li, S.M. Bawaked, P. McMorn, R.P.K. Wells, A. Burrows, C.J. Kiely, G. Hutchings, *Catal. Lett.*, **110** (2006) 135.
114. P.B. Wells, R.P.K. Wells, *Chiral Catalyst Immobilisation and recycling*. (Eds. D.E. De Vos, I.F.J. Vankelecom, P.A. Jacobs), Wiley-VCH, Weinheim, 2000.
115. A. Vargas, A. Baiker, *J. Catal.*, **239** (2006) 220.
116. T. Burgi, A. Baiker, *J. Am. Chem. Soc.*, **120** (1998) 12920.
117. M. Bartok, M. Sutyinski, K. Felfoldi, G. Szollosi, *Chem. Commun.*, (2002) 1130.
118. H.-U. Blaser, M. Garland, H.P. Jalett, *J. Catal.*, **144** (1993) 569.
119. G.C. Bond, P. B. Wells, *J. Catal.*, **150** (1994) 329.
120. T. Evans, A.P. Woodhead, A. Gutierrez-Sosa, G. Thornton, T.J. Hall, A.A. Davis, N.A. Young, P.B. Wells, R.J. Oldman, O. Plashkevych, O. Vahtras, H. Agren, V. Carravtta, *Surf. Sci.*, **436** (1999) 691.
121. P.B. Wells, *Surface Chemistry and Catalysis*. (Eds. Carley *et al.*), Kluwer Academic/Plenum Publisher, New York, 2002.
122. V. Morawsky, U. Prube, L. Witte, K.-D. Vorlop, *Catal. Commun.*, **1** (2000) 15.

123. A. Baiker, U.-H. Balser, in: *Handbook of Heterogeneous Catalysis*,. (Eds. G. Ertl, H. Knozinger, J. Wentcamp), VCH Publisher, Weinheim, 1997.
124. R. Wandeler, N. Kunzle, M.S. Schneider, T. Mallat, A. Baiker, *J. Catal.*, **200** (2001) 377.
125. D. Ferri, T. Burgi, K. Borszeky, T. Mallat, A. Baiker, *J. Catal.*, **193** (2000) 139.
126. J.M. Bonello, R.M. Lambert, N. Kunzle, A. Baiker, *J. Am. Chem. Soc.*, **122** (2000) 9864.
127. J.M. Bonello, F.J. Williams, A.K. Santra, R.M. Lambert, *J. Phys. Chem. B*, **104** (2000) 9696.
128. A.J. Bard, L.R. Faulkner, *Electrochemical Methods, Fundamentals and applications*. John Wiley & Sons, Inc, New York, 1980.
129. E. Gileadi, E. Kirowa-Eisner, J. Penciner, *Interfacial Chemistry: An Experimental Approach*. Addison-Wesley, U.S.A, 1975.
130. A.I. Slygin, A.N. Frumkin, *Acto. Physiochim URSS*, **3** (1935) 791.
131. A.I. Slygin, A.N. Frumkin, *Compt. Rend. Acad. Sci. URSS*, **2** (1934) 173.
132. F.G. Will, C.F. Knorr, *Z. Elektrochem.*, **64** (1960) 258.
133. F.G. Will, *J. Electrochem. Soc.*, **112** (1965) 451.
134. B.E. Conway, B. Barel, H. Angerstein-Kozłowska, B. Tiluk, *J. Chem. Phys.*, **93** (1990) 8361.
135. A.G. Naumoves, Z. Zhang, *Surf. Sci.*, **500** (2002) 414.

- 136. R.M. Ishikawa, A.T. Hubbard, *J. Electroanal. Chem.*, **69** (1976) 317.
- 137. K. Yamamota, D.M. Kolb, R. Kotz, G. Lempfuhr, *J. Electroanal. chem.*, **96** (1979) 233.
- 138. P.N. Ross, *J. Electrochem. Soc.*, **126** (1979) 67.
- 139. J. Clavilier, R. Faure, G. Guinet, R. Durand, *J. Electroanal. chem.*, **107** (1980) 205.
- 140. J. Clavilier, *J. Electroanal. Chem.*, **107** (1980) 200.
- 141. J. Clavilier, K. El Achi, A. Rodes, *Chem. Phys.*, **141** (1990) 1.
- 142. G.A. Attard, A. Ahmadi, D.J. Jenkins, O.A. Hazzazi, P.B. Wells, K.G. Griffin, P. Johnston, J.E. Gillies, *Chem. Phys. Chem.*, **4** (2003) 123.

CHAPTER TWO

EXPERIMENTAL

2.1 Introduction

Enantioselective hydrogenation of ethyl pyruvate to ethyl lactate on modified bimetallic supported catalysts has been investigated. Pt/graphite catalysts were used, sintered at different temperatures. It was found that the catalyst sintered at 700K gave the highest enantiomeric excess. Cyclic voltammetry was used to characterise the deposition of metals on supported Pt catalysts with particular emphasis on the 700 K sintered Pt catalysts.

2.2 Materials

2.2.1 Catalysts

In this study, two types of supported platinum catalysts were used:

- 1) Pt/graphite (Pt/G) was 5 wt% of Pt supported on graphite, with a Pt surface area of $2.1 \text{ m}^2\text{g}^{-1}$ and a mean Pt particle size of 14 nm; supplied by Johnson Matthey.
- 2) The standard reference catalyst EUROPT-1, 6.3% Pt/SiO₂, with a total surface area of $185 \text{ m}^2\text{g}^{-1}$ and a mean Pt particle size of 2 nm; was manufactured by Johnson Matthey. Its characterisation has been reported previously [1, 2].

2.2.2 Reagents

Ethyl pyruvate (EP, Fluka, >97%) was used as received. In this study cinchonidine is mainly used for enantioselective hydrogenation. Cinchonine, the near enantiomer of cinchonidine was used for few experiments. The cinchona alkaloids are white crystalline solids and were supplied by Fluka (purity, 98%) and were also used as received. Dichloromethane (DCM) was the solvent that has been used in most reactions (Fisher, HPLC 99.9%). It was used as received.

2.2.3 Other materials

Other materials used are listed in Table 2.1 and were used as received unless otherwise stated.

Table 2.1. Other materials used in this study.

Material	Supplier	Specification
Bismuth nitrate	BDH	98%
Sodium sulphide	Fisher scientific	35.5%
Palladium nitrate solution	Johnson Matthey	14.8% Pd by weight
Hydrogen hexachloroplatinic acid solution	Johnson Matthey	25.15% Pt by weight
Rhodium chloride	Johnson Matthey	42.4% Rh by weight
Hydrogen	BOC Gases	99.995%
5% H ₂ /Ar	BOC Gases	Specshield
Helium	BOC Gases	99.995%
Nitrogen	BOC Gases	High purity
Air	BOC Gases	High purity
Methanol	Fisher scientific	99.5%
Sulphuric acid	Fisher scientific	98%
Toluene	Fisher scientific	HPLC 99.98%
Potassium permanganate	BDH	GBR
Acetic acid	Fisher	Glacial

2.3 Apparatus and procedure

2.3.1 Reactors

Enantioselective hydrogenation reactions were carried out in two autoclave reactors.

2.3.1.1 Baskerville mechanically stirred reactor

Most experiments (those which were catalysed by Bi, S, Pt, and Pd modified Pt/graphite catalysts and sintered catalysts) were carried out in the 100 ml high pressure stainless steel Baskerville reactor (Figure 2.1). Reactions took place in a glass liner (80 ml) which was placed in the stainless steel vessel. The vessel was attached into the body of the reactor. A Teflon ring was placed between the vessel and the body of the reactor in order to prevent any gas leakage. A sealed mechanical impeller stirred the reactor and was driven by an integrated motor and magnetic drive unit. The reaction mixture was typically stirred at 1000 rpm.

Reaction progress was monitored by a Buchi gas controller 9901 dosing system controlled by a computer. By using this system, a constant pressure could be set before the reaction started. In the reaction vessel, the pressure (P_2) was kept constant. Gas consumed was compensated via doses from a gas reservoir vessel which was held at pressure (P_1), higher than the reactor vessel in order to keep the reaction pressure constant. Consumed H_2 gas was calculated using the ideal gas law:

$$P V = n R T$$

Where $P = (P_1 - P_2)$, V and R are the volume and the universal gas constant. Temperature (T) was the ambient temperature during all experiments of 298 K. n is the H_2 uptake that was consumed in the reaction measured in moles. The recorded uptake data was then analysed using Microsoft ExcelTM. A typical hydrogen uptake curve is shown in Figure 2.2. The slope maximum of hydrogen uptake was taken as the maximum rate of the reaction in the units of $\text{mol h}^{-1} \text{g}_{\text{cat}}^{-1}$.

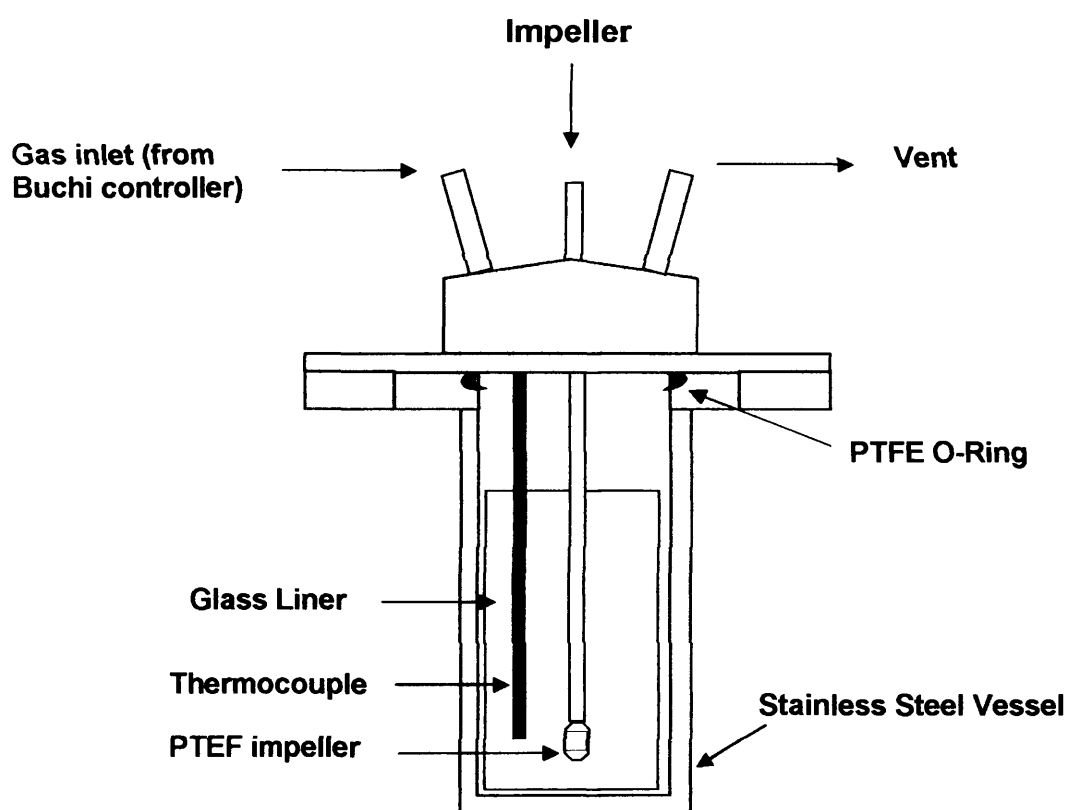


Fig. 2.1. Schematic representation of the Baskerville reactor.

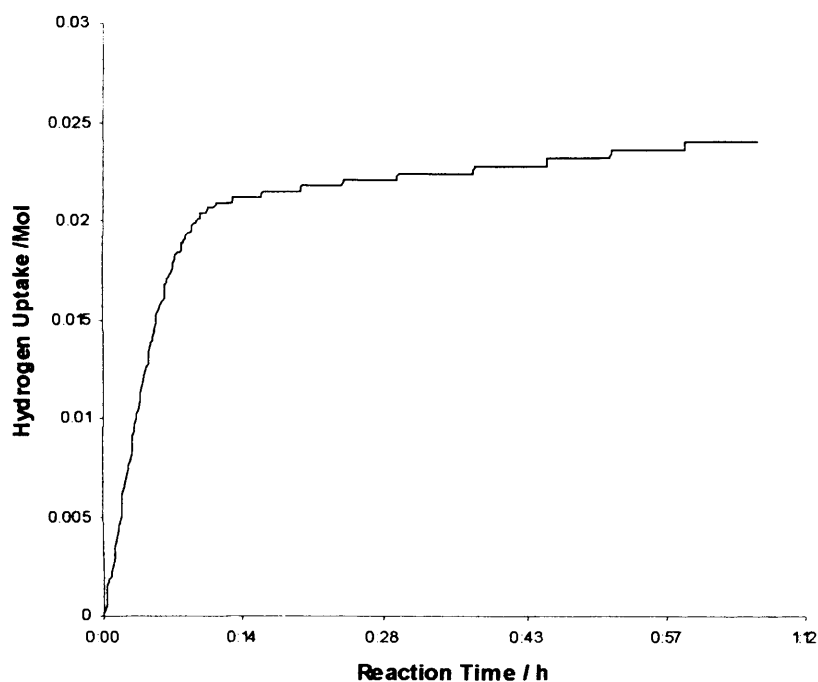


Fig. 2.2. A typical H_2 uptake curve for the hydrogenation of ethyl pyruvate over Pt/G catalyst.

2.3.1.2 Autoclave engineers magnadrive II mechanically stirred reactor

The Autoclave Engineers reactor (Figure 2.3) consists of a 120 ml stainless steel vessel reactor which was equipped with a pressure gauge, a thermocouple, and a sealed mechanical stirrer driven by an integrated motor and magnetic drive unit. The stirrer and thermocouple were connected to the electronic control tower in order to control the stirrer speed and monitor the reaction temperature. Reactions took place in a 70 ml glass liner vessel. The progress of the catalytic reaction was monitored by a gas dosing system which was built in-house (Figure

2.4). The digital pressure display measures the change in the fixed volume gas reservoir, and was connected to high resolution data logger (ADC-16) processor and computer in order to measure the hydrogen uptake. The data recorded was then analysed using programs such as Microsoft Excel™ or Microcal Origin™. Rhodium modified Pt/G catalyst experiments were carried out using this reactor.

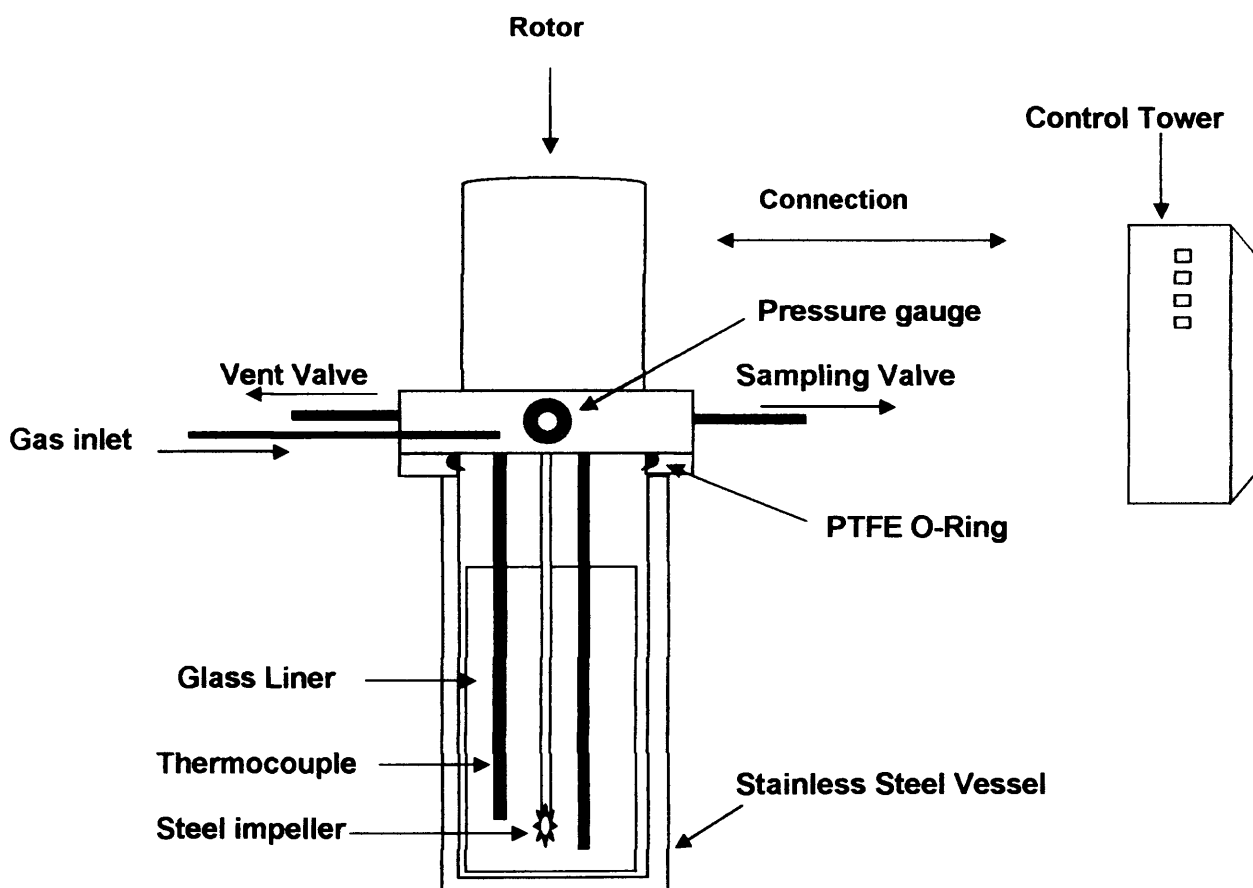


Fig. 2.3. Schematic representation of the Autoclave Engineers Magnadrive II.

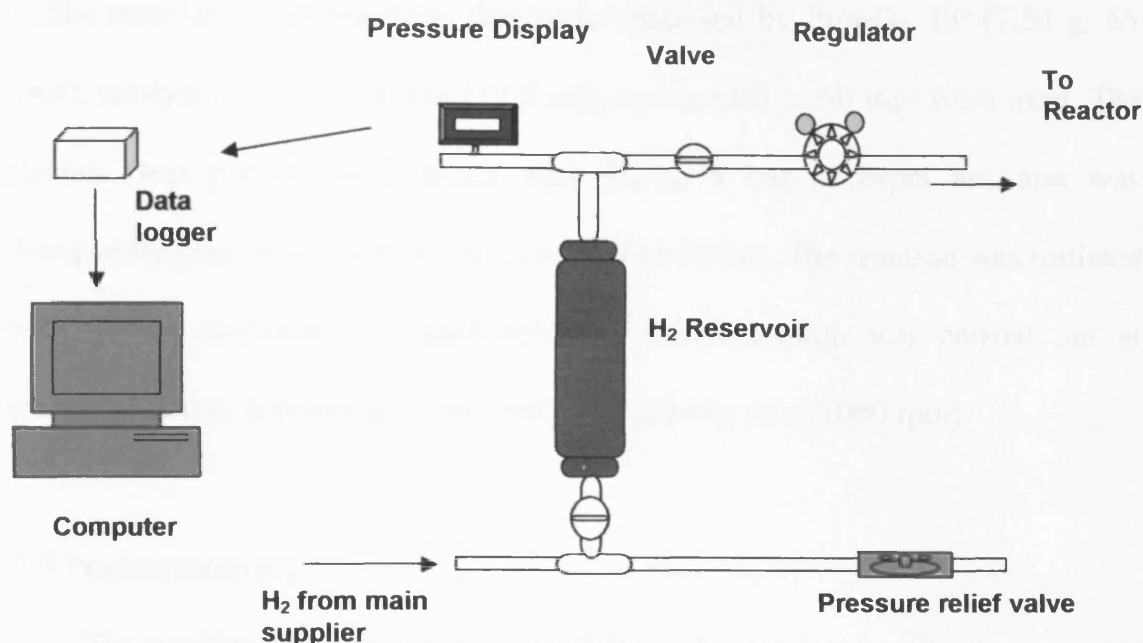


Fig. 2.4. Schematic representation of gas dosing system used in Autoclave Engineers Magnadrive II reactor.

2.3.2 Experimental procedure

Reactors were cleaned rigorously before use by methanol reflux at 80°C for 2-6 h, then tested with catalyst sample with known ee and conversion to ensure that reactors were clean after use by other workers. After each experiment, the reactor liner, stirrer, and vessel were thoroughly washed with acetone followed by dichloromethane and dried. The *in situ* modification of catalysts was used for all experiments and accomplished by adding all reaction components into the reaction

vessel before H₂ admission. Typically, EP (2.32 g, 20 mmol), modifier (20 mg), catalyst (0.25 g), and solvent (12.5 ml) were placed in the glass liner and sealed into the autoclave. For reactions that were catalysed by Pt/SiO₂, EP (7.54 g, 65 mmol), catalyst (0.25 g), solvent (12.5 ml), and modifier (50 mg) were used. The autoclave was purged three times with H₂ at 4 bar to expel air, and was subsequently pressurised with H₂ to either 30 or 35 bar. The reaction was initiated when stirring commenced. Enantioselective hydrogenation was carried out at constant pressure, temperature (ambient), and stirring rate (1000 rpm).

2.3.3 Product recovery

The reaction mixture was separated from the catalyst by filtration using a funnel with a Whatman No1 filter paper. 6 ml samples of the filtrate were taken and passed through a pipette plugged with cotton wool into a sample vial in order to analyse it by GC.

2.4 Procedure for catalyst modifications

2.4.1 Deposition of Bi on Pt/G and Pt/SiO₂

0.35 g samples of sintered catalyst were placed in a 100 ml evaporating basin with a magnetic stirrer bar. Different volumes (0.25-50 cm³) of Bi(NO₃)₃ solution (2.9 x 10⁻⁴ M) were added to each sample and stirred for 3 h. The slurry

was then filtered off under vacuum and washed with 200 ml of ultrapure water.

The catalyst was left to dry at ambient temperature overnight.

2.4.2 Deposition of S, Pd, and Rh on Pt/G and Pt on Pd/G

0.35 g samples of sintered catalyst were placed in a 100 ml glass bubbler. For each sample a specific volume of adsorbate solution [Na_2S (1.5×10^{-3} M), H_2PtCl_6 (7.4×10^{-4} M), $\text{Pd}(\text{NO}_3)_2$ (8.6×10^{-4} M), and RhCl_3 (1.0×10^{-2} M)] was added. H_2 was passed through the slurry for 30 min, then the mixture sparged for another 30 min with N_2 . Then, the catalyst was filtered off under vacuum, washed with 200 ml of ultrapure water and dried at ambient temperature overnight.

2.5 Thermal annealing and sintering of catalyst

Samples (3-4 g) were placed into a silica boat and inserted into a Carbolite tube furnace (Figure 2.5). A continuous flow of 5% H_2/Ar was passed through the tube furnace for 30 min in order to expel air. The tube furnace was then heated to the required temperature at a rate of 10K min^{-1} . Upon reaching the required temperature; the catalyst was left for 4 h. Then the catalyst was allowed to cool to ambient temperature under the flow of 5% H_2/Ar . Prepared samples were transferred to sealed sample vials and used within 6 days.

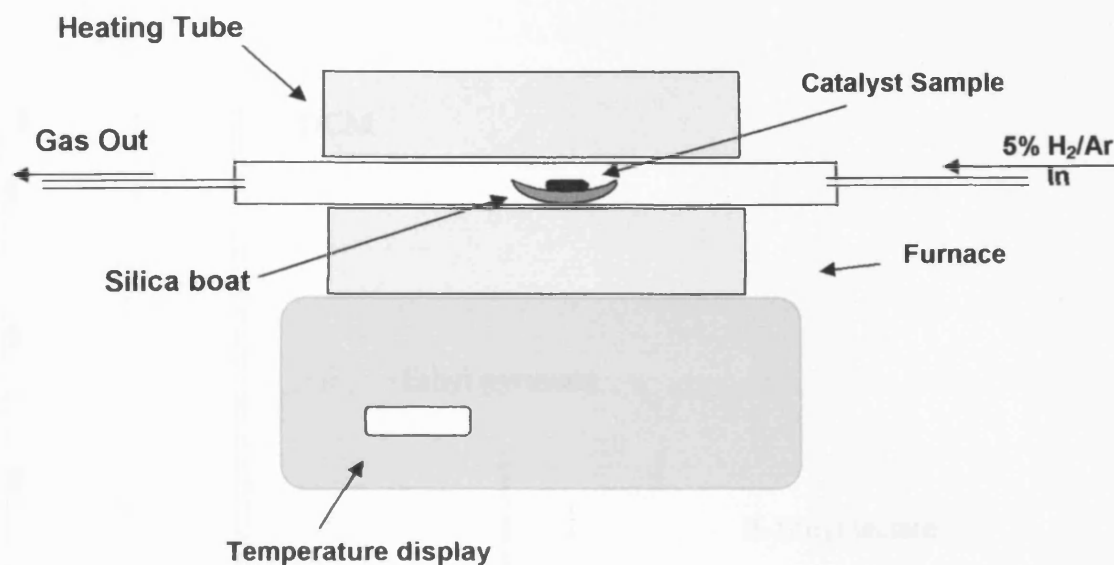


Fig. 2.5. Carbolite furnace used for catalyst sintering.

2.6 Product analysis

The enantiomeric excess (ee) and conversion were determined by use of gas chromatography (GC) (Varian 3900 series), fitted with flame ionisation detector (FID) and chiral capillary column (25 m, Varian) coated with a chiral β -cyclodextrin phase. Data were recorded and processed by using the software package *Star Chromatography Workstation for Windows* (Varian). The products of EP hydrogenation were analysed by injection of aliquots (0.1 μ l) of the products into the GC using a column oven temperature of 80°C (isothermal), with FID and injector ovens set at 200°C and 250°C respectively.

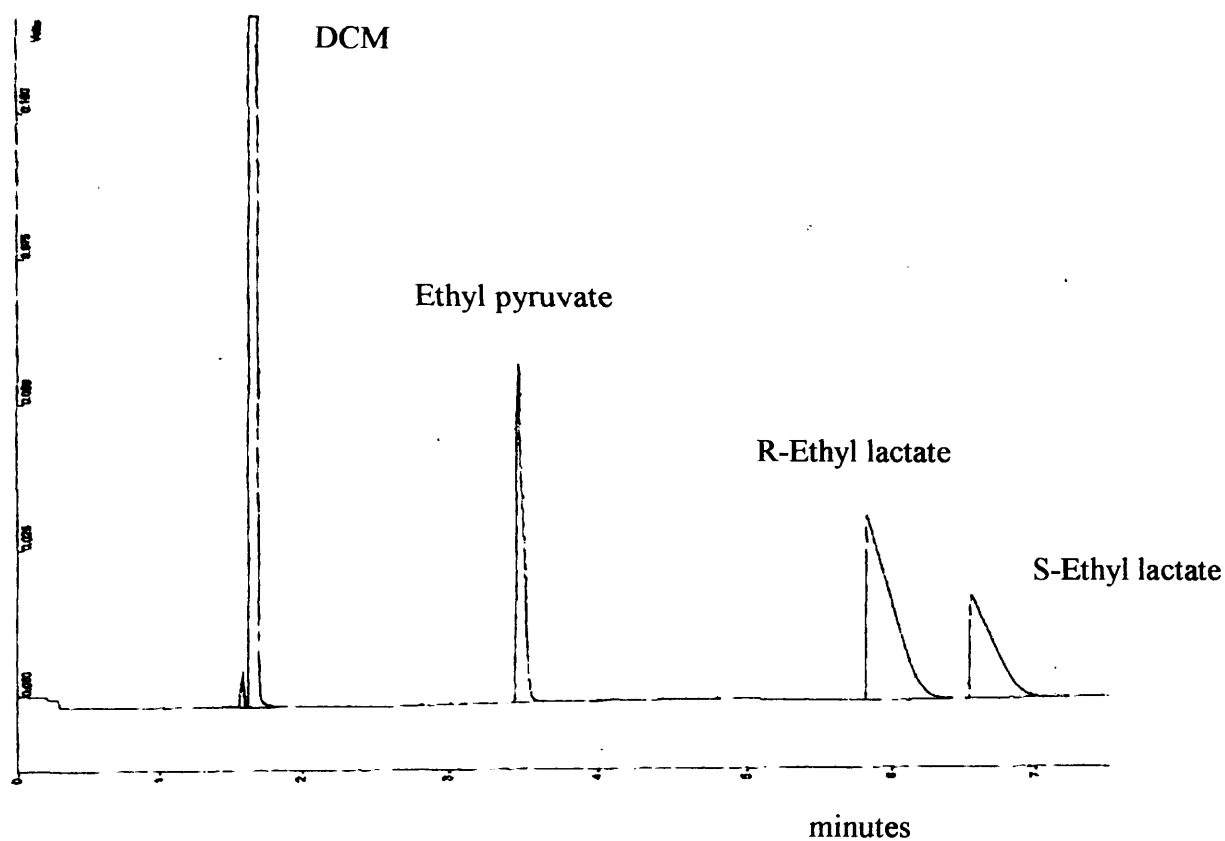


Fig. 2.6. A typical chromatogram of DCM, ethyl pyruvate, and ethyl lactate (R- and S-).

A typical chromatogram is illustrated in Figure 2.6. The peaks were eluted in the sequence of increasing retention time, corresponding to solvent (DCM), ethyl pyruvate, (R)-ethyl lactate, and (S)-ethyl lactate.

2.6.1 Determination of enantiomeric excess

The enantiomeric excess (ee%) is defined by the equation:

$$ee (\%) = \frac{([R] - [S])}{([R] + [S])} \times 100 \quad 2.1$$

Where [R] and [S] represent the concentration of (R)- and (S)-ethyl lactate respectively, which were determined from the integrated peak areas of the gas chromatograph.

2.6.2 Determination of conversion

Conversion is defined by the equation:

$$\text{Conversion (\%)} = \frac{(\alpha_1 A_{[R]} + \alpha_2 A_{[S]})}{(\alpha_1 A_{[R]} + \alpha_2 A_{[S]} + A_{[EP]})} \times 100 \quad 2.2$$

Where $A_{[R]}$, $A_{[S]}$, and $A_{[EP]}$ are the integrated peak areas of (R)- and (S)-ethyl lactate and ethyl pyruvate respectively and α_1 and α_2 are the coefficient correction factors for (R)- and (S)- ethyl lactate respectively.

2.7 Electrochemical study of catalysts

2.7.1 Equipment

Cyclic voltammetry (CV) is a technique that was used in this investigation to study the catalyst morphology and the effect of catalyst modification by metal adsorption and thermal annealing on the enantiomeric excess and reaction rate. Figure 2.7 shows the arrangement of the components that comprise the equipment used in obtaining CVs. The electrochemical cell (Figure 2.8) was attached to a potentiostat (750a, CH instruments) which was connected to a computer running the control program “CHI”. All collected data was stored in the computer and was analysed by using Microcal OriginTM.

2.7.2 The electrochemical cell

The electrochemical cell (Figure 2.8) consists of two Pyrex glass compartments (a and b) which contains three electrodes. The working electrode was a Pt mesh which supported the catalyst sample. The Pt mesh was connected to a thin platinum wire which was inserted into a narrow bore glass tube fitted with Teflon collar working as a holder. The Teflon collar has a screw on its side to adjust the glass tube up and down. The Pd/H reference electrode was housed in the small compartment (b), which was to produce a stable and fixed potential for a period around 6 h. The platinum mesh counter electrode was placed beneath the working electrode in a luggin capillary in compartment (a). It was used in order to

complete the electrical circuit by measuring the current passing between it and the working electrode. The two compartments were connected to each other by two bridges, one above and the other below the fill line level of the electrolyte to allow the electrolyte to diffuse between the two compartments. All three gas inlets were connected to the cell. Inlet (c) in compartment (b) was used to admit H_2 gas into the cell to charge the Pd/H reference electrode. The second inlet (d) in the upper bridge was used to introduce N_2 gas to keep the cell under an inert atmosphere. The third inlet (e) connected to compartment (a) to pass N_2 gas through to de-gas the electrolyte.

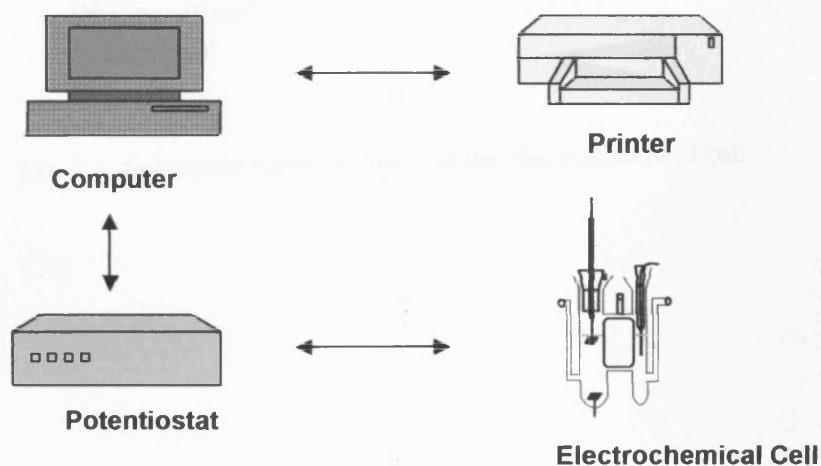


Fig. 2.7. The arrangement of the electrochemical apparatus.

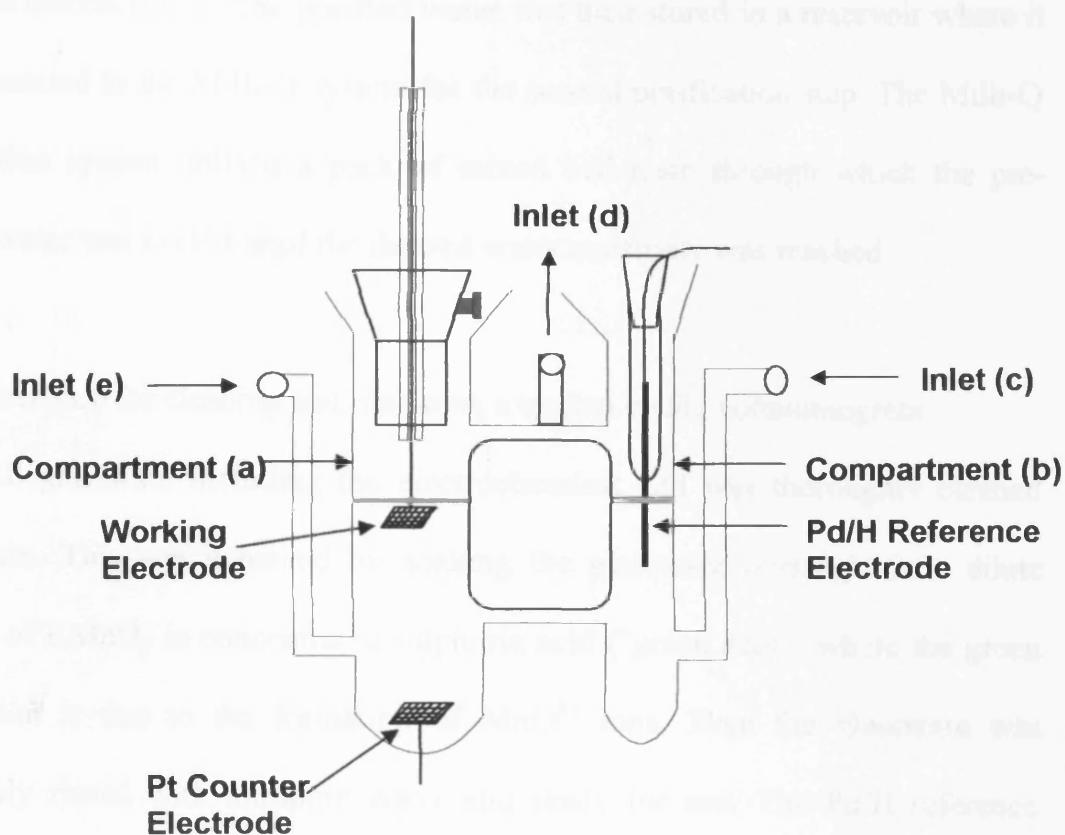


Fig. 2.8. Schematic representation of the electrochemical cell.

2.7.3 Water purification system

In all solution preparations and cleaning, ultrapure water was used. It was produced by using the Milli-Q purification system [3], with a resistivity of 18.2 M Ω cm and total organic content (TOC) below 10 ppb. The purification process

consisted of two steps. The first step was initial purification of mains tap water by using a Milli-RO 10 plus system which, utilises reverse osmosis membranes and activated carbon filters. The purified water was then stored in a reservoir where it was connected to the Milli-Q system for the second purification step. The Milli-Q purification system utilised a pack of mixed bed resin through which the pre-filtered water was cycled until the desired water resistivity was reached.

2.7.4 Procedure for cleaning and obtaining a typical cyclic voltammogram

All glassware including the electrochemical cell was thoroughly cleaned before use. This was achieved by soaking the glassware overnight in a dilute solution of KMnO_4 in concentrated sulphuric acid ("green acid") where the green colouration is due to the formation of MnO^{3+} ions. Then the glassware was thoroughly rinsed with ultrapure water and ready for use. The Pd/H reference electrode was heated in a Bunsen flame [4] to remove surface contaminants. It was then inserted in the cell which was filled with ultrapure water. The palladium electrode was charged by passing hydrogen gas over the reference electrode via the gas inlet of the reference chamber for 30-40 minutes. The electrolyte (sulphuric acid 0.5 M) was then replaced by ultrapure water and de-gassed by N_2 gas for 30 minutes in order to remove dissolved oxygen. A positive pressure of N_2 gas was maintained over the electrolyte surface during every cyclic voltammetry measurement. The platinum working electrode and platinum wire were flamed to remove surface contaminants followed by pressing of 2.7 mg of catalyst sample

into the platinum mesh working electrode. The platinum working electrode was then placed in the electrochemical cell in compartment (a) and adjusted by a Teflon holder to a level such that the catalyst sample was situated just below the electrolyte surface. All electrochemical connections were then made to the potentiostat starting with reference electrode followed by counter electrode then working electrode. The potential was then held at 0.0 V for 5 min to remove the oxide layer on the catalyst and relieve the associated surface reconstruction [5].

2.7.6 Calculation of adsorbate coverage

2.7.6.1 Adsorbate coverage of Bi and S

The surface coverage of adsorbate was calculated by measuring the integrated area below the voltammogram which represents the total charge Q . The total integrated area below the CV of the unmodified (clean) catalyst (Figure 2.9) can be considered as $\theta_{\text{cat}} = 1$. The decrease in the integrated area was attributed to adsorbate coverage. So the adsorbate coverage can be determined by using the following equation:

$$\theta_{ad} = \frac{Q_{clean} - Q_{mod}}{Q_{clean}} \quad 2.3$$

where: θ_{ad} is the surface coverage of adsorbate, Q_{clean} is the total integrated charge for the clean catalyst, and Q_{mod} is the total integrated charge for the modified catalyst. θ_{ad} may be considered as the fraction of free Pt sites remaining after adsorption.

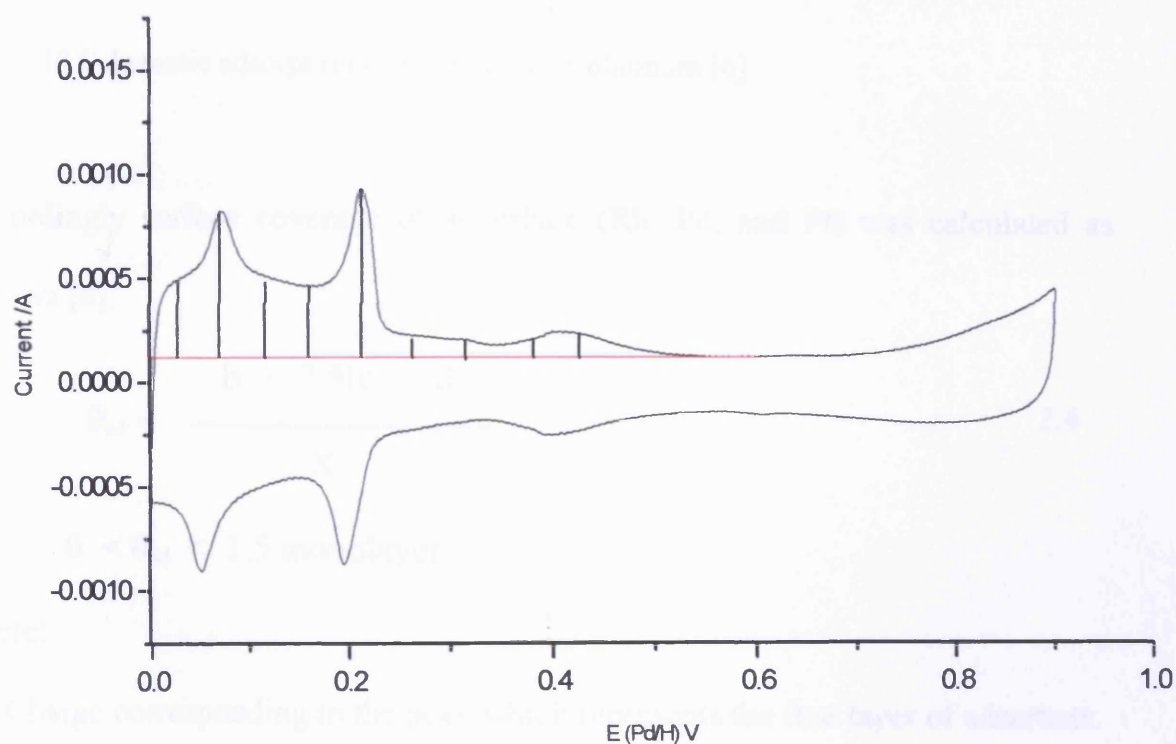


Fig. 2.9. Voltammogram of a clean Pt/G catalyst showing the total integrated charge (shaded).

2.7.6.1 Adsorbate coverage of Rh, Pd, and Pt

Adsorption of Rh and Pd on a 5% Pt/G supported catalyst and Pt on a 5% Pd/G supported catalyst was described in Chapter 3. It was found that the second layer commence before the completion of the first (Figure 2.10).

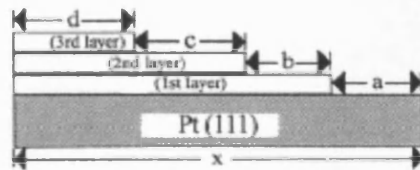


Fig. 2.10 Schematic adsorption of Rh and Pd on platinum [6].

Accordingly surface coverage of adsorbate (Rh, Pd, and Pt) was calculated as follows [6]:

$$\theta_{ad} = \frac{b + 2.5(c + d)}{X} \quad 2.4$$

$$0 < \theta_{ad} < 1.5 \text{ monolayer}$$

where:

b = Charge corresponding to the peak which represents the first layer of adsorbate.

$c + d$ = Charge corresponding to the peak which represents the second and third layers of adsorbate.

X = Charge observed for one perfect monolayer of layer of adsorbate.

2.8 Transition electron microscopy (TEM)

TEM images were used to analyse metal particle-size and morphology of Pt/G catalysts at Johnson Matthey Technology Centre. Images were collected using an FEI microscope (F20 S-TWIN), fitted with a Schottky field emission electron source. It was operated at accelerating voltages of up to 200 kV.

2.9 References

1. G.C. Bond, P.B. Wells, *Appl. Catal.*, **18** (1985) 225.
2. J.W. Geus, P.B. Wells, *Appl. Catal.*, **18** (1985) 231.
3. Millipore General Catalogue, Millipore U.K. Ltd., Watford.
4. J. Clavilier, *J. Electroanal. Chem.*, **107** (1980) 200.
5. G.A. Attard, J.E. Gillies, C.A. Harris, D.J. Jenkins, P. Johnston, M.A. Price, D.J. Watson, P.B. Wells, *Appl. Catal. A.*, **222** (2001) 393.
6. G.A. Attard, R. Price, A. Al-Akl, *Surf. Sci.*, **335** (1995) 52.



CHAPTER THREE

RESULTS

3.1 Introduction

In this chapter, the influence of thermal annealing at different temperatures on a 5% Pt/G catalyst has been studied and tested via the enantioselective hydrogenation of ethyl pyruvate to ethyl lactate. Also, the effect of adatom adsorption on the same reaction using the following catalysts has been investigated:

- M(M = Bi, S, Pd, and Rh)-CD-modified 5% Pt/G catalyst sintered at different temperatures.
- Bi-CD-modified 6.3% Pt/SiO₂ catalyst sintered at 450 K.
- Pt-CD-modified 5% Pd/G catalyst sintered at 700 K.

The objective of this study was to investigate the effects of thermal annealing and adsorption of adatom on the step and terrace sites of the aforementioned catalysts on the reaction rate and enantioselectivity. Cyclic voltammetry (CV) and transmission electron microscopy (TEM) were used as tools to characterise modified catalysts and thermally annealed catalysts.

3.2 Thermal annealing of Pt/G and its influence on enantioselective hydrogenation

The effect of catalyst sintering on enantioselective hydrogenation was studied by heating the 5% Pt/G catalyst in 5% H₂/Ar at different temperatures as described in section 2.5 followed by characterisation using CV and TEM. Each sintered catalyst was investigated as described in the experimental section 2.4.1 in order to study the effect of sintering on the reaction rate and the enantioselectivity.

3.2.1 CV and TEM characterisation

Figure 3.1 shows the CVs of the unsintered 5% Pt/G catalyst and catalysts sintered in 5% H₂/Ar at 450, 600, 700, 800, and 900 K. In general, as annealing temperature was increased, the H_{UPD} area decreased for a fixed mass of catalyst. All CV features were attenuated to varying extents as described by Attard *et al.* [1]. As shown in Figure 3.1, the magnitude of the {111}x{111} and {100}x{111} step peaks relative to unsintered samples was more pronounced and narrower when annealing temperature was increased. As a proportion of the total H_{UPD} charge, the {100} terrace features at 0.27 V (Pd/H) increased in intensity significantly, but then became less marked as annealing temperature reached 600 K and were completely attenuated after that. For Pt{111} terrace voltammetric peaks, there was both a shift to a more negative potential and a slight increase in relative area, as the annealing temperature increased. This was consistent with an increase in the average of {111} terrace width of the Pt particles [2]. Surface area

was calculated for each sintered catalyst by integration of the H_{UPD} charge. The relative surface area of each catalyst decreased as sintering temperature increased as shown in Table 3.1.

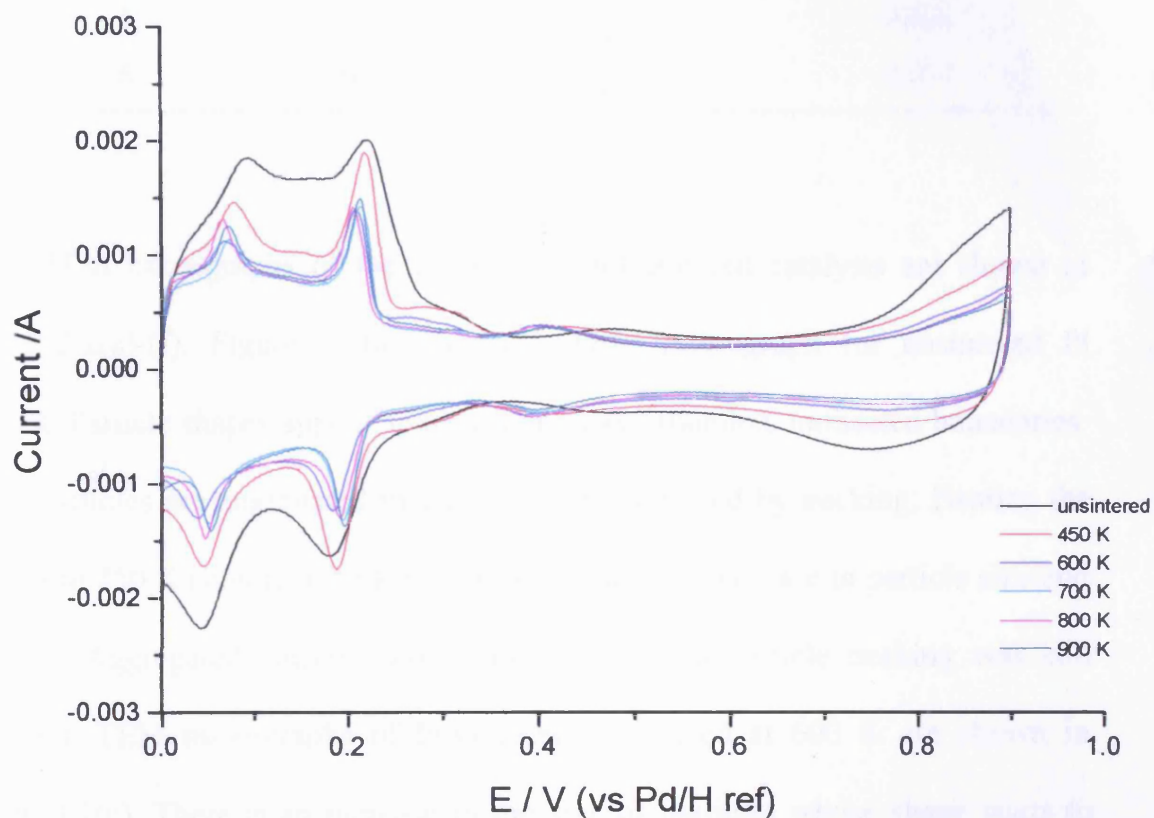


Fig. 3.1 CVs of Pt/G sintered at different temperatures in 0.5M H_2SO_4 . Sweep rate 50 mV s^{-1} .

Table 3.1 Effect of thermal annealing on Pt surface area and Pt{100} terraces of 5% Pt/G sintered catalysts.

Entry	Annealing temperature/K	Relative Pt surface area %	Pt{100}terraces relative area
1	unsintered	100	0.046
2	450	51	0.103
3	600	44	0.118
4	700	36	0.086
5	800	25	0.091
6	900	24	0.011

TEM micrographs of the unsintered and sintered catalysts are shown in Figure 3.2(a)-(f). Figure 3.2(a) shows a TEM micrograph for unsintered Pt catalyst. Particle shapes appear spherical and have rounded, unfaceted boundaries. Some particles are aggregated in clusters and connected by necking. Heating the catalyst to 450 K (Figure 3.2(b)) was accompanied by increase in particle size and faceting. Aggregated clusters started to disperse but particle necking was still observed. TEM micrographs of Pt/G catalyst sintered at 600 K are shown in Figure 3.2(c). There is an increase in the size of particles whose shape starts to become hexagonal and boundaries between particles become clearer. Clusters continued to disperse and particle necking decreased markedly. TEM micrographs of Pt/G catalyst sintered at 700 K (Figure 3.2(d)) show an increase in particles size and faceting. Hexagonal forms are orderly in shape and most particles dispersed. When the heating temperature exceeded 700 K, hexagonal particles continued to

grow and became larger (Figures 3.2(e) and 3.2(f)). Necking connections were lost completely when temperature reached to 900 K (Figure 3.2(f)).

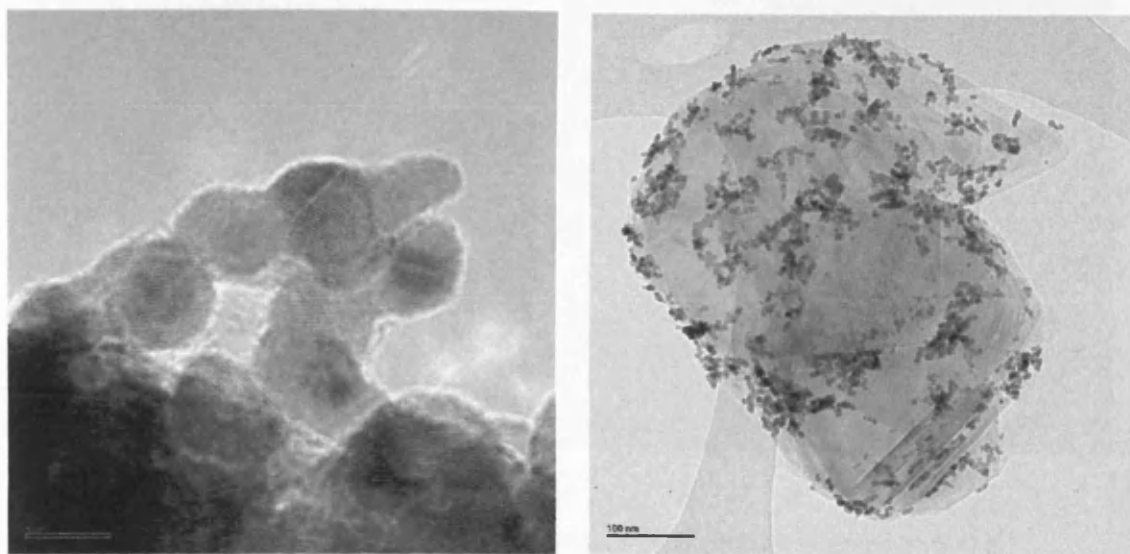


Fig. 3.2(a) TEM micrographs of unsintered Pt/G catalyst.

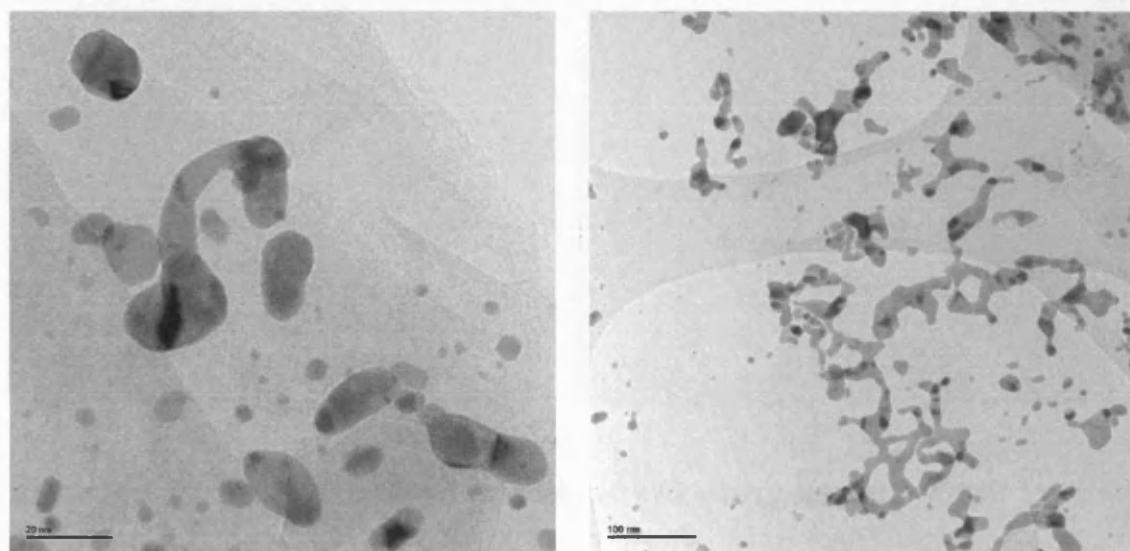


Fig. 3.2(b) TEM micrographs of Pt/G catalyst sintered at 450 K.

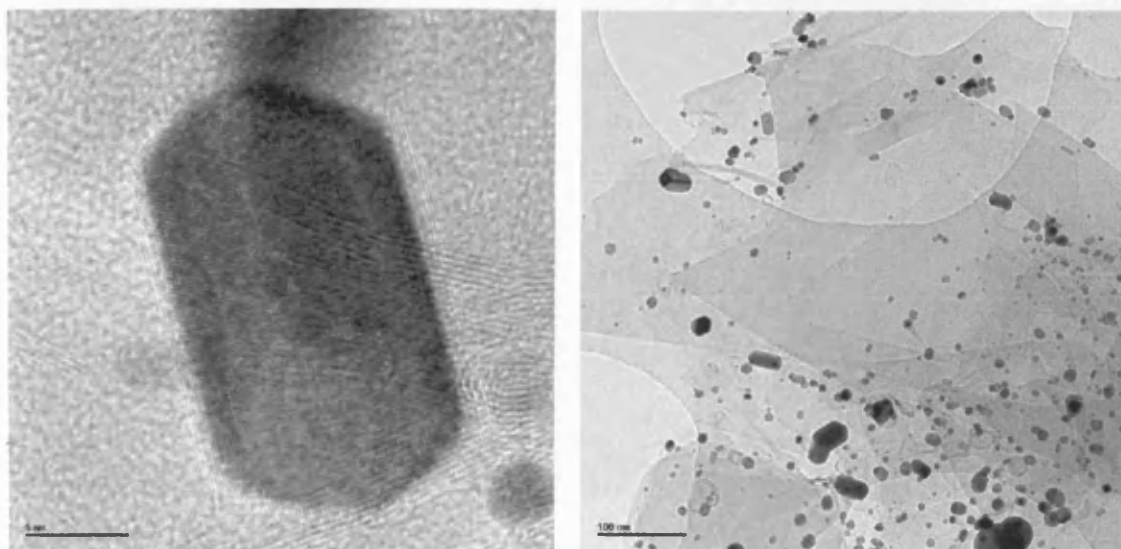


Fig. 3.2(c) TEM micrographs of Pt/G catalyst sintered at 600 K.

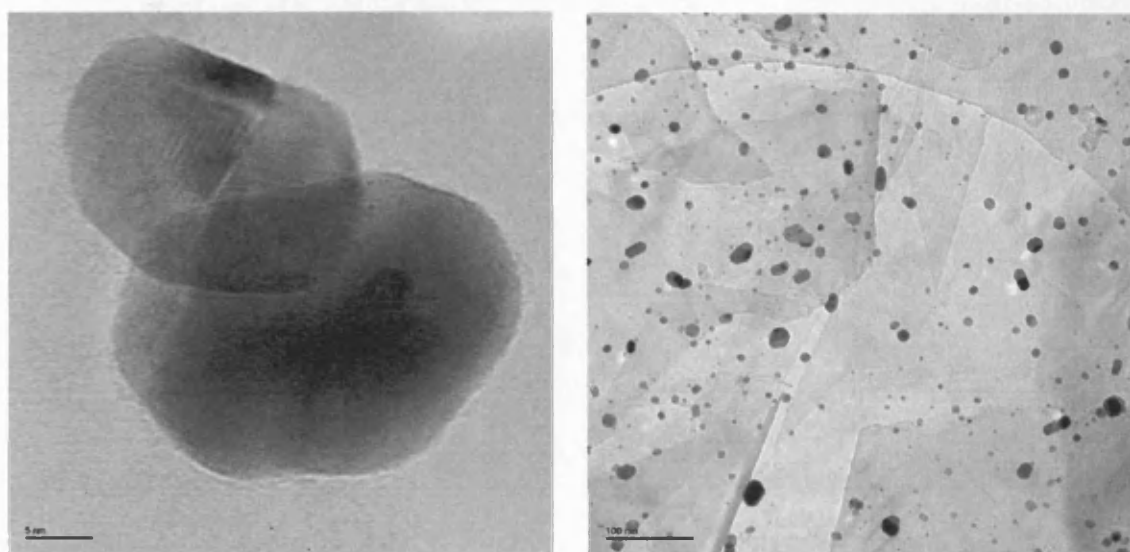


Fig. 3.2(d) TEM micrographs of Pt/G catalyst sintered at 700 K.

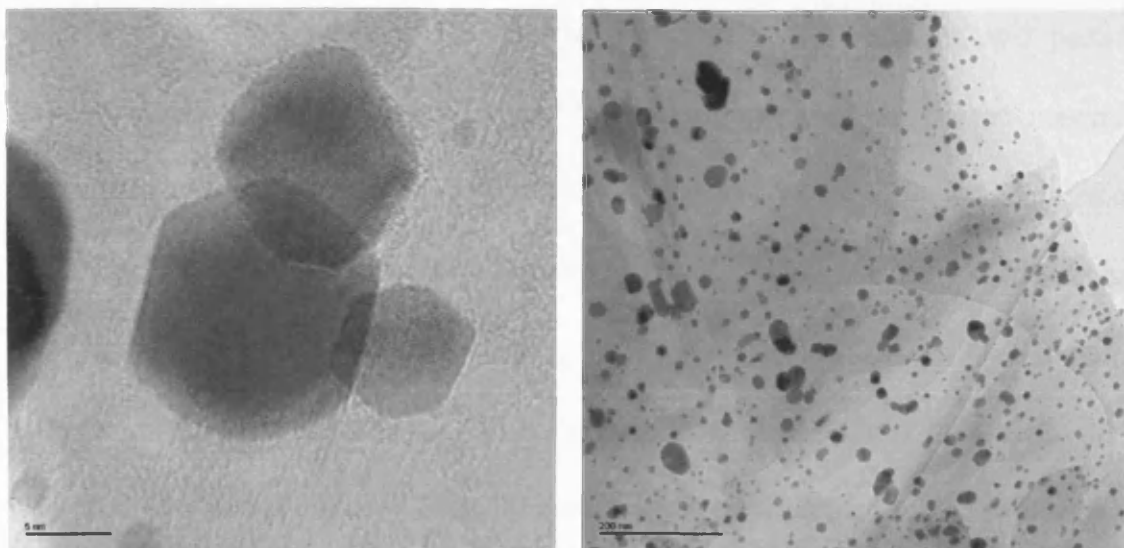


Fig. 3.2(e) TEM micrographs of Pt/G catalyst sintered at 800 K.

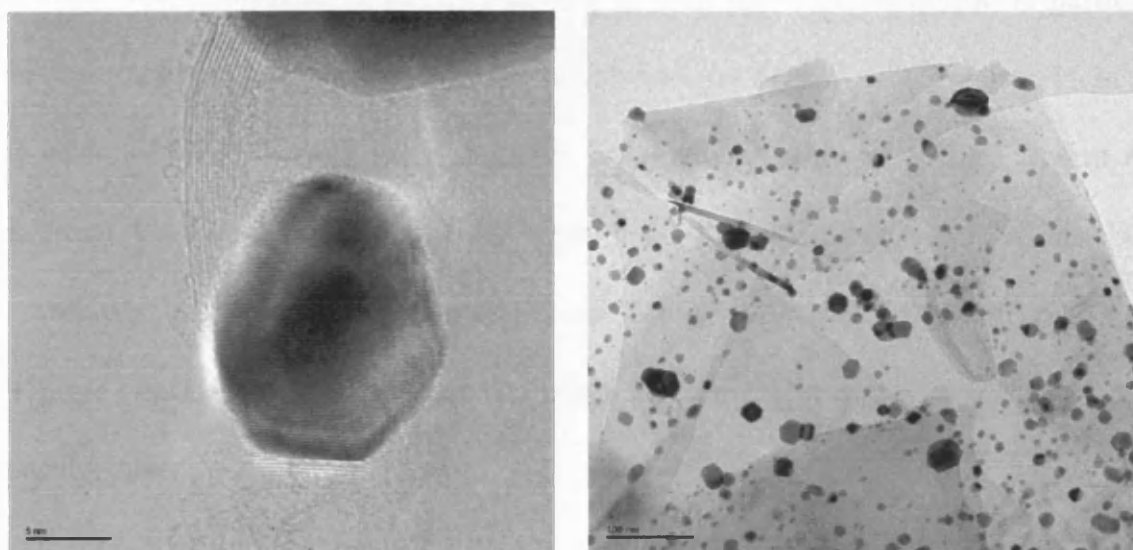
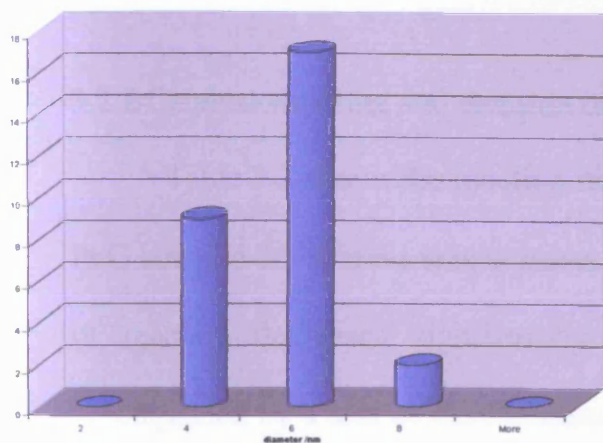
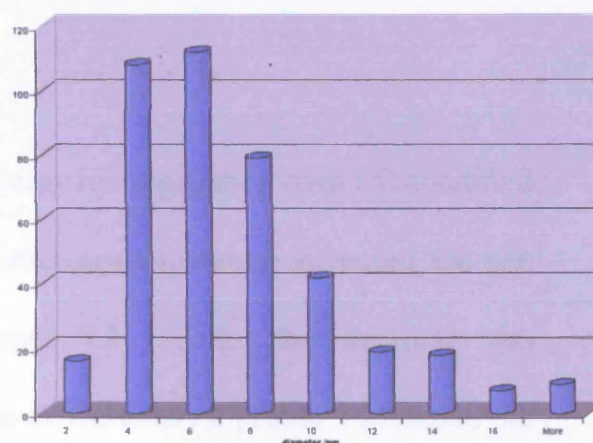


Fig. 3.2(f) TEM micrographs of Pt/G catalyst sintered at 900 K.

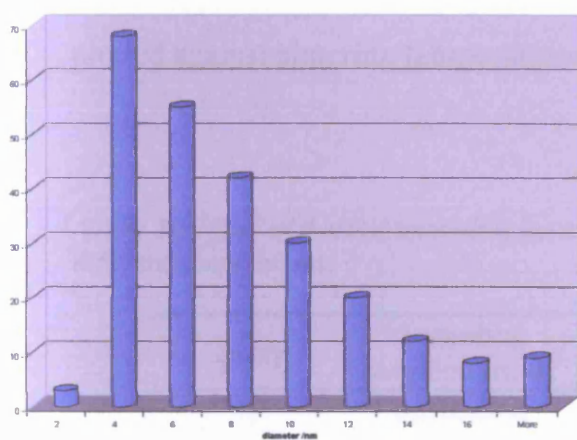
Particle size distributions for the unsintered Pt/G catalyst and particles sintered at 450, 600, 700, 800, and 900 K (Figure 3.3(a)-(f)) were measured. Unsintered catalyst (Figure 3.3(a)) particles exhibited an average particle size of 6 nm. However, it should be noted that this analysis tended to ignore the large number of particles connected together. If this was taken into account, the average particle size was much larger. The particle size distribution for Pt/G catalyst annealed at 450 K (Figure 3.3(b)) showed the appearance of particles which had diameters between 8 – 16 nm. Pt/G catalysts annealed at 600 K showed an increase in average particle size to 16 nm. Figure 3.3(c)-(e) showed the particle size distribution for the catalysts annealed at 700, 800, and 900 K respectively. Particle size continued to increase at 700 K then upon reaching 800 K particles lost connection and started to grow as shown in Figure 3.3(f). Clearly, in all measurements of particle size, a rather broad distribution of values around the average was observed. It will be seen later that there appeared to be little correlation between particle size and ee (as found previously in earlier studies [3, 4]) and hence emphasizing the need to relate ee to catalyst morphology rather than particle size.



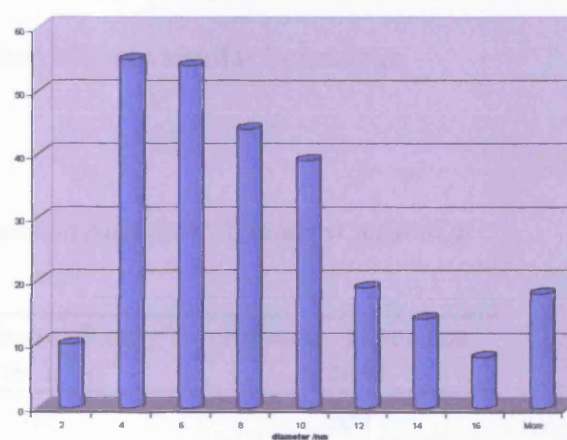
(a)



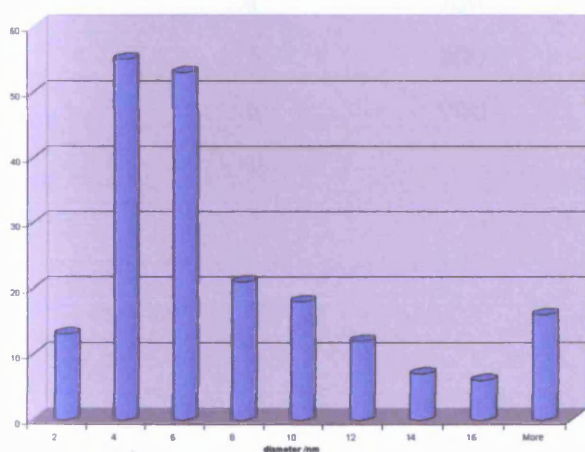
(b)



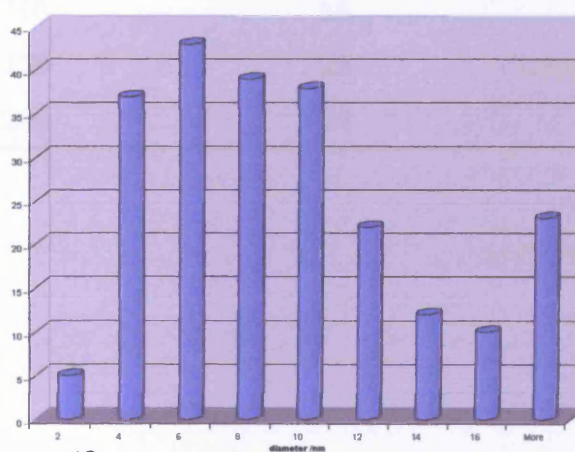
(c)



(d)



(e)



(f)

Fig. 3.3 Pt particle size distribution for unsintered (a) Pt/G and sintered at (b) 450, (c) 600, (d) 700, (e) 800, and (f) 900 K. Sintering was carried out under 5% H₂/Ar.

3.2.2 Catalyst sintering and reaction rate

Table 3.2 shows the reaction rates of etpy hydrogenation over CD-modified Pt/G sintered at different temperatures. As sintering temperature increased, the rate of reaction decreased significantly (Figures 3.3 - 3.4). This decrease was accompanied by a loss of the Pt surface area of the catalyst (Table 3.2) due to the growth in Pt particle size. When both the relative area and the reaction rate were plotted against sintering temperature, it exhibited closely similar behaviour.

Table 3.2 Effect of thermal annealing on maximum reaction rates for Pt/G catalyst sintered at different temperatures.

Entry	Annealing temperature /K	Maximum Rate /mmol h ⁻¹ g ⁻¹	Relative Pt surface area %
1	unsintered	611	100
2	450	189	51
3	600	174	44
4	700	250	36
5	800	170	25
6	900	200	24

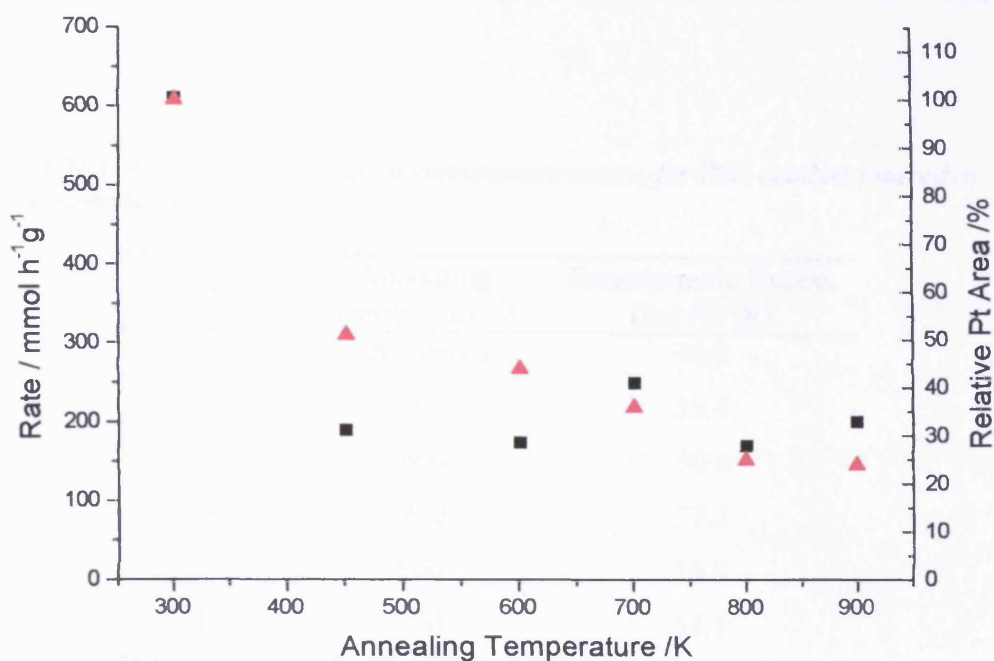


Fig. 3.4 Influence of thermal annealing on the reaction rate of etpy hydrogenation over CD-modified Pt/G (left y-axis) and on the relative Pt surface area (right y-axis). Filled squares data points for reaction rate. Filled triangles data points for relative surface area.

3.2.3 Effect of thermal annealing on enantioselectivity

Table 3.3 shows the effect of thermal annealing on enantiomeric excess at 100% conversion. As annealing temperature was increased, the ee for the catalyst annealed at 450 K decreased from the value of 40% to 35.4%. By contrast, the catalysts annealed at 600 K and above all showed an increase in ee and exhibited a maximum at 700 K followed by a slight decrease at 800-900 K. A similar rise and fall in ee were reported by Attard *et al.* [1, 5], Orito *et al.* [3], and Baiker *et al.* [6] when they examined the dependence of ee on catalyst reduction temperature.

However, the decrease in ee, below 600 K, is new and we will return to this point later.

Table 3.3 Effect of thermal annealing on enantiomeric excess for Pt/G catalyst sintered at different temperatures.

Entry	Annealing temperature /K	Enantiomeric Excess (ee) /% (R)
1	unsintered	40.0
2	450	35.4
3	600	50.4
4	700	57.3
5	800	54.0
6	900	52.1

3.3 Bismuth adsorption on supported platinum and its influence on enantioselective hydrogenation of ethyl pyruvate

3.3.1 Adsorption of Bi on Pt/G sintered at 450 K

3.3.1.1 CV characterisation

Figure 3.5 shows CVs of Bi adsorption on sintered Pt/G in 5% H₂/Ar at 450 K. Table 3.4 shows Bi(NO₃)₃ dosing volumes and surface coverages calculated according to the method described in section 2.7.6. Preparation of bismuthated samples for each sintered Pt/G catalyst was described in section 2.4.1. Adsorption

of Bi at $\theta_{\text{Bi}} = 0.0 - 0.55$ first occurred at $\{111\} \times \{111\}$ and $\{100\} \times \{111\}$ step sites as shown by loss of the CV peak area of these sites [5, 7]. At the same time, Pt $\{100\}$ terrace sites diminished significantly by the first dose of Bi and then continued to diminish in magnitude. A growth of Bi on Pt $\{111\}$ terrace sites (indicated by surface redox processes at 0.54 V [7]) commenced at $\theta_{\text{Bi}} = 0.55$ and Pt $\{111\}$ terrace sites were almost completely attenuated at $\theta_{\text{Bi}} = 0.73$. As more Bi was deposited, Pt H_{UPD} voltammetric features were gradually extinguished and the Bi surface redox peak at 0.54 V continued to increase in magnitude.

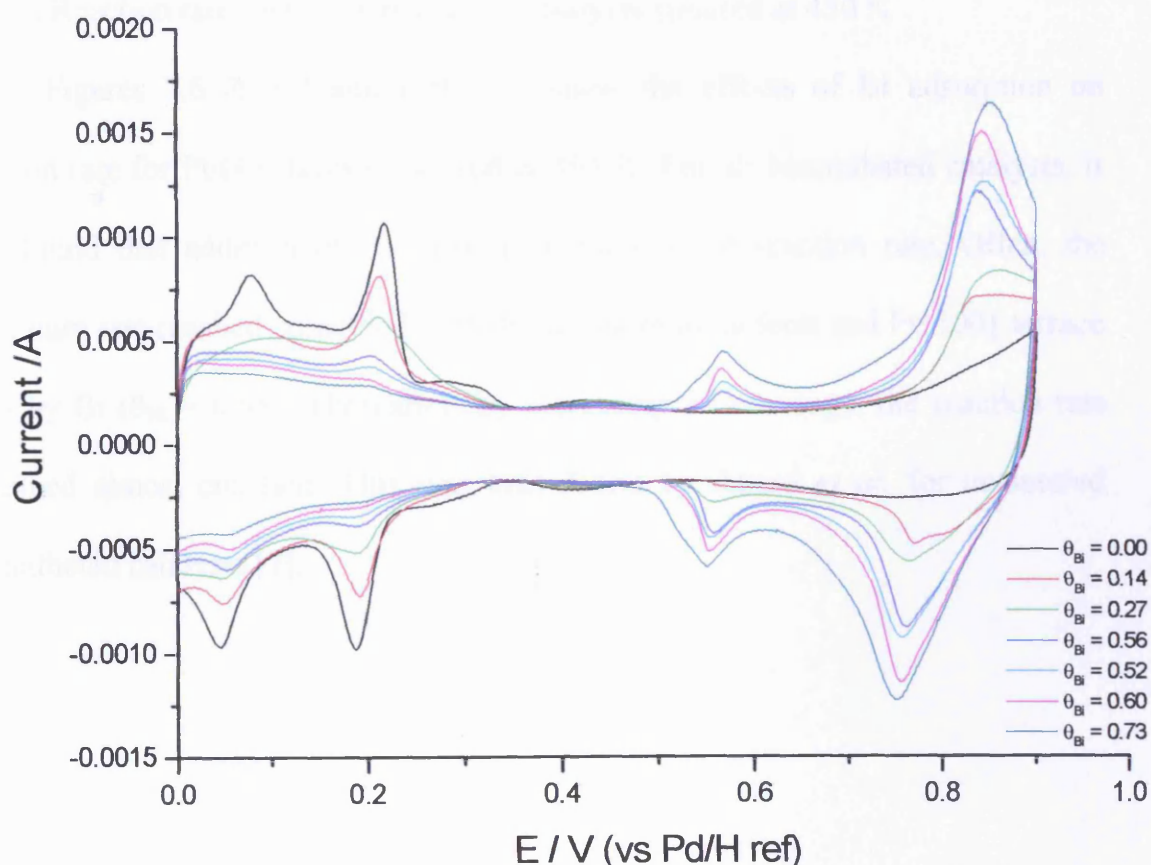


Fig. 3.5 CVs of Bi modified Pt/G (sintered at 450 K) in 0.5M H₂SO₄. Sweep rate 50 mV s⁻¹.

Table 3.4 Dosing volumes of $\text{Bi}(\text{NO}_3)_3$ and surface coverages for Pt/G catalyst sintered at 450 K.

Entry	Dosing Volume /cm ³	Surface Coverage / θ_{Bi}
1	0.0	0.00
2	2.8	0.14
3	7.0	0.27
4	10.5	0.56
5	12.0	0.52
6	18.0	0.60
7	24.0	0.73

3.3.1.2 Reaction rates using bismuthated catalysts sintered at 450 K

Figures 3.6 & 3.7 and table 3.5 show the effects of Bi adsorption on reaction rate for Pt/G catalysts sintered at 450 K. For all bismuthated catalysts, it was found that addition of Bi caused an increase in reaction rate. Often, the maximum rate reached coincided with the filling of all defects and Pt{100} terrace sites by Bi ($\theta_{\text{Bi}} = 0.55$). Thereafter, by increasing Bi coverage, the reaction rate remained almost constant. This was also found by Attard *et al.* for unsintered bismuthated catalysts [7].

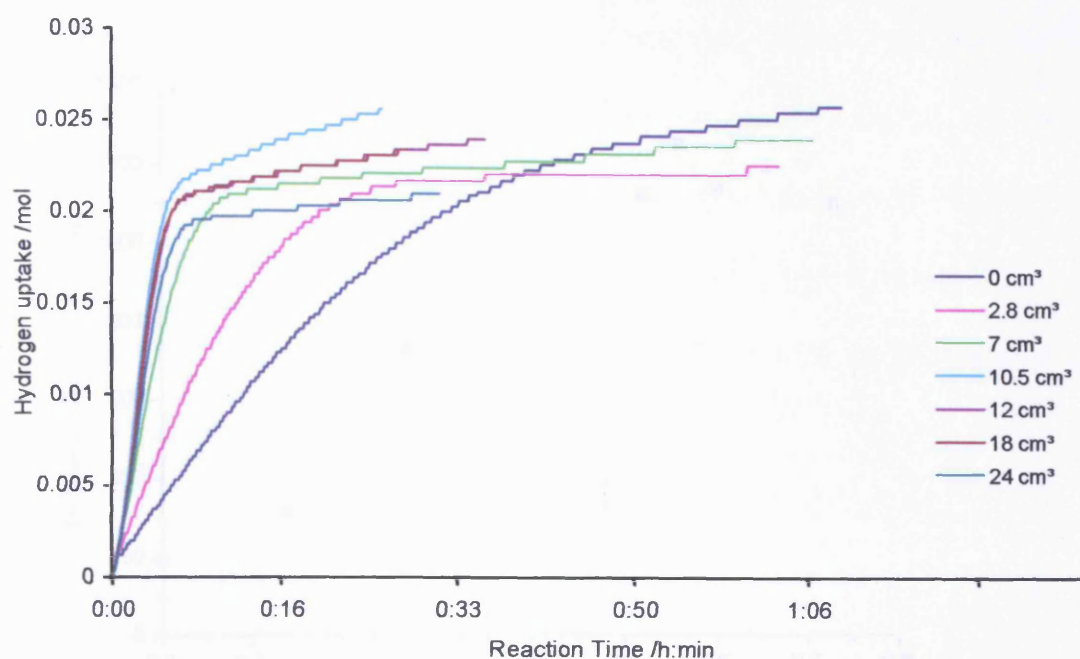


Fig. 3.6 H_2 uptake curves for etpy hydrogenation over CD-modified Pt/G catalyst sintered at 450 K at different $\text{Bi}(\text{NO}_3)_3$ coverages.

Table 3.5 Effect of Bi adsorption on reaction rates for Pt/G catalyst sintered at 450 K.

Entry	Dosing Volume / cm^3	Surface Coverage / θ_{Bi}	Maximum Rate / $\text{mmol h}^{-1} \text{g}^{-1}$
1	0.0	0.00	189
2	2.8	0.14	314
3	7.0	0.27	728
4	10.5	0.56	1252
5	12.0	0.52	1117
6	18.0	0.60	1141
7	24.0	0.73	1100

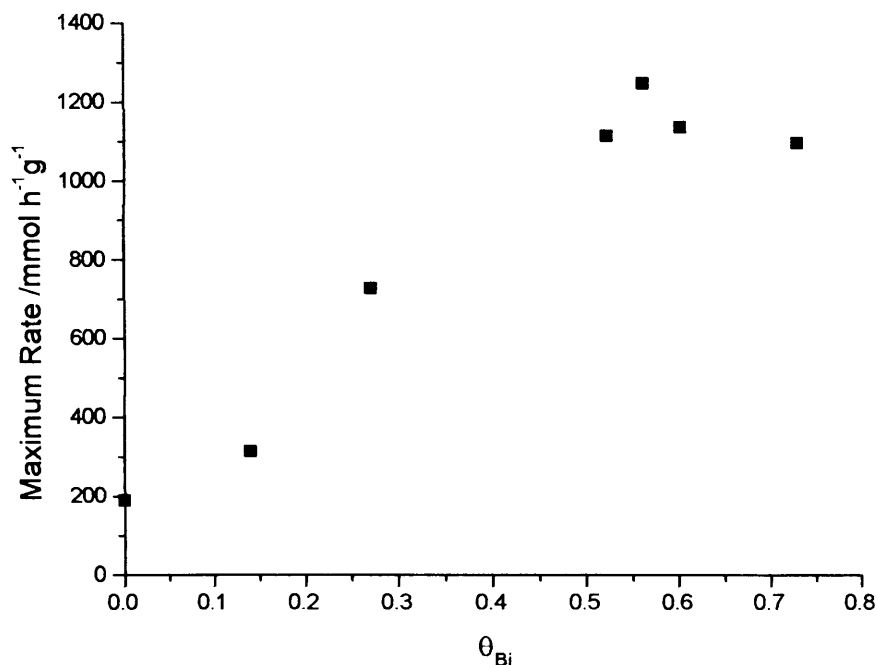


Fig. 3.7 Maximum rate versus Bi coverage for etpy hydrogenation over CD-modified Pt/G catalyst sintered at 450 K.

3.3.1.3 Enantioselectivity

Figure 3.8 and Table 3.6 show the influence of Bi adsorption on the enantioselectivity of etpy hydrogenation. Although the addition of Bi to Pt caused an overall decrease in ee from 35% to 31%, a reproducible increase in ee from 35% to 39% was always observed when a small amount of Bi was adsorbed. It should also be noted that in relation to the unsintered Pt/G catalyst, the ee of the 450 K sintered catalyst was rather low. The increase in ee caused by the initial uptake of Bi for the catalyst was always consistent with blocking of large domains

of Pt{100} terraces i.e. a tentative explanation of this phenomena could be that the presence of Pt{100} terrace domains is actually detrimental to overall ee. If such sites represent a large proportion of the total platinum surface area, one would then expect a relatively poor ee. By blocking {100} terraces with Bi, one should expect an increase in ee. The decrease in ee was significant at $\theta_{\text{Bi}} = 0 - 0.55$ which is coincident with the blockage of Pt step sites [7]. At higher coverage ($\theta_{\text{Bi}} > 0.50$), the decrease in ee was less marked which is coincident with the blockage of {111} terrace sites as found in reference [7].

Table 3.6 Variation in enantioselectivity with increasing Bi coverage for Pt /G catalyst sintered at 450 K.

Entry	Dosing Volume /cm ³	Surface Coverage / θ_{Bi}	Enantiomeric Excess (ee) /% (R)
1	0.0	0.00	35.4
2	2.8	0.14	38.3
3	7.0	0.27	34.2
4	10.5	0.56	31.5
5	12.0	0.52	31.0
6	18.0	0.60	32.5
7	24.0	0.73	30.7

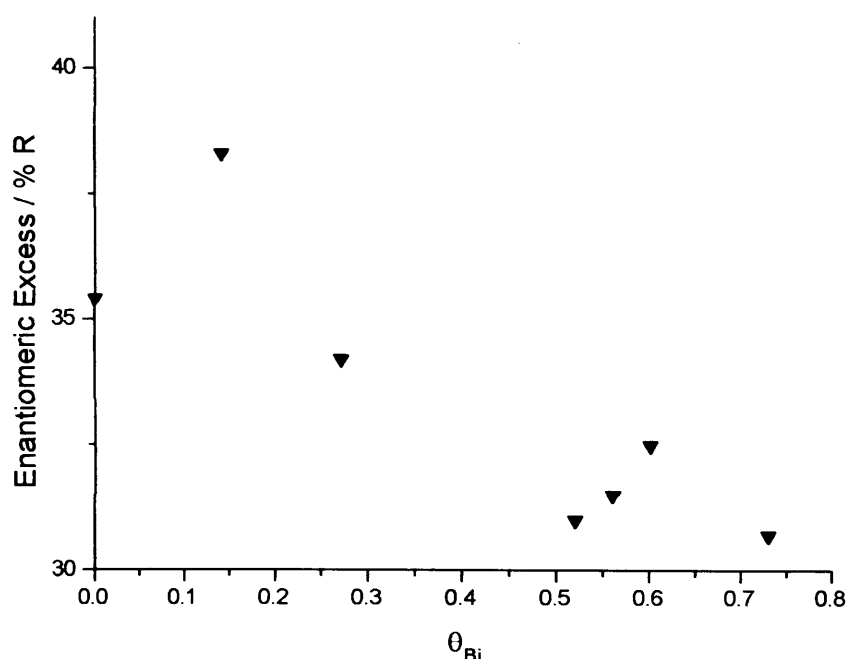


Fig. 3.8 Bi coverage and enantiomeric excess for Pt/G catalyst sintered at 450 K.

3.3.2 Adsorption of Bi on Pt/G sintered between 600 K– 900 K

3.3.2.1 CV characterisation

Preparation of five bismuthated samples for each sintered Pt/G catalyst was described in section 2.4.1. Figures 3.9 - 3.12 show CVs of clean Pt/G and Bi-Pt/G catalysts that were sintered in 5% H₂/Ar at 600, 700, 800, and 900 K. Tables 3.7 – 3.10 show Bi(NO₃)₃ dosing volumes and surface coverages calculated according to the method described in section 2.7.6. Initially, adsorption of Bi ($\theta_{\text{Bi}} = 0.0$ to 0.3 ± 0.05) on Pt/G occurred at $\{111\} \times \{111\}$ and $\{100\} \times \{111\}$ step sites as can be seen from a diminution of step site features. It was also associated with an attenuation

of the {100} terrace site feature at 0.27 V. Growth of new features observed at 0.55 V were due to surface redox processes resulting from the chemisorption of Bi on {111} terraces. These results would be consistent with previous work reported by Attard *et al.* [5, 7, 8]. Adsorption at {111} terraces began at $\theta_{\text{Bi}} = 0.30 \pm 0.05$ as signified by an attenuation of {111} terrace site voltammetric features. As Bi coverage increased, Bi adsorption on {111} terrace sites continued and features of the Pt-H_{UPD} region almost disappeared. The Bi-Pt{111} voltammetric peaks at 0.55 V were noticeably sharper than for unsintered catalysts and catalysts annealed below 600 K. The data for the 800 K sintered catalysts is particularly striking in this regard. This behaviour is again consistent with the wider average {111} terrace width of the sintered catalysts [2].

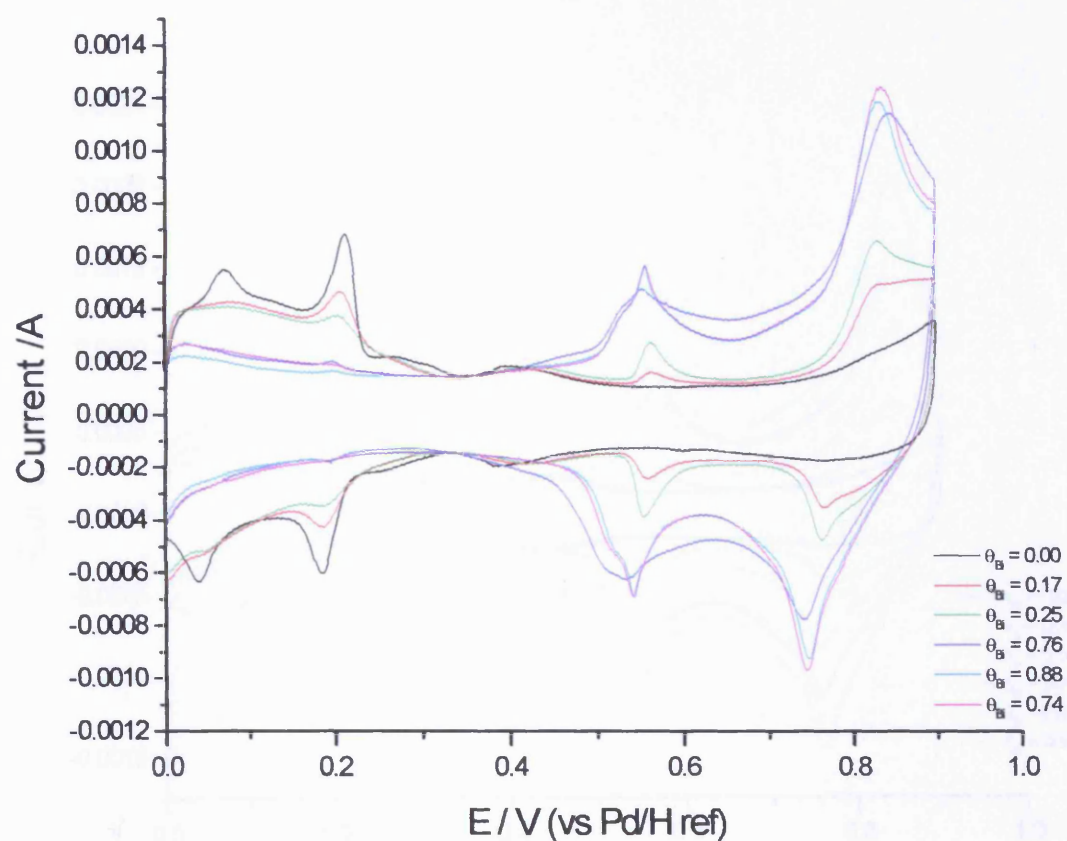


Fig. 3.9 CVs of Bi modified Pt/G (sintered at 600 K) in 0.5M H_2SO_4 . Sweep rate 50 mV s^{-1} .

Table 3.7 Dosing volumes of $\text{Bi}(\text{NO}_3)_3$ and surface coverages for Pt/G catalyst sintered at 600 K.

Entry	Dosing Volume $/\text{cm}^3$	Surface Coverage θ_{Bi}
1	0.0	0.00
2	2.8	0.17
3	7.0	0.25
4	12.0	0.76
5	18.0	0.88
6	24.0	0.74

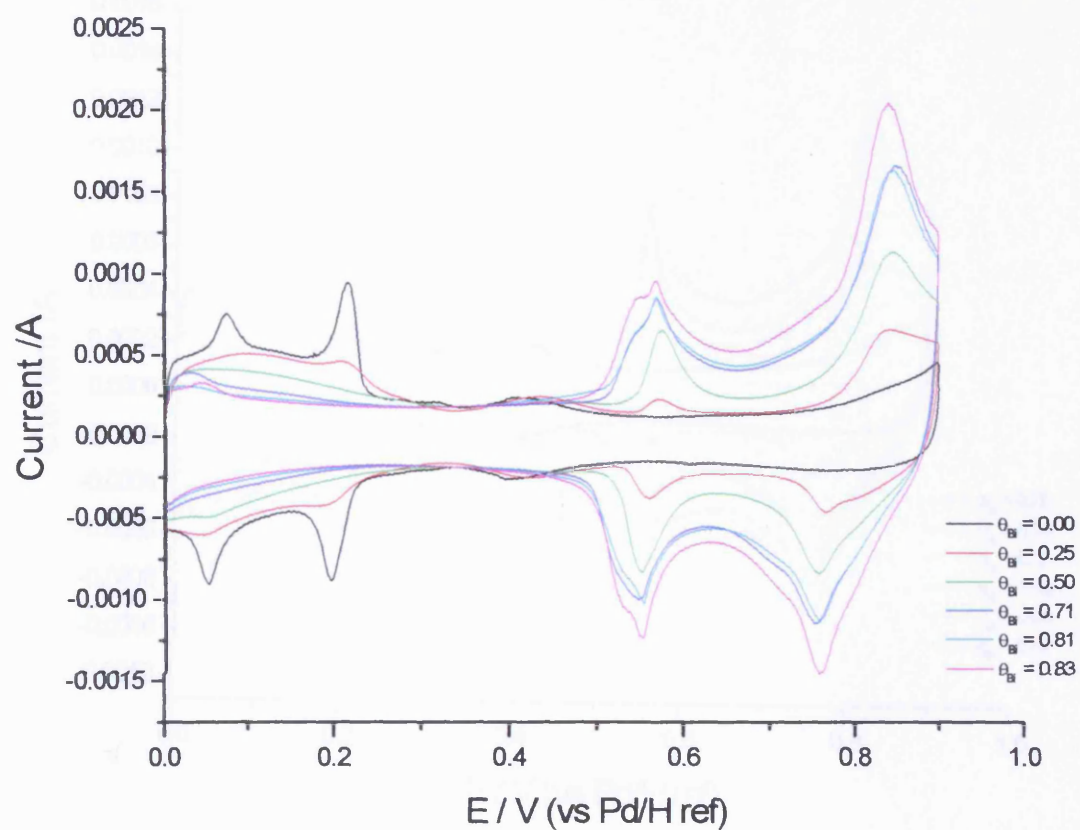


Fig. 3.10 CVs of Bi modified Pt/G (sintered at 700 K) in 0.5M H₂SO₄. Sweep rate 50 mV s⁻¹.

Table 3.8 Dosing volumes of Bi(NO₃)₃ and surface coverages for Pt/G catalyst sintered at 700 K.

Entry	Dosing Volume /cm ³	Surface Coverage θ_{Bi}
1	0.0	0.00
2	2.8	0.25
3	7.0	0.50
4	12.0	0.71
5	18.0	0.81
6	24.0	0.83

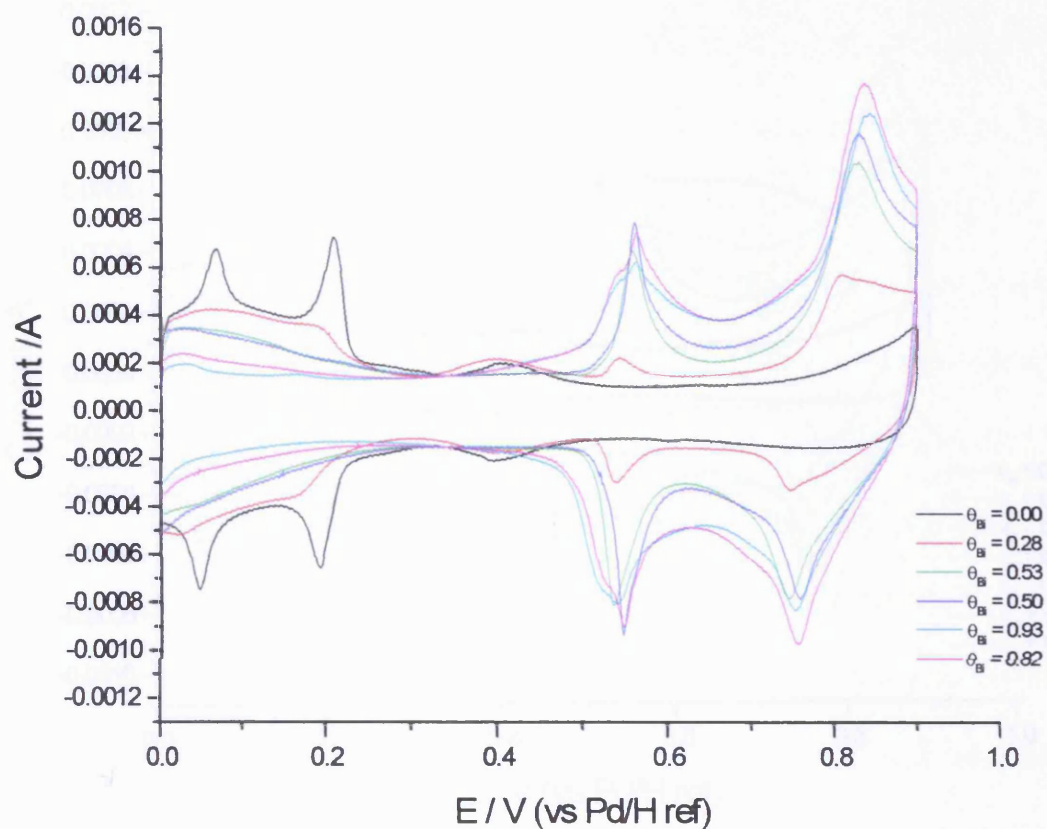


Fig. 3.11 CVs of Bi modified Pt/G (sintered at 800 K) in 0.5M H₂SO₄. Sweep rate 50 mV s⁻¹.

Table 3.9 Dosing volumes of Bi(NO₃)₃ and surface coverages for Pt/G catalyst sintered at 800 K.

Entry	Dosing Volume /cm ³	Surface Coverage /θ _{Bi}
1	0.0	0.00
2	2.8	0.28
3	7.0	0.53
4	12.0	0.50
5	18.0	0.93
6	24.0	0.82

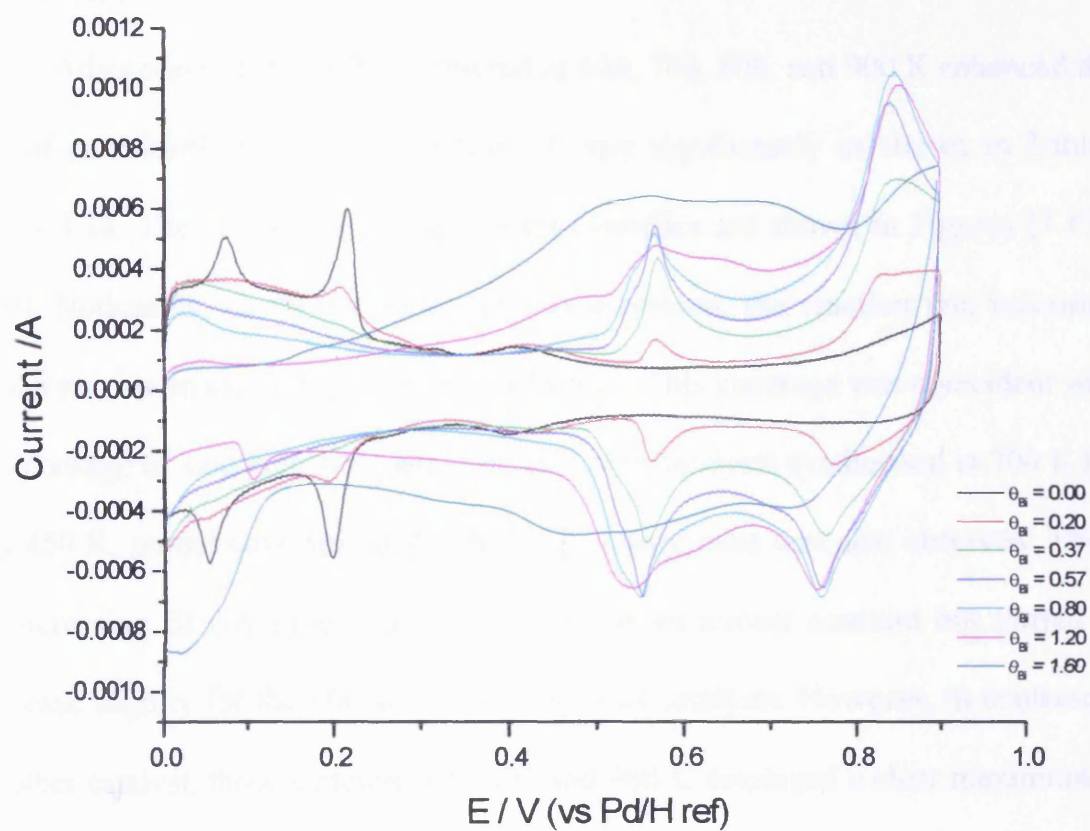


Fig. 3.12 CVs of Bi modified Pt/G (sintered at 900 K) in 0.5M H₂SO₄. Sweep rate 50 mV s⁻¹.

Table 3.10 Dosing volumes of Bi(NO₃)₃ and surface coverages for Pt/G catalyst sintered at 900 K.

Entry	Dosing Volume /cm ³	Surface Coverage /θ _{Bi}
1	0.0	0.00
2	2.8	0.20
3	7.0	0.37
4	10.5	0.57
5	12.0	0.80
6	18.0	1.20
7	24.0	1.60

3.3.2.2 Reaction rate

Adsorption of Bi on Pt/G sintered at 600, 700, 800, and 900 K enhanced the rate of enantioselective hydrogenation of etpy significantly as shown in Tables 3.11 - 3.14. The resulting hydrogen uptake profiles are shown in Figures (3.13 - 3.20). Noticeably, as the Bi coverage was increased, the reaction rate increased until a maximum rate at $\theta_{\text{Bi}} = 0.6$ was achieved. This coverage was coincident with the blockage of step/kink sites and, in contrast to catalysts synthesised at 300 K [9] and 450 K, partial coverage of the Pt{111} terrace sites was also observed. Then, by increasing Bi coverage, reaction rate remained almost constant but started to decrease slightly for the 600 and 700 K sintered catalysts. However, in contrast to all other catalyst, those sintered at 800 K and 900 K displayed a clear maximum in rate as a function of Bi coverage that coincided roughly with the onset of filling of {111} terrace sites by Bi followed by a sharp decrease as shown in Figure 3.18 and 3.20.

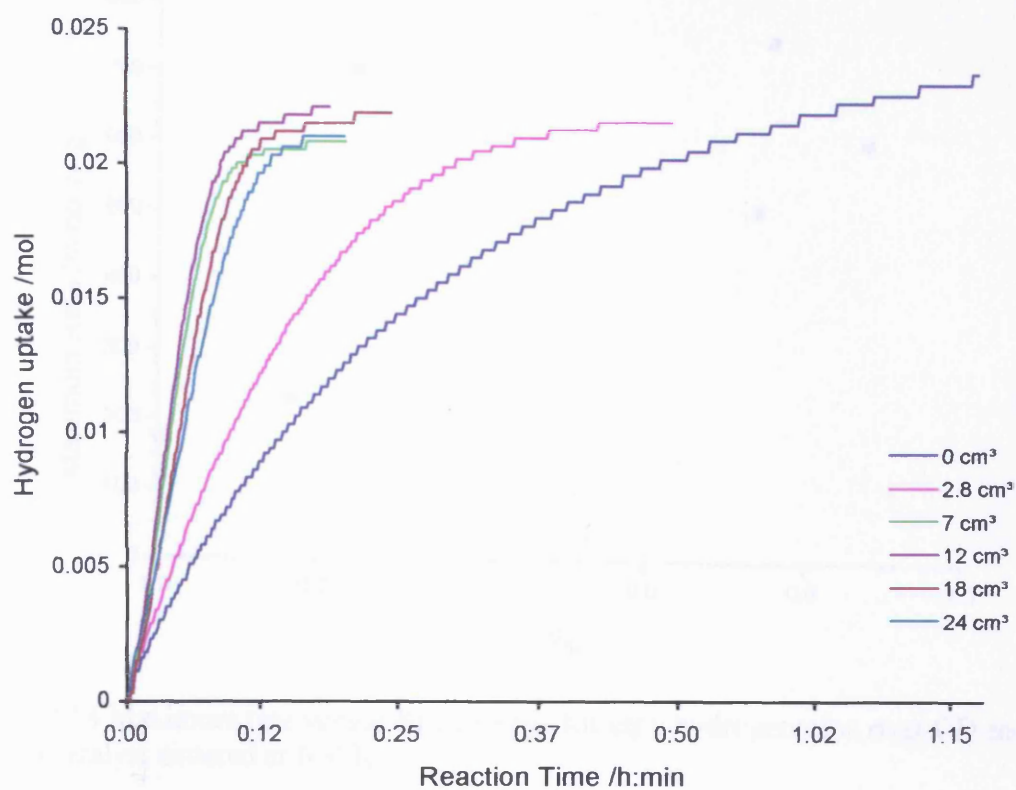


Fig. 3.13 H_2 uptake curves for etpy hydrogenation over CD-modified Pt/G catalyst sintered at 600 K at different $\text{Bi}(\text{NO}_3)_3$ coverages.

Table 3.11 Effect of Bi adsorption on reaction rates for Pt/G catalyst sintered at 600 K.

Entry	Dosing Volume / cm^3	Surface Coverage / θ_{Bi}	Maximum Rate / $\text{mmol h}^{-1} \text{g}^{-1}$
1	0.0	0.00	174
2	2.8	0.17	228
3	7.0	0.25	705
4	12.0	0.76	752
5	18.0	0.88	604
6	24.0	0.74	506

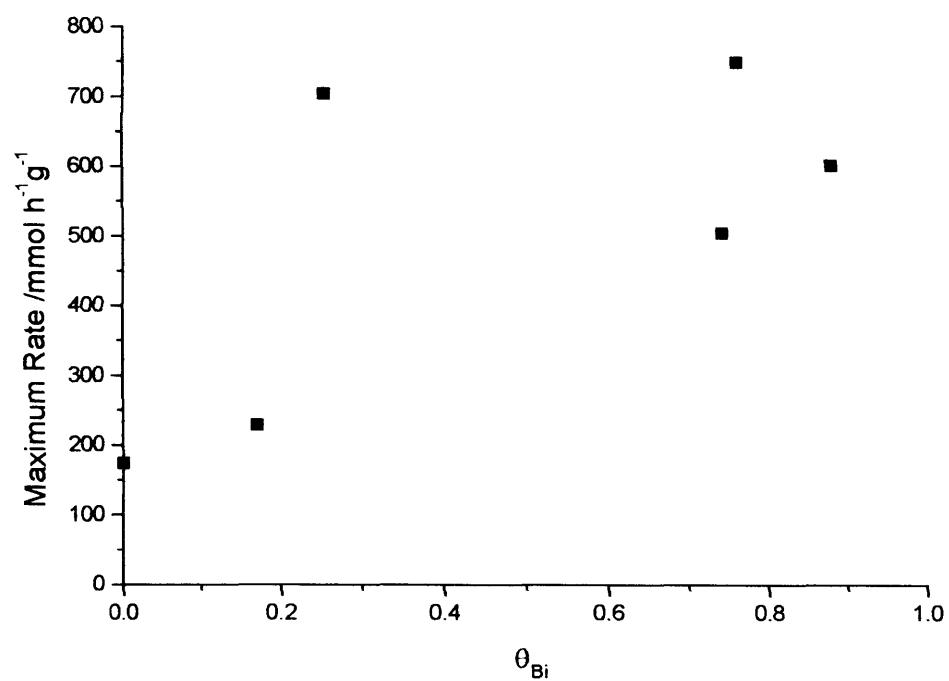


Fig. 3.14 Maximum rate versus Bi coverage for etpy hydrogenation over CD-modified Pt/G catalyst sintered at 600 K.

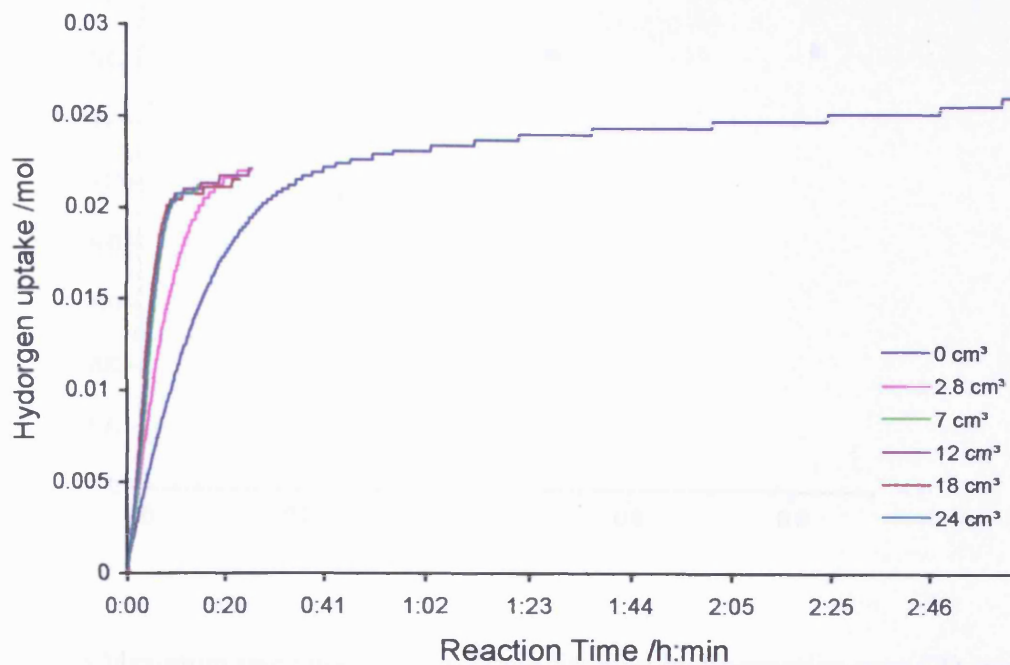


Fig. 3.15 H_2 uptake curves for etpy hydrogenation over CD-modified Pt/G catalyst sintered at 700 K at different $\text{Bi}(\text{NO}_3)_3$ coverages.

Table 3.12 Effect of Bi adsorption on reaction rates for Pt/G catalyst sintered at 700 K.

Entry	Dosing Volume / cm^3	Surface Coverage $/\theta_{\text{Bi}}$	Maximum Rate / $\text{mmol h}^{-1} \text{g}^{-1}$
1	0.0	0.0	250
2	2.8	0.25	477
3	7.0	0.5	718
4	12.0	0.71	827
5	18.0	0.81	834
6	24.0	0.83	727

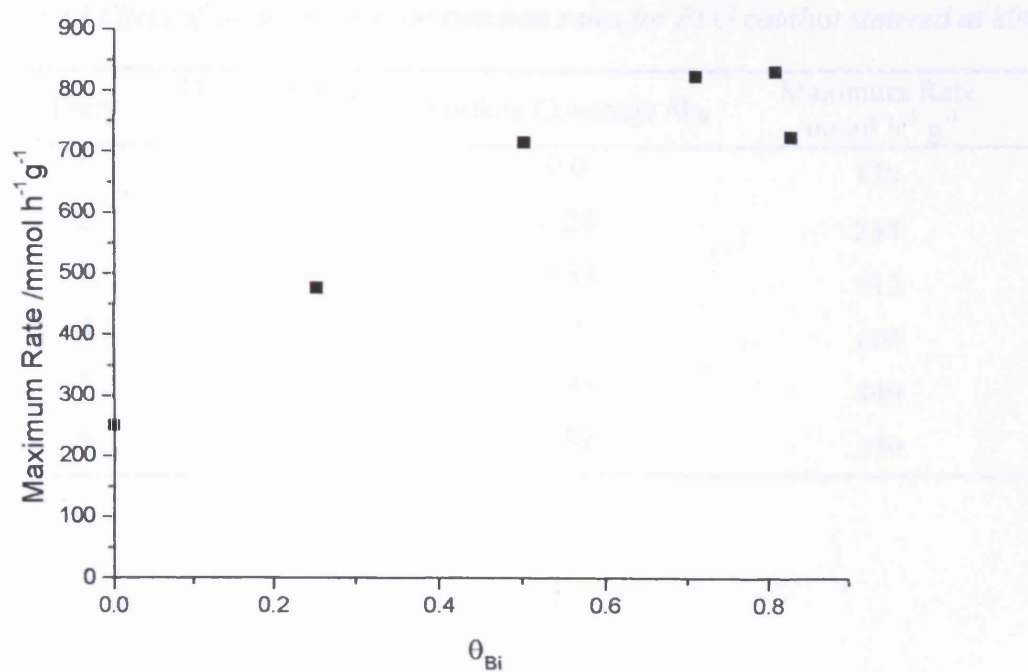


Fig. 3.16 Maximum rate versus Bi coverage for etpy hydrogenation over CD-modified Pt/G catalyst sintered at 700 K.

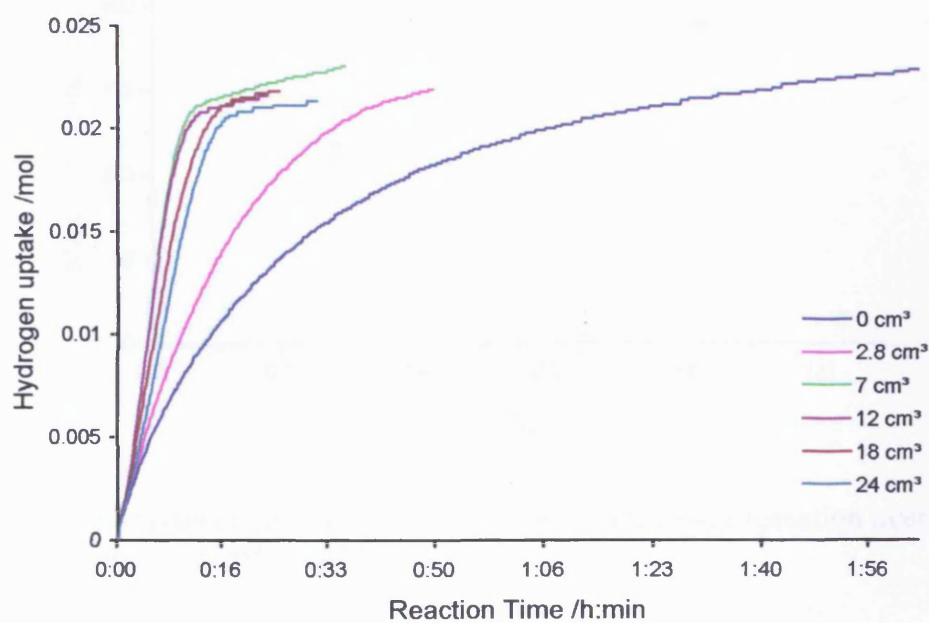


Fig. 3.17 H₂ uptake curves for etpy hydrogenation over CD-modified Pt/G catalyst sintered at 800 K at different Bi(NO₃)₃ coverages.

Table 3.13 Effect of Bi adsorption on reaction rates for Pt/G catalyst sintered at 800 K.

Entry	Dosing Volume /cm ³	Surface Coverage / θ_{Bi}	Maximum Rate /mmol h ⁻¹ g ⁻¹
1	0.0	0.0	170
2	2.8	0.28	234
3	7.0	0.53	612
4	12.0	0.5	604
5	18.0	0.93	449
6	24.0	0.82	379

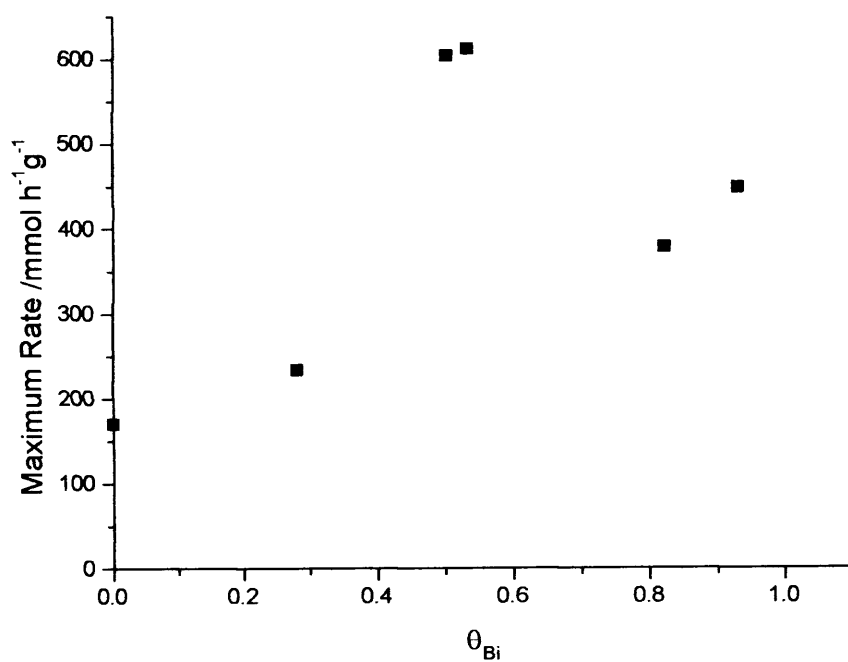


Fig. 3.18 Maximum rate versus Bi coverage for etpy hydrogenation over CD-modified Pt/G catalyst sintered at 800 K.

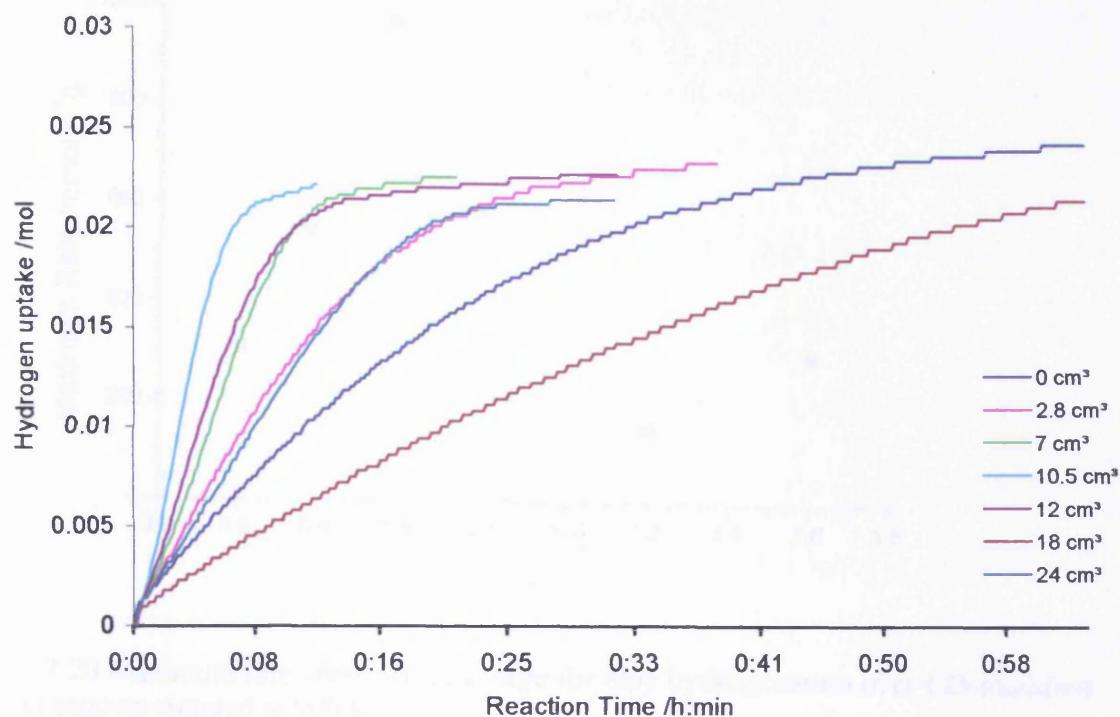


Fig. 3.19 H_2 uptake curves for etpy hydrogenation over CD-modified Pt/G catalyst sintered at 900 K at different $\text{Bi}(\text{NO}_3)_3$ coverages.

Table 3.14 Effect of Bi adsorption on reaction rates for Pt/G catalyst sintered at 900 K.

Entry	Dosing Volume / cm^3	Surface Coverage / θ_{Bi}	Maximum Rate / $\text{mmol h}^{-1} \text{g}^{-1}$
1	0.0	0.00	200
2	2.8	0.20	302
3	7.0	0.37	544
4	10.5	0.57	966
5	12.0	0.80	589
6	18.0	1.20	150
7	24.0	1.60	298

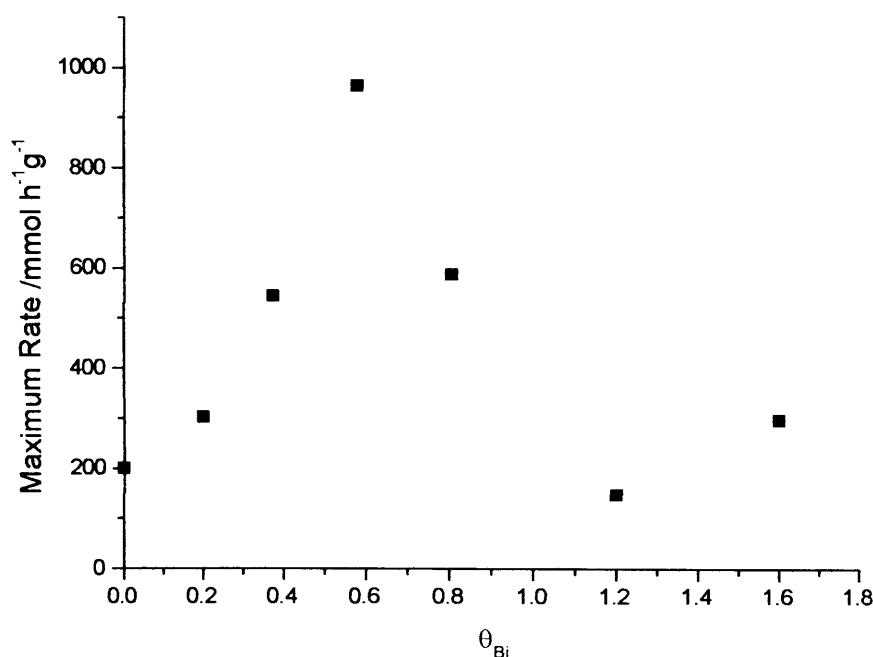


Fig. 3.20 Maximum rate versus Bi coverage for etpy hydrogenation over CD-modified Pt/G catalyst sintered at 900 K.

3.3.2.3 Enantioselectivity

Figures 3.21 - 3.24 and Tables 3.15 - 3.18 show the effect of Bi adsorption on Pt/G sintered at 600, 700, 800, and 900 K. As the Bi coverage was increased, the ee decreased. Furthermore, the decrease in ee in the range of blocking step/kink sites ($\theta_{\text{Bi}} = 0 - 0.3 \pm 0.05$) was larger than that in the range of blocking terrace sites ($\theta_{\text{Bi}} > 0.30 \pm 0.05$). From these findings it could be suggested that step sites have a more significant influence on ee than terrace sites. In previous work by Jenkins *et al.* [9], it was suggested that the abrupt change in slope of ee as a function of Bi-loading was an internal measure of the complete blocking of all defect and {100} terrace sites by Bi and hence the ee obtained at this point, could

be ascribed solely to the ee of the {111} terrace sites. The gradual decrease of ee as Bi populated {111} terrace sites (but not complete attenuation of reaction rate and ee) was ascribed both to the lower inherent enantio-selectivity of CD-modified {111} terrace and also the stability of Bi adsorbate at {111} sites under reaction conditions. Clearly, if the Bi on narrower {111} terraces (300 – 700 K annealed catalysts) was less stable than Bi adsorbed on extended {111} terraces (800 and 900 K sintered catalysts) then an explanation of the rate maximum for the 800 and 900 K Bi-modified catalysts is immediately afforded since a stable Bi adlayer on extended {111} terraces would block Pt reaction sites. Hence a correlation was sought between the ee ascribable to the {111} terraces for each sintered catalyst using the data presented Figures 3.7-3.8 and 3.21-3.24 together with previous data for the unsintered catalyst [7]. By plotting the maximum ee of Pt{111} terraces vs. the annealing temperature (Figure 3.25) of each annealed bismuthated catalyst, it was found that the maximum ee of Pt{111} increased as the annealing temperature increased and reached a plateau at 38% ee irrespective of the average {111} terrace width. Hence we ascribed this upper limit of ee as being the maximum possible ee obtained from a Pt{111} terrace.

Table 3.15 Variation in enantioselectivity with increasing Bi coverage for Pt /G catalyst sintered at 600 K.

Entry	Dosing Volume /cm ³	Surface Coverage / θ_{Bi}	Enantiomeric Excess (ee) /% (R)
1	0.0	0.00	50.4
2	2.8	0.17	41.8
3	7.0	0.25	37.6
4	12.0	0.76	40.7
5	18.0	0.88	39.7
6	24.0	0.74	38.0

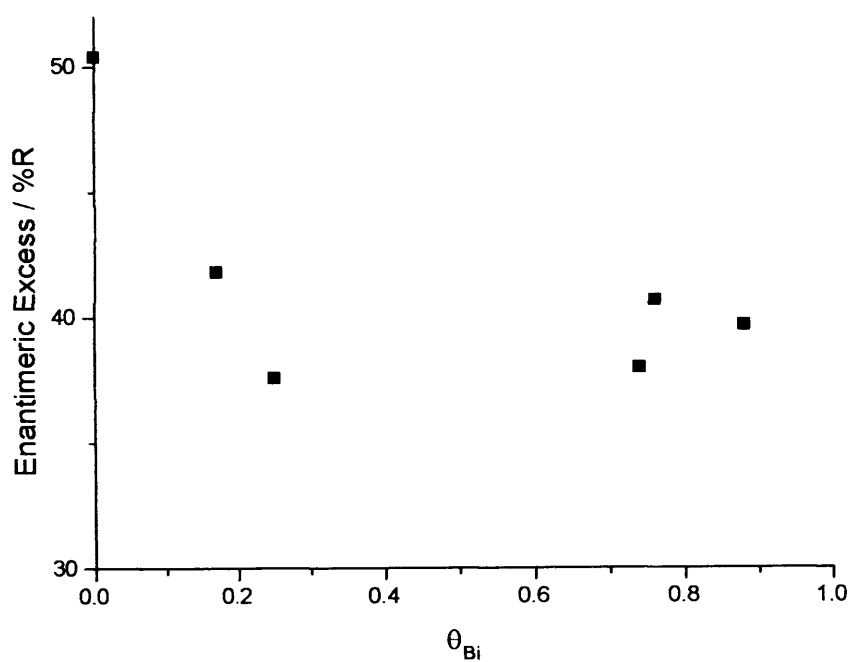


Fig. 3.21 Bi coverage and enantiomeric excess for Pt/G catalyst sintered at 600 K.

Table 3.16 Variation in enantioselectivity with increasing Bi coverage for Pt /G catalyst sintered at 700 K.

Entry	Dosing Volume /cm ³	Surface Coverage / θ_{Bi}	Enantiomeric Excess (ee) /% (R)
1	0.0	0.00	57.3
2	2.8	0.25	47.8
3	7.0	0.50	37.6
4	12.0	0.71	44.0
5	18.0	0.81	40.7
6	24.0	0.83	40.1

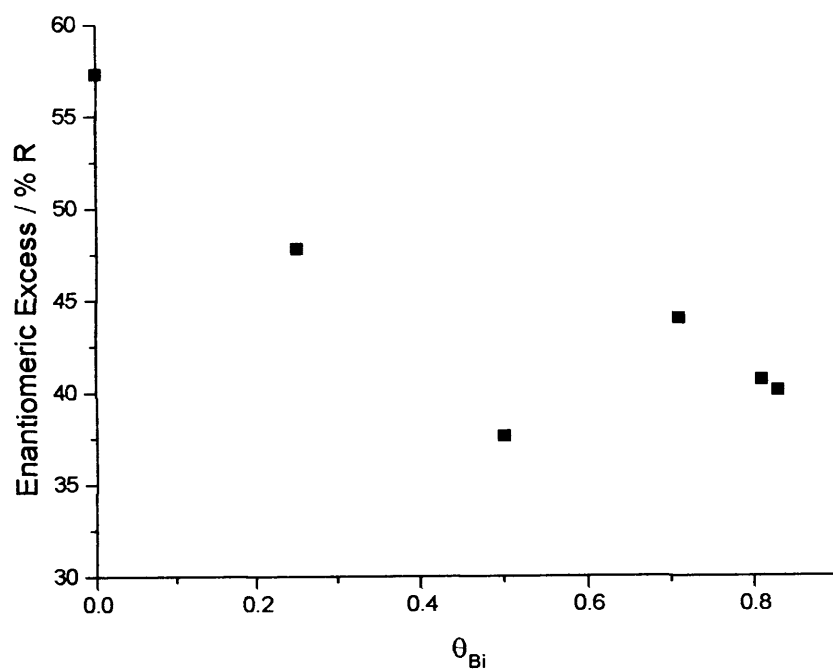


Fig. 3.22 Bi coverage and enantiomeric excess for Pt/G catalyst sintered at 700 K.

Table 3.17 Variation in enantioselectivity with increasing Bi coverage for Pt /G catalyst sintered at 800 K.

Entry	Dosing Volume /cm ³	Surface Coverage / θ_{Bi}	Enantiomeric Excess (ee) /% (R)
1	0.0	0.00	54.0
2	2.8	0.28	43.2
3	7.0	0.53	39.2
4	12.0	0.50	39.5
5	18.0	0.93	41.4
6	24.0	0.82	35.7

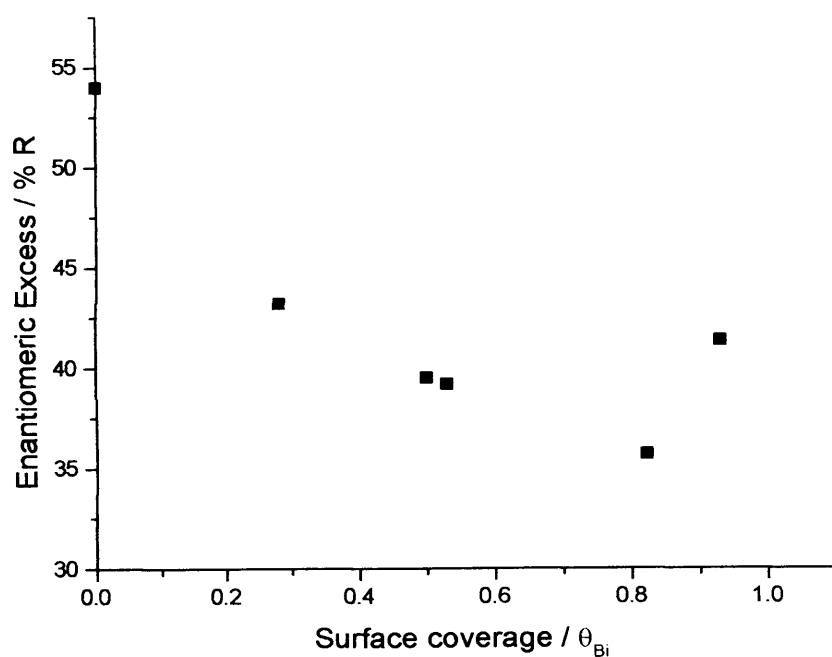


Fig. 3.23 Bi coverage and enantiomeric excess for Pt/G catalyst sintered at 800 K.

Table 3.18 Variation in enantioselectivity with increasing Bi coverage for Pt /G catalyst sintered at 900 K.

Entry	Dosing Volume /cm ³	Surface Coverage / θ_{Bi}	Enantiomeric Excess (ee) /% (R)
1	0.0	0.00	52.1
2	2.8	0.20	48.2
3	7.0	0.37	38.7
4	10.5	0.57	38.9
5	12.0	0.80	37.5
6	18.0	1.20	33.4
7	24.0	1.60	29.7

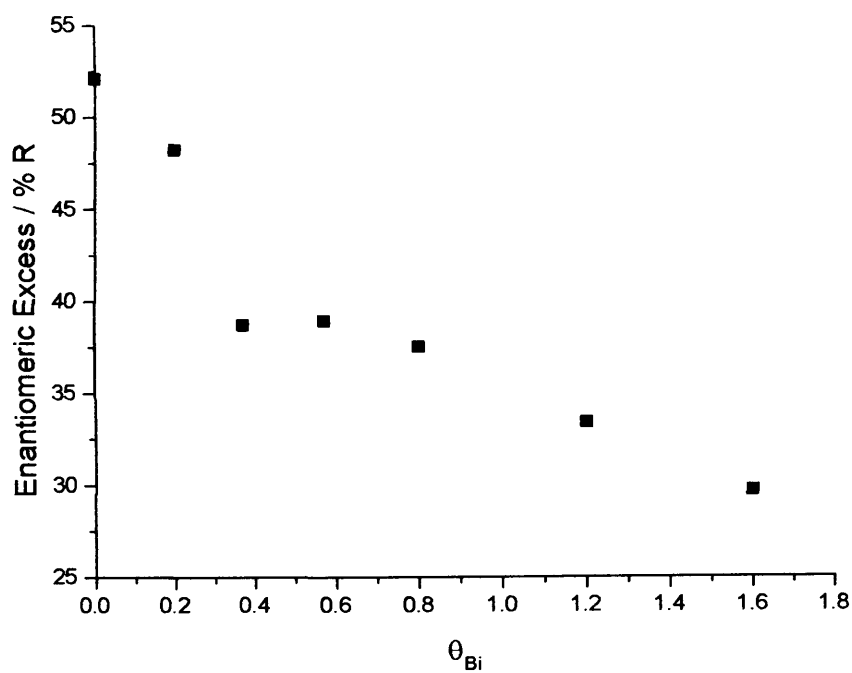


Fig. 3.24 Bi coverage and enantiomeric excess for Pt/G catalyst sintered at 900 K.

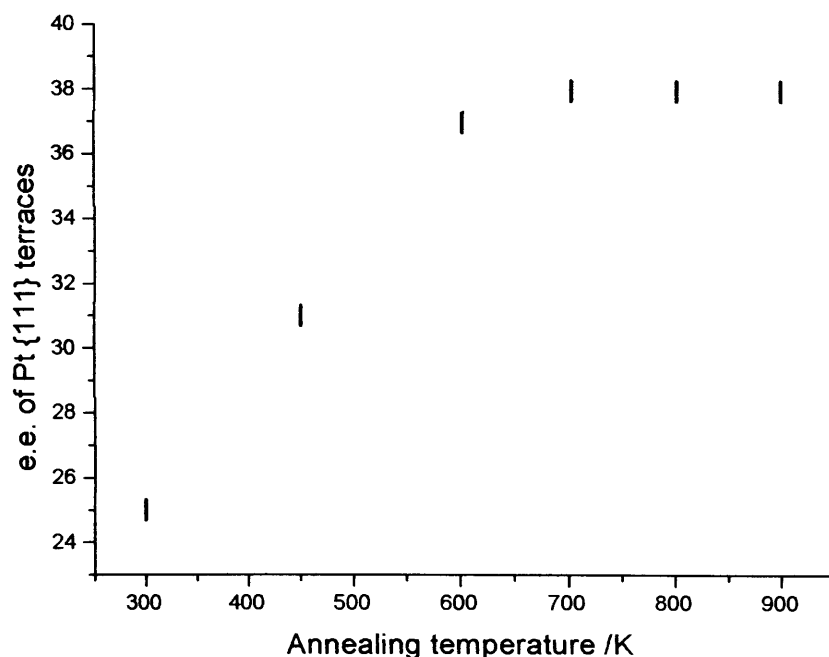


Fig. 3.25 Plot of enantiomeric excess for Pt{111} terraces (all defects and {100} terraces blocked by Bi) versus annealing temperature. Enantiomeric excess at 300 K obtained from reference [9].

3.3.3 Adsorption of Bi on Pt/SiO₂

3.3.3.1 Reaction rate

Adsorption of Bi on 6.5% Pt/SiO₂ (EUROPT-1) sintered at 450 K enhanced the rate of etpy hydrogenation as shown in Figures 3.26 & 3.27 and table 3.19. As the Bi coverage was increased, the reaction rate also increased. A maximum reaction rate of 3761 mmol h⁻¹ g⁻¹ was achieved when the Bi dose was 20 cm³. Then the reaction rate started to decrease as the Bi coverage was further increased, until it reached 1249 mmol h⁻¹ g⁻¹ at Bi doses of 48 cm³. This is similar to the

effect Bi coverage had on Pt/G catalysts. Thus, it is expected that the significant increase in reaction rate at the low coverage ($0 - 20 \text{ cm}^3$) is due to the blockage of Pt step/kink sites and $\{100\}$ terraces.

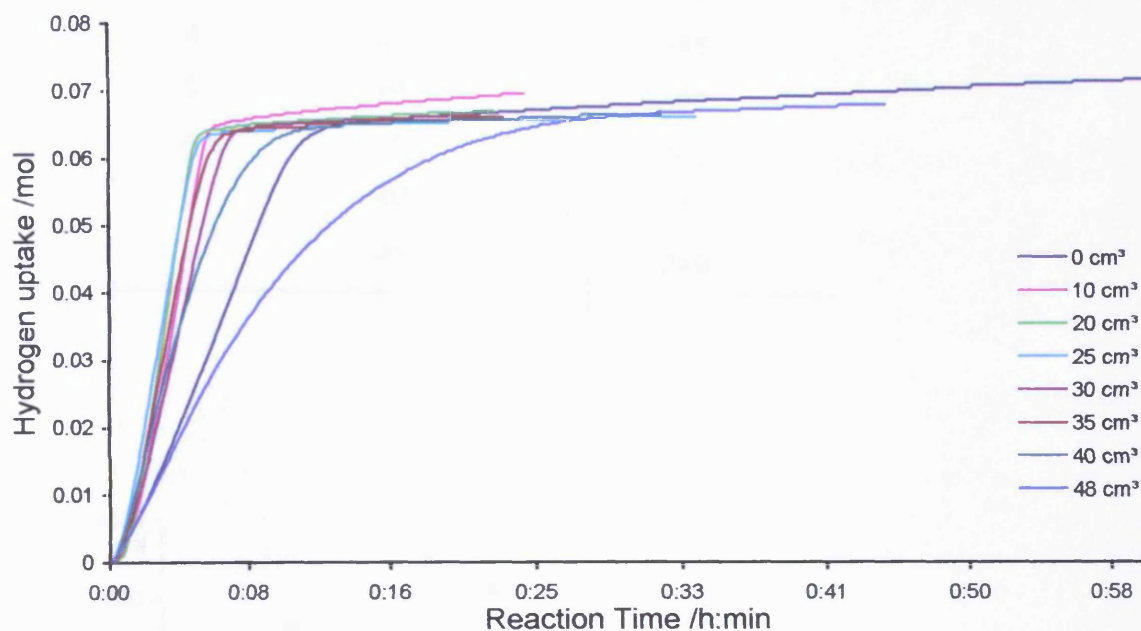


Fig. 3.26 H_2 uptake curves for etpy hydrogenation over CD-modified Pt/SiO_2 catalyst sintered at 450 K at different $\text{Bi}(\text{NO}_3)_3$ coverages.

Table 3.19 Effect of Bi adsorption on reaction rates for Pt/SiO₂ catalyst sintered at 450 K.

Entry	Dosing Volume /cm ³	Maximum Rate /mmol h ⁻¹ g ⁻¹
1	0	1446
2	10	3347
3	20	3761
4	25	3585
5	30	2607
6	35	3208
7	40	2314
8	48	1249

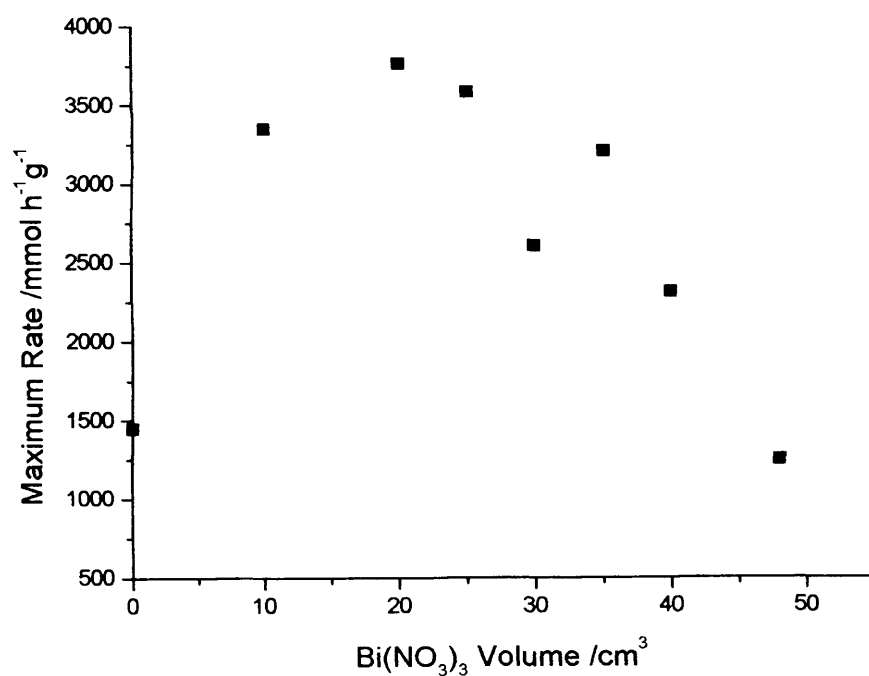


Fig. 3.27 Maximum rate versus Bi coverage for etpy hydrogenation over CD-modified Pt/SiO₂ catalyst sintered at 450 K.

3.3.3.2 Enantioselectivity

Investigation of the effect of Bi adsorption on 6.5% Pt/SiO₂ on enantioselectivity as a function of Bi loading was similar to Pt/G. It was found that as the Bi coverage was increased, the ee decreased as shown in table 3.20. Although it was not possible to study this catalyst by CV because it is an insulator, by using the catalytic behaviour as an internal calibration of this system, it was deduced that the most significant decrease in ee was coincident with the blockage of kink/step sites and {100} terraces in Figure 3.28 at a dosing volume of 30 cm³. The low ee, almost 20% at this point, would be consistent with very narrow {111} terrace sites for this catalyst relative to the Pt/G and this is consistent with the smaller average particle size [1]. The rapid decrease in rate following the filling of {111} sites by Bi would however be consistent with a “large” average terrace width (see previous explanation of 800 and 900 K sintered catalysts) in which Bi adatoms become more and more stable as the average {111} terrace width is increased. It is speculated that the interaction of the “small” platinum particle with silica may lead to an electronic perturbation causing a stabilisation of the Bi. It should be noted that, from the existing literature discussing characterization of EUROPT-1 [10], it apparently consists of one to two atomic thick “rafts” of the Pt{111}. This is quite different to the many atomic layers characteristic of the platinum monoparticles supported on graphite (hence negligible surface electronic perturbation of the support is expected in this case)

Table 3.20 Variation in enantioselectivity with increasing Bi coverage for Pt/SiO₂ catalyst sintered at 450 K.

Entry	Dosing Volume /cm ³	Enantiomeric Excess (ee) /% (R)
1	0	72.9
2	10	53.6
3	20	33.6
4	25	26.7
5	30	21.1
6	35	18.8
7	40	19.3
8	48	16.9

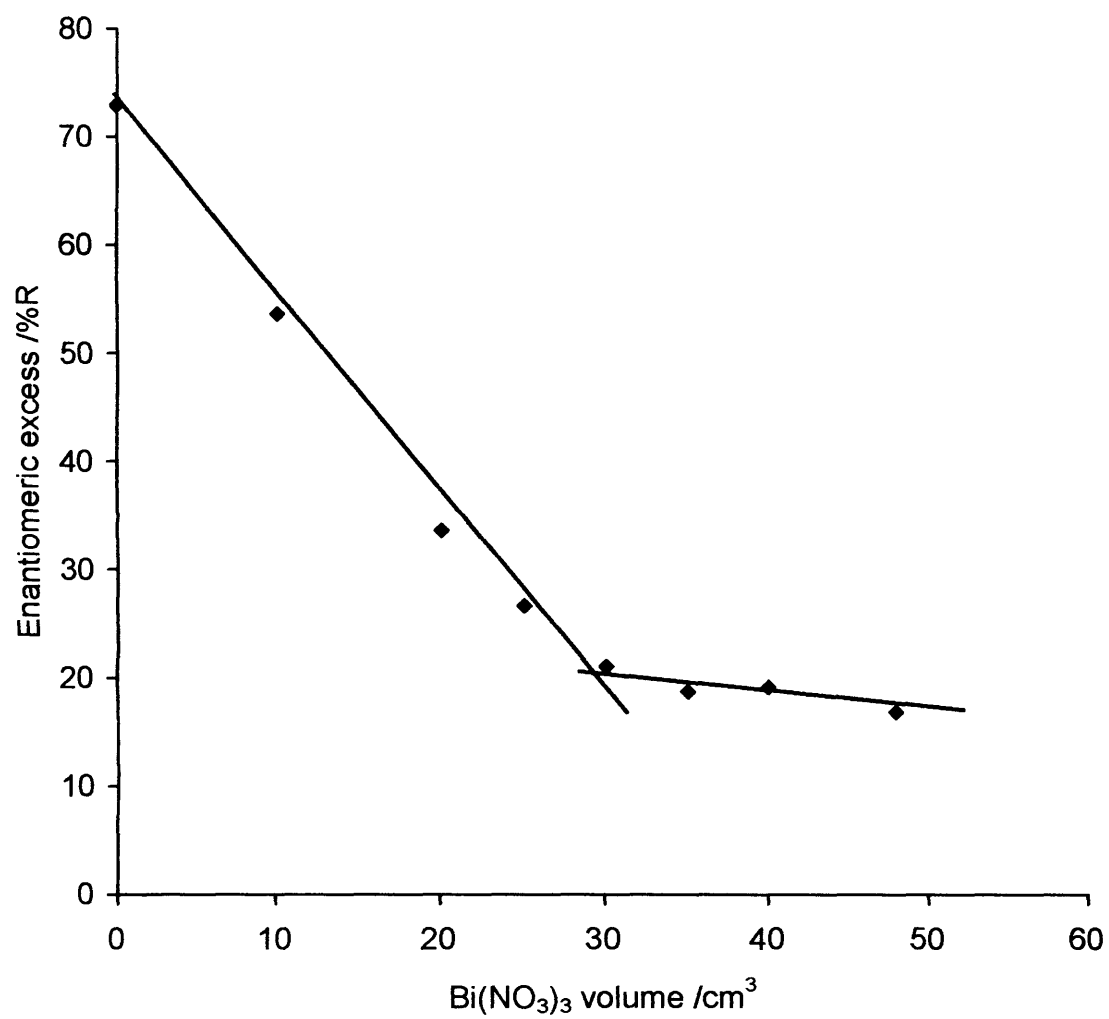


Fig. 3.28 Bi coverage and enantiomeric excess for Pt/SiO_2 catalyst sintered at 450 K.

3.4 Sulphur adsorption on graphite supported platinum and its influence on enantioselective hydrogenation

3.4.1 CV characterisation

A series of S adsorbed on Pt/G catalysts annealed at different temperatures was prepared using the method described in the experimental section 2.4.2. Figures 3.29 - 3.32 show the cyclic voltammetry of the sulphided catalysts. Tables 3.21 - 3.24 show $\text{Na}_2\text{S}_{(\text{aq})}$ dosing volumes and surface coverages calculated according to the method described in section 2.7.6. Sulphur adsorption was found to attenuate almost all CV features to some extent at low coverages with the Pt{100} terraces at 0.26 V significantly attenuated in the unsintered catalyst, and those sintered at 450, and 500 K (small attenuation in 700 K). Pt{100}x{111} step sites at 0.2 V were more attenuated than {111}x{111} step sites at 0.06 V. At higher S coverage ($\theta_s > 0.26$), Pt{100} terrace features were lost completely and Pt{111} terrace features at 0.43 V were gradually extinguished for the unsintered catalyst but remained almost the same for the remaining annealed catalysts. Adsorption of S on Pt/G differed from Bi in that for Bi, step sites were blocked completely at high coverage, whereas for S, a large fraction of these sites remained unblocked. It could be said therefore that adsorption of S on Pt/G occurred mainly on terrace sites. Adsorption of S on Pt{111} terraces shifted the {111} voltammetric feature towards a more positive potential in catalysts annealed at 450, 500, and 700 K consistent with the breaking up of long range Pt{111}

order [1]. Moreover, sulphur adsorption, on Pt/G, unlike Bi, does not present a redox peak in the potential range studied.

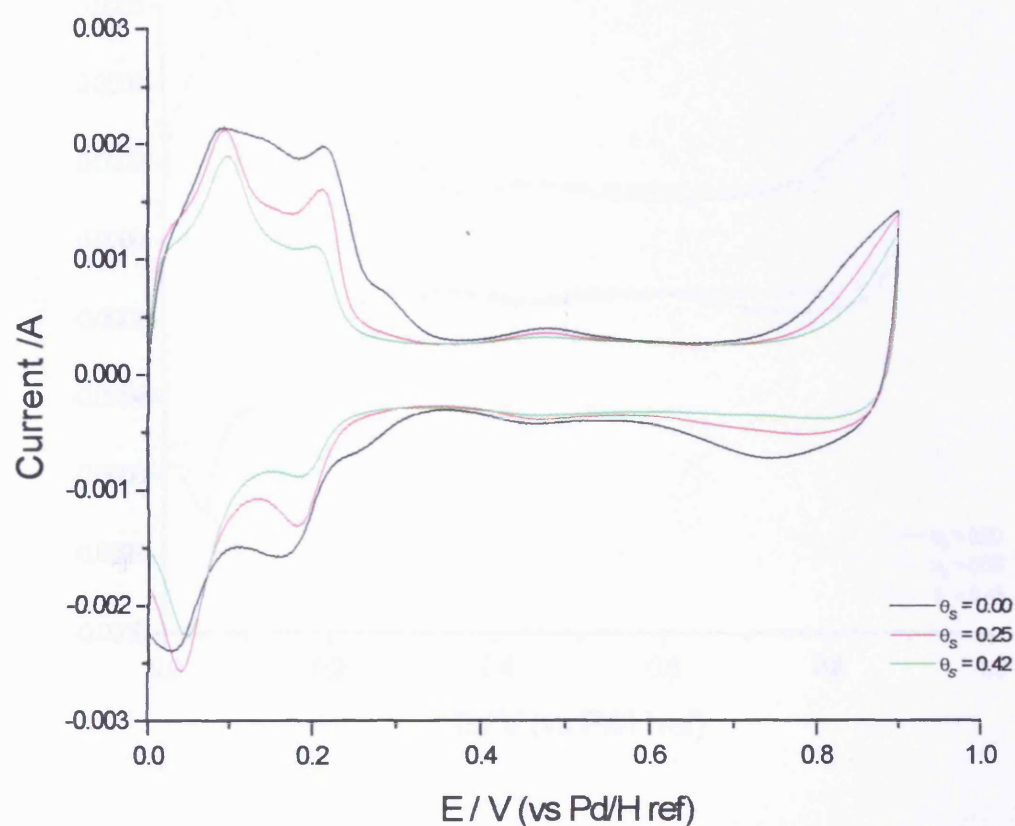


Fig. 3.29 CVs of S modified unsintered Pt/G in 0.5M H₂SO₄. Sweep rate 50 mV s⁻¹.

Table 3.21 Dosing volumes of Na₂S and surface coverages for unsintered Pt/G catalyst.

Entry	Dosing Volume /cm ³	Surface Coverage /θ _s
1	0.0	0.00
2	0.1	0.25
3	0.5	0.42

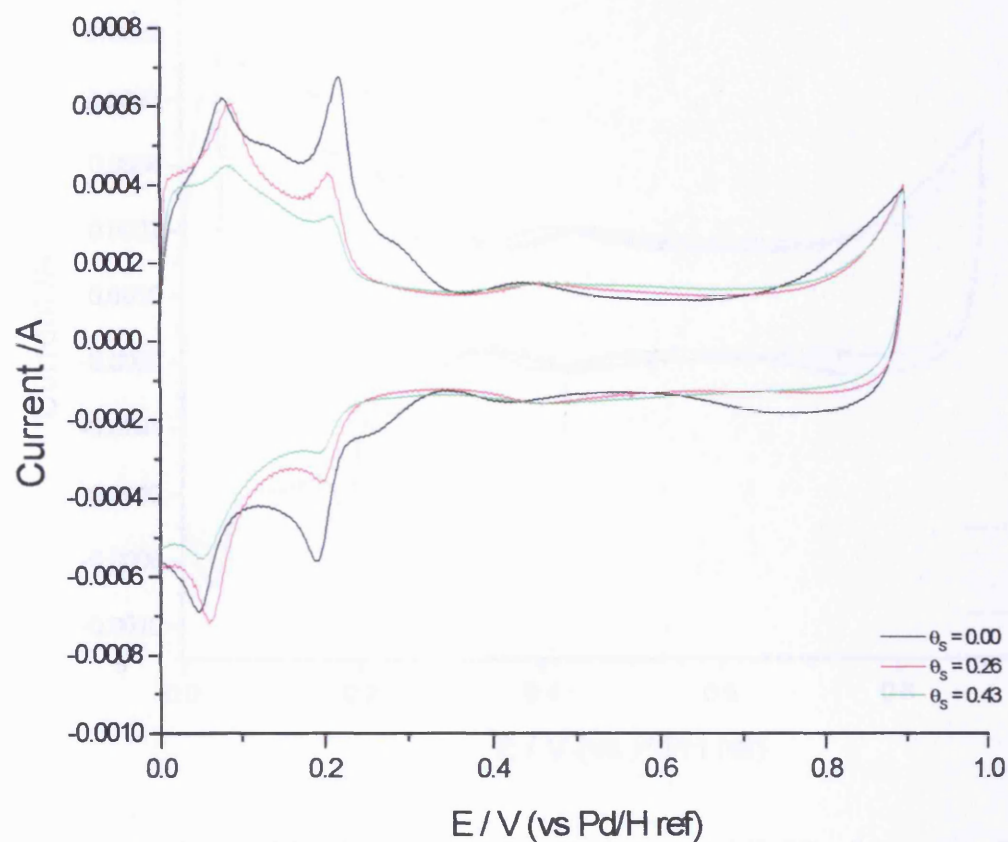


Fig. 3.30 CVs of S modified Pt/G sintered at 450K in 0.5M H₂SO₄. Sweep rate 50 mV s⁻¹.

Table 3.22 Dosing volumes of Na₂S and surface coverages for Pt/G catalyst sintered at 450 K.

Entry	Dosing Volume /cm ³	Surface Coverage /θ _s
1	0.0	0.00
2	0.1	0.26
3	0.2	0.43

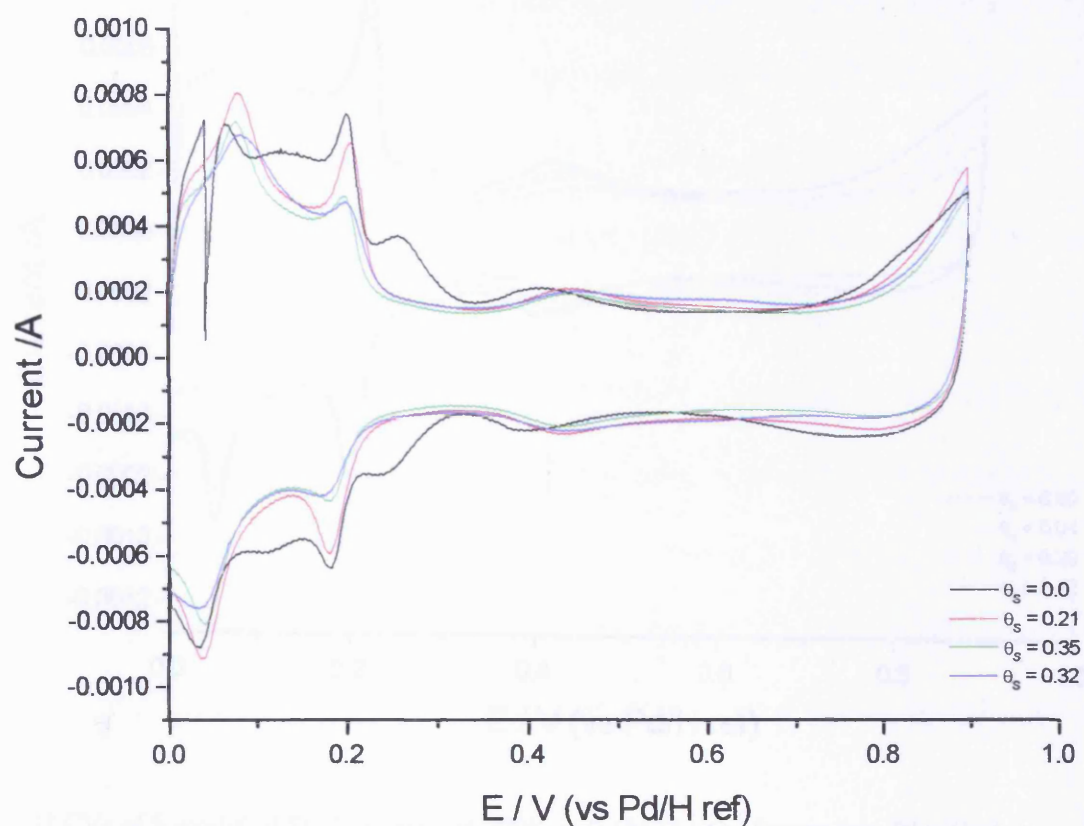


Fig. 3.31 CVs of S modified Pt/G sintered at 500K in 0.5M H₂SO₄. Sweep rate 50 mV s⁻¹.

Table 3.23 Dosing volumes of Na₂S and surface coverages for Pt/G catalyst sintered at 500 K.

Entry	Dosing Volume /cm ³	Surface Coverage /θ _s
1	0.0	0.00
2	0.1	0.21
3	0.2	0.35
4	0.3	0.32

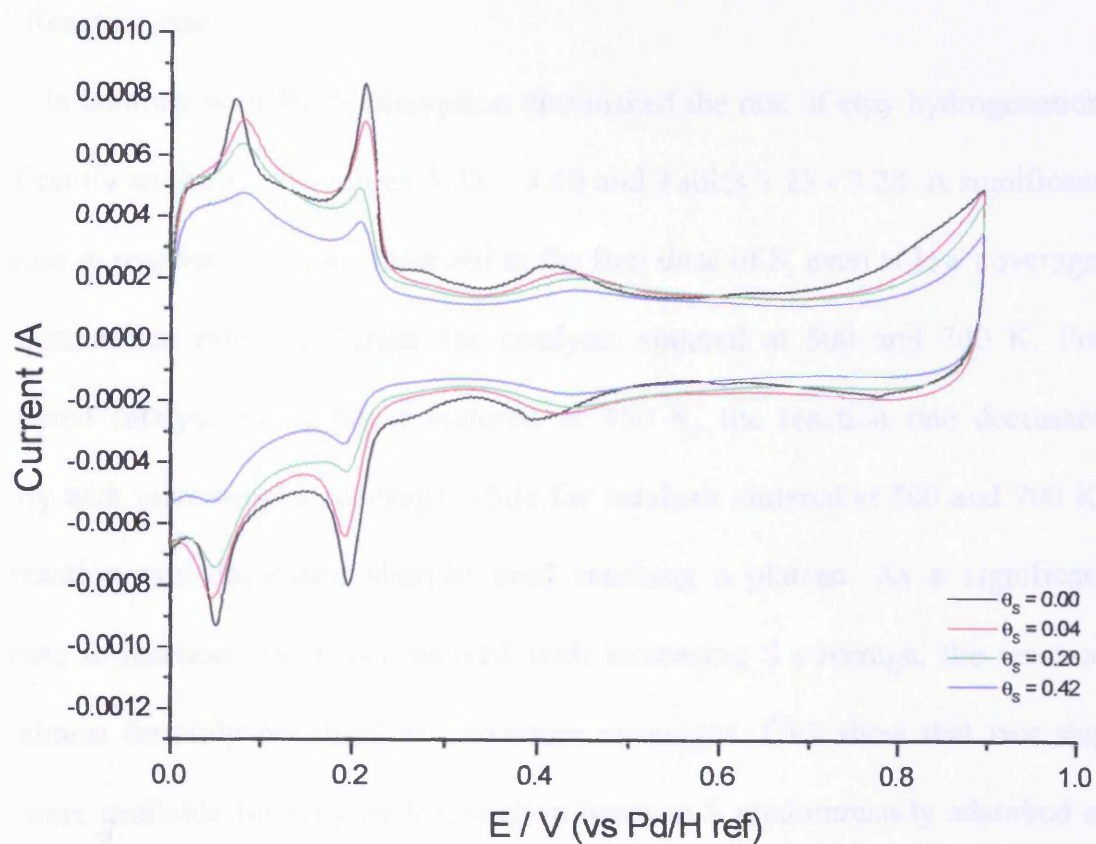


Fig. 3.32 CVs of S modified Pt/G sintered at 700K in 0.5M H₂SO₄. Sweep rate 50 mV s⁻¹.

Table 3.24 Dosing volumes of Na₂S and surface coverages for Pt/G catalyst sintered at 700 K.

Entry	Dosing Volume /cm ³	Surface Coverage /θ _s
1	0.0	0.00
2	0.1	0.04
3	0.2	0.20
4	0.3	0.42

3.4.2 Reaction rate

In contrast with Bi, S adsorption diminished the rate of etpy hydrogenation significantly as shown in Figures 3.33 – 3.40 and Tables 3.25 - 3.28. A significant decrease in reaction rate was observed at the first dose of S, even at low coverage. The decrease in rate was larger for catalysts sintered at 500 and 700 K. For unsintered catalyst and catalyst sintered at 450 K, the reaction rate decreased linearly with increasing S coverage while for catalysts sintered at 500 and 700 K, the reaction rate decreased sharply until reaching a plateau. As a significant decrease in reaction rate was observed with increasing S coverage, the reaction was almost certainly poisoned at maximum coverages. CVs show that free step sites were available for etpy hydrogenation because S predominantly adsorbed at terrace sites.

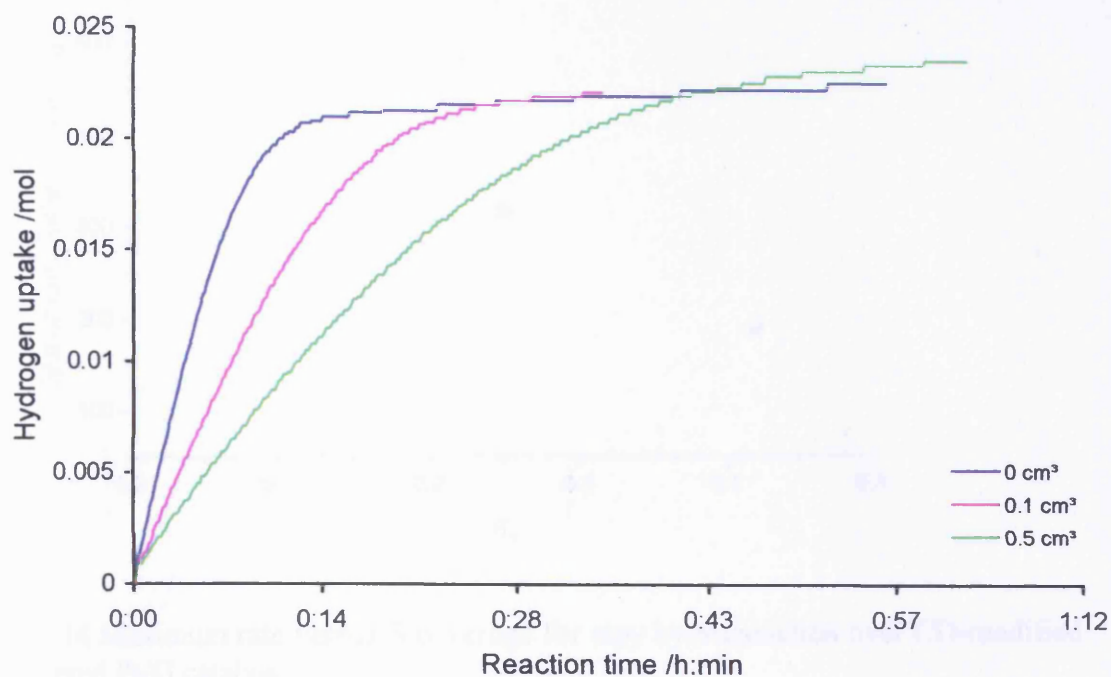


Fig. 3.33 H₂ uptake curves for etpy hydrogenation over CD-modified unsintered Pt/G catalyst: influence of Na₂S adsorption.

Table 3.25 Effect of S adsorption on reaction rates for unsintered Pt/G catalyst.

Entry	Dosing Volume /cm ³	Surface Coverage /θ _s	Maximum Rate /mmol h ⁻¹ g ⁻¹
1	0.0	0.00	611
2	0.1	0.25	317
3	0.5	0.42	190

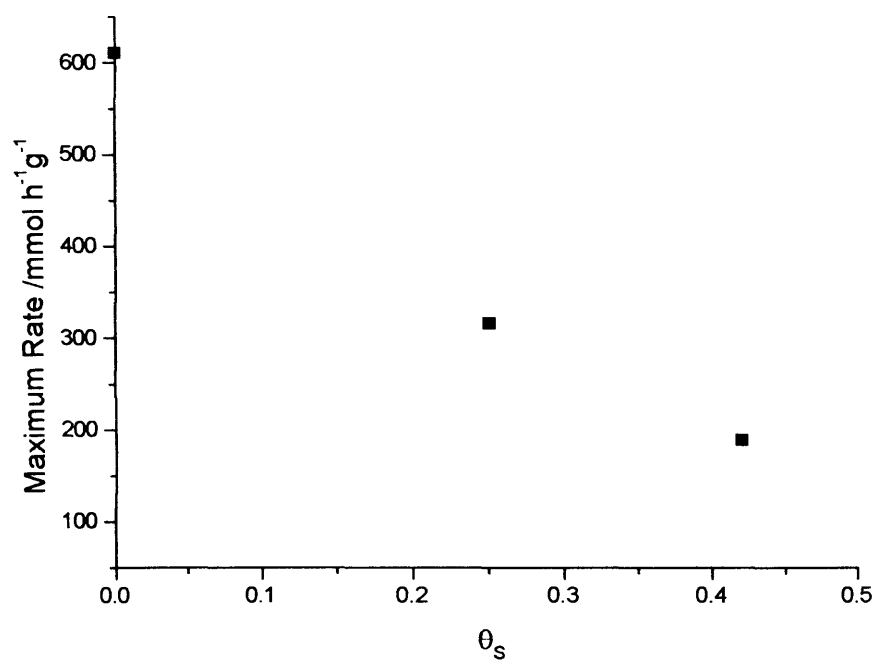


Fig. 3.34 Maximum rate versus S coverage for etpy hydrogenation over CD-modified unsintered Pt/G catalyst.

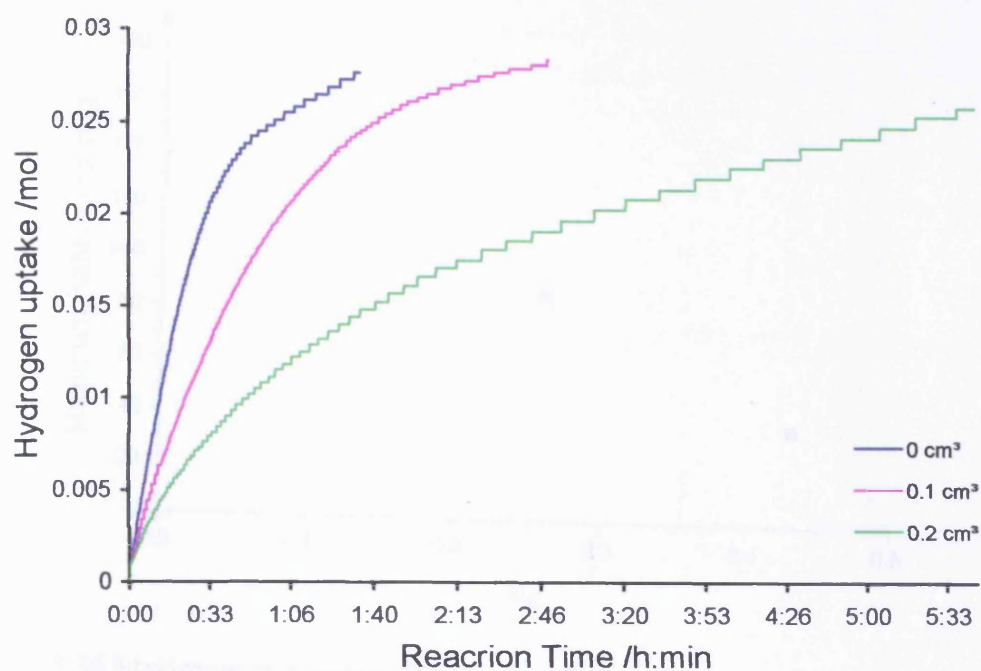


Fig. 3.35 H_2 uptake curves for etpy hydrogenation over CD-modified Pt/G catalyst sintered at 450 K: influence of Na_2S adsorption.

Table 3.26 Effect of S adsorption on reaction rates for Pt/G catalyst sintered at 450 K.

Entry	Dosing Volume / cm^3	Surface Coverage $/\theta_s$	Maximum Rate / $\text{mmol h}^{-1} \text{g}^{-1}$
1	0.0	0.00	189
2	0.1	0.26	87
3	0.2	0.43	37

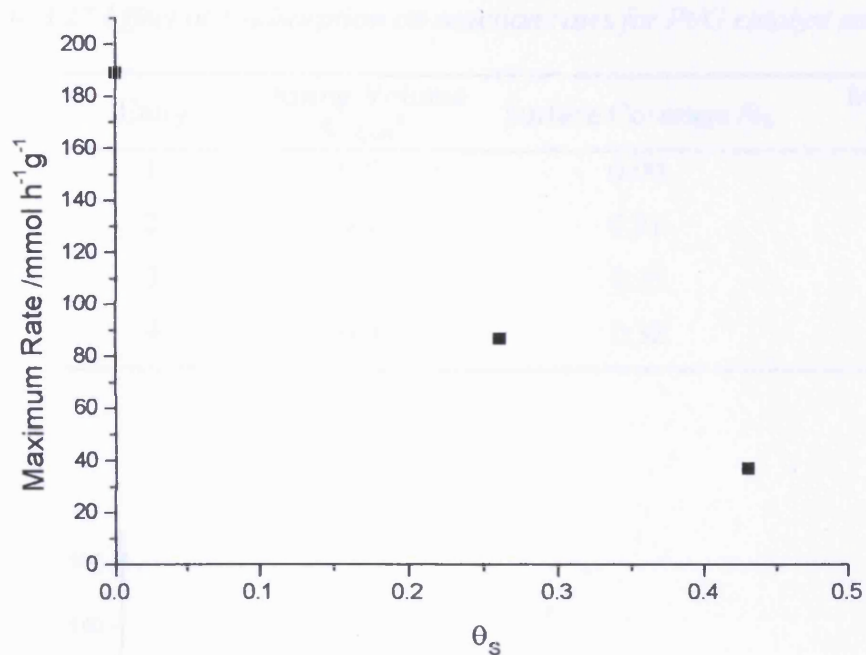


Fig. 3.36 Maximum rate versus S coverage for etpy hydrogenation over CD-modified Pt/G catalyst sintered at 450 K.

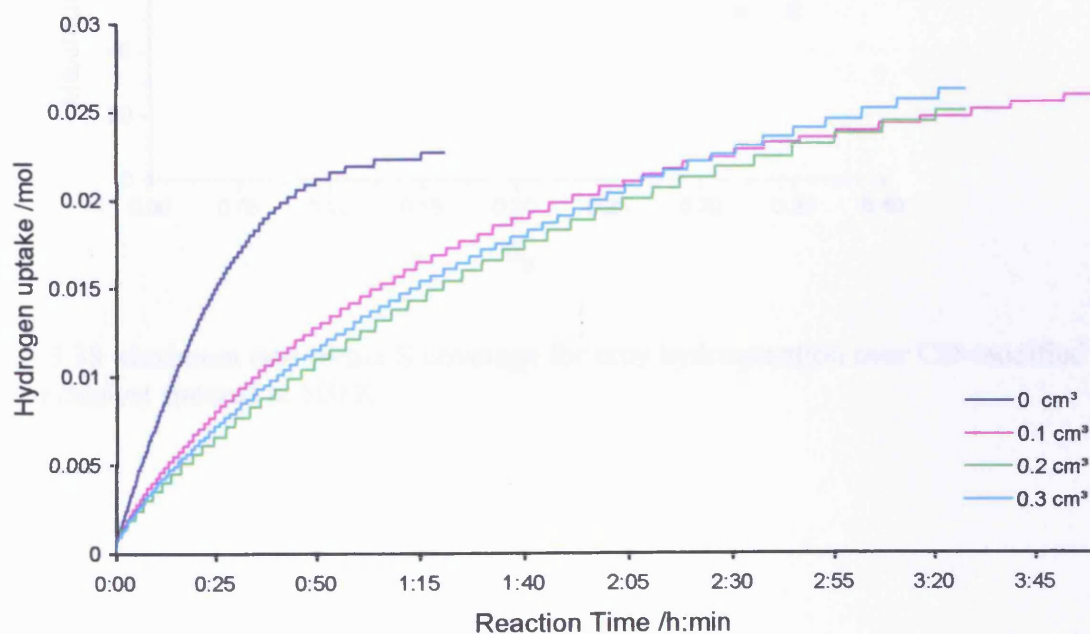


Fig. 3.37 H_2 uptake curves for etpy hydrogenation over CD-modified Pt/G catalyst sintered at 500 K; influence of Na_2S adsorption.

Table 3.27 Effect of S adsorption on reaction rates for Pt/G catalyst sintered at 500 K.

Entry	Dosing Volume S /cm ³	Surface Coverage / θ_s	Maximum Rate /mmol h ⁻¹ g ⁻¹
1	0.0	0.00	161
2	0.1	0.21	65
3	0.2	0.35	52
4	0.3	0.32	52

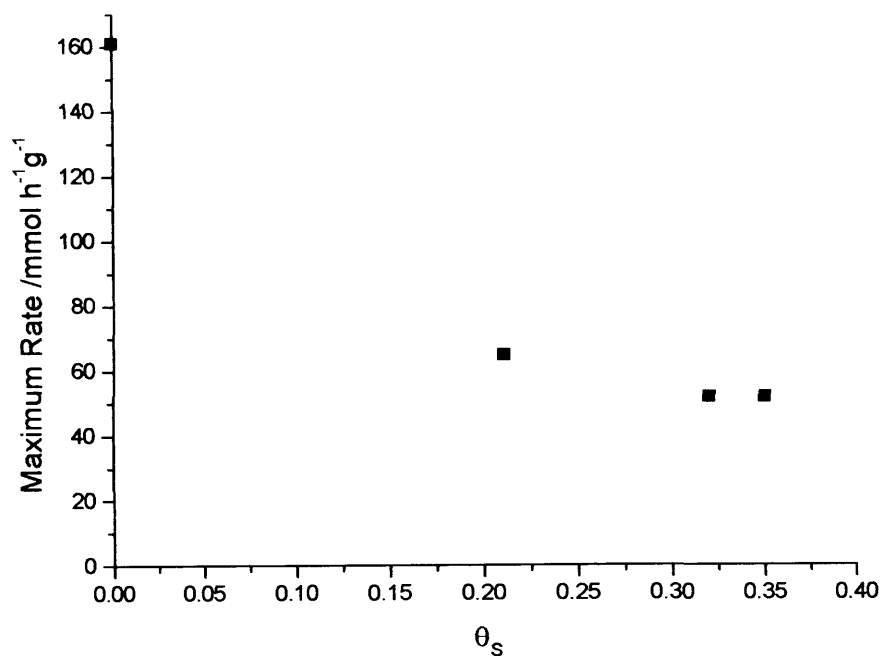


Fig. 3.38 Maximum rate versus S coverage for etpy hydrogenation over CD-modified Pt/G catalyst sintered at 500 K.

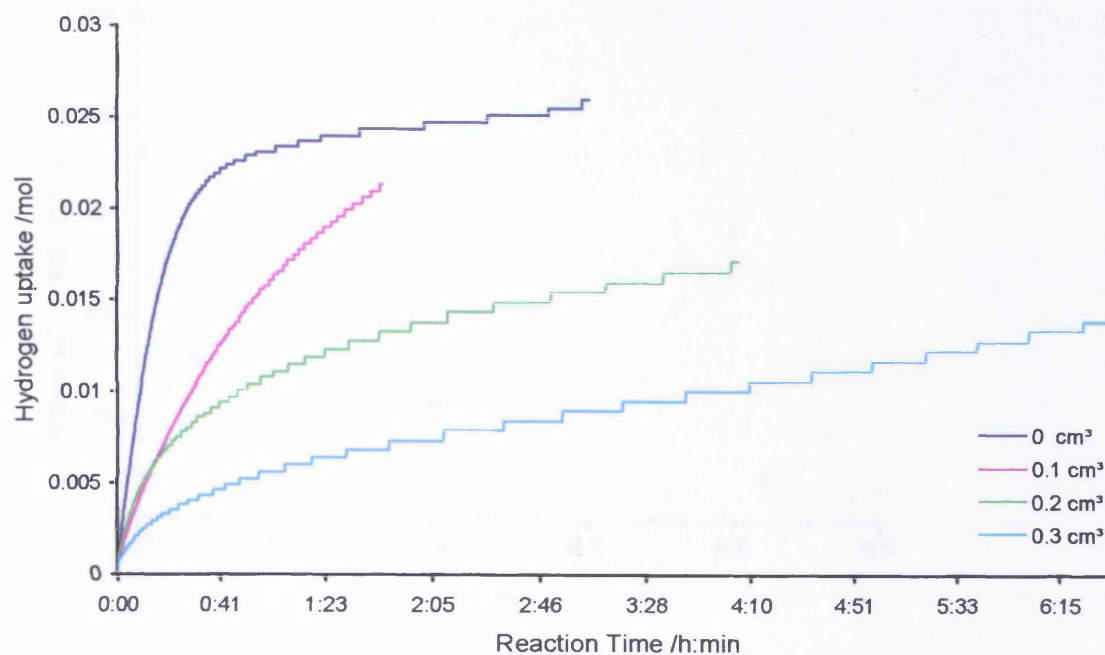


Fig. 3.39 H_2 uptake curves for etpy hydrogenation over CD-modified Pt/G catalyst sintered at 700 K : influence of Na_2S adsorption.

Table 3.28 Effect of S adsorption on reaction rates for Pt/G catalyst sintered at 700 K.

Entry	Dosing Volume /cm ³	Surface Coverage / θ_s	Maximum Rate /mmol h ⁻¹ g ⁻¹
1	0.0	0.00	250
2	0.1	0.04	79
3	0.2	0.20	57
4	0.3	0.42	20

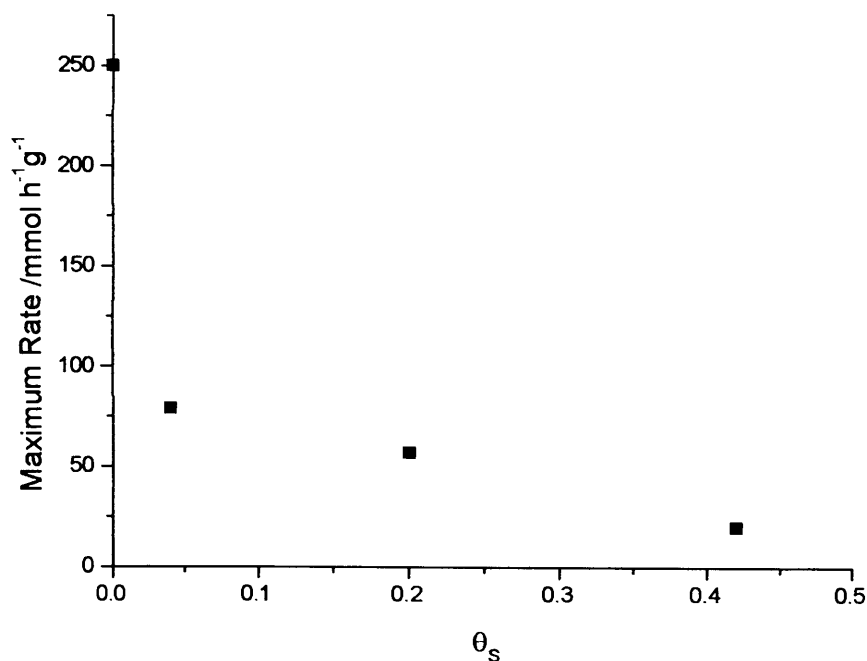


Fig. 3.40 Maximum rate versus S coverage for etpy hydrogenation over CD-modified Pt/G catalyst sintered at 700 K.

3.4.3 Enantioselectivity

Tables 3.29 - 3.32 and Figures 3.41 - 3.44 show the results of enantioselective hydrogenation over S modified Pt/G sintered at different temperatures and coverages. For S modified unsintered catalyst and those sintered at 450, and 500 K, enantiomeric excess increased as the S coverage increased. This increase appeared to be correlated with the blockage of {100} terraces. On the other hand, the ee of the catalyst sintered at 700 K (Table 3.28) decreased with increase of S coverage. Referring to the CV of the catalyst sintered at 700 K and comparing it with other sintered catalysts, we can conclude that the Pt{100}

terrace sites for the clean catalyst that was annealed at 700 K were much less abundant than the others and the number of step sites in the 700 K catalyst was also significantly lower.

Table 3.29 Variation in enantioselectivity with increasing S coverage for unsintered Pt/G catalyst.

Entry	Dosing Volume /cm ³	Surface Coverage / θ_s	Enantiomeric Excess (ee) /% (R)
1	0.0	0.00	40.0
2	0.1	0.25	48.4
3	0.5	0.42	50.4

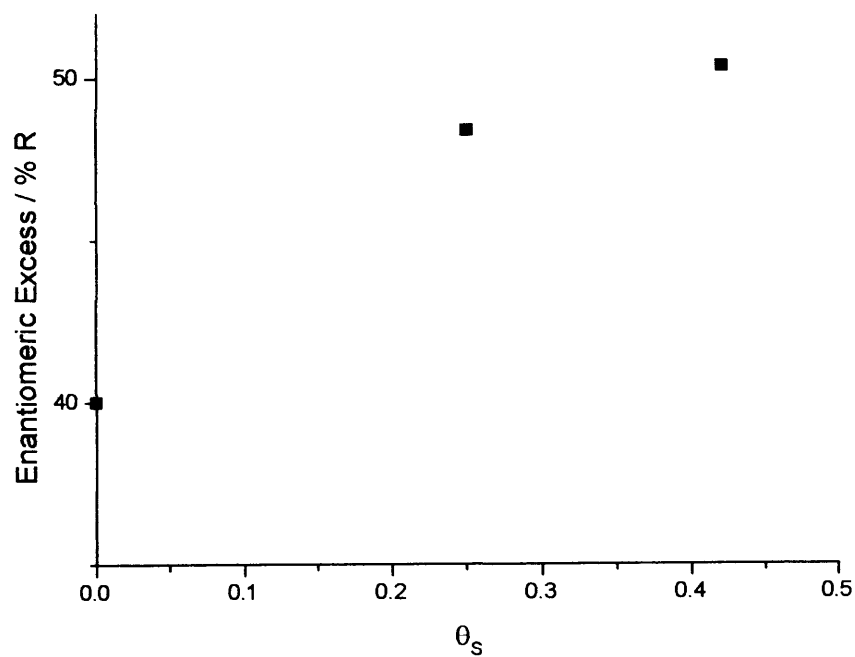


Fig. 3.41 S coverage and enantiomeric excess for unsintered Pt/G catalyst.

Table 3.30 Variation in enantioselectivity with increasing *S* coverage for Pt/G catalyst sintered at 450 K.

Entry	Dosing Volume /cm ³	Surface Coverage / θ_s	Enantiomeric Excess (ee) /% (R)
1	0.0	0.00	35.4
2	0.1	0.26	44.5
3	0.2	0.43	41.1

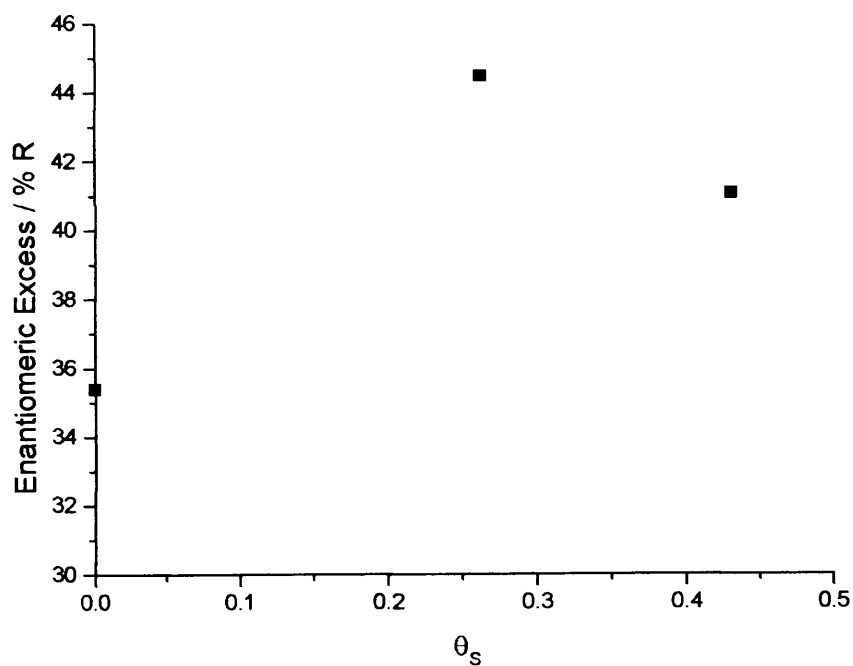


Fig. 3.42 *S* coverage and enantiomeric excess for Pt/G catalyst sintered at 450 K.

Table 3.31 Variation in enantioselectivity with increasing *S* coverage for Pt/G catalyst sintered at 500 K.

Entry	Dosing Volume S / cm^3	Surface Coverage θ_s	Enantiomeric Excess (ee) / % (R)
1	0.0	0.00	34.3
2	0.1	0.21	42.5
3	0.2	0.35	42.5
4	0.3	0.32	43.0

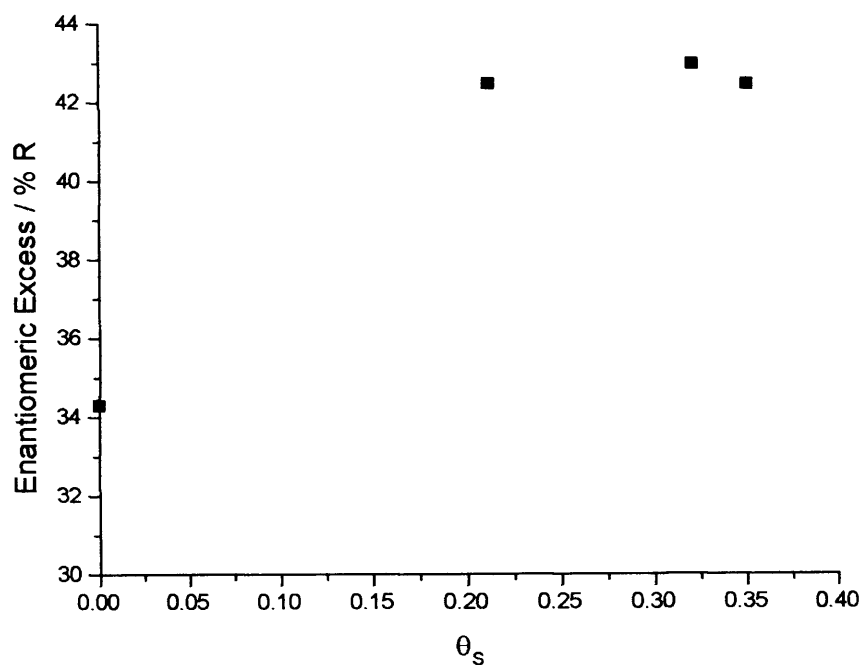


Fig. 3.43 *S* coverage and enantiomeric excess for Pt/G catalyst sintered at 500 K.

Table 3.32 Variation in enantioselectivity with increasing *S* coverage for Pt/G catalyst sintered at 700 K.

Entry	Dosing Volume /cm ³	Surface Coverage / θ_s	Enantiomeric Excess (ee) /% (R)
1	0.0	0.00	57.3
2	0.1	0.04	47.6
3	0.2	0.20	43.9
4	0.3	0.42	37.6

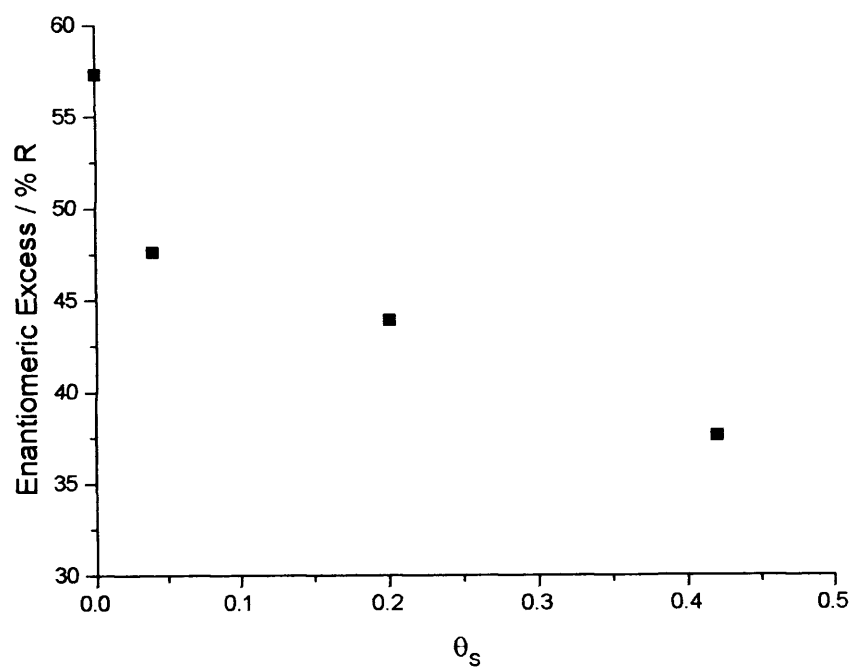


Fig. 3.44 *S* coverage and enantiomeric excess for Pt/G catalyst sintered at 700 K.

3.5 Palladium adsorption on Pt/G sintered at 700 K and its influence on enantioselective hydrogenation

3.5.1 CV characterisation

A series of nine Pd on Pt/G catalysts sintered at 700K was prepared as described in section 2.4.2. Voltammograms illustrating the effect of Pd adsorption on these nine Pt/G catalysts are shown in Figure 3.45. Table 3.33 shows Pd(NO₃)₂ dosing volumes and surface coverages of Pd on Pt/G. At low coverages, Pd adsorption occurred at {111}x{111} and {100}x{111} step/kink sites ($\theta_{\text{Pd}} = 0.06 - 0.12$). As Pd coverage increased ($\theta_{\text{Pd}} = 0.2 - 0.72$), a sharp Pd{111} peak at 0.17 V was observed [11-19] and the clean surface features were attenuated. Upon exceeding one monolayer ($\theta_{\text{Pd}} = 1.2 - 4.8$) a second Pd peak was observed at 0.21 V. The appearance of peak at 0.21 V has already been reported [13-15, 17-20] and ascribed to the formation of Pd in the second layer. The magnitude of the 0.17 V adsorption peak was significantly reduced and broadened slightly as the intensity of the second layer peak increased, attesting to the truly surface sensitive nature of cyclic voltammetry. Moreover, there was some attenuation at Pt{100} terrace sites at 0.25V and a decrease in Pt{111} terraces, until they disappeared completely, concurrent with the increase of palladium coverage.

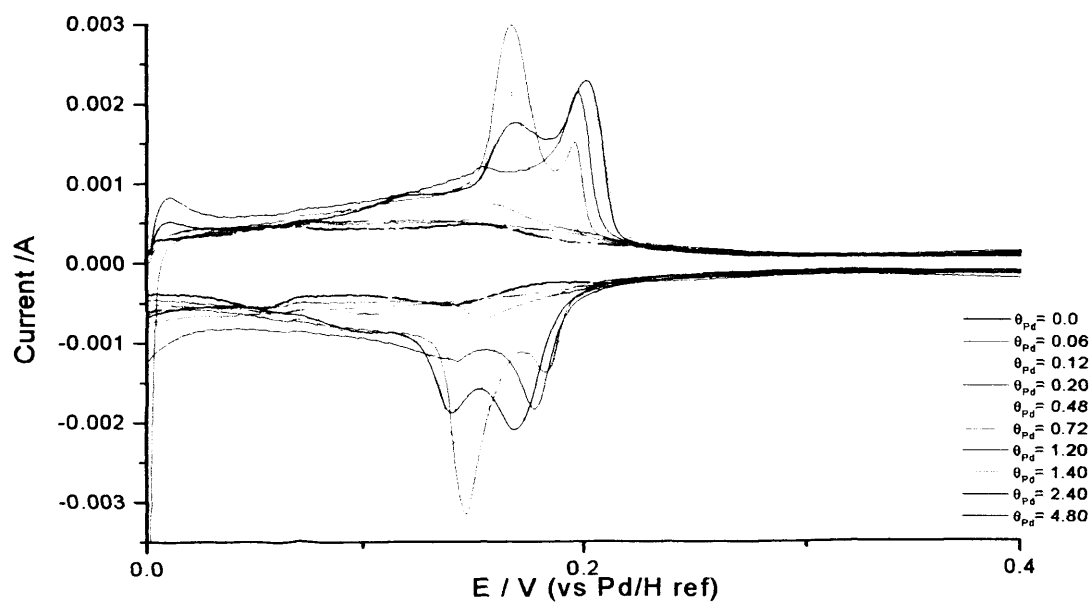
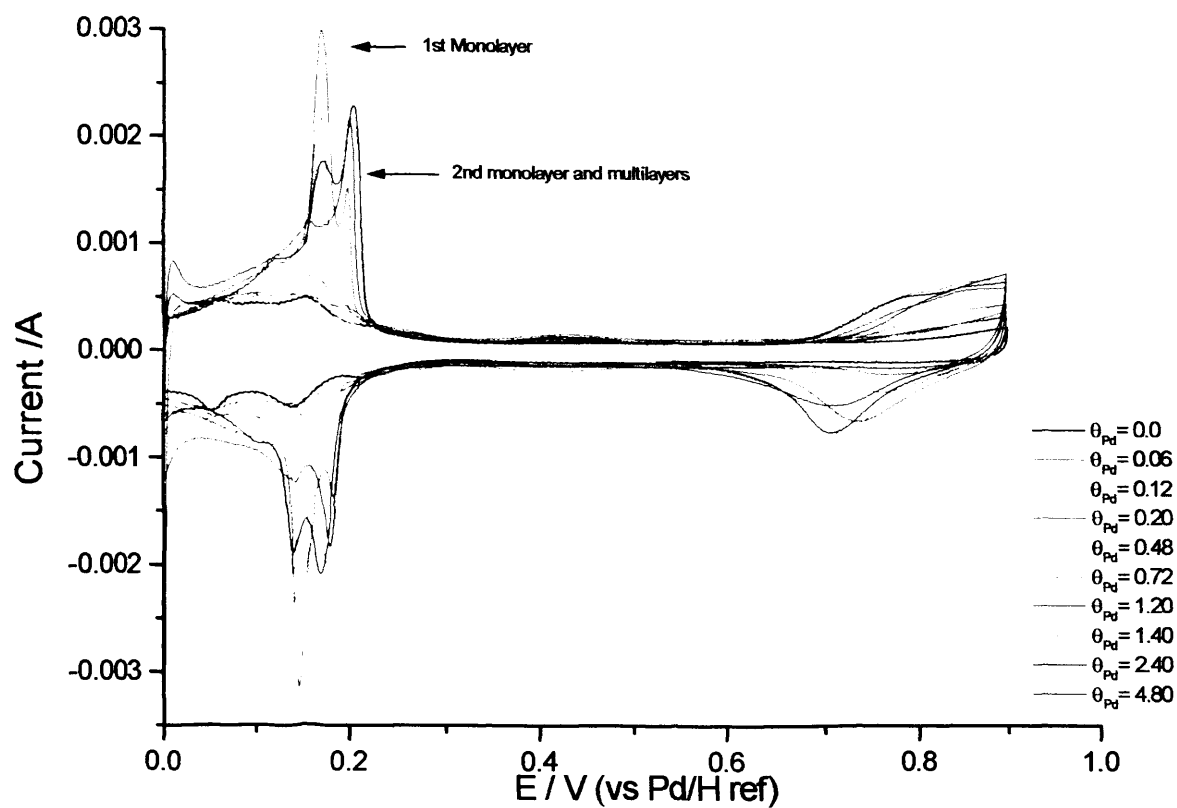


Fig. 3.45 CVs of Pd modified Pt/G in 0.5M H₂SO₄. Sweep rate 10 mV s⁻¹.

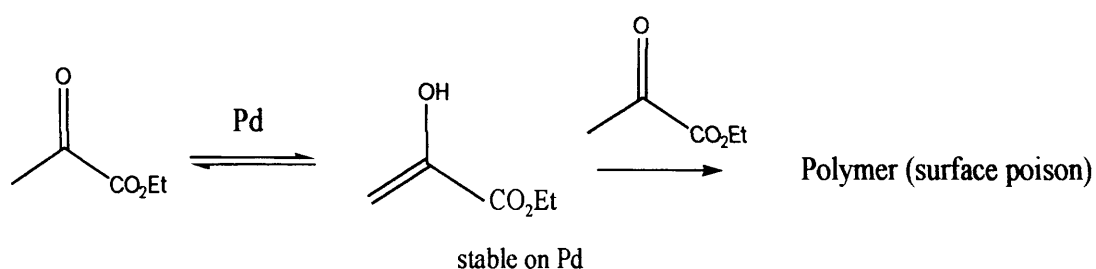
Table 3.33 Dosing volumes of $\text{Pd}(\text{NO}_3)_2$ and surface coverages for Pt/G catalyst sintered at 700 K.

Entry	Dosing Volume / cm^3	Surface Coverage θ_{Pd}
1	0.00	0.00
2	0.25	0.06
3	0.50	0.12
4	1.00	0.20
5	2.00	0.48
6	3.00	0.72
7	5.00	1.20
8	7.00	1.40
9	10	2.40
10	20	4.80

3.5.2 Reaction rate

Adsorption of Pd on the Pt/G catalyst sintered at 700 K inhibited the rate of ethyl pyruvate hydrogenation significantly. It was found that the higher the Pd coverage, the slower the reaction proceeded, as shown in Figures 3.46(b) - 3.47 and Table 3.34. The decrease in reaction rate was marked in the coverage region of $\theta_{\text{Pd}} = 0 - 0.72$, whereas it remained almost constant at coverage of $\theta_{\text{Pd}} = 0.72 - 4.8$. It has already been reported that Pd tends to favour enol as a surface intermediate and moreover, favour an S-enantiomeric excess using CD as modifier [21-23]. The formation of S-lactate is consistent with hydrogenation of the C=C enol substituent compared to the C=O keto group as found with Pt. Since in

previous work [9], the presence of enol surface species has been implicated in surface polymer formation, the low rate of enantioselective hydrogenation on Pd relative to Pt, as also found here for Pd adlayers supported on Pt might be related to surface self poisoning by polymeric species:



Again the enantioselectivity over Pd (unlike that over Pt) is not rate enhanced [21], in fact it is *reduced* in the presence of CD.

When CN was used as modifier, a decrease in the racemic rate from 83 to 15 mmol h⁻¹ g⁻¹ was observed (Figure 3.46(a)). This substantial decrease in rate is accompanied by an excess of the R-product. This is in contrast to Pt which would give an excess of S-product. Hence, Pd differs very much from Pt in terms of its behavior. This is in accord with the present findings using Pd/Pt/G catalysts whereby the same rapid rate deceleration upon adsorption Pd is observed.

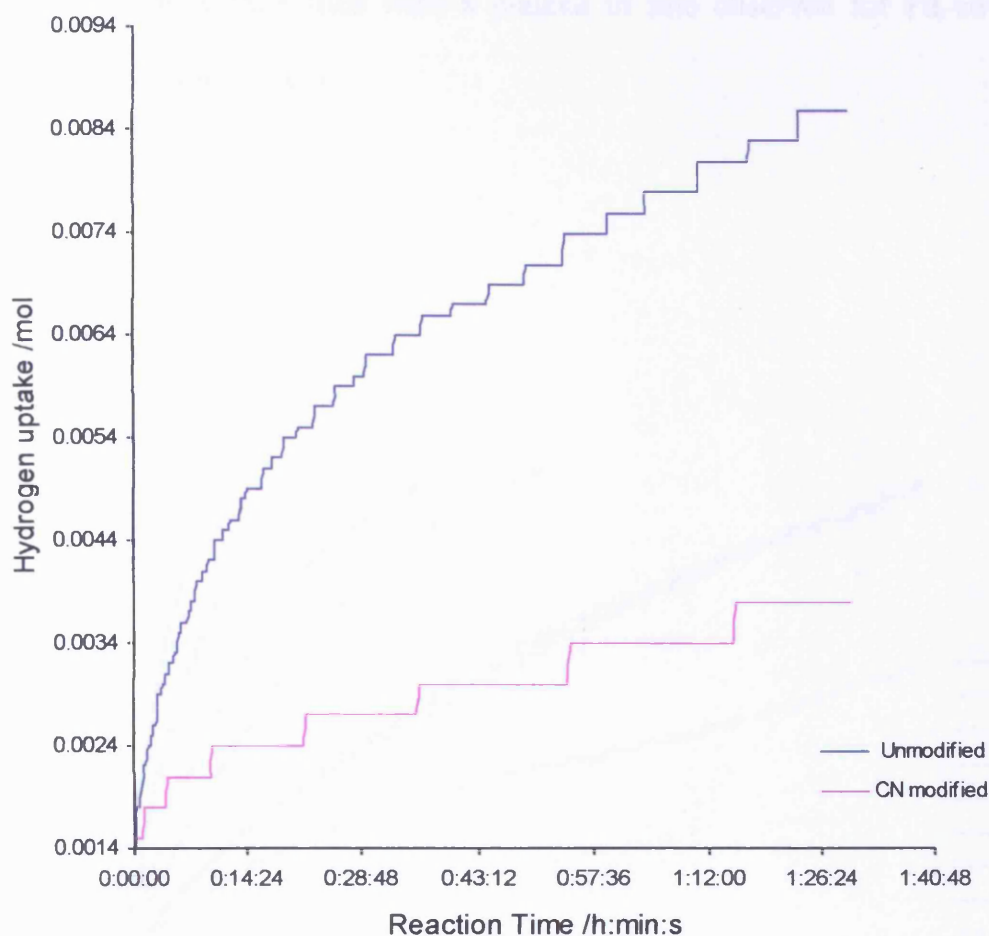


Fig. 3.46(a) H₂ uptake curves for etpy hydrogenation for CN-modified Pd/G catalyst and unmodified catalyst.

Previous work by Timothy [24] using stepped Pt single crystals has demonstrated that Pd strongly prefers adsorption at defect sites relative to {111} terraces. There is support for this behaviour by close inspection of Figure 3.45 which shows, at lowest Pd loadings complete attenuation of Pt CV defect sites. Hence the initial marked decrease in rate (Figure 3.47) may be ascribed wholly to step filling by Pd followed by further less marked decrease in rate associated with

occupation of terrace sites with a plateau in rate observed for Pd coverages in excess of one monolayer.

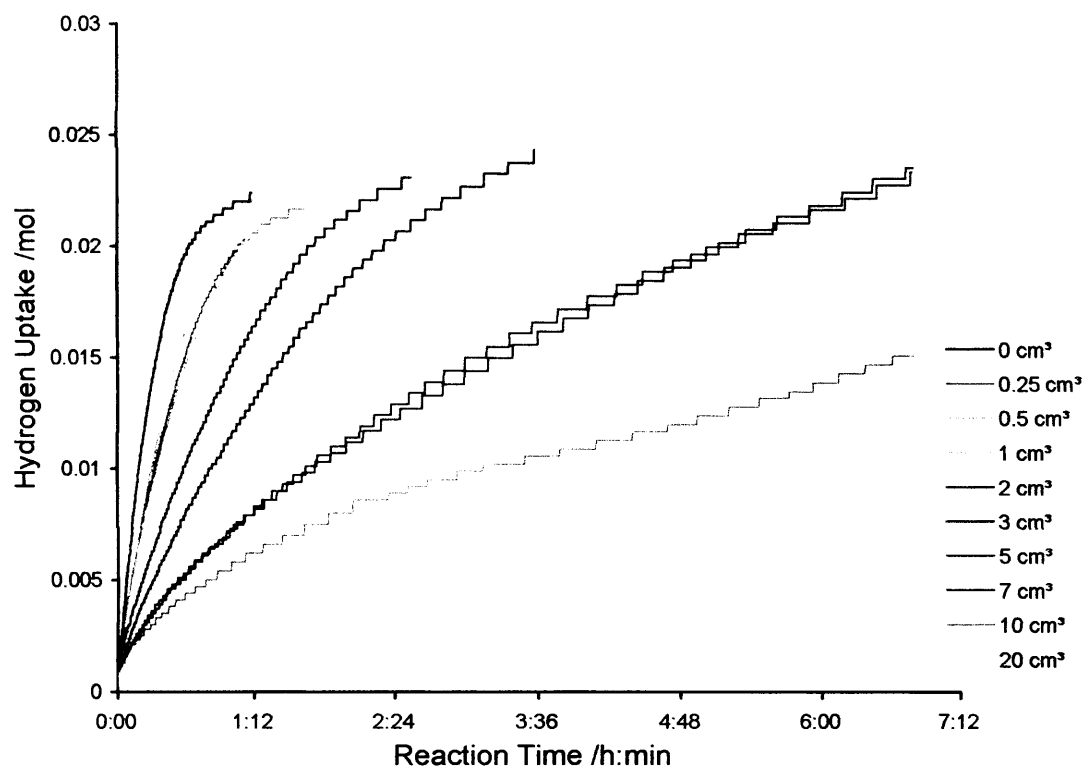


Fig. 3.46(b) H_2 uptake curves for etpy hydrogenation over CD-modified Pt/G catalyst sintered at 700 K : influence of $\text{Pd}(\text{NO}_3)_2$ adsorption.

Table 3.34 Effect of Pd adsorption on reaction rates for Pt/G catalyst sintered at 700 K.

Entry	Dosing Volume /cm ³	Surface Coverage θ_{Pd}	Maximum Rate mmol h ⁻¹ g ⁻¹
1	0.00	0.00	250
2	0.25	0.06	122
3	0.50	0.12	134
4	1.00	0.20	114
5	2.00	0.48	64
6	3.00	0.72	43
7	5.00	1.20	24
8	7.00	1.40	23
9	10	2.40	20
10	20	4.80	13

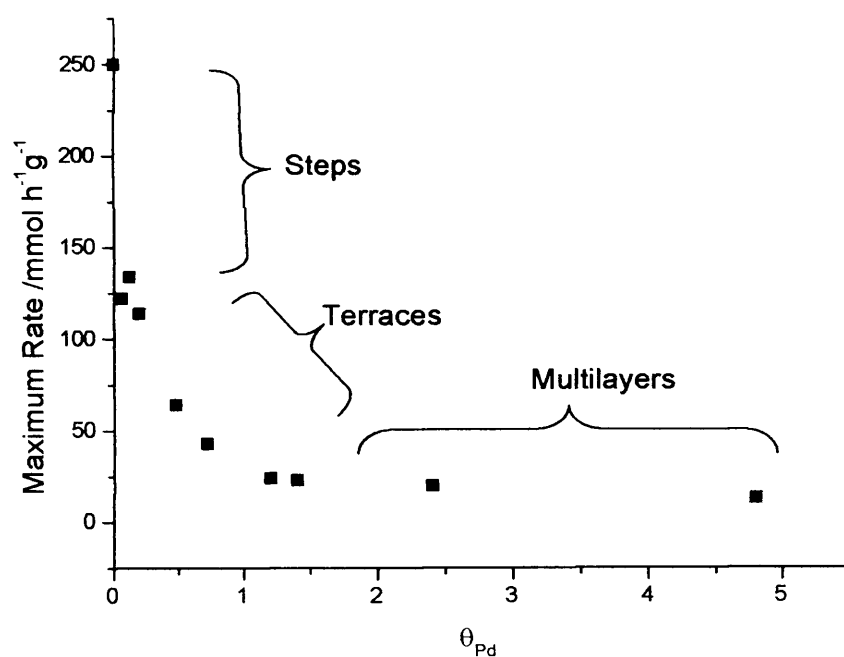


Fig. 3.47 Maximum rate versus Pd coverage for etpy hydrogenation over CD-modified Pt/G catalyst sintered at 700 K. Preferential filling of particular surface sites is also indicated.

3.5.3 Enantioselectivity

Table 3.35 presents the effect of Pd adsorption on the CD-modified Pt/G catalyst sintered at 700 K on the enantiomeric excess in the hydrogenation of ethyl pyruvate. Palladium adsorption reduced the ee from 57.3 to 1.5 % at high Pd coverage ($\theta_{\text{Pd}} = 4.8$). This behaviour is ascribed to the fact that Pd tends to form S-enantiomer under these conditions as mentioned earlier [21-23]. By plotting ee vs Pd coverage, it has been deduced that the most significant decrease in ee was coincident with the blockage of kink and step sites at $\theta_{\text{Pd}} = 0 - 0.3$ (as shown in Figures 3.48 - 3.49) and that ee clearly mimics the rate behavior outlined in Figure 3.47. This behavior (in relation to ee) is similar to that found with of Bi-modified Pt catalysts.

Table 3.35 Variation in enantioselectivity with increasing Pd coverage for Pt/G catalyst sintered at 700 K.

Entry	Dosing Volume /cm ³	Surface Coverage θ_{Pd}	Enantiomeric Excess (ee) /% (R)
1	0.00	0.00	57.3
2	0.25	0.06	36.0
3	0.50	0.12	30.0
4	1.00	0.20	24.0
5	2.00	0.48	18.0
6	3.00	0.72	17.0
7	5.00	1.20	14.0
8	7.00	1.40	12.5
9	10	2.40	10.7
10	20	4.80	1.5

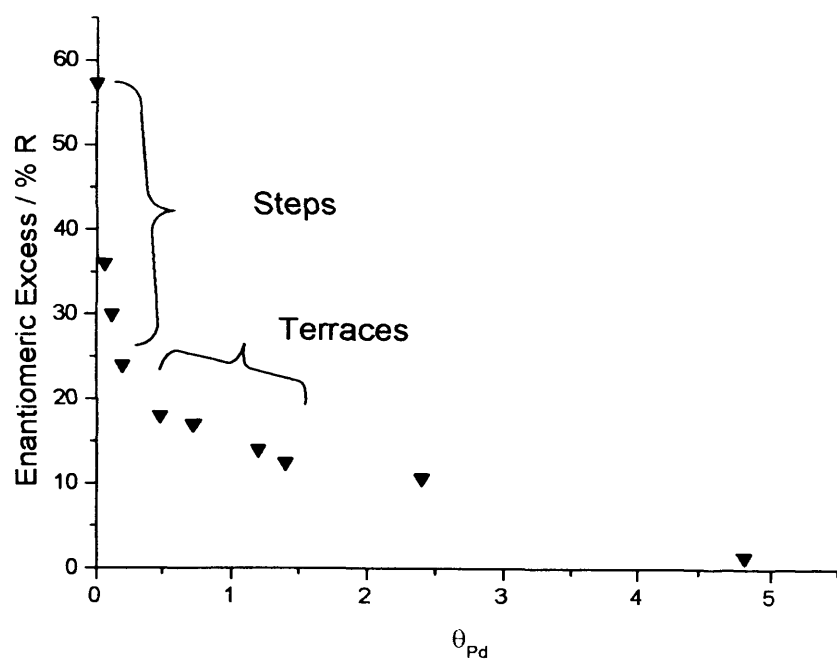


Fig. 3.48 Pd coverage and enantiomeric excess for Pt/G catalyst sintered at 700 K.

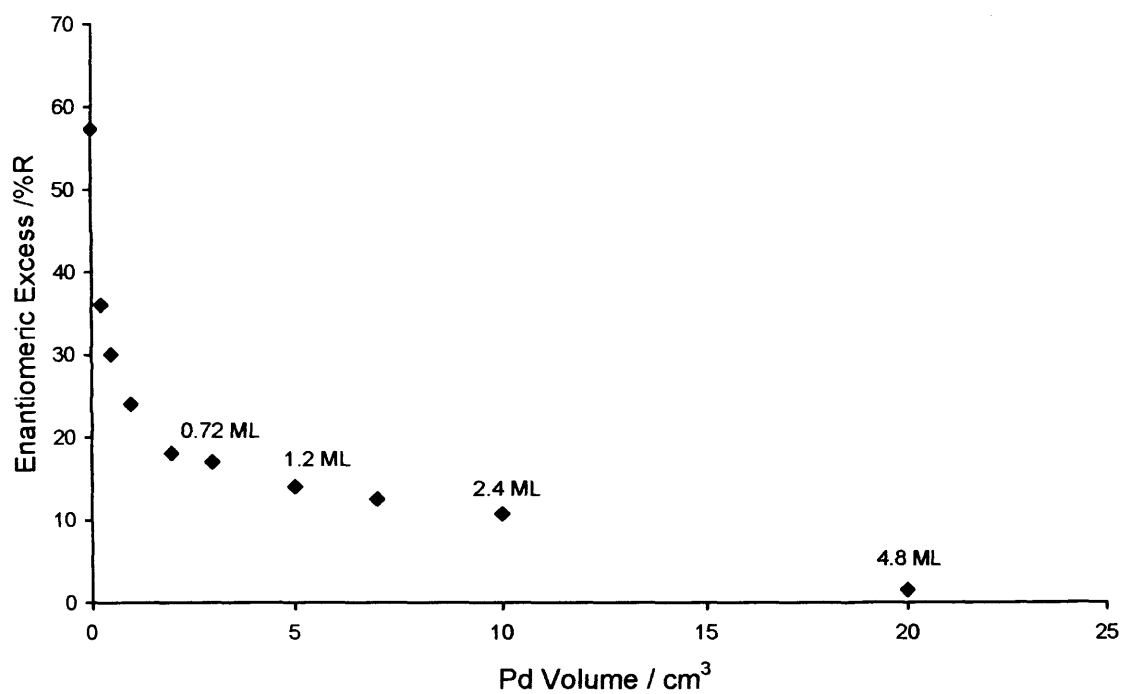


Fig. 3.49 Pd coverage in terms of volumes added and enantiomeric excess for Pt/G catalyst sintered at 700 K. 5 cm³ is equivalent to a Pd coverage of 1.2 ML (monolayer) from CV.

3.6 Platinum adsorption on Pd/G sintered at 700 K and its influence on enantioselective hydrogenation

3.6.1 CV characterisation

A series of seven Pt-Pd/G catalysts sintered at 700 K was prepared using the method described in experimental 2.42. Voltammograms showing the effect of Pt adsorption on Pd/G catalyst are depicted in Figure 3.50. The sharp peak at 0.19 V is a characteristic surface palladium peak ($\theta_{\text{Pt}} = 0$) [12, 13]. As the amount of Pt deposited on the surface was increased, the palladium voltammetric features were gradually extinguished as seen for $\theta_{\text{Pt}} = 0.13 - 0.75$. Upon reaching one monolayer, the sharp palladium peak disappeared. Multilayer growth was observed at coverages of $\theta_{\text{Pt}} = 1.75 - 6$ with features of bulk Pt surfaces becoming visible in this range of coverage and bulk absorption of hydrogen into Pd becoming increasingly less well marked (peak at ≈ 0 V). Table 3.36 shows dosing volumes of H_2PtCl_6 and surface coverages of Pd on Pt/G.

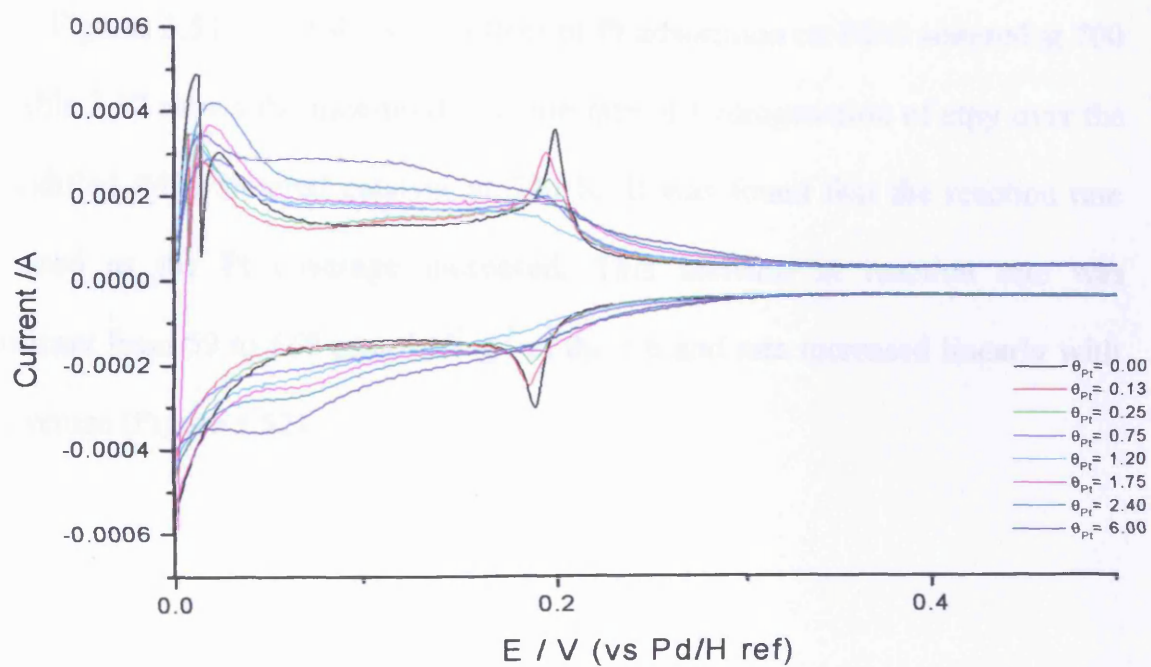
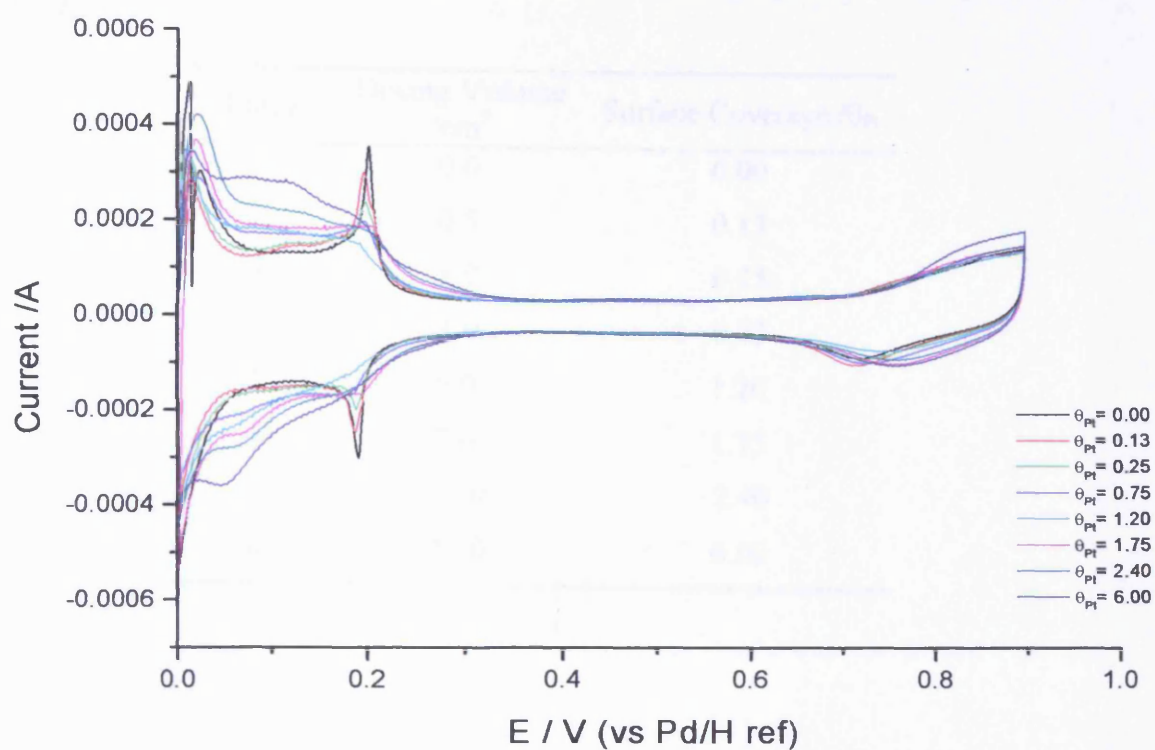


Fig. 3.50 CVs of Pt modified Pd/G in 0.5M H₂SO₄. Sweep rate 10 mV s⁻¹.

Table 3.36 Dosing volumes of H_2PtCl_6 and surface coverages for Pd/G catalyst sintered at 700 K.

Entry	Dosing Volume /cm ³	Surface Coverage / θ_{Pt}
1	0.0	0.00
2	0.5	0.13
3	1.0	0.25
4	3.0	0.75
5	5.0	1.20
6	7.0	1.75
7	10.0	2.40
8	25.0	6.00

3.6.2 Reaction rate

Figures 3.51 - 3.52 show the effect of Pt adsorption on Pd/G sintered at 700 K. Table 3.37 shows the measured reaction rate of hydrogenation of etpy over the Pt modified Pd/G sintered catalyst at 700 K. It was found that the reaction rate increased as the Pt coverage increased. This increase in reaction rate was significant from 59 to 668 mmol h⁻¹ g⁻¹ at $\theta_{Pt} = 6$ and rate increased linearly with Pt coverage (Figure 3.52).

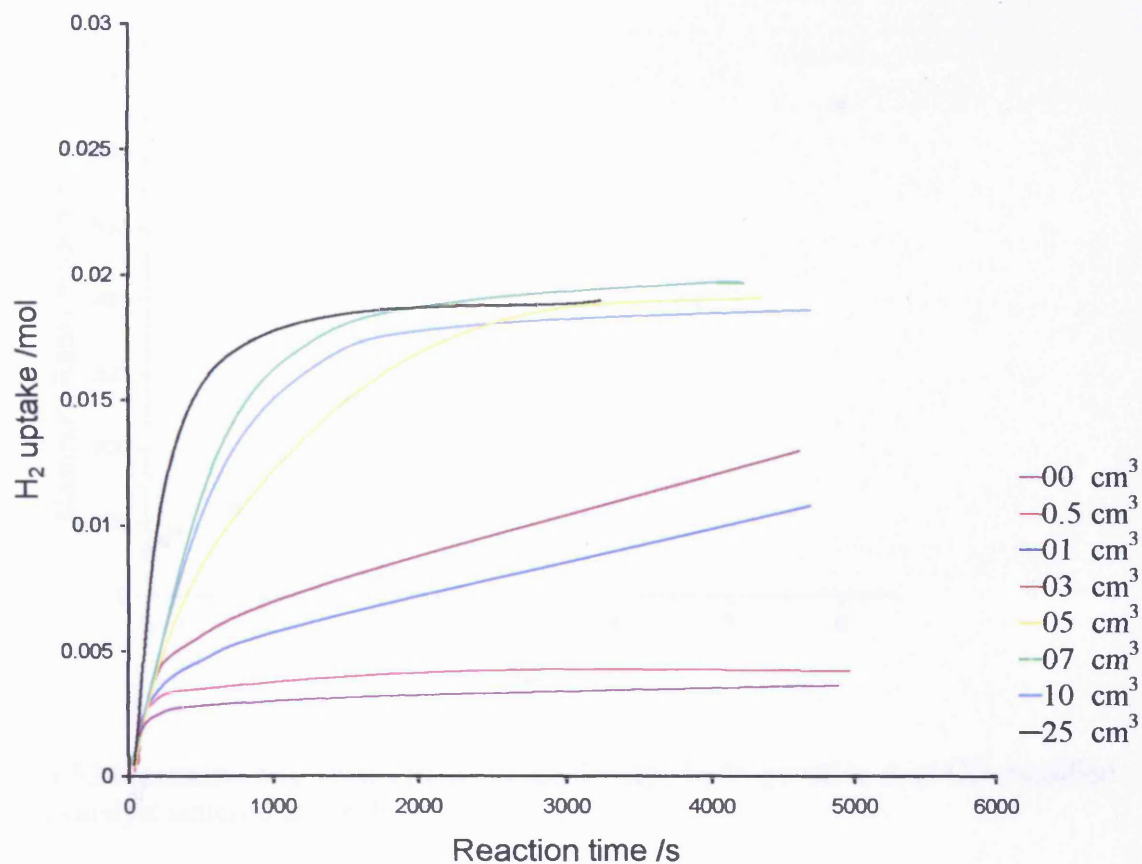


Fig. 3.51 H₂ uptake curves for etpy hydrogenation over CD-modified Pd/G catalyst sintered at 700 K : influence of H₂PtCl₆ adsorption.

Table 3.37 Effect of Pt adsorption on reaction rates for Pd/G catalyst sintered at 700 K.

Entry	Dosing Volume /cm ³	Surface Coverage / θ_{Pt}	Maximum Rate /mmol h ⁻¹ g ⁻¹
1	0.0	0.00	59
2	0.5	0.13	74
3	1.0	0.25	89
4	3.0	0.75	119
5	5.0	1.20	178
6	7.0	1.75	267
7	10.0	2.40	297
8	25.0	6.00	668

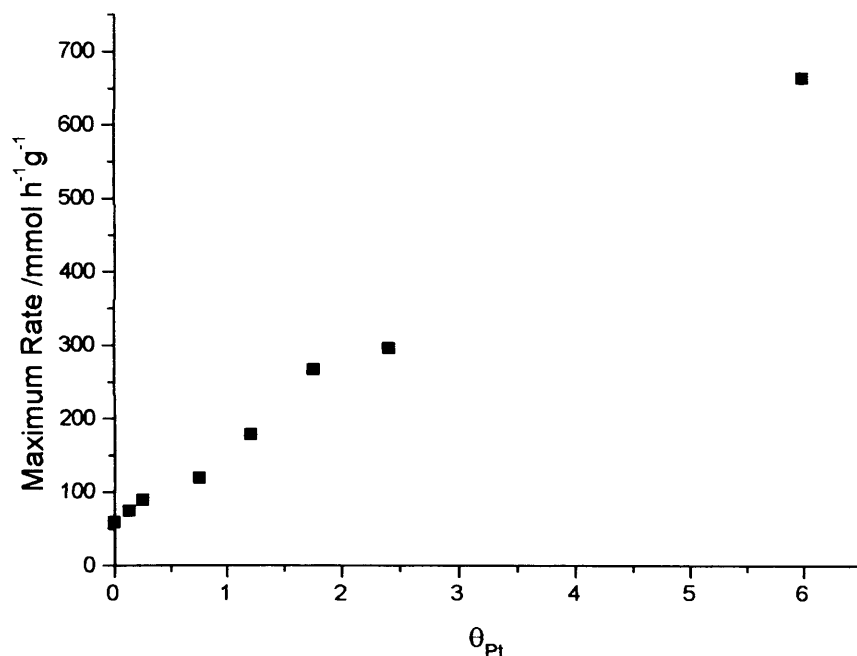


Fig. 3.52 Maximum rate versus Pt coverage for etpy hydrogenation over CD-modified Pd/G catalyst sintered at 700 K.

3.6.3 Enantioselectivity

Table 3.38 shows the effect of increasing Pt coverage on the enantioselectivity of etpy hydrogenation. Adsorption of Pt on the Pd/G catalyst sintered at 700 K increased the ee significantly, up to 42.0% at highest coverage ($\theta_{Pt} = 6$). At low dosage of Pt ($\theta_{Pt} = 0 - 1.0$), the ee increase was rapid, from 0 to 37.9% (table 3.38). At higher coverage ($\theta_{Pt} = 1.0 - 6.0$), the ee remained in the range, 37.9 to 42.0%. The ee behaviour with Pt coverage is shown in Figure 3.53.

Table 3.38 Variation in enantioselectivity with increasing Pt coverage for Pd/G catalyst sintered at 700 K.

Entry	Dosing Volume /cm ³	Surface Coverage / θ_{Pt}	Enantiomeric Excess (ee) /% (R)
1	0.0	0.00	a *
2	0.5	0.13	17.9
3	1.0	0.25	26.9
4	3.0	0.75	35.9
5	5.0	1.20	37.9
6	7.0	1.75	38.2
7	10.0	2.40	40.5
8	25.0	6.00	42.0

a * = The conversion of reaction was very low (1%), so that ee was not available.

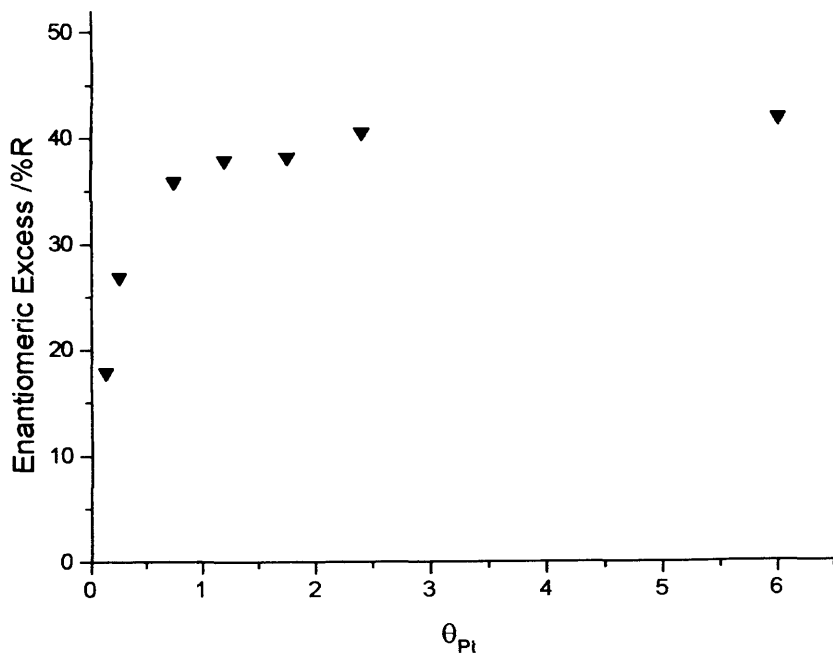


Fig. 3.53 Pt coverage and enantiomeric excess for Pd/G catalyst sintered at 700 K.

3.7 Rhodium adsorption on Pt/G sintered at 700 K and its influence on enantioselective hydrogenation

3.7.1 CV characterisation

A series of nine Rh modified Pt/G catalysts, each sintered at 700 K before Rh adsorption, was prepared as described in section 2.4.2. Figure 3.54 illustrates voltammograms of Rh adsorption on Pt/G. Table 3.39 shows the amount of Rh and its coverages deposited on the catalyst. Initial growth of rhodium was signified by the growth of a sharp peak at 0.11 V. As the amount of rhodium deposition increased ($\theta_{\text{Rh}} = 0.2 - 0.6$), the peak at 0.11 V gradually increased, while the Pt{100}x{111} step sites simultaneously decreased. As soon as a second layer of rhodium began growing, a new voltammetric peak was observed at 0.06 V. Upon exceeding one monolayer ($\theta_{\text{Rh}} = 2 - 6$) there was a simultaneous decrease and slight broadening in the magnitude of the 0.11 V peak and the Pt{100}x{111} step voltammetric features were lost. The existence of the two peaks at 0.06 V and 0.11 V has previously been reported by Attard and co-workers [15, 25, 26] and attributed to electrochemical processes occurring on rhodium mono- and multilayers respectively. They are similar in character to those of palladium deposited in Pt/G except that, for Rh, the multi-layer peak is situated at a potential more negative than the monolayer peak. It is also reported that Rh does not grow in a simple layer-by-layer manner [15, 25, 26]. Rather, Rh second layer growth begins on Pt{111} at a coverage of ≈ 0.7 monolayer [25]. These facts have been taken into account in studying Rh coverage from voltammetry. Clearly one must

expect second and multi-layer Rh growth to commence before all Pt sites are blocked and this indeed is observed in Figure 3.54. Furthermore, the strong preference of Rh to adsorb in defect sites rather than $\{111\}$ terraces is also noted in the relative rates of attenuation of voltammetric peaks associated with Pt.

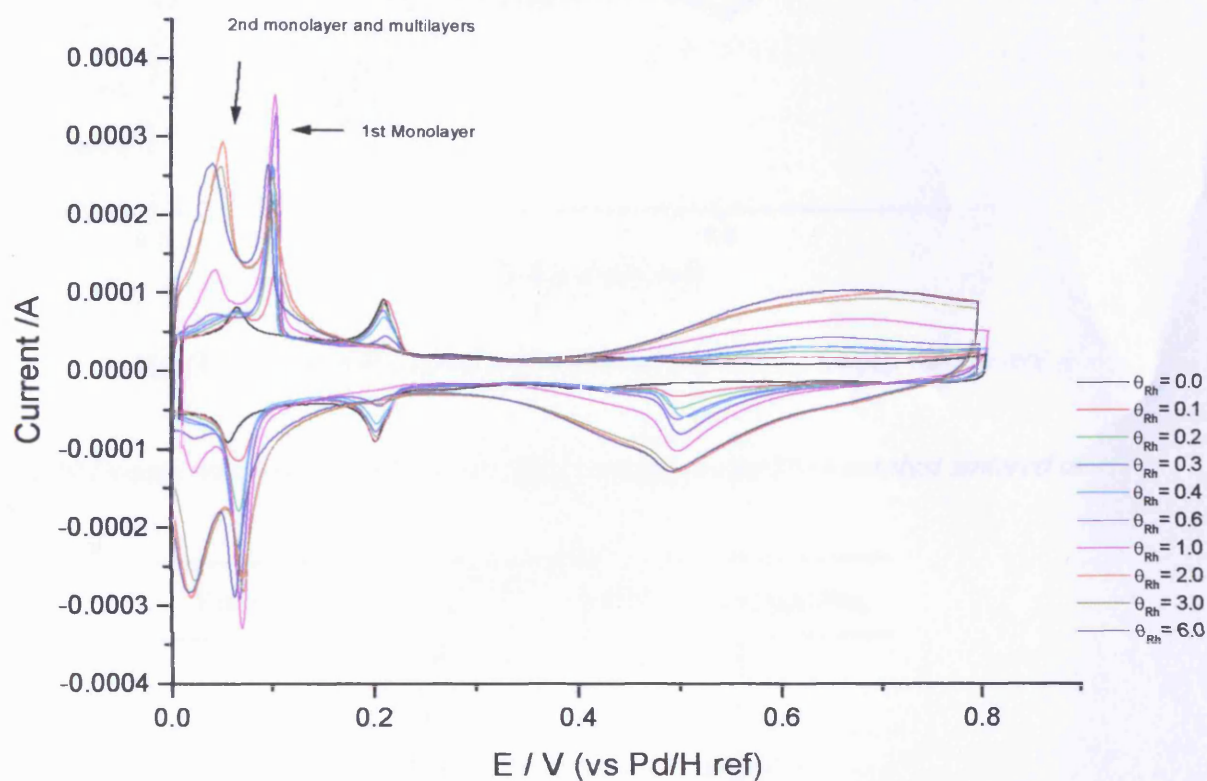


Fig. 3.54 CVs of Rh modified Pt/G in 0.5M H_2SO_4 . Sweep rate 50 mV s^{-1}

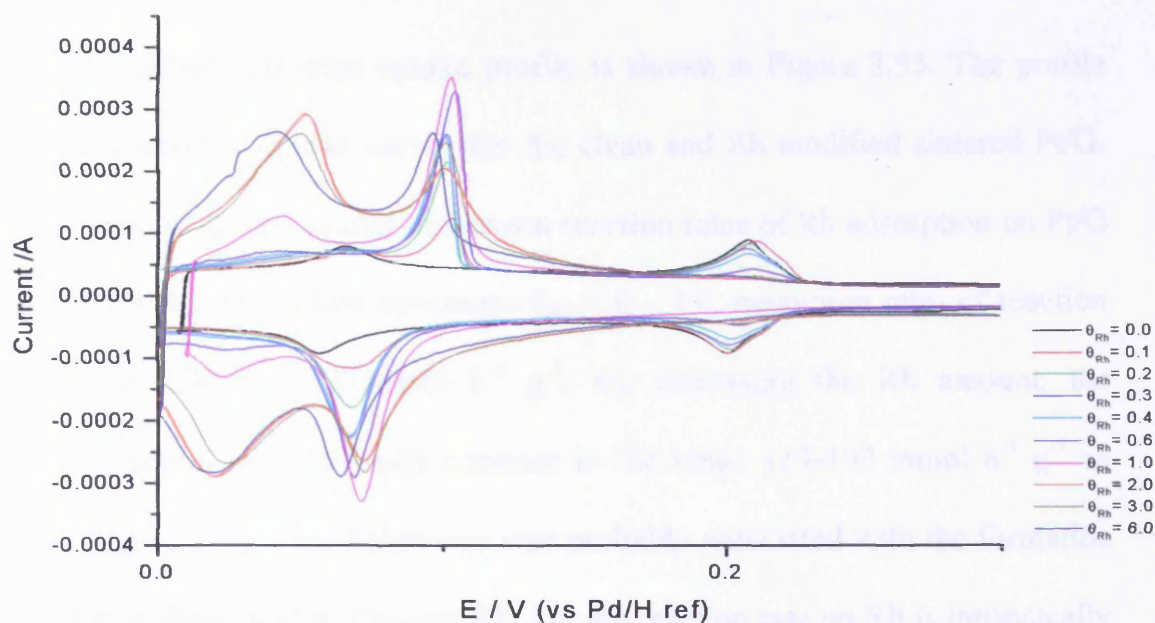


Fig. 3.54 CVs of Rh modified Pt/G in 0.5M H₂SO₄. Sweep rate 50 mV s⁻¹.

Table 3.39 Dosing volumes of RhCl₃ and surface coverages for Pt/G catalyst sintered at 700 K.

Entry	Dosing Volume /cm ³	Surface Coverage /θ _{Rh}
1	0.0	0.0
2	0.2	0.1
3	0.4	0.2
4	0.6	0.3
5	0.8	0.4
6	1.2	0.6
7	2.0	1.0
8	4.0	2.0
9	6.0	3.0
10	12.0	6.0

3.7.2 Reaction rate

The resulting hydrogen uptake profile is shown in Figure 3.55. The profile reveals the hydrogen uptake curves for the clean and Rh modified sintered Pt/G. Table 3.40 shows the measured maximum reaction rates of Rh adsorption on Pt/G sintered at 700 K. At Rh low coverages $\theta_{\text{Rh}} = 0 - 1.0$, maximum rates of reaction plunged from 250 to 113 $\text{mmol h}^{-1} \text{g}^{-1}$. By increasing the Rh amount, the maximum reaction rate remained constant in the range 113-109 $\text{mmol h}^{-1} \text{g}^{-1}$ as shown in Figure 3.56. This behaviour was probably associated with the formation of second monolayer and multilayer Rh, i.e. the reaction rate on Rh is intrinsically lower than Pt but faster than on Pd.

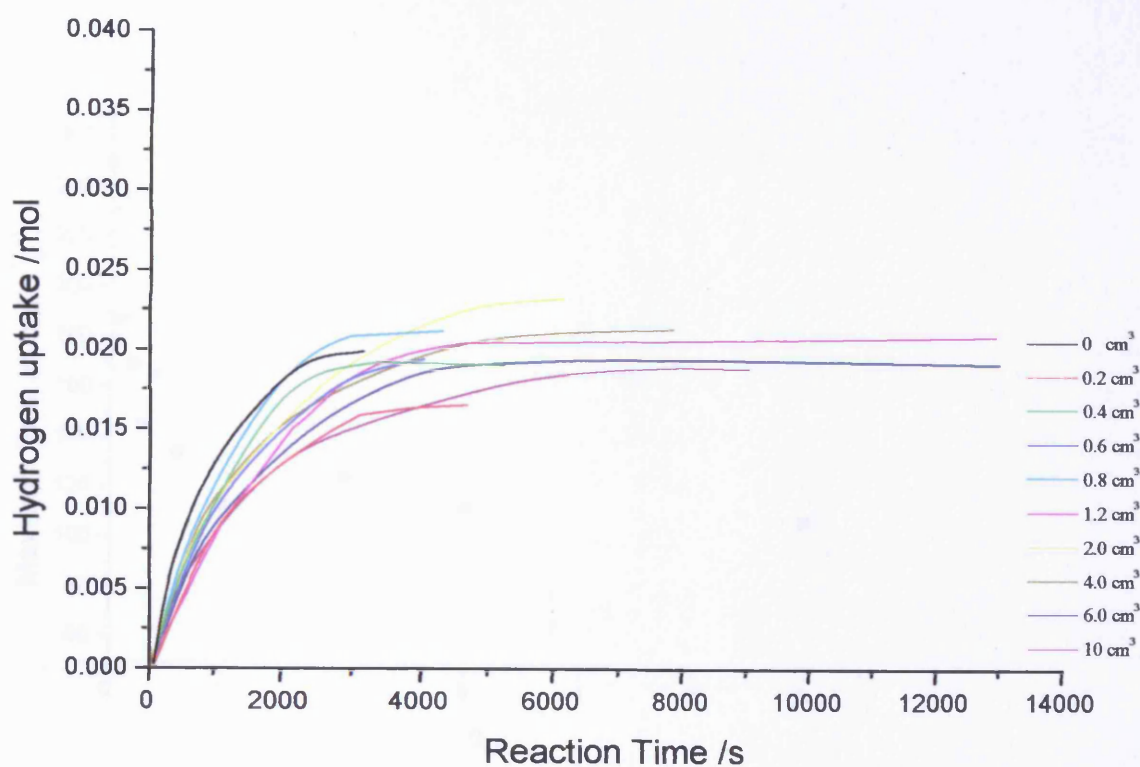


Fig. 3.55 H_2 uptake curves for etpy hydrogenation over CD-modified Pt/G catalyst sintered at 700 K: influence of RhCl_3 adsorption.

Table 3.40 Effect of Rh adsorption on reaction rates for Pt/G catalyst sintered at 700 K.

Entry	Dosing Volume $/\text{cm}^3$	Surface Coverage $/\theta_{\text{Rh}}$	Maximum Rate $/\text{mmol h}^{-1} \text{g}^{-1}$
1	0.0	0.0	250
2	0.2	0.1	187
3	0.4	0.2	169
4	0.6	0.3	145
5	0.8	0.4	165
6	1.2	0.6	134
7	2.0	1.0	113
8	4.0	2.0	125
9	6.0	3.0	113
10	12.0	6.0	109

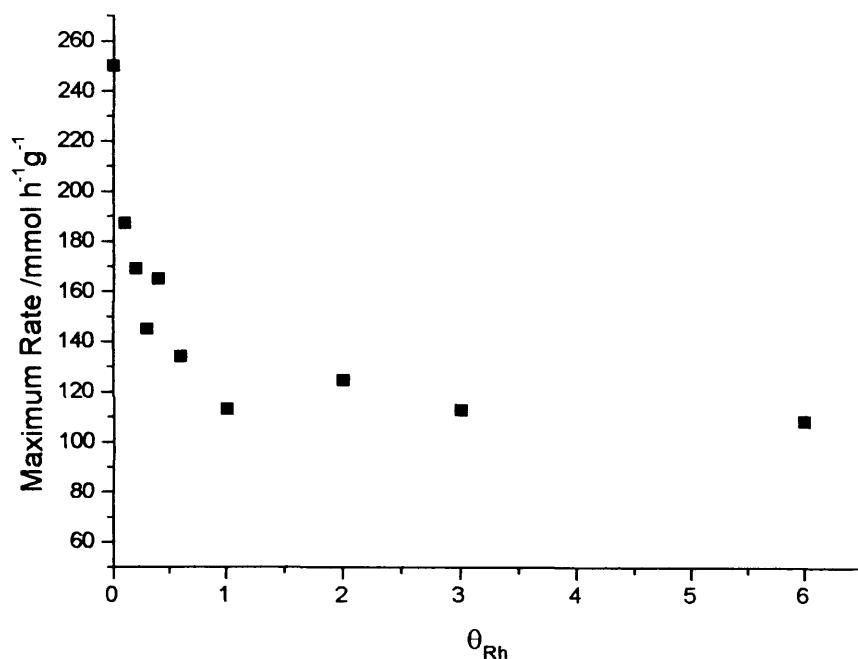


Fig. 3.56 Maximum rate versus Rh coverage for etpy hydrogenation over CD-modified Pt/G catalyst sintered at 700 K.

3.7.3 Enantioselectivity

Rhodium adsorption on the Pt/G catalyst sintered at 700 K in the presence of CD reduced the ee significantly, from 57.0 to 24.4% as shown in table 3.41. The most significant decrease was in the coverage region of $\theta_{Rh} = 0 - 1.0$, as depicted in Figure 3.57. This coincided with total blockage of $\text{Pt}\{100\} \times \{111\}$ step sites and the formation of the second Rh monolayer. Upon exceeding one monolayer, the ee remained constant, within the range 31.7 - 24.4% substantially higher than for Pd.

Table 3.41 Variation in enantioselectivity with increasing Rh coverage for Pt/G catalyst sintered at 700 K.

Entry	Dosing Volume /cm ³	Surface Coverage / θ_{Rh}	Enantiomeric Excess (ee) /% (R)
1	0.0	0.0	57.3
2	0.2	0.1	47.0
3	0.4	0.2	44.2
4	0.6	0.3	42.3
5	0.8	0.4	42.5
6	1.2	0.6	37.1
7	2.0	1.0	31.7
8	4.0	2.0	29.6
9	6.0	3.0	26.3
10	12.0	6.0	24.4

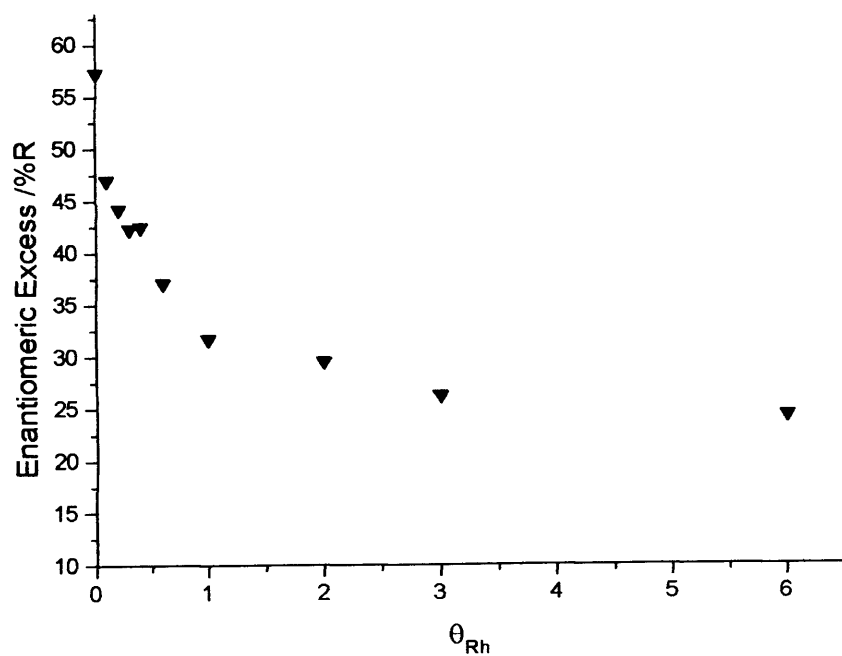


Fig. 3.57 Rh coverage and enantiomeric excess for Pt/G catalyst sintered at 700 K.

3.8 References

1. G.A. Attard, K.G. Griffin, D.J. Jenkins, P. Johnston, P.B. Wells, *Catal. Today*, **114** (2006) 346.
2. J. Clavilier, K. El Achi, A. Rodes, *J. Electroanal. Chem.*, **141** (1990) 1.
3. Y. Orito, S. Imai, S. Niwa, *J. Chem. Soc. Jpn.*, **8** (1979) 1118.
4. H.-U. Blaser, H.P. Jalett, D.M. Monti, J.T. Wehrl, *Appl. Catal.*, **52** (1989) 19.
5. G.A. Attard, A. Ahmadi, D.J. Jenkins, O.A. Hazzazi, P.B. Wells, K.G. Griffin, P. Johnston, J.E. Gillies, *Chem. Phys. Chem.*, **4** (2003) 123.
6. T. Mallat, S. Frauchiger, P.J. Kooyman, M. Schürch, A. Baiker, *Catal. Lett.*, **63** (1999) 121.
7. D.J. Jenkins, A.M.S. Alabulrahman, G.A. Attard, K.G. Griffin, P. Johnston, P.B. Wells, *J. Catal.*, **234** (2005) 230.
8. R.W. Evans, G.A. Attard, *J. Electroanal. Chem.*, **345** (1993) 337.
9. D.J. Jenkins. Ph.D. Thesis, Cardiff University, 2003.
10. S.D. Jackson, M.B.T. Keegan, G.D. McLellan, P.A. Meheux, R.B. Moyes, G. Webb, P.B. Wells, R. Whyman, J. Willis, *Preparation of Catalysis*. (Eds. G. Poncelet et al.), V, Elsevier, Amsterdam, 1991.
11. G.A. Attard, A. Bannister, *J. Electroanal. Chem.*, **300** (1991) 467.
12. G.A. Attard, R. Price, A. Al-Akl, *Electrochim. Acta.*, **39** (1994) 1525.

13. J. Clavilier, M.J. Llorca, J.M. Feliu, A. Aldaz, *J. Electroanal. Chem.*, **310** (1991) 429.
14. M.J. Llorca, J.M. Feliu, A. Aldaz, J. Clavilier, *J. Electroanal. Chem.*, **351** (1993) 299.
15. J. Inukai, M. Ito, *J. Electroanal. Chem.*, **358** (1993) 307.
16. B. Alvarez, J.M. Feliu, J. Clavilier, *Electrochem. Comm.*, **4** (2002) 379.
17. M.J. Ball, C.A. Lucas, N.M. Markovic, V. Stamenkovic, P.N. Ross, *Surf. Sci.*, **518** (2002) 201.
18. N.M. Markovic, C.A. Lucas, V. Climent, V. Stamenkovic, P.N. Ross, *Surf. Sci.*, **465** (2000) 103.
19. M.J. Ball, C.A. Lucas, N.M. Markovic, V. Stamenkovic, P.N. Ross, *Surf. Sci.*, **540** (2003) 295.
20. G.A. Attard, R. Price, *Surf. Sci.*, **335** (1995) 63.
21. P.B. Wells, A. Wilkinson, *Top. Catal.*, **5** (1998) 39.
22. H.-U. Blaser, H.P. Jalett, D.M. Monti, J.F. Reber, J.T. Wehrli, *Stud. Surf. Sci. Catal.*, **41** (1988) 153.
23. T.J. Hall, P. Johnston, W.A.H. Vermeer, S.R. Watson, P.B. Wells, *Stud. Surf. Sci. Catal.*, **101** (1996) 221.
24. B.A. Timothy. Ph.D. Thesis Cardiff University, 2000.
25. G.A. Attard, R. Price, A. Al-Akl, *Surf. Sci.*, **335** (1995) 52.
26. R. Gomez, J.M. Feliu, *Electrochim. Acta.*, **44** (1998) 1191.

CHAPTER FOUR

DISCUSSION

4.1 Introduction

We have seen in chapter three that the enantioselective hydrogenation of etpy is extremely sensitive to platinum surface morphology and surface composition. In the present chapter, a coherent model of rate enhancement and enantioselection will be proposed. It is believed that such an appraisal of these fundamental aspects of Orito-type reaction may lead on to the development of superior enantioselective catalysts.

4.2 Thermal annealing of Pt/G and its influence on enantioselective hydrogenation

Enantioselective hydrogenation of etpy has been investigated using sintered Pt/G catalysts at 450, 600, 700, 800, and 900 K under 5% H₂/Ar. CV and TEM were also used to study the catalyst morphology of each of the sintered catalysts. As annealing temperature was increased, all CV features (Figure 3.1) were attenuated as reported previously [1]. Step peaks were more pronounced and narrower when annealing temperature was increased. The Pt{100} terrace contribution increased in magnitude initially, but then decreased as annealing temperature reached to 600 K.

It was observed that as sintering temperature increased, the reaction rate significantly decreased from 611 to 170 mmol h⁻¹ g⁻¹ (Figure 3.2). This decrease was accompanied by a decrease in the platinum surface area which was attributed to the growth of larger Pt nanoparticles as shown in TEM images (Figure 3.2) i.e.

particle dispersion was reduced upon annealing. Enantiomeric excess (ee) was also decreased upon heating to 600 K and this occurred in parallel with the significant increase in Pt{100} terrace features. The catalysts annealed at 600 K and above exhibited an increase in ee and a maximum ee was obtained at 700 K. The increase and subsequent decreases in ee has been reported previously by Attard *et al.* [1, 2] and was attributed to both the catalyst morphology and the influence of particle size. Particle size dependence has also been reported by other workers [3, 4]. In references [1, 2], a model was put forward to interpret the ee behaviour as a function of particle size based on CV and TEM data together with the known sensitivity of ee on the nature of the particle support [5]. In essence, an active site located at the intersection of the support and the metal particle perimeter was proposed. Any changes in the morphology or composition of this site would have profound effects on ee because such edges contain corner sites that are intrinsically chiral. This is shown in Figure 4.1.

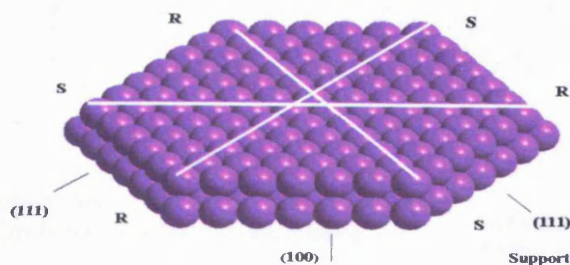


Fig. 4.1 A schematic diagram of a flat hexagonal Pt nanoparticle on a support. It is observed that the corners of the hexagon are chiral with alternating R- and S-sites.

TEM images in reference [1, 2] and also the present study revealed that at elevated temperature in hydrogen, Pt nanoparticles formed faceted structures, particularly hexagons. The corners of these hexagons are chiral [1, 2] and hence the adsorption of CD at these sites would generate a diastereoisomeric adsorption site. In Figure 4.2 these sites are depicted as circles to distinguish them from other chiral sites formed as a consequence of CD adsorption on terraces and linear steps. It is seen from Figure 4.2 that if particle size is small, the active site ensemble of CD + corner site overlap and, because the diastereomeric nature of the site would be removed, this would lead to a poor ee. It is known that ee is very low for very small Pt particles [6-10].

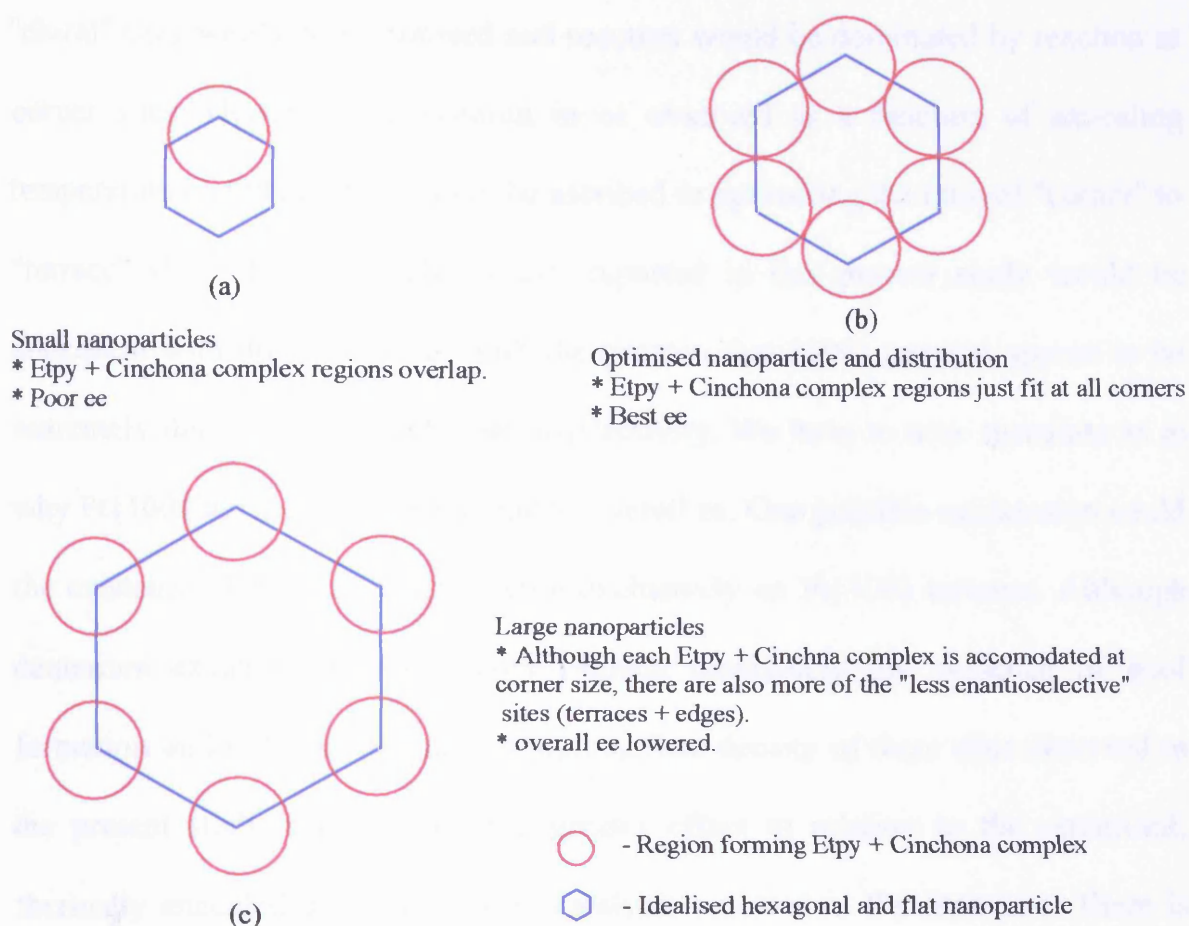


Fig. 4.2 A schematic presentation of the mechanism of ee behaviour as annealing temperature of Pt/G increased according to reference [1]. (b) optimum arrangement of diastereomeric enantioselective sites formed by alkaloid adsorption at the chiral kink sites around a hexagonal Pt particle; (a) and (c) non-optimum arrangement of such sites. Reproduced from [1, 2]

Similarly, for extremely large hexagonal particles, although the active sites (indicated by circles) are now well separated, they also allow for CD to adsorb at linear step and terrace sites which would be expected to generate enantiomeric excesses of lower value since a "chiral" rather than a "diastereomeric" adsorption site would be created by adsorption of CD. For particles of intermediate size, these

"chiral" sites would be minimised and reaction would be dominated by reaction at corner sites. Hence, the maximum in ee observed as a function of annealing temperature of Pt/G catalysts may be ascribed to optimising the ratio of "corner" to "terrace" sites of the Pt. The results reported in this present study would be consistent with this model but with the proviso that {100} terraces appear to be extremely detrimental to high enantioselectivity. We have to now speculate as to why Pt{100} terraces are detrimental to overall ee. One possible explanation could be the existence of the enol form of etpy exclusively on Pt{100} terraces. Although deuterium exchange measurements exclude completely the presence of enol formation on Pt, it may be that the high surface density of these sites observed in the present study may engender a greater effect in relation to the optimised, thermally annealed oxide supported catalysts reported in the literature. There is theoretical support for thermodynamic stability of enol versus keto on Pt in the work of Willock *et al.* [11] Hence there are good theoretical calculations that state that enol should be more stable than keto forms of etpy on Pt. Clearly, if the enol-form cannot be detected on Pt (in contrast to palladium), this can only be due to kinetic factors which remain as yet, unknown.

4.3 Adatom adsorption on supported platinum and its influence on enantioselective hydrogenation

4.3.1 Differences in growth mode of the various adatoms on Pt

The adsorption of bismuth and sulphur on platinum single crystal and supported platinum has been investigated previously by CV [12-14]. Deposition of Bi on Pt occurred preferentially at step/kink sites and {100} terrace sites, whilst S adsorption took place initially at Pt{111} terrace sites [12-14].

In the present study, Bi adsorption on Pt/G catalysts sintered at 450 K (Figure 3.5) indicates that, at low Bi doses, adsorption occurred preferentially at step sites and Pt{100} terrace sites. This was observed as a loss of CV peak intensity as a function of coverage. It was noted that the loss of Pt{100} peak area was significant and appeared to have an influence on the ee of the Orito reaction. *It should be noted that this was also seen when particles were annealed to generate {100} sites.* At higher coverages, adsorption of Bi took place at Pt{111} terraces and eventually all Pt H_{UPD} voltammetric features were diminished. Figures 3.5 and 3.9 - 3.12 show the adsorption of Bi at Pt/G annealed between 600 - 900 K. Similar adsorption behaviour to that described in the case of catalysts prepared at temperatures < 500 K was observed except that the filling of defect sites occurred at lower coverages ($0.3 \pm .05$) relative to catalysts annealed at $T \leq 500$ K. The decrease in Pt{100} terrace CV intensity was less marked because the initial surface density of Pt{100} terraces on the high temperature annealed catalysts was already rather small. S adsorption on Pt/G catalysts annealed at different

temperatures was also investigated as shown in Figures 3.29 – 3.32. At low coverages, S adsorption was found to reduce all H_{UPD} adsorption peaks to some extent, whilst Pt{100} terrace sites were attenuated significantly for all sintered catalysts. For unannealed Pt/G catalysts, preferential adsorption of S at terrace sites was reported [14].

Differences in surface diffusion have been used to interpret the deposition behaviour of Bi on Pt [12, 13]. It was reported that Bi diffuses quickly over Pt{111} terraces [12, 15]. When Bi adatoms diffuse on {111} terraces of Pt, they diffuse to the step/kink sites which exhibit a higher adsorption energy than the {111} terraces for Bi. Because of a further electrostatic attraction for the electropositive Bi atoms for the step, this also facilitated preferential binding at step sites. Then, as Bi coverage increases, the deposition on steps proceeds until they are all filled. At this point, deposition of Bi on {111} terraces commences. In contrast, diffusion of Bi on Pt{100} has been found to be slow (for example a sharp $c(2 \times 2)$ Bi-Pt{100} LEED pattern is observed at room temperature whereas Bi-Pt{111} only gives rise to a very weak, diffuse background [15]). This is consistent with what is found here in that deposition of Bi occurred on both steps and {100} terraces preferentially. A relationship between the work function of adsorbed adatoms and the substrate was reported by Herrero [13] to interpret the electrostatic influence of steps. If the work function of the adsorbate is greater than that of Pt (= 5.7 eV), for example S (\approx 6.2 eV), this would favour deposition at terrace sites close to the terrace edge. If it is smaller than Pt, e.g. for Bi (= 4.2 eV),

this would favour deposition at steps [13]. This behaviour is explained by the electronic charge density being smoothed at the

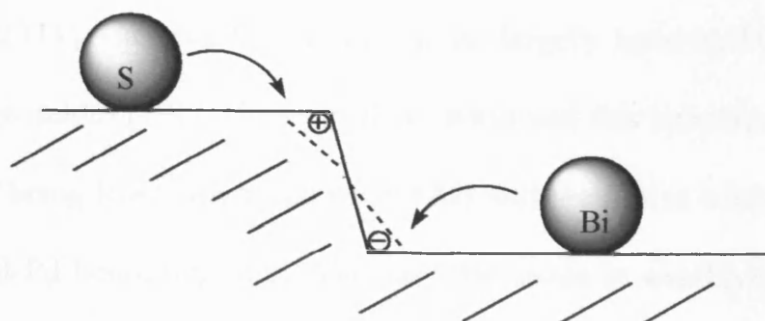


Fig. 4.3 Schematic representation of the proposed interaction between adatom ($\text{Bi} = \delta^+$, $\text{S} = \delta^-$) and step sites, as a function of the charge density carried by the adatom and the step dipole [13].

step edge, which creates a dipole moment with the positive charge at the upper part and the negative charge at the lower part of the step due to the Smoluchowski effect [13] as shown in Figure 4.3.

Deposition of Pd on Pt/G occurred by the forced deposition of Pd^{2+} on to the Pt surface using H_2 gas as the reducing agent. The irreversible adsorption of Pd on Pt/G has been investigated by CV (Figure 3.45). It was found that at low coverage of Pd, adsorption occurred at step sites followed by subsequent adsorption at terrace sites at higher Pd coverages as signified by attenuation of the $\text{Pt}\{111\}$ terrace peak at 0.45 V. It was found that the emergence of the second monolayer Pd CV peak begins just before completion of the first layer according to the CV profile. So the growth mode is expected to be essentially Frank-Van der Merwe, and it is the same as found for single crystals [16]. These findings are

consistent with those obtained by Feliu *et al.* [17]. Attard [18] reported that the growth mode of Pd on Pt{100} (using Auger, LEED, and CV) depended on the reconstructive state of the Pt{100} surface. Unlike on Pt{100}, palladium growth on Pt{111} surfaces was found to be largely layer-by-layer (the Frank-van der Merwe mode) [19]. These workers attributed this behaviour to the surface energy of Pd being lower than that of Pt [20] and the lattice constant difference between Pt and Pd being negligible (hence little strain in overlayer). Inukai and Ito [21] also suggested that Pd grows epitaxially in pseudomorphic structures on Pt{100} and Pt{111}. Ball *et al.* [22] examined the electrochemical deposition of Pd thin films on a Pt{001} electrode surface by *in situ* surface X-ray scattering and CV. Analysis indicated that Pd grows epitaxially via pseudomorphic island formation onto the first monolayer which was characteristic of a pseudomorphic Stranski-Krastanov growth mode [22]. However, later *in situ* STM work appeared to show that Pd on Pt did not grow exactly as layer-by-layer but simultaneous multilayer growth could also be observed, i.e. second layer and subsequent growth occurred with incomplete filling of the previous Pd layer.

Rh adsorption on Pt/G has been examined by CV. At low coverages, the growth of a sharp peak at 0.11 V was observed. This voltammetric peak was also reported by Inukai and Ito [21]. As Rh deposition increased, a second voltammetric peak was observed at 0.06 V. This is an indication of the formation of the second and multi-layer Rh forming at $\theta_{\text{Rh}} = 0.70$. These two peaks were identified previously [21, 23, 24]. Rh growth was reported not to be layer-by-layer

[21, 23, 24]. Rather, the growth mode of Rh on Pt surface was observed to exhibit a pseudomorphic Stranski-Krastanov (SK) growth mode in which second and multi-layer Rh begins to grow before completion of the first layer. This is also deduced from the CVs (Figure 3.54) since second layer Rh is observed before all Pt-features are attenuated. Evidently, the growth of rhodium differs from that of palladium on Pt{111}. It was concluded that since Rh had a larger surface energy than Pd and a smaller lattice constant that this would affect the growth mode on Pt between Rh and Pd leading to the differences observed [25].

Pt deposition on Pd/G was studied by CV as shown in Figure 3.50. The characteristic CV peak observed for clean, bulk Pd was observed at 0.19 V. This has been observed previously by Attard [19, 26] and Clavilier [17, 27]. Palladium oxide (Pd-O) formation was observed to commence at 0.72 V. Formation of the first monolayer was observed by both the disappearance of a sharp Pd CV peak and the formation of Pt-O at 0.77 V. Pt multi-layers were observed at high coverage $\theta_{\text{Pt}} > 1.75$ with electrochemical features characteristic of bulk Pt formation emerging and subsequently increasing in intensity. It should be noted that the adsorption and growth of Pt on Pd does not appear to have been reported previously in the literature.

4.3.2 Reaction rate

4.3.2.1 Bismuth adsorption on supported platinum

Cinchonidine-modified Pt promotes a reaction rate of pyruvate hydrogenation by a factor of 20 to 100 [28-30]. When Bi was adsorbed on Pt/G, an additional rate enhancement was observed [14]. In this work, Bi-modified Pt increased the reaction rate of etpy hydrogenation up to 7-fold (see table 3.5). For Bi modified Pt/G annealed at different temperatures and Pt/SiO₂ in the presence of CD as modifier, it was found that as Bi coverage was increased, the reaction rate increased until it reached a maximum rate. This increase was correlated with the blockage of kink/step sites and {100} terrace sites and also to some of the Pt{111} terrace sites being blocked in the case of catalyst annealed at 600, 700, 800, and 900 K. This contrasts with behaviour of catalysts annealed at $T \leq 500$ K. By increasing Bi coverage still further, the reaction rate remained constant for Pt/G catalysts annealed at 450, 600, and 700 K. This was consistent with previous data reported by Attard *et al.* [14]. However, for those catalysts annealed at 800 and 900 K, a decrease in reaction rate was observed after the maximum rate was achieved. This is a new observation. Hazzazi has reported that small Pt{111} terraces are not conducive to Bi adsorption whereas for $n\{111\} \times \{100\}$ Pt single crystals ($n > 4$), Bi could be readily adsorbed on Pt{111} terraces [12]. This inhibition of Bi adsorption at narrow {111} terraces may interpret the rate behaviour of catalysts annealed at high temperatures. The inhibition found with Pt/G catalysts formed at low annealing temperatures could be ascribed to a

majority of Pt{111} terrace sites were $n < 4$. For catalysts annealed at high temperature, the average of Pt{111} terrace width is greater than $n > 4$, consistent with TEM images and CV response. This would suggest that Bi on narrow {111} terraces was unstable under conditions of enantioselective hydrogenation whereas for catalyst containing extended {111} terraces, bismuth adlayers would be more stable. Hence hydrogen adsorption at larger Pt{111} terraces is blocked by Bi leading to a decrease in rate after going through a maximum. For catalysts annealed at low temperatures, the hydrogenation rate reached a plateau as a function of Bi terrace corresponding to the desorption of weakly adsorbed Bi from small ($n < 4$) Pt{111} terraces. But what could cause the Bi-induced rate enhancement? Bi rate enhancements observed upon blocking of step/kink sites was attributed to the decrease of by-product surface poison formation which formed preferentially at these sites [14] based on work by Lambert [31]. Lambert reported polymerisation of methyl pyruvate on Pt{111} single crystal in the absence of hydrogen. These surface poisoning polymeric chains were studied by scanning tunnelling microscopy (STM) as shown in Figure (1.22a). In the presence of a background pressure of H_2 , the polymerisation of methyl pyruvate was suppressed and methyl pyruvate monomers appeared to migrate to the steps of the Pt surface (Fig. 1.22b).

Baiker and Lambert [32] studied the influence of H_2 starvation on the rate of the Orito reaction on a Pt surface using a fixed-bed reactor system. They found that hydrogenation on the Pt surface after H_2 “starvation” dropped dramatically.

These authors attributed the loss of catalyst activity to the self-condensation of the methyl pyruvate with blocking of H adsorption sites. It was therefore necessary to maintain H_2 pressure at all reaction times and not to let the reactant contact the Pt surface in the absence of H_2 . Attard *et al.* reported [14] the formation of higher molecular weight by-products (HMWPs) which existed in high concentration in the presence of an alkaloid in dichloromethane. These HMWPs included a dimer formed between ethyl pyruvate and ethyl lactate (etpy-etlac) (Figure 4.4) together with the simple dimer (etpy) $_2$. These species were identified by GC-MS spectroscopy.

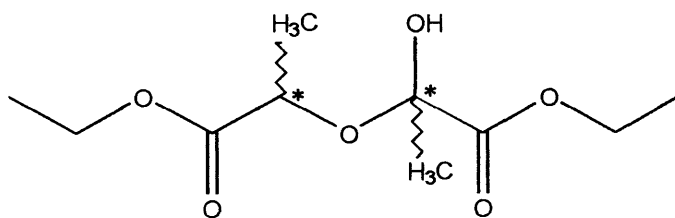


Fig. 4.4 Structure of the dimer of etpy-etlac.

In the presence of CD and etpy only, Baiker *et al.* [33] reported CD-catalysed deprotonation of etpy was followed by aldol condensation of ethyl pyruvate. The aldol product was in two tautomeric forms. The enol form was believed to protonate CD which increased the ee of etpy hydrogenation. Attard *et al.* suggested the formation of etpy dimer on the catalyst surface in the absence CD would account for low reaction rate. Subsequent CD adsorption was

speculated as catalysing dimer decoupling to ethyl pyruvate monomers (Figure 4.5). This reaction differs from the aldol-type reactions reported by Lambert and Baiker above [33] in that this reaction occurs without condensation and hence should be reversible. It could therefore be said that CD and H_2 inhibit the formation of surface poisons.

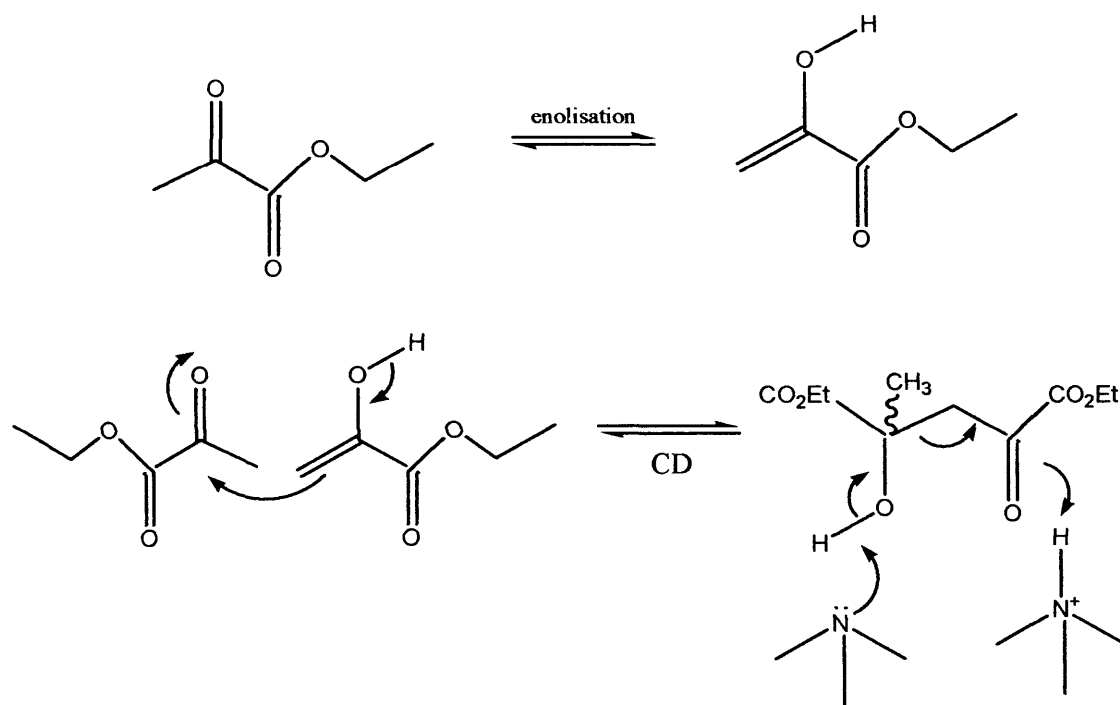


Fig. 4.5 Proposed reactions for CD-catalysed decoupling of dimer to etpy monomers [14].

CO formation from etpy decomposition on the Pt surface has also been reported [34-36]. Baiker *et al.* [34] observed in the absence of CD, strong adsorption of CO on the step edge and corners of the Pt catalyst, which formed

when some etpy decomposed on the Pt surface. In the presence of CD, etpy decomposition rate reduced significantly by a factor of 60, so formation of CO was limited. It was also found that CD displaced the adsorbed CO from the Pt surface which enhanced the reaction rate. Additional rate enhancement can be expected when Bi deposits on Pt step sites. This is attributed to the inhibition of both the formation and adsorption of CO [14] and the mechanism of polymer poison outlined in reference [14]. In work conducted by Harris [37], it was reported that the adsorption of Bi on the Pt step sites acts as a site blocker which, inhibited surface poison formation (CO) during the electrooxidation of glucose in sulphuric acid electrolyte and therefore was found to enhance the glucose electrooxidation reaction rate. Bi has also this effect during HCOOH oxidation on Pt{111} of enhancing rate by suppression CO formation [38, 39].

In conclusion, the reaction rate was promoted by CD, H₂, and Bi. The greatest increase was due to CD and it is speculated that the “unzipping” of the etpy dimer as suggested in reference [14] is still valid as an explanation of the previous results. The Bi rate enhancement may also be attributed to site blocking of specific sites of the catalyst which leads to suppression of CO and polymer formation *in situ*. In the hydrogenation reaction, the presence of Bi on the surface did not affect the rate order, and when the Bi modified catalyst was used in cyclohexene hydrogenation, the reaction rate decreased with increasing Bi coverage attesting to the lack of an electronic effect such as Bi/Bi²⁺ redox surface

chemistry i.e. a linear dependence of cyclohexene hydrogenation rate and Pt free sites was observed [14].

4.3.2.2 Sulphur adsorption on Pt/G

Reaction rate decreased significantly when S was adsorbed on Pt/G. This decrease in reaction rate was observed at low coverages of S. It was found that reaction rate for catalysts annealed at 500 and 700 K decreased sharply, whilst the reaction rate of unsintered catalysts and catalysts annealed at 450 K decreased linearly. This could be ascribed to the decrease in surface area for those catalysts annealed at 500 and 700 K. As can be seen from CV measurements (Figures 3.29-3.32), S preferentially adsorbs at terrace sites. These findings are consistent with previous work [14]. As mentioned above, when step sites remain unblocked, surface poison formation (polymer/dimer) would occur on those sites, which would slow down the reaction rate markedly as was observed experimentally. Tables 3.25-3.28 show a significant decrease in reaction rate for the first S dose, while for the remaining doses there was no significant decrease, possibly because unblocked step sites had the most effect on reaction rate. Subsequent decreases in rate as a function of S coverage could be ascribed to blocking of Pt{111} terrace sites, which decreases the number of available Pt sites for performing reaction.

4.3.2.3 Palladium adsorption on Pt/G

Enantioselective hydrogenation over Pd was active and produced high ee in α,β -unsaturated acids where C=C groups were hydrogenated. In α -ketoesters,

enantioselective hydrogenation of alkyl pyruvate over CD modified Pd was slow and produced S-enantiomer in excess, which is the reverse of the situation encountered with Pt [40, 41]. Wells *et al.* using deuterium exchange measurements reported [9, 41] that the enantioselectivity of alkyl pyruvates over Pd differed significantly from that over Pt. In the presence of CD, reaction rate over Pd was reduced, whilst it was enhanced over Pt. Enantioselective hydrogenation proceeded exclusively via hydrogenation of the carbonyl group (O=C) for α -ketoesters over Pt whereas it occurred via the adsorbed enol form (C=C) over Pd [41]. These experiments were conclusive since the product of hydrogenation of methyl pyruvate with D₂ over Pd was CX₃CX(OX)COOCH₃ (X = H or D), whilst the product over Pt was CH₃CX(OX)COOCH₃ [41]. Recently, Murzin reported [42] that enantioselective hydrogenation of 1-phenylpropane-1,2-dione over CD-modified Pd/alumina proceeded via hydrogenation of the C=O(1) group, not via the enol formed from the C=O(2) group - Figure 4.6, although the C=O(1) substituent was very active, it showed no enantioselectivity. These workers attributed this behaviour to the C=O(1) group in

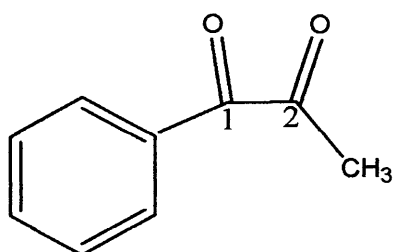


Fig. 4.6 Structure of 1-phenylpropane-1,2-dione.

1-phenylpropane-1,2-dione and the adjunct phenyl ring being conjugated, which lowered the bond energy of C=O(1) and made it easier for hydrogenation compared to the C=O(2) group. Finally, the product of hydrogenation over Pt was found to be the R-enantiomer, whilst S-enantiomer formed over Pd. This is discussed later.

Baiker and co-workers reported [43] hydrogenation of etpy over CD modified Pd-Pt/alumina using a series of Pd-Pt/alumina catalysts. They concluded that Pd deposition on supported Pt decreases both reaction rate (90% loss in activity at coverage of one third of the Pt atoms) and ee.

In the current work, palladium deposited on the Pt/G catalyst sintered at 700 K reduced the reaction rate of etpy hydrogenation by a factor of 19 (see table 3.34). It was found that by increasing Pd coverage, reaction rates were reduced significantly to $13 \text{ mmol h}^{-1} \text{ g}^{-1}$ at coverage of $\theta_{\text{Pd}} = 4.80$. The decrease in rate was most marked following the filling of step sites, with a less marked decrease associated with filling of terrace sites. Finally, a plateau in rate was observed for coverages exceeding one monolayer. This significant decrease in rate is attributed to enol formation, which was enhanced by the presence of Pd. CD is unable to "unzip" the enol forms of the dimer to generate the monomer (Figure 4.7) as in the case of Pt [14]. Figure 4.7 shows a plausible mechanism of surface poison formation over Pd in the presence of CD and indicates why these dimers cannot be "unzipped" to generate monomer.

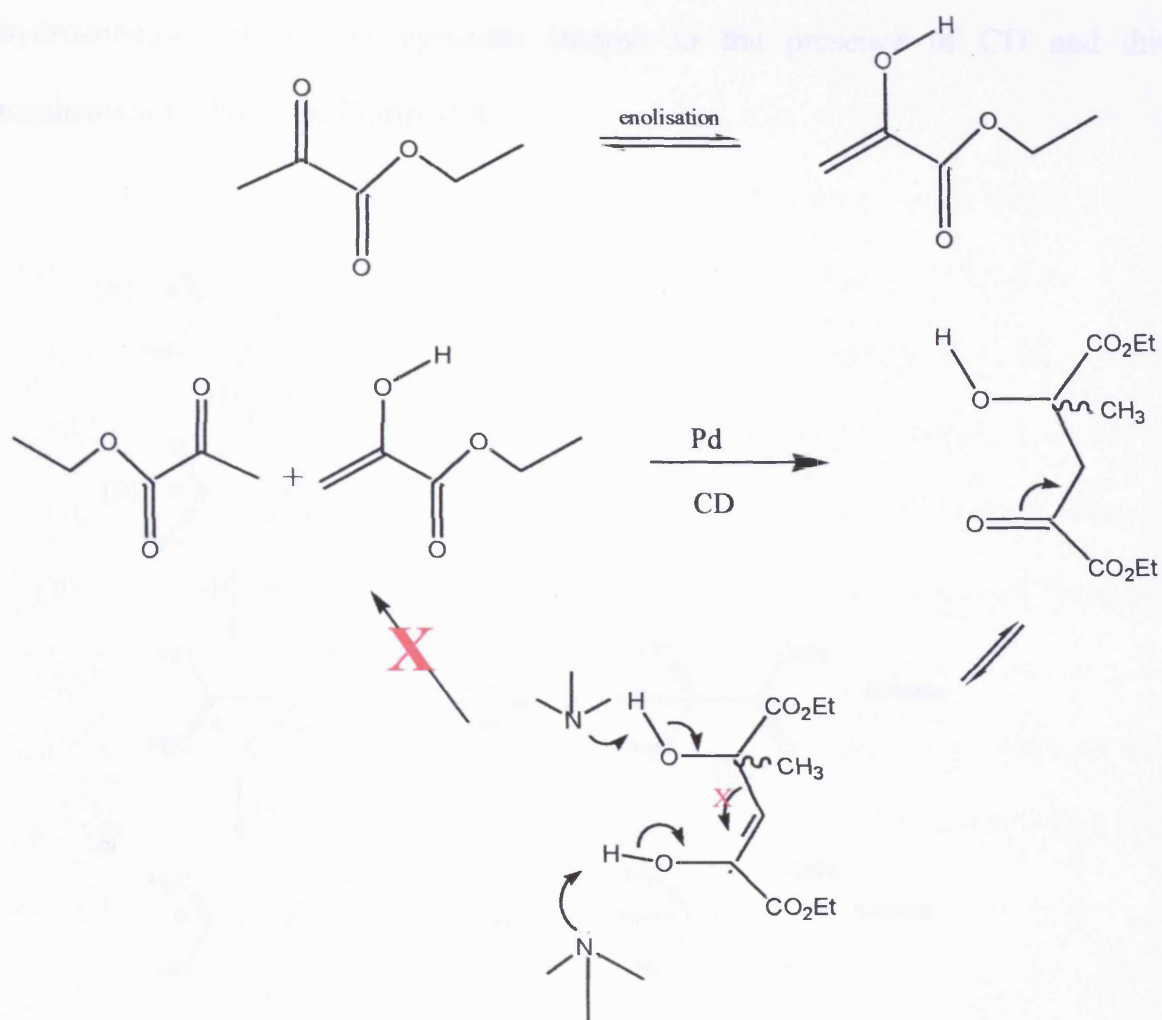


Fig. 4.7 Proposed reaction pathways for surface poison formation on CD-modified Pd-Pt/G catalyst. X = indicates that enol formation will prevent the unzipping reaction occurring [14].

If poison formation was enhanced at steps, then Pd adsorbed at step sites would almost certainly generate enol forms of the poison and hence a rapid deactivation of the catalyst.

Wells *et al.* [9] suggested a mechanism for Pd enantioselective hydrogenation of methyl pyruvate (mepy) in the presence of CD and this mechanism is shown in Figure 4.8.

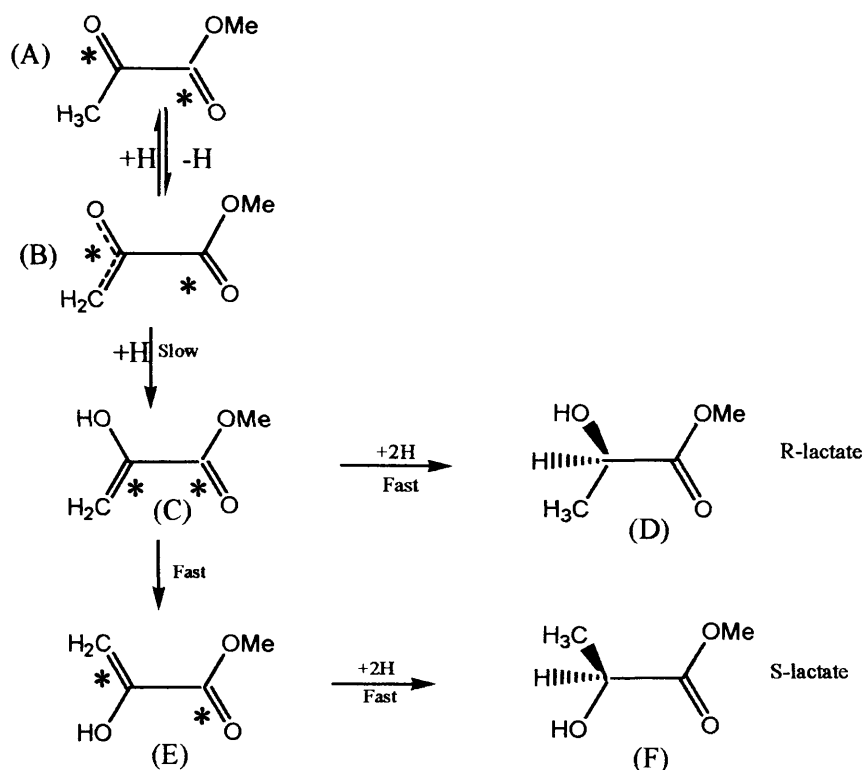


Fig. 4.8 Plausible mechanism of the enantioselective hydrogenation of mepy over CD modified Pd [9]. Asterisk (*) stands for Pd surface.

The decrease in reaction rate was attributed by Wells *et al.* to the formed intermediates showing no indication of forming hydrogen bonds to the quinuclidine–N atom of the modifier [9].

4.3.2.4 Platinum adsorption on Pd/G

Deposition of Pt on Pd/G sintered at 700 K enhanced the rate of enantioselective hydrogenation of etpy in the presence of CD, from 59 to 668 mmol h⁻¹ g⁻¹ at high coverage ($\theta_{\text{Pt}} = 6$) (see table 3.36). It was found that the reaction rate increased as the coverage of Pt increased. This rate enhancement with the increase of Pt coverage was due to the reaction of supported Pt in the presence of CD proceeding at a very fast rate [28-30]. The increase in reaction rate showed a linear relationship with platinum coverage (Figure 3.52). The highest rate was achieved at $\theta_{\text{Pt}} = 6$ (668 mmol h⁻¹ g⁻¹), almost the same as when fresh unsintered Pt/G was used (611 mmol h⁻¹ g⁻¹), indicating that the influence of Pt was dominant and there was no effect of Pd/G at this coverage of Pt. Hence, there appears to be negligible effect of bi-metallic Pt-Pd (nor for that matter for Pd adsorbed on Pt) in that a simple 1:1 relationship between rate and available Pt sites is observed.

4.3.2.5 Rhodium Adsorption on Pt/G

Enantioselective hydrogenation of etpy over Rh modified Pt/G sintered at 700 K in the presence of CD was examined. It was noticed that the reaction rate decreased with the increase of Rh coverage. The decrease was sharp in the coverage range $\theta_{\text{Rh}} = 0 - 1.0$ (from 250 to 113 mmol h⁻¹ g⁻¹), while the reaction rate remained constant (in the range of 113 – 109 mmol h⁻¹ g⁻¹) after the formation of the first monolayer. This behaviour was attributed to the first monolayer of Rh exhibiting a rate intrinsically slower than that of Pt. Murzin *et al.* [42] reported

that the activity over CD modified Rh catalysts was lower than over Pt for the enantioselective hydrogenation 1-phenylpropane-1,2-dione. In this work, rate remained almost constant in the second monolayer and multilayer of Rh because of the dominant effect of Rh in agreement with the present study.

Like Pt, it has been reported that addition of CD to a rhodium surface not only induces enantioselectivity, but also enhances ethyl pyruvate hydrogenation reaction rate by a factor of 10 to 52 [44-46].

4.3.3 Enantioselectivity

4.3.3.1 Bismuth adsorption

Bi adsorption on supported Pt was found to decrease ee overall, whereas the reaction rate increased, in contrast to previous reports which indicated that enantioselectivity and reaction rate always showed the same trend and were intimately connected so far as existing models of enantio-differentiation are concerned [14]. The exception to the behaviour observed in this study was the first adsorption dose of Bi on Pt/G catalysts sintered at 450 K which produced a *higher* ee. The observed increase in ee was from 35% for the clean catalyst to 39% for the Bi-modified catalyst as shown in Table 3.6. CVs of Bi-Pt/G sintered at 450 K (Figure 3.5) show a significant diminution in the Pt{100} terrace sites with the first Bi dose. It is inferred from this observation that the presence of large Pt{100} terrace sites was detrimental to overall ee. Thus, by blocking these sites with Bi,

an increase in ee would be expected. Subsequent adsorption of Bi produced a decrease in ee because the blocking of step sites was more extensive than had occurred at the lower Bi coverage. This would lead to a reduction in the ee since these defect sites are reported to be crucial for the generation of high ee [14].

The decrease in ee as Bi coverage increased was significant during the blockage of step/kink sites. At higher Bi coverage, the decrease in ee was relatively small and coincident with the blockage of {111} terrace sites. Thus, step/kink sites are important to the production of high ee. It has been reported that kink surface sites of metals have an intrinsic chiral structure [47-50]. Chirality for a flat hexagonal supported Pt is shown in Figure 4.2. The effect of a chiral surface on enantioselectivity has also been demonstrated by glucose electro-oxidation experiments using a D- or l-glucose [51]. In the absence of the modifier, kink sites consist of a racemic mixture of R- and S-enantiomers since both sites are equal in their surface density. Surface poisons that formed in kink sites might also therefore exhibit a chirality. When the modifier (CD) interacts preferentially with chiral poison molecules at R-kinks for instance, these sites are then expected to be free of surface poison which allows CD to adsorb on these sites preferentially and produce "CD-kink sites" which cause enantio-induction to form R-enantiomer. When Bi blocks these sites, this inhibits enantiodifferentiation at these sites and a decrease in ee is expected [52].

The present study has demonstrated that kink sites are crucial to obtain the highest values of ee for the Orito reaction using etpy. Unfortunately, from this

study, it is impossible to differentiate between the two competing models of enantio-induction (McBreen [53] and Baiker [7]). Therefore, in what follows, an attempt is made to incorporate the kink site into both models (up to this point, McBreen and Baiker assume a Pt{111} substrate).

It is recalled that the Baiker model interprets the enantioselectivity according to the kinetics of the interaction of alkaloid (CD). By including chiral kink sites [52] (Figure 4.9) instead of Pt{111} terrace sites (adsorption model [7, 54]) one gains perspective concerning the importance of the cinchona carbon atom C₉ in enantiodifferentiation. In this model, CD is mainly proposed to interact with Pt via a quinoline ring parallel to the Pt surface (as usual) at a terrace-step edge via C₉, while the OH substituent at C₉ interacts with the chiral kink sites. It should be noted that changing the OH at C₉ H reduces ee from 97% to 44% [55, 56].

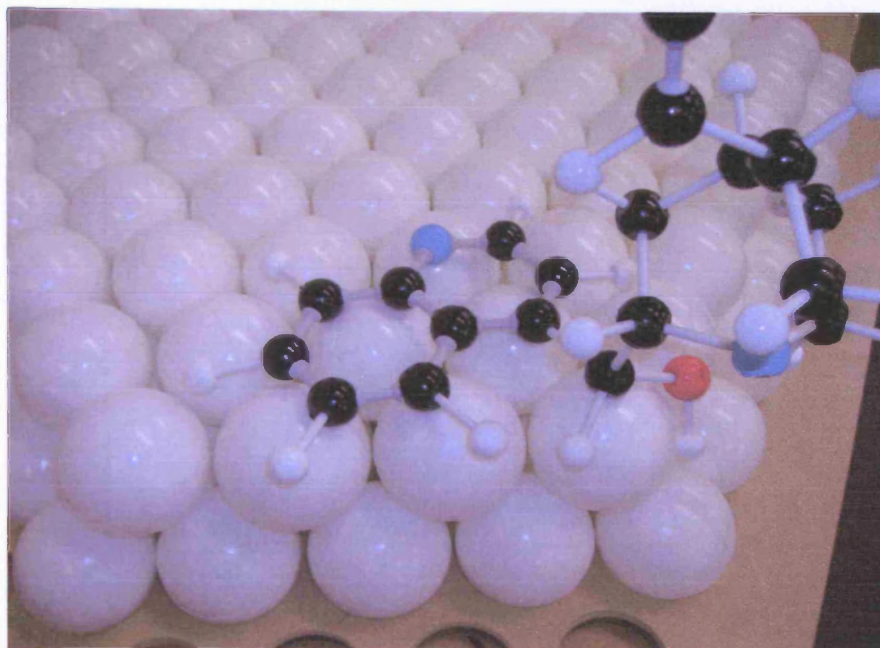


Fig. 4.9 Schematic representing the proposed interaction of CD (open 3) with a Pt kink site; red = O, black = C, blue = N, small white = H, and large white = Pt surface.

The difference in activation energies of the transition state of the Orito reaction when using CD as modifier leads to excess formation of R-ethyl lactate. This is due to Pro-R being more stable than the pro-S transition state (Figure 4.10) (the difference in transition state energy is expected to be small). The proposed interaction of CD with kink sites shown in Figure 4.9 may lead to a lower activation energy which is thought to be responsible for enantio-discrimination effectively forming different transition states (Figure 4.10) upon addition of the second hydrogen atom. This interaction on a chiral site is the rate-determining step and will lead to the formation of R-lactate in excess at kink sites, as shown in Figure 4.11 (adsorption model).

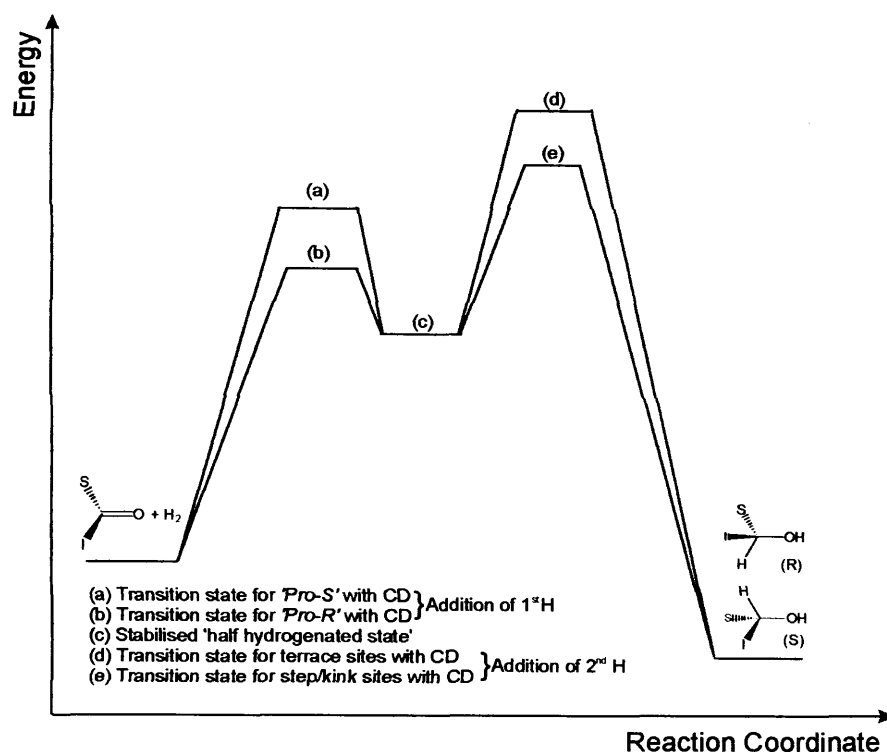


Fig. 4.10 Schematic energy level diagram for the hydrogenation of ethyl pyruvate with and without a cinchona modifier [5, 52].

Applying the McBreen interactions at kink sites will produce the proposed model as shown in Figure 4.12. Again the C₉ carbon is crucial since it “senses” the chirality to the kink. It should also be noted that changes in the “bulkiness” of the substituent attached to C₉ yielded inversion of ee.

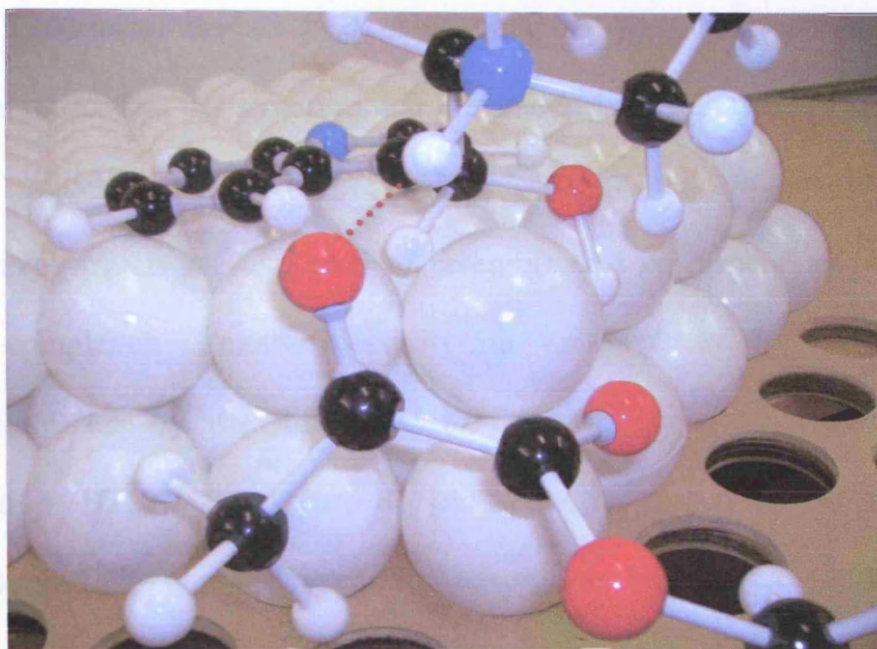


Fig. 4.11 Proposed interaction of CD and pro-R at Pt step sites (kink model) for the Orito reaction (modified Baiker model).

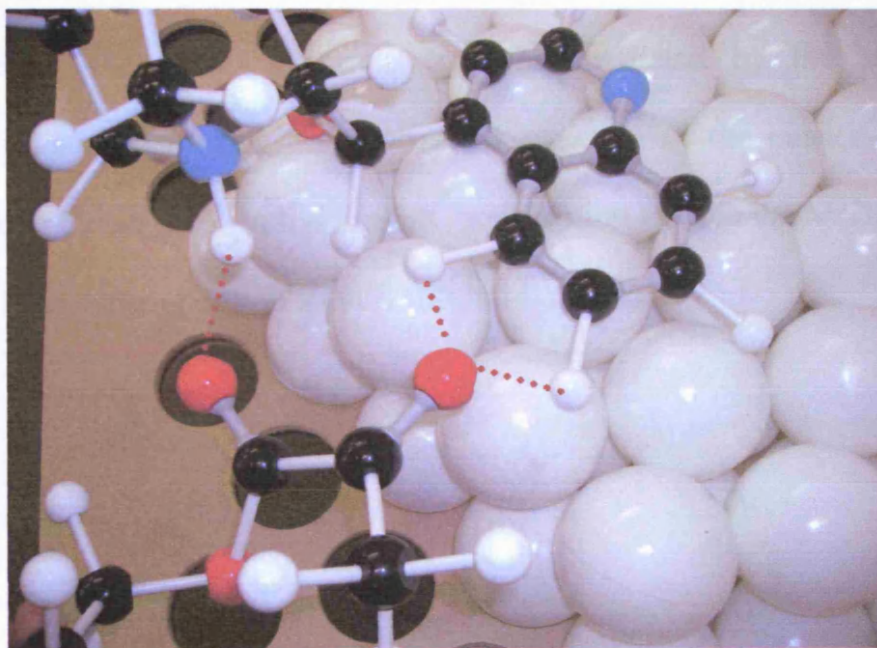


Fig. 4.12 Proposed interaction of CD and pro-R at Pt step sites for the Orito reaction using the McBreen model.

Theoretical studies [57] using quantum chemistry techniques have been used to rationalise the structure and the stability of the reactant-modifier complex. These calculations predict feasible structures of the enantiodifferentiating complexes which are expected to resemble that corresponding to the transition state complexes. Enantioselectivity is assumed to be thermodynamically controlled, i.e. by the difference in free energy in adsorption and complex formation ΔG_{ad}° state of pro-R, $[\text{reactant-CD}]_{ad}^R$ and pro-S, $[\text{reactant-CD}]_{ad}^S$ complexes [57]. Upon CD-reactant adsorption, the relative surface coverage of $[\text{reactant-CD}]_{ad}^R$ (θ_{R*}) and $[\text{reactant-CD}]_{ad}^S$ (θ_{S*}) can be expressed as $\theta_{R*}/\theta_{S*} = \exp(-\Delta\Delta G_{ad}^{\circ}/RT)$. When no kinetic factor is present, the ratio of surface coverage can predict the ratio of enantiomeric product as follows $(R)/(S) = \theta_{R*}/\theta_{S*}$. Therefore, the enantioselectivity can be predicted by the stability of the intermediate complexes. The optimised structure of the enantiodifferentiating is shown in Figure 4.13. In the present modification of both the McBreen and Baiker models, this interpretation should still hold.

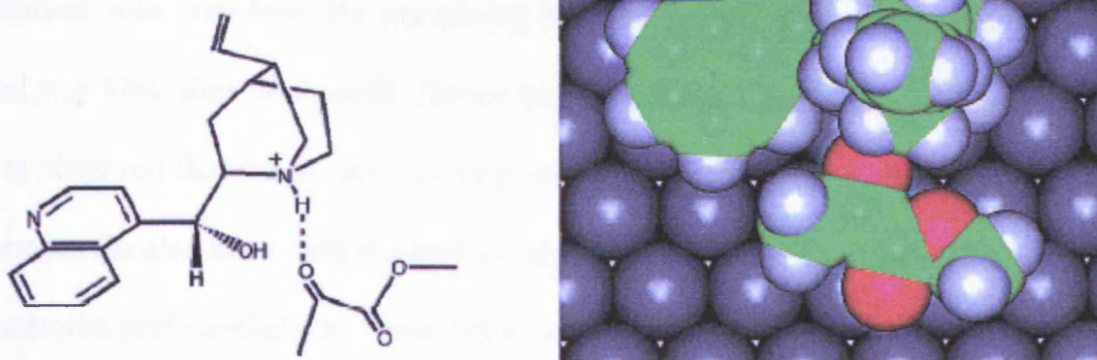


Fig. 4.13 Calculated structure of adsorbed Methyl pyruvate(mepy)-CD, $[\text{Mepy-CD}]_{\text{ad}}^{\text{R}}$ leading to R-methyl lactate upon hydrogenation. C = green, O = red, N = blue H = white, and Pt = gray. Reprinted from reference [57].

4.3.3.2 Sulphur adsorption

Enantioselective hydrogenation of etpy over S modified Pt/G using unsintered and sintered catalysts at 450, 500, and 700 K was also examined. Adsorption of S, as indicated earlier, occurred mainly at terrace sites while step/kink sites remained almost free. For S modified unsintered Pt/G catalysts and catalysts sintered at 450 and 500 K, it was found that as S coverage increased, so the ee increased. This again is ascribed to the significant decrease of {100} terraces observed from CV profiles. Hence both adsorption and annealed data support the contention that Pt{100} sites are detrimental to the achievement of good ee. Hydrogenation reactions over S-Pt/G sintered at 700 K differed from previously reported measurements (unsintered S-modification Pt/G). It was

noticed that by increasing the S coverage, the ee was decreased. CVs of the catalysts showed that the density of {100} terraces relative to the other sintered catalysts was very low. By increasing S coverage, the decrease in {100} terraces and step/kink sites was small. Hence how might the decrease in ee be reconciled? It is observed that the number of step sites are markedly reduced relative to {111} terraces (as also seen with Bi) and in this case (larger {111} planes), it appears that S adsorbs preferentially at steps before adsorption on terraces. Thus, if steps were essential to the achievement of good ee, step adsorption of S would lead to the observed decrease in ee for catalysts annealed at 700 K. Hence all catalysts annealed at $T > 600$ K differ from the other catalysts because they contain more extended {111} terraces.

4.3.3.3 Palladium adsorption

Enantioselective hydrogenation using CD modified Pd-Pt/G catalysts sintered at 700 K showed a decrease in ee, from 57.3% at zero Pd coverage to 1.5% at high Pd coverage ($\theta_{\text{Pd}} = 4.80$) (Table 3.35). The decrease in ee was marked during the blockage of step sites but less evident in the blockage of terrace sites as seen in Figures 3.48 and 3.49 (this behaviour mimics that of rate as seen in Figure 3.47). The decrease in ee behaviour when Pd was adsorbed at steps is reminiscent of that for Bi on Pt/G. The decrease in ee when Pd was used was attributed mainly to Pd catalysed reaction forming S-enantiomer preferentially [9, 41] and to Pd acting as a step/kink site blocker. The formation of S-enantiomer

was likely to be due to the repulsion between C=C and C=O groups in complex (C) (Figure 4.3) [9] which might convert complex (C) to complex (E) which produces S-enantiomer [9]. In enantioselective hydrogenation experiments conducted by Baiker and co-workers [43] over CD modified Pd-Pt/alumina, the ee also decreased as the Pd coverage increased (Figure 4.14). At low coverage of Pd (Pd/Pt atomic ratio = 0 - 0.3), the ee remained almost constant, whilst at higher coverages it decreased significantly, which is rather different from what is found in the present study. It would have been interesting to have seen what might had happened had Baiker *et al.* used a Pd/Pt ratio of 0.5 since such a precipitous fall in rate and ee would then correspond more to the present study. The Pt/Al₂O₃ catalyst used by Baiker *et al.* may have had a different ratio of steps/terraces as compared to the Pt/G used in this work.

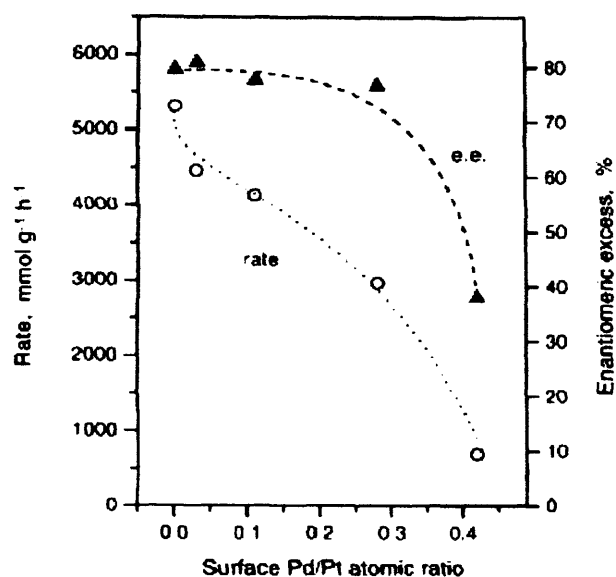


Fig. 4.14 Influence of surface Pd/Pt atomic ratio on the rate and enantioselectivity of etpy hydrogenation over Pd-Pt/alumina (conditions: 100 mg catalyst, 15 mg HCD, 10 ml etpy, 20 ml toluene, 60 bar, 20 °C). Reprinted from [43].

4.3.3.4 Platinum adsorption

Increasing the Pt:Pd ratio in Pt-Pd/G increased the ee of the enantioselective hydrogenation sharply to 38% in the monolayer region whereas it remained almost constant (40 – 42%) in the coverage over one monolayer. Pt, as mentioned earlier produces R-enantiomer while Pd produces S-enantiomer. Hence the first dose of Pt produced a low ee, 27.9%. As the Pt coverage was increase, so the ee increased, reaching a maximum 42% at coverage of $\theta_{\text{Pt}} = 6$. This ee was the same as that for the clean unsintered Pt/G, which means the influence of Pt sites was dominant. In fact, since only one monolayer of Pt leads to the majority of Pt ee being attained, the observed reactivity may be ascribed entirely to rapid

hydrogenation on Pt versus very slow hydrogenation on Pd under reaction conditions with a weak electronic perturbation of the Pt monolayer by Pd leading to a lower ee relative to bulk Pt.

4.3.3.5 Rhodium adsorption

Rhodium deposition on Pt/G sintered at 700 K reduced the ee of etpy hydrogenation sharply, from 57 to 31% as Rh coverage increased ($\theta_{\text{Rh}} = 0 - 1.0$) (Figure 3.57). This decrease coincided with the blockage of step sites and the formation of the second Rh monolayer. By increasing the coverage of Rh to the multilayer range, the ee was within the range 31.7 – 24.4% which was higher than for Pd. Hence we deduce that Rh exhibits an intrinsically lower ee than Pt. In unpublished work from the Attard group [58], unsintered Rh/G was used for etpy hydrogenation and gave rise to an ee of 30% (R-enantiomer in excess using CD as modifier). Publications referring to Rh catalyst use for enantioselective hydrogenation are sparse. It has been reported [44-46] that the presence of CD as modifier in etpy hydrogenation using Rh catalysts induced enantioselectivity which resembles Pt behaviour. Blaser *et al.* have reported that using alumina supported Rh for etpy hydrogenation in the presence of CD as a modifier, afforded an ee of 20 – 30% [40]. Recently, there has been a report that CD modified Rh-Pt/alumina gave an ee of 64% [59]. The highest ee for Rh (80%) has been achieved [60] by Sonderger and Baiker when alumina supported Rh was used in the presence of CD for hydrogenation of 2-hydroxy-1-(4-methoxy-phenyl)-

ethanone. Xiong *et al.* reported [61] an ee of 65% in the hydrogenation of etpy using alumina supported Rh nanocluster catalyst which modified by CD.

4.4 References

1. G.A. Attard, K.G. Griffin, D.J. Jenkins, P. Johnston, P.B. Wells, *Catal. Today*, **114** (2006) 346.
2. G.A. Attard, A. Ahmadi, D.J. Jenkins, O.A. Hazzazi, P.B. Wells, K.G. Griffin, P. Johnston, J.E. Gillies, *Chem. Phys. Chem.*, **4** (2003) 123.
3. Y. Orito, S. Imai, S. Niwa, *Nippon Kagaku Kaishi*, **8** (1979) 1118.
4. T. Mallat, S. Frauchiger, P.J. Kooyman, M. Schürch, A. Baiker, *Catal. Lett.*, **63** (1999) 121.
5. M. Studer, H.-U. Blaser, C. Exner, *Adv. Synth. Catal.*, **345** (2003) 45.
6. J.T. Wehrli, A. Baiker, D.M. Monti, H.-U. Blaser, *J. Mol. Catal.*, **49** (1989) 195.
7. J.T. Wehrli, A. Baiker, D.M. Monti, H.-U. Blaser, *J. Mol. Catal.*, **61** (1990) 207.
8. A. Baiker, *J. Mol. Catal.*, **115** (1997) 473.
9. P.B. Wells, A. Wilkinson, *Top. Catal.*, **5** (1998) 39.
10. P.B. Wells, in: *Surface Chemistry and Catalysis*. (Eds. Carley *et al.*), Kluwer Academic/Plenum Publisher, New York, 2002.
11. E.L. Jeffery, R. Mann, G.J. Hutchings, S.H. Taylor, D.J. Willock, *Catal. Today*, **105** (2005) 85.
12. O.A. Hazzazi. Ph.D. Thesis, Cardiff University, 2002.

13. E. Herrero, V. Climent, J.M. Feliu, *Electrochem. Comm.*, **2** (2000) 636.
14. D.J. Jenkins, A.M.S. Alabdulrahman, G.A. Attard, K.G. Griffin, P. Johnston, P.B. Wells, *J. Catal.*, **234** (2005) 230.
15. M.T. Paffett, G.T. Campbell, T.N. Taylor, *J. Chem. Phys.*, **85** (1986) 6176.
16. J. Clavilier, J.M. Feliu, A. Fernandez-Vega, A. Aldaz, *J. Electroanal. chem.*, **269** (1989) 175.
17. M.J. Llorca, J.M. Feliu, A. Aldaz, J. Clavilier, *J. Electroanal. Chem.*, **351** (1993) 299.
18. G.A. Attard, R. Price, *Surf. Sci.*, **335** (1995) 63.
19. G.A. Attard, R. Price, A. Al-Akl, *Electrochim. Acta.*, **39** (1994) 1525.
20. W.R. Tyson, W.A. Miller, *Surf. Sci.*, **62** (1977) 267.
21. J. Inukai, M. Ito, *J. Electroanal. Chem.*, **358** (1993) 307.
22. M.J. Ball, C.A. Lucas, N.M. Markovic, V. Stamenkovic, P.N. Ross, *Surf. Sci.*, **540** (2003) 295.
23. G.A. Attard, R. Price, A. Al-Akl, *Surf. Sci.*, **335** (1995) 52.
24. R. Gomez, J.M. Feliu, *Electrochim. Acta.*, **44** (1998) 1191.
25. R. Price. Ph.D. Thesis, Cardiff University, 1995.
26. G.A. Attard, A. Bannister, *J. Electroanal. Chem.*, **300** (1991) 467.
27. J. Clavilier, M.J. Llorca, J.M. Feliu, A. Aldaz, *J. Electroanal. Chem.*, **310** (1991) 429.
28. I.M. Sutherland, A. Ibbotson, R.B. Moyes, P.B. Wells, *J. Catal.*, **125** (1990) 77.

-
29. G. Bond, P.A. Meheux, A. Ibbotson, P.B. Wells, *Catal. Today*, **10** (1991) 371.
 30. H.-U. Blaser, H.-P. Jalett, M. Garland, M. Studer, H. Thies, A. Wirth-Tijani, *J. Catal.*, **173** (1998) 282.
 31. J.M. Bonello, F.J. Williams, A.K. Santra, R.M. Lambert, *J. Phys. Chem. B*, **104** (2000) 9696.
 32. J.M. Bonello, R.M. Lambert, N. Kunzle, A. Baiker, *J. Am. Chem. Soc.*, **122** (2000) 9864.
 33. D. Ferri, T. Burgi, K. Borszeky, T. Mallat, A. Baiker, *J. Catal.*, **193** (2000) 139.
 34. D. Ferri, T. Burgi, A. Baiker, *J. Phys. Chem. B*, **108** (2004) 14384.
 35. Z. Liu, X. Li, P. Ying, Z. Feng, C. Li, *J. Phys. Chem. C*, **111** (2007) 823.
 36. D. Ferri, S. Diezi, M. Maciejewski, A. Baiker, *Appl. Catal. A: General*, **297** (2006) 165.
 37. C.A. Harris. Ph.D. Thesis, Cardiff University
 38. E. Herrero, A. Fernandez-Vega, J.M. Feliu, A. Aldaz, *J. Electroanal chem.*, **350** (1993) 73.
 39. M.D. Macia, E. Herrero, J.M. Feliu, *J. Electroanal chem.*, **554-555** (2003) 25.
 40. H.-U. Blaser, H.P. Jalett, D.M. Monti, J.F. Reber, J.T. Wehrli, *Stud. Surf. Sci. Catal.*, **41** (1988) 153.

-
41. S.D. Jackson, B.M. Glanville, J. Willis, G.D. McLellan, G. Webb, R.B. Moyes, S. Simpson, P.B. Wells, R. Whyman, *J. Catal.*, **139** (1993) 221.
 42. E. Toukoniitty, S. Franceschini, A. Vaccari, D.Y. Murzin, *Appl. Catal A: General*, **300** (2006) 147.
 43. T. Mallat, S. Szabó, M. Schürch, U.W. Göbel, A. Baiker, *Catal. Lett.*, **47** (1997) 221.
 44. Y. Huang, Y. Li, J. Hu, P. Cheng, H. Chen, R. Li, X. Li, C.W. Yip, A.S.C. Chan, *J. Mol. Catal. A:Chemical*, **189** (2002) 219.
 45. H. Ma, H. Chen, Q. Zhang, X. Li, *J. Mol. Catal. A:Chemical*, **196** (2003) 131.
 46. Y. Huang, J. Chen, H. Chen, R. Li, Y. Li, L. Min, X. Li, *J. Mol. Catal. A:Chemical*, **170** (2001) 143.
 47. G.A. Attard, A. Ahmadi, J. Feliu, A. Rodes, E. Herrero, S. Blais, G. Jerkiewicz, *J. Phys. Chem. B*, **103** (1999) 1381.
 48. G.A. Attard, *J. Phys. Chem. B*, **105** (2001) 3158.
 49. C.F. McFadden, P.S. Cremer, A.J. Gellman, *Langmuir*, **12** (1996) 2483.
 50. T.D. Power, D.S. Sholl, *Top. Catal.*, **18** (2002) 201.
 51. A. Ahmadi, G. Attard, J. Feliu, A. Rodes, *Langmuir*, **15** (1999) 2420.
 52. D.J. Jenkins. Ph.D. Thesis, Cardiff University, 2003.
 53. S. Lavoie, M.-A. Laliberte, I. Temprano, P.H. McBreen, *J. Am. Chem. Soc.*, **128** (2006) 7588.

-
54. K.E. Simons, P.A. Meheux, S.P. Griffiths, I.M. Sutherland, P. Johnston, P.B. Wells, A.F. Carley, M.K. Rajumon, M.W. Roberts, A. Ibbotson, *Recl. Trav. Chim. Pays-Bas*, **113** (1994) 465.
55. X. Zuo, H. Liu, M. Liu, *Tetrahedron. Lett.*, **39** (1998) 1941.
56. H.-U. Blaser, H.P. Jalett, D.M. Monti, A. Baiker, J.T. Wehrl, *Stud. Surf. Sci. Catal.*, **67** (1991) 147.
57. A. Baiker, *J. Mol. Catal. A*, **163** (2000) 205.
58. G.A. Attard, M. Aban., to be published.
59. H.-B. Cho, J.-S. Kang, Y.-H. Park, *J. Korean Ind. Eng. Chem.*, **17** (2006) 369.
60. O.J. Sonderegger, G.M.W. Ho, T. Burgi, A. Baiker, *J. Catal.*, **230** (2005) 499.
61. W. Xiong, H. Ma, Y. Hong, H. Chen, X. Li, *Tetrahedron: Asym.*, **16** (2005) 1449.

CHAPTER FIVE

SUMMARY AND FUTURE WORK

5.1 Summary and future work

Platinum bimetallic catalysts including Bi-, Pd-, Rh-, and S-Pt/G and Bi-Pt/silica have been investigated in detail using the enantioselective hydrogenation of α -ketoester (etpy) (Orito reaction) as a model system. The main backbone of this study was to examine the influence of catalysts on the title enantioselective reaction which is achieved by blocking step, kink, and terrace sites and then to test activity and selectivity. The Pt{100} terrace sites showed an interesting effect on enantiomeric excess. A mechanism has been developed to interpret the interaction of platinum-modifier-substrate. However, a comprehensive understanding of the Orito reaction mechanism still requires further investigation. The present study has broadened our understanding of the effect of catalyst morphology on enantioselective reactions. Adsorption of Bi, Pd, and Rh, on step/kink sites has been investigated also including the interaction of these sites with CD and ethyl pyruvate in the enantioselective hydrogenation reaction. This interaction was found to be crucial to obtain high enantiomeric excess. The preferential adsorption of S at terrace sites strengthens the result that step/kink sites are responsible for high enantiomeric excess. Models to interpret this interaction were discussed.

The effect of the catalyst morphology on the reaction rate was also investigated. It was found that the adsorption of Bi, Pd, and Rh on the step/kink sites will affect the reaction rate significantly. It is proposed that blocking the step/kink sites with Bi increases the reaction rate by inhibiting the formation of surface poisons (such

as polymer or CO), while Pd and Rh decreases the reaction rate due to the effect of these metals on forming poisoning species. S adsorption was associated with the blockage of terrace sites leaving most of the step/kink sites free which makes them a good environment for forming surface poisons.

However, the following suggestions for experiments are proposed in order to investigate the enantioselective hydrogenation of ethyl pyruvate in more detail:

- Deposition of Ir and Ru on sintered and unsintered 5% Pt/G at different coverages to examine catalyst activity and selectivity by enantioselective hydrogenation of etpy. The investigation of Ir and Ru will almost complete of the elements of 4 and 5 row in group VIII A of the periodic table and their influence on enantioselective reaction.
- Different chiral modifiers such as those containing bulky substituent at C₉ are reported to give both inversion of ee and systematic change in ee at different modifier concentrations depending in Bi coverage [1, 2]. Therefore, using such modifiers with clean Pt/G and Rh, Pd, Bi, S modified Pt/G catalysts may indicate that step + terrace sites again play a crucial a role in chiral inversion during modifier adsorption. CV measurements to confirm whether or not Bi occupies steps or terraces leading to this effect would be useful.

- Catalyst annealing and sintering produced high ee in enantioselective hydrogenation of etpy over Pt/G [3]. This study could be repeated on Pt/alumina and Pt/silica which is expected to produce high ee as well. Unfortunately direct CV measurements in this case cannot be performed due to the insulating nature of the support. Therefore, we have demonstrated that for Bi/Pt/SiO₂ at least, the kinetics of the Orito reaction (once calibrated against a conducting surface) may be used to deduce step + terrace filling by adatoms.
- Acetic acid and toluene showed a high enantioselectivity and reactivity when they were used as a solvents over Pt/alumina and Pt/silica [4]. Baiker *et al.* [5] ascribed activity of acetic acid to it inhibiting formation of etpy dimer in the solution phase. So, using these solvents in enantioselective hydrogenation of etpy over Pt/G and Rh, Pd, Bi, S modified Pt/G catalysts, would one observe similar change in rate as described in the present study?
- Rhodium has showed mild activity and selectivity. Therefore depositing different coverage of Pt, Pd, Ru, and Ir on sintered and unsintered Rh/G to examine activity and selectivity might also be expected to produce interesting results. Hence an expansion of the number of bimetallic systems in general should lead to an optimisation. Bi-metallic surfaces and the Orito reaction is still a relatively unexplored area of study.

- *In situ* spectroscopic measurements in order to detect either 1:1 modifier : substrate interactions and/or surface dimer formation would also be beneficial. The decoration of kink, step, and terrace by Bi, Pd, Rh, and S might also give new information via variation in the vibration spectroscopy of adsorbed etpy on CD.

5.2 References

1. N.F. Dummer, R. Jenkins, X. Li, S.M. Bawaked, P. McMorn, A. Burrows, C.J. Kiely, R.P.K. Wells, D.J. Willock, G. Hutchings, *J. Catal.*, **243** (2006) 165.
2. R.L. Jenkins, N.F. Dummer, X. Li, S.M. Bawaked, P. McMorn, R.P.K. Wells, A. Burrows, C.J. Kiely, G. Hutchings, *Catal. Lett.*, **110** (2006) 135.
3. D.J. Jenkins, A.M.S. Alabdulrahman, G.A. Attard, K.G. Griffin, P. Johnston, P.B. Wells, *J. Catal.*, **234** (2005) 230.
4. M. Bartok, K. Balazsik, G. Szollosi, T. Bartok, *J. Catal.*, **205** (2002) 168.
5. D. Ferri, S. Diezi, M. Maciejewski, A. Baiker, *Appl. Catal. A: General*, **297** (2006) 165.

